KINETIC STUDIES OF LYOTROPIC STRUCTURE FORMATION WITH MICROFLUIDICS AND SMALL ANGLE X-RAY SCATTERING

Dissertation

to be awarded the degree of Doctor rerum naturalium (Dr. rer. nat.) at the Faculty of Biology, Chemistry and Earth Science, University of Bayreuth

submitted by

M. Sc. Carolin Fürst

From Schwäbisch Hall

Bayreuth 2016

Die vorliegende Arbeit wurde in der Zeit von Januar 2012 bis Juli 2016 in Bayreuth am Lehrstuhl der Physikalischen Chemie unter Betreuung von Herrn Professor Dr. Stephan Förster angefertigt.

Vollständiger Abdruck der von der Fakultät für Biologie, Chemie und Geowissenschaften der Universität Bayreuth genehmigten Dissertation zur Erlangung des akademischen Grades eines Doktors der Naturwissenschaften (Dr. rer. nat.).

Dissertation eingereicht am	29.07.2016
Zulassung durch die Promotionskommission	22.08.2016
Wissenschaftliches Kolloquium am	02.12.2016

Amtierender Dekan: Prof. Dr. Stefan Schuster

Prüfungsausschuss:

Prof. Dr. Stephan Förster (Erstgutachter)

Prof. Dr. Jürgen Senker (Zweitgutachter)

Prof. Dr. Peter Strohriegl (Vorsitz)

JProf. Dr. Markus Retsch

Summary ..... **IV**

Zusammenfassung ..... **VII**

1 Introduction and Motivation **1**

2 Fundamentals **4**
2.1 Mesoscale Materials 4
2.1.1 Amphiphiles 4
2.1.2 Self-assembly 6
2.1.2.1 Calculation of Self-assembled Structures *8*
2.1.2.2 Lyotropic Phases *11*
2.1.3 Structural Hierarchies 14
2.2 Microfluidics 15
2.2.1 Motion of Fluids 16
2.2.1.1 The Navier-Stokes Equation *17*
2.2.1.2 No-slip Boundary Condition *23*
2.2.1.3 Pressure Driven Flow *24*
2.2.1.4 The Reynolds Number *30*
2.2.1.5 Diffusion and Convection *31*
2.2.1.6 Péclet Number and Taylor Dispersion *36*
2.2.2 Device Fabrication 38
2.2.2.1 Soft Lithography *39*
2.2.2.2 Hot Embossing *41*
2.2.2.3 Rapid Prototyping *41*
2.3 Small Angle X-ray Scattering 43
2.3.1 Physical Fundamentals of Small Angle X-ray Scattering 43
2.3.2 The Correlation Function 51
2.3.3 Form Factor 53
2.3.4 Structure Factor 55
2.3.5 Analyzation of Measured Scattering Patterns 55
2.3.6 Experimental Set-up 60
2.4 Further Characterization Methods 62
2.4.1 Confocal Laser Scanning Microscopy (CLSM) 63
2.4.2 Cryogenic Transmission Electron Microscopy (Cryo-TEM) 65

3 Experiments **69**
3.1 Small Angle X-ray Scattering 69
3.2 Confocal Laser Scanning Microscopy 69
3.3 Cryogenic Transmission Electron Microscopy 69
3.4 COMSOL Multiphysics 70

4 Results and Discussion **71**
4.1 Materials for Microfluidic Devices 71
4.1.1 Solvent Resistant Chip Materials 71

4.1.2 Optical Properties of Chip Materials ... 75
4.1.3 Microfluidic Device Design ... 79
4.2 Vesicle Formation Pathways Under Very Fast and Very Slow Formation Conditions ... 81
4.2.1 Introduction ... 81
4.2.2 Materials and Methods ... 83
4.2.3 Results and Discussion ... 86
4.2.4 Conclusions ... 106
4.3 Solvent Resistant Microfluidic-Hybrid-Chip for Three-Dimensional Hydrodynamic Flow Focusing ... 107
4.3.1 Introduction ... 107
4.3.2 Results and Discussion ... 108
4.3.2.1 Flow and Device Design ... 108
4.3.2.2 Device Fabrication ... 110
4.3.2.3 Flow Control ... 111
4.3.2.4 Application ... 113
4.3.3 Experimental ... 115
4.3.4 Conclusion ... 116
4.4 Self-assembly of Block Copolymers via Micellar Intermediate States into Vesicles on Time Scales from Milliseconds to Days ... 118
4.4.1 Introduction ... 118
4.4.2 Materials and Methods ... 120
4.4.3 Results and Discussion ... 123
4.4.3.1 Experiments in a 2D-Polyimide Microfluidic Device ... 123
4.4.3.2 Experiments in SIFEL Microfluidic Device ... 128
4.4.3.3 Determination of the Mixing Point ... 131
4.4.3.4 Capillary Interdiffusion Experiments ... 136
4.4.3.5 Cryo-Transmission Electron Microscopy (cryo-TEM) ... 139
4.4.4 Conclusion ... 142
4.5 Kinetic Studies of Biocompatible PEG-(*b*)-PLA Block Copolymers ... 143
4.5.1 Introduction ... 143
4.5.2 Results and Discussion ... 145
4.5.2.1 Experiments in the Microfluidic Device ... 145
4.5.2.2 Experiments in the Glass Capillary ... 151
4.5.2.3 Cryogenic Transmission Electron Microscopy Measurements ... 162
4.5.3 Conclusion ... 164

5 Conclusion and Outlook ... 165

References ... 169

Appendix ... 179

A) Supplementary Information ... 179

B) List of Abbreviations ... 182

C) List of Figures 184

D) List of Tables 191

E) Publications 193

F) Poster Presentations 193

Acknowledgment/Danksagung 194

Declaration/(Eidesstattliche) Versicherungen und Erklärung 196

Summary

The self-assembly of amphiphilic matter is an extensive field describing the evolution of mesoscopic arrangements and is thus fundamental for many applications in medicine, biology, chemistry and physics. However, the underlying processes of self-assembly are still not completely understood. In this dissertation, a combination of two fields, namely microfluidics and small angle X-ray scattering (SAXS), was used to investigate self-assembly processes of amphiphilic surfactants and block copolymers. This combination offers several key advantages, such as the small quantity of sample required, a controlled mixing by diffusion, *in-situ* investigation and the possibility to adjust the temporal resolution due to the translation of time to space in the microfluidic channels.

Initially, appropriate materials were searched for the microfluidic device fabrication. The chip material had to hold many different properties, depending on the intended purposes. Besides the transparency and the ease of device fabrication, a material with low background scattering in small angle X-ray scattering was needed. Therefore, many different materials were tested with the in-house rotating anode. Furthermore, for systems or reactions requiring organic solvents, the device material had to be solvent resistant, in order to prevent the channel from swelling, resulting in the alteration of the chip geometry and thus the disruption of the flow profile. Subsequently, the materials were tested for their solvent resistance.

The first kinetic process analyzed in a microfluidic device was the self-assembly of an anionic and a zwitterionic surfactant in water. The experiments were performed in a NOA81 based microchip with a perpendicular channel cross and an adjacent meander. The anionic surfactant, lithium perfluorooctanoate, formed spherical micelles in water above the CMC (critical micelle concentration), whereas the zwitterionic tetradecyldimethylamine oxide formed cylindrical micelles. The fast mixing in the microfluidic chip was compared to the slow interdiffusion experiment in the glass capillary. The two experiments showed different structural pathways. In the microchannel the spherical micelles and cylindrical micelles fused instantly when getting in contact and formed disks with 1:1 stoichiometry. Subsequently, the disks grew *via* fusion and developed a larger lateral dimension leading to a lamellar correlation in the SAXS measurements. The mixing of both surfactants in the capillary led to a shift of the original

sphere peak by the fusion of TDMAO cylinder strands with LPFO spherical micelles. This indicated the formation of non-stoichiometric LPFO-rich micelles, which aggregation number increased causing a shift of the scattering peak. Eventually, the disk-like micelles of 1:1 stoichiometry evolved, observed in a lamellar peak in SAXS. In this work, a very good temporal resolution of the early beginnings of the self-assembly process was obtained, followed by an insight into the synergistic effect of microfluidic and small angle X-ray scattering.

In addition, new designs of microfluidic devices were developed and tested in this thesis to overcome the problem of the no-slip boundary condition at the MF-channel walls. For the investigation of the self-assembly process of diblock copolymers, a new three-dimensional flow-focusing hybrid device was developed to meet the requirements, such as no contact between the reagents and the channel walls, solvent resistance of the chip material and low scattering of the device at the analyzed position. Consequently, a solvent resistant perfluoropolyether based material (SIFEL) was used to obtain the mixing component, followed by the use of a thin walled glass capillary with low background scattering, acting as the extension to the main channel, which also served as the analysis component. Furthermore, the sheathing streams in the 3D chip design surrounding the two reactant streams prevented the contact to the channel walls, and thus avoided the disturbance of the self-assembly process induced by the no-slip boundary condition. An additional buffer stream flowing centrically between reactant A and B allowed the control of the position of the mixing point of the two reactants. The predicted flow in the new device was proven by CLSM (confocal laser scanning microscopy). SAXS measurements displayed an enhanced quality of the measurements due to the low background scattering of the hybrid device compared to polyimide MF-chips. Additionally, the new chip design led to a parallel flow of the reagent streams. This feature is advantageous compared to the conventional concentric flow, since SAXS measurements also allowed the measurement in y-direction, therefore increasing the spatial resolution.

Subsequently, the self-assembly processes of the PI_{70}-(*b*)-PEO_{60} diblock copolymer was investigated. First, the polymer was dissolved in dioxane and then mixed with water. The continuous flow experiments in the microfluidic chip revealed that this solvent-induced self-assembly process led to the building of micellar structures by interdiffusion in the first few milliseconds. These micelles arrange into lyotropic phases and the morphological transitions were followed with SAXS in the microfluidic channel.

Different flow rates of the individual streams allowed the access to different time spans after mixing. Calculation showed the fast evolution of spherical micelles within 10 ms after mixing and the arrangement of these micelles after 0.77 s. Eventually, this face centered cubic (FCC) ordering became more pronounced at later positions in the microfluidic channel. These results were compared to slow mixing experiments of PI-(*b*)-PEO/dioxane topped with water in a glass capillary. In these experiments, the concentration gradient scan showed a stronger segregation of the micellar cores at longer time scales. Furthermore, cryo-TEM measurements showed the coexistence of spherical and cylindrical micelles, vesicles and intermediate "jellyfish"-like structures. These measurements confirmed the evolution of spherical micelles to cylindrical micelles, which fused into vesicle bilayers.

Eventually, the kinetic investigations of the self-assembly of PEG-(*b*)-PLA block copolymers were performed. Therefore, two PEG-(*b*)-PLA block copolymers with varying chain lengths were used. Both PEG-(*b*)-PLA block copolymers were studied in the SIFEL-capillary-hybrid chip, exhibited the fast diffusion-driven formation of cylindrical micelles. For the PEG_{217}-(b)-PLA_{532} block copolymer with the higher molecular weight, the microfluidic investigation showed no structural evolution and instead a time dependent capillary experiment was performed. The measurement showed the evolution of cylindrical micelles to vesicles over a long period of time (19 hours). Finally, these experiments were compared to longer period measurements in glass capillaries, as the microfluidic chip measurements only revealed the micelles formation but no further evolution. The capillary scan measurements showed that for all concentrations, the unit cell dimension a increased as the measurements proceeded from the polymer phase towards the water phase. Also, the core radius increased for all concentrations except for the 20 wt% PEG_{84}-(*b*)-PLA_{130}/dioxane, where the core radius decreased due to the effusion of dioxane in the water phase.

Zusammenfassung

Die Selbstorganisation amphiphiler Stoffe ist ein umfangreiches Thema, das die Aggregationen von Partikeln im Mesobereich, beschreibt und somit grundlegend für viele Prozesse mit Anwendungen in der Medizin, Biologie, Chemie und der Physik ist. Diese Prozesse sind jedoch weitestgehend noch nicht erforscht. In dieser Dissertation wurden zwei Methoden kombiniert, die Mikrofluidik (MF) und die Röntgenkleinwinkelstreuung (SAXS), um die Selbstorganisierung von amphiphilen Tensiden und Blockcopolymeren zu untersuchen. Diese Kombination führt zu einigen Vorteilen, wie zum Beispiel geringer Probenverbrauch und kontrollierte Mischbedingungen durch Diffusion. Außerdem können Messungen *in-situ* durchgeführt werden und da im Mikrofluidikkanal die Zeitskala auf eine Längenskala aufgespannt wird, kann die zeitliche Auflösung der Analysemethode gesteuert werden.

Zunächst wurde geeignetes Material für die Produktion von Mikrofluidikchips gesucht. Das Material soll je nach gewünschter Anwendung verschiedene Eigenschaften haben. Neben optischer Transparenz und leichter Herstellung, war es wichtig ein Material mit geringer Hintergrundstreuung im Röntgenkleinwinkelbereich zu finden. Dafür wurden verschiedenste Polymere mit der hauseigenen Drehanode analysiert. Des Weiteren wurde das Chipmaterial auf ihre Lösungsmittelstabilität getestet. Das Material sollte im Lösungsmittel nicht quellen und somit nicht die gewollte Geometrie des Chips und dessen Flussprofil verändern.

Mit einem geeigneten Mikrofluidikchip bestehend aus NOA81 wurde die Selbstassemblierung eines anionischen und eines zwitterionischen Tensids in Wasser untersucht. Das Chipdesign bestand aus einem rechtwinkligen Kanalkreuz und einem anschließenden langen Mäander. Das anionische Tensid, Lithiumperfluoroctanoat, bildet kugelförmige Mizellen bei einer Konzentration oberhalb der kritischen Mizellkonzentration (CMC), wobei das zwitterionische Tensid, Tetradeclydimehtylaminoxid, zylindrische Mizellen bildet. Für die kinetische Untersuchung wurden zwei verschiedene Experimente miteinander verglichen, die schnelle Mischung im MF-Kanal und die langsame diffusive Mischung in der Glaskapillare. Die Experimente zeigten unterschiedliche Verläufe der Strukturentwicklung. Im Mikrofluidikkanal bildete sich sofort eine neue Struktur von scheiben-artigen Mizellen, an der Grenzfläche von TDMAO und LPFO.

Diese Scheiben wuchsen anschließend durch Fusionierung mit einem stöchiometrischen Verhältnis von 1:1 der Komponenten. Durch die Entwicklung einer größeren lateralen Ausdehnung der Scheiben, beobachtete man eine lamellare Korrelation in den SAXS Kurven. Die Kapillarexperimente zeigten eine Verlagerung des Peaks ausgehend von der Kugelmizelle (LPFO). Durch das Fusionieren von einzelnen TDMAO Zylindersträngen mit den LPFO Kugelmizellen und der daraufhin folgende Anstieg der Aggregationszahl dieser Mizellen, kam es zu der Verlagerung des SAXS-peaks. Schließlich bildeten sich auch im Kapillarexperiment scheiben-artige Mizellen mit einer 1:1 Stöchiometrie von TDMAO und LPFO. Diese wuchsen an und zeigten daraufhin einen lamellaren Peak in der SAXS-Kurve. In den Experimenten konnten sehr frühe Stadien der Selbstassemblierung untersucht werden. Ebenso zeigten diese ersten Messungen das Leistungsvermögen, das durch die Kombination von Mikrofluidik und Röntgenkleinwinkelstreuung erreicht werden kann.

Anschließend, wurden neue Designs entwickelt, um Hürden wie die *no-slip boundary* Bedingung an den Kanalwänden zu überwinden. Um den Selbstorganisationsprozess von Diblockcopolymeren zu untersuchen, wurde ein neuer Hybridchip entwickelt, der zum einen eine dreidimensionale Flussfokussierung ermöglichte und zum anderen einen Kontakt der Reaktanten mit den Kanalwänden durch die dreidimensionale Fokussierung vermied. Es wurde lösungsmittelstabiles Material (SIFEL) zur Chipproduktion verwendet und eine Glaskapillare wurde als Fortsatz für den Hauptkanal angebracht, um eine geringe Hintergrundstreuung bei SAXS Messungen zu erhalten. Somit fand die kontrollierte Mischung der Probe im Bereich des SIFEL-Mikrofluidikchip statt, während die SAXS-messung in der dünnwandigen Kapillare durchgeführt wurde. Außerdem beinhaltete das Chipdesign zusätzliche sogenannte *sheathing streams*, die die beiden Reaktanten umhüllten und somit von den Kanalwänden fernhielten. Ein zusätzlicher Strom floss als Puffer zwischen den beiden Reagenzien. Mit diesem Pufferfluss konnte der Mischpunkt der beiden Reagenzienströme kontrolliert und verändert werden. Das prognostizierte Flussprofil der einzelnen Ströme im Kanal, wurde mit Hilfe der CLSM (confocal laser scanning microscopy) nachgewiesen. SAXS Messungen zeigten eine höhere Qualität der Messung verglichen mit auf Poly(imid) basierenden MF-Chips. Zusätzlich führte das neue Chipdesign zum parallelen Fließen beider Reaktantenströme.

Dieser parallele Fluss ist vorteilhaft im Vergleich zu dem konventionellen konzentrischen Fluss, da bei SAXS Messungen mit einem kleinen Röntgenstrahl (wenige µm) in einem z.B. 100 µm breiten Kanal nicht nur in Flussrichtung sondern auch senkrecht dazu (y-scan) analysiert werden kann. Ein paralleler Fluss führt somit zu einer besseren örtlichen Auflösung in y-Richtung, da die einzelnen Komponenten im Kanal entlang y aufgetrennt sind.

Anschließend wurden mit diesem neuen Chipdesign die Selbstassemblierung von PI_{70}-(*b*)-PEO_{60} Blockcopolymer untersucht. Das Blockcopolymer wurde zunächst in Dioxan gelöst und anschließend mit Wasser gemischt. Die SAXS-messungen im Mikrofluidikkanal zeigten, dass dieser Lösungsmittel induzierte Selbstorganisationsprozess in den ersten Millisekunden zur Bildung mizellarer Strukturen führte. Diese Mizellen ordneten sich anschließend zu einer lyotropen Phase an. Es wurden verschiedene Flussraten der einzelnen Ströme induziert, womit verschiedene Zeitspannen erreicht wurden. Mit Hilfe von Berechnungen konnte schließlich eine Strukturentwicklung von sphärischen Mizellen innerhalb von 10 ms und eine Anordnung dieser Mizellen nach 0,77 s beschrieben werden. Diese FCC-Ordnung wurde anschließend im Verlauf der Messung an späteren Messpositionen intensiver. Die Ergebnisse wurden mit langsamen Mischexperimenten in Glaskapillaren verglichen. Dazu wurde PI-(*b*)-PEO/Dioxan mit Wasser überschichtet und der ausgebildete Konzentrationsgradient mit SAXS untersucht. Der Konzentrationsscan entlang der Kapillare zeigte eine stärkere Segregation der Mizellkerne über die Zeit. Cryo-TEM Messungen zeigten eine Koexistenz von Kugel- und Zylindermizellen, sowie Vesikeln und quallen-artige Übergangstrukturen, was die angenommene Entwicklung von sphärischen Mizellen zu Zylindermizellen, welche schließlich zu Vesikel-Doppelschichten zusammenwuchsen, bestätigte.

Für die Untersuchungen des biokompatiblen Poly(ethyleneglykol)-(*b*)-poly(lactid) Blockcopolymers wurden zwei Polymere mit unterschiedlichen Molekulargewichten untersucht. Mit beiden PEG-(*b*)-PLAs wurden MF-Chip Messungen durchgeführt. Die SAXS-messungen zeigten eine schnelle diffusionsgesteuerte Bildung von Zylindermizellen. Bei dem PEG_{84}-(*b*)-PLA_{130} mit dem geringeren Molekulargewicht trat außerdem noch ein Anstieg der Einheitszellendimension auf. Bei dem PEG_{217}-(*b*)-PLA_{532} mit dem höheren Molekulargewicht wurden keine Strukturveränderungen im MF-kanal beobachtet, woraufhin eine zeitabhängige Kapillarmessung durchgeführt wurde.

Die Kapillarmessung zeigte eine Entwicklung von Zylindermizellen zu Vesikeln innerhalb von 19 Stunden. Anschließend wurden die Ergebnisse mit SAXS-messungen des Konzentrationsgradienten in der Glaskapillare durchgeführt, um einen längeren zeitlichen Bereich abzudecken. Die Kapillarmessungen zeigten, dass bei allen Konzentrationen ein Größenanstieg der Einheitszelle auftrat, wenn ausgehend von der Polymerphase in Richtung Wasserphase gemessen wurde. Ebenso stieg der Kernradius der Zylindermizellen für alle Konzentrationen, außer für das 20 wt% PEG_{84}-(*b*)-PLA_{130}, an. Der Kernradius des 20 wt% PEG_{84}-(*b*)-PLA_{130} Blockcopolymers hingegen sank, durch die stärkere Segregation in der Wasserphase.

1 Introduction and Motivation

Nowadays, chemists and physicist are confronted amongst others with one important insight: *Size does matter*. Bulk material in the macroscale behaves different than particles in the mesoscale or molecules in the microscale. Since everyone deals with macroscopic effects every day, these phenomena are normal to us. But these phenomena change dramatically if we decrease the size of the observed material and thus, are surprising and interesting.

If we leave the macroscopic world, we reach the mesoscale. Self-assembly rules this world and producing beautiful ordered structures, such as DNA, proteins, vesicles and many more. Some structures bridge over all three length scales, from the microscopic, over the mesoscopic to the macroscopic world. Examples are biomorphs,[1] or we ourselves as humans, consisting of molecules, assembled to DNA, cells, organs and the whole body. Therefore, the underlying mechanisms and processes are of greatest interest and were investigated during this dissertation by following the self-assembly of amphiphilic matter.

Amphiphiles, like surfactants or block-copolymers, are exciting due to their ability to build structures like micelles, vesicles or at higher concentrations lyotropic structures. These self-assembled structures are useful for many different applications like drug delivery, stabilization in food and cosmetics, the use as detergents, thickeners or as wetting and foaming agents. However, for such applications it is advantageous to produce uniform and customized structures. To this day this is realized by empirical optimization. With the investigation of the fundamental processes, it was tried to change this “try and error” method to a predictable strategy.

The difficulty of this project is the implementation. What kind of analysis method is possible to investigate the early beginnings of a fast reaction, as for example the self-assembly of a surfactant solution? Commonly used techniques for the analysis of structures and particles in the liquid state and with a size range of few nanometers to hundreds of nanometers, such as cryo-TEM (cryogenic transmission electron microscopy), DLS (dynamic light scattering) and SAXS (small angle X-ray scattering), are not suitable for the studies of fast kinetics because of the lacking high temporal resolution. Therefore, a combination of two different methods is necessary to achieve the desired requirements.

Microfluidics combined with small angle X-ray scattering offers many advantages. Only a small quantity of samples is necessary due to microfluidics and the device design can be changed quickly because of the rapid prototyping explained in chapter 2.2.1.9. Furthermore, the combination of Microfluidics with SAXS enables *in-situ* measurements of the sample. The probably biggest benefit is the conversion of the time scale to the length scale. [2] Due to the continuous flow in the microfluidic channel, the progress of a reaction is related to specific positions along the microfluidic device, as illustrated in Figure 1.

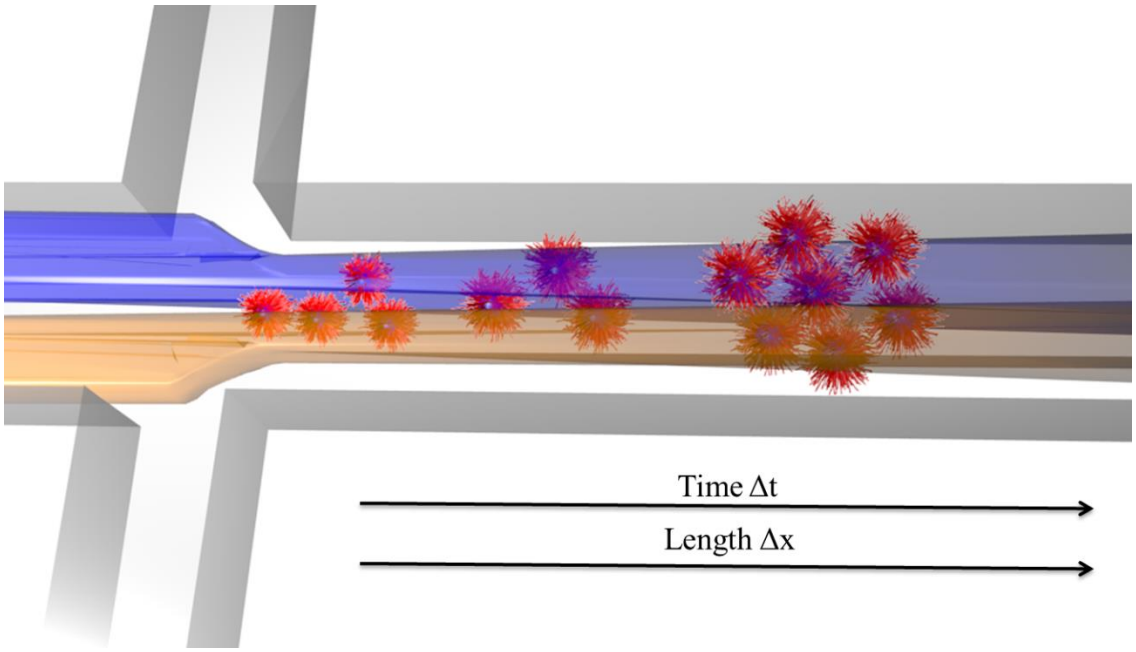

Figure 1. Schematic section of a microfluidic device described in chapter 4.2 with the second channel cross, where two separated streams are focused. The reaction progress of growing micelles forming a hexagonal ordering is schematically shown, demonstrating the transformation of the time scale to the length scale along the channel.

Hence, the possible temporal resolution of the investigation can be adjusted, since it is only restricted by the size of the X-ray beam and the flow velocity. With a smaller beam size a smaller sample volume is analyzed. Therefore, a closer mesh of adjacent measurements can be applied, which increases the temporal resolution. Furthermore, for a given beam size a better temporal resolution can be realized by increasing the flow velocity of the sample. The relation of the flow velocity and the temporal resolution is shown in Eq. (1).

$$\Delta t = \frac{V_F}{v} \quad (1)$$

Δt is the passed time since the start of the reaction, V_F is the flown through volume and v is the overall flow velocity of the pumped in reactants.

In addition, the application of microfluidics leads to defined mixing conditions because the only mixing process perpendicular to the applied flow is diffusion, which is explained in section 2.2.1.5. Given that in the microfluidic channel there is a permanent stable flow leading to a steady state, and the time scale is converted to the length scale, every position can be measured repeatedly and at any time. Also, there is no beam damage of the sample because of the continuous flow delivering "fresh" sample. From this it follows a further advantage, the good signal to noise ratio, as the sample in the microfluidic channel can be measured for long periods of time.

Thus, challenging systems, such as fast reactions or sensitive samples, are suitable for the investigation with SAXS in a microfluidic channel. For example, fast self-assembly processes at early beginnings and with all individual intermediate structures can be analyzed and led to the accomplishment of this work.

2 Fundamentals

2.1 Mesoscale Materials

Meso is usually meant as in-between molecular and solid-state chemistry or in-between covalent chemistry and micro-mechanical approach. Mesophases have at least one spatial dimension in the length scale of 1 to 100 nm and are usually associated with order and self-organization. Due to this length scale of several nanometers new physical properties occur, which are different to the behavior of single molecules or bulk materials. Furthermore, in the mesoscopic scale, there exist more different types of order and structural complexity, than in the macroscopic world. [3]

There are two approaches of building mesoscale structures, the bottom-up and the top-down method. Top-down approaches are lithography, chemical vapor composition and coating techniques. The bottom-up approach is the building of mesoscale systems with self-assembly, which is explained in chapter 0. In the field of mesoscale, the control of the morphology, ordering, size, shape, curvature, texture, surface area and topological defects is of great importance. Moreover, analytical methods, like Transmission Electron Microscopy (TEM), Scanning Electron Microscopy (SEM), Grazing Incidence Small Angle X-ray Scattering (GISAXS) and Small Angle X-ray Scattering (SAXS), for mesoscale materials become more and more important because micro- and macroscopic analysis methods are not suitable. Above all, top-down approaches have a limit in the minimum accessible size, which is several nanometers. [3–5] Hence, self-assembly is an elegant way to achieve ordered structures at a large length scale range. Therefore, we first have to consider, what kind of matter can undergo self-assembly.

Amphiphiles

Amphiphilic matter consists of at least two parts with different chemical and physical properties. [6] One part is lyophilic, which means it is solvent-loving, and the other part is called lyophobic, non-solvent-loving. [7] If the solvent is water, the different parts are called hydrophilic and hydrophobic. Two important representatives of the family of amphiphiles are surfactants and block copolymers, which are both discussed within this work.

Surfactants usually contain at least one polar head group covalently bonded to minimum one alkyl chain, as shown in Figure 2. If the solvent is water, then the polar head group is the hydrophilic part and the alkyl chain tail is hydrophobic part. In general, surfactants have a relatively low molecular weight (<500 Da) and can be ionic (anionic, cationic, zwitterionic,) or nonionic. [7,8] Surfactants or surface-active agents have the ability to segregate to an air water interface and thus, lower the surface tension. A further characteristic of surfactants is the critical micelle concentration (CMC), which is the concentration, where micelles start to form. The CMC depends on the chemical structure of the surfactant, e.g. the alkyl chain length, charge of the polar head group and so on. [7]

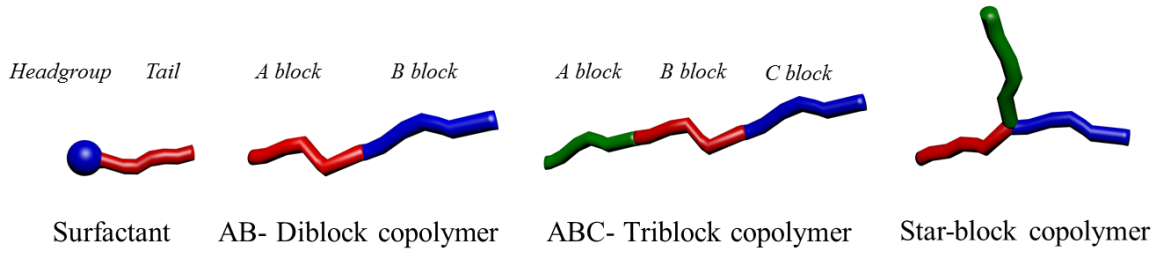

Figure 2. Illustration of the different self- assembly monomers: a surfactant with the blue head group and the red tail and various block copolymers where different colors show the different blocks. Adapted with permission from Blanazs, A., Armes, S.P., Ryan, A.J., Self-Assembled Block Copolymer Aggregates: From Micelles to Vesicles and their Biological Applications. Copyright (2009) John Wiley and Sons and from Schacher, F.H.,Rupar, P.A., Manners, I., Funktionale Blockcopolymere: nanostrukturierte Materialien mit neuen Anwendungsmöglichkeiten. Copyright (2012) John Wiley and Sons [9,10]

Block copolymers consist of two or more different polymer blocks, which are covalently linked together. These polymer blocks have in general a large number of individual repeating units. Block copolymers also have a CMC, at which they start to build micellar aggregates, but the concentration is much lower than for low molecular surfactants. [11] Depending on the type of reaction, various types of block copolymers can be realized, e.g. diblock- (AB), triblock- (ABC) or star-block copolymers, presented in Figure 2. [8,12] In this thesis only AB diblock copolymers were used and hence, are discussed in detail in the following sections.

Self-assembly

The spontaneous arrangement of particles in an ordered way due to the intrinsic properties of matter has been and is still a fascinating field. Self-assembly affects every creature, since proteins, cells, viruses and many more structures are an assembly of numerous molecules and/or particles. [4,13] The occurring interactions during the self-assembly are noncovalent and reversible secondary bindings, such as hydrogen bonding, ligand or coulomb binding and amphiphilic character. [3,14] This reversibility enables the possibility of switching the nanostructured morphologies to external stimuli. [13] Hence, amphiphilic substances as mentioned above can self-assemble due to their bivalent properties. [5]

The lyophilic and lyophobic parts of an amphiphile are connected via a covalent bond and therefore, they cannot decompose to form macroscopic phase separation, as e.g. a water in oil emulsion. This spatial limitation and the immiscibility of the different blocks, lead to the formation of many small closed interfaces. This so called microphase separation is a possibility to avoid undesired states. [11,13] If we assume water as the solvent of our amphiphile, then the hydrophobic part tries to avoid any contact with water, which is called the hydrophobic effect. This effect leads to self-assembly of the amphiphiles into micelles or other structures, at concentrations above the critical micelle concentration (CMC). [8] The hydrophobic effect is besides hydrogen bonds one of the most important driving force for the self-assembly process, especially in soft matter. [13] The self-assembled structures have characteristic sizes of the order of 10 to 100 nm, which is a few times the radius of gyration, R_g, of the constituent blocks. [11,15] These segregated microdomains, especially their morphologies are dependent on the Flory-Huggins parameter, the temperature, the composition of the different parts and the polymerization index. Microdomains themselves form macrolattices, which means they arrange in a periodic way, which is further explained in chapter 0. [16]

As mentioned above amphiphiles are bonded covalently, which means there is a short range attractive force due to the bond. The lyophilic and lyophobic parts of the amphiphile lead to a long range repulsive force. Beside the covalent bond and the lyophobicity and lyophilicity of the amphiphile, there are many more short range attractive (e.g. electroneutrality) and long range repulsive (e.g. coulomb repulsion) forces, depending on the used system. If there are several different forces acting on a system, the system is called “frustrated”, which leads to polymorphism in ordering. [17]

As a consequence to this short range attractive and long range repulsive forces, amphiphiles from assemblies like micelles, disks, cylindrical micelles and vesicles in dilute solutions, as illustrated in Figure 3. [18]

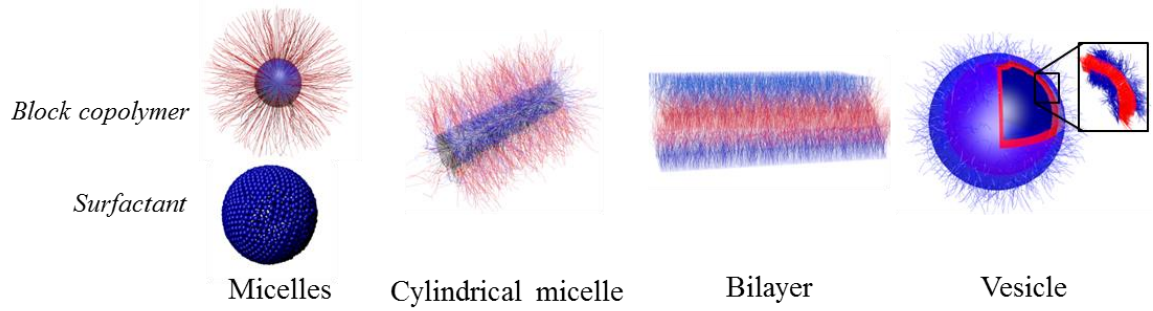

Figure 3. Illustration of the self-assembly of amphiphiles like diblock copolymers or surfactants at low concentration. Adapted with permission from Blanazs, A., Armes, S.P., Ryan, A.J., Self-Assembled Block Copolymer Aggregates: From Micelles to Vesicles and their Biological Applications. Copyright (2009) John Wiley and Sons and from Nagarajan, R., Ruckenstein, E., Theory of surfactant self-assembly: a predictive molecular thermodynamic approach. Copyright (1991) American Chemical Society.[10,19]

Micelles consist of an insoluble core (lyophobic part) and a soluble outer part (lyophilic part) stretching into the solvent. The size of the micelles can be predicted with the scaling law,

$$Z = Z_0 N_A^{\alpha} N_B^{-\beta} \qquad (2)$$

Z is the aggregation number or the number of surfactants or block copolymers in a micelle, $\alpha = 2$, $\beta = 0.8$. N_B is the polymerization degree of the soluble block and N_A is the polymerization degree of the insoluble block. Z_0 is related to the Huggins interaction parameter χ, the monomer volume and the packing parameter p and depends on the mixing enthalpy of block A with the solvent. Z_0 is for many systems one. Hence, the aggregation number and the size of the micelles can be predicted from the polymerization degrees of the polymer blocks or the extended length of the surfactant molecule. [6,7,17,20]

So far, we considered the reason for self-assembly with a virtual prospect. With the Gibbs free energy, it is possible to describe the self-assembly process thermodynamically. Therefore, the different contributions for entropy and enthalpy have to be considered. If we assume micellation of a surfactant in water, the interactions of the lyophobic parts increase, which is energetically favorable and leads to the enthalpic contribution.

Water usually arranges in a loose tetrahedron and the unassociated alkyl chains break up these loose bonds. Hence, locally there is a higher order. Therefore, due to micellation, less unassociated alkyl chains are present to disrupt the water bonds. This is energetically favorable and leads to the entropic contribution. [8] For diblock copolymers the Gibbs free energy is contributed by the interfacial energy of the two blocks and by the loss of entropy due to ordering in the self-assembly process. If the interfacial energy is large and the loss of entropy small, as for example for stiff polymer chains, the minimization of the interfacial area per volume unit exceeds the entropy loss and the system assembles. [21]

2.1.1.1 Calculation of Self-assembled Structures

As already mentioned, besides micelles, also other structures can be observed in diluted systems, as shown in Figure 3.

A typical way to predict the resulting structure in a self-assembly process is to compare the hydrophilic with the hydrophobic part of the system. This relation leads to a curvature, which is described by the mean curvature H and its Gaussian curvature K.

$$H = \frac{1}{2}\left(\frac{1}{R_1} + \frac{1}{R_2}\right) \tag{3}$$

$$K = \frac{1}{R_1 R_2} \tag{4}$$

Whereas R_1 and R_2, the two radii of curvature, are depicted in Figure 4. [21]

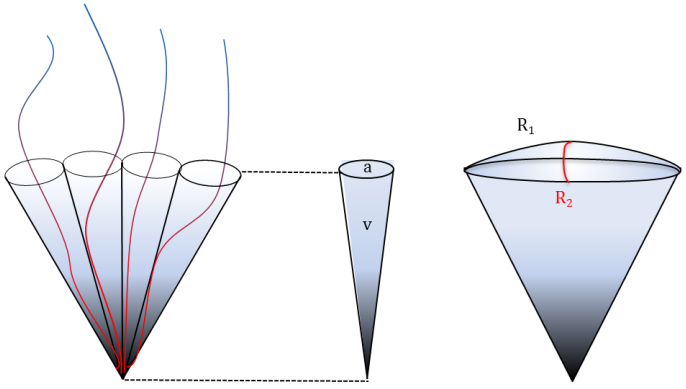

Figure 4. Scheme of the structure determination of block copolymers. Adapted with permission from Antonietti, M., Förster, S., Vesicles and Liposomes: A Self-Assembly Principle Beyond Lipids. Copyright (2003) John Wiley and Sons [21]

With

$$\frac{v}{al} = 1 + Hl + \frac{Kl^2}{3} \tag{5}$$

a relation to the surfactant packing parameter p

$$p = \frac{v}{al} \tag{6}$$

can be made, while v is the hydrophobic volume, a the interfacial area and l the chain length normal to the interface. Therefore, for certain shapes typical values for the curvature and the packing parameter can be calculated, as listed in Table 1. [20–22]

Table 1. Calculations for the different shapes, with $R = R_1 = R_2$. Adapted with permission from Antonietti, M., Förster, S., Vesicles and Liposomes: A Self-Assembly Principle Beyond Lipids. Copyright (2003) Jon Wiley and Sons and Israelachvili, J. N., Mitchell, D. J., Ninham, B. W. Theory of self-assembly of hydrocarbon amphiphiles into micelles and bilayers. *J. Chem. Soc., Faraday Trans. 2* **1976**, *72*, 1525 [20,21]

Shape	$\frac{v}{al}$	**H**	**K**
Sphere	$\frac{1}{3}$	$\frac{1}{R}$	$\frac{1}{R^2}$
Cylinder	$\frac{1}{2}$	$\frac{1}{(2R)}$	0
Bilayer	1	0	0

Consequently, copolymers bearing a large soluble block B, have a small curvature radii R and therefore, form spherical micelles. However, a small soluble block B, leads to a larger curvature radii R and cylindrical micelles are formed preferably. [17,23] Besides the regular structures, also inverse structures exist. Depending on the polarity of the solvent the lyophilic part can point outwards or inwards, leading to regular or inverse structures. [18]

In the recent years especially vesicles (Figure 3, the furthest right) have been in the focus because of their ability to encapsulate not only hydrophilic but also lipophilic substances, due to their double layer. The formation process of vesicles is not yet fully understood and is approached with three different self-assembly processes in literature. [21,24]

The first method describes a two-step mechanism, where first the amphiphile forms a bilayer and second the bilayer closes to form a vesicle. In Table 1 the conditions for the formation of a bilayer are listed. For a block copolymer with a given volume v and length l, bilayers are obtained by adjusting the interfacial area a until the packing parameter reaches unity. This is done by e.g. decreasing the length of the hydrophilic block and hence, by decreasing the hydrophilic/hydrophobic block ratio. The closure of the bilayer to a vesicle is explained by the energetically preference of the amphiphiles to arrange parallel. At low concentration this sheet-like aggregates are very large. Hence, the energy loss due to surface tension effects is high and thus, overcomes the bending energy of the closure of the bilayer to form a hollow vesicle. [21] Theoretical calculations postulated two further procedures for vesicle formation. Both start with the fast formation of small spherical micelles. In the first mechanism, which is especially predicted for lipid molecules and short surfactants in water, the spherical micelles grow larger due to collision and minimization of the interfacial energy of the micelles. The larger oblate micelles, like cylindrical micelles, or open disk-like micelles, curve and close up to form vesicles. In the second mechanism the micelles grow to larger spherical micelles by an evaporation-condensation-like process. At a critical size $\sim(2R_g)$ the copolymers flip-flop and form so-called semi-vesicles. To lower the energy, the large semi-vesicles absorb solvent, which swells the inner lyophilic polymer, building a vesicle. [24–26]

Polymeric vesicles, or so-called polymersomes, are of great interest because of their better stability compared to phospholipids. The higher stability is due to the larger size of the building blocks, which leads to a slower building block exchange and thicker double layers. [27] In addition, they can be tailored due to the already described change of the block length, or change of the chemical structure (e.g. adding different functional groups). Consequently, vesicles with new chemical, physical and biological properties can be obtained. There are many possible fields of application for polymer vesicles in pharmacy, agro-chemistry, sensors and material synthesis. [21] As mentioned above, block copolymers have a much lower CMC than surfactants and hence, are much more stable compared to lipids or surfactants.

This makes them more suitable as nanocontainers for drug delivery. Due to the low CMC the unimers do not dissociate, if they are diluted in the blood stream. Furthermore, the kinetic stability of block-copolymer aggregates can be adjusted on a second to the hour timescale. Thus, the drugs can be transported to the desired release area. [11,18]

Furthermore, macromolecules are particularly well suited for implementing physical, chemical, and biological functions at the same time, because of the adaptability of the different blocks. [17] Besides drug delivery, block copolymers can be used as stabilizers, detergents, thickeners and as wetting and foaming agents. Thus, they are used for emulsion polymerization, stabilization of pigments or the formulation of cosmetics or food. Additionally, self-assembled structures can serve as templates for inorganic materials, like molecular pores, and for many more applications. [6,8,13,18] Also in nature, polymer-like amphiphiles, like proteins or polysaccharides, can be found.

2.1.1.2 Lyotropic Phases

So far, we only considered relatively diluted systems, where the self-assembled structures are dispersed randomly. At higher concentrations, amphiphiles can order into lyotropic structures. [8,13] Surfactants are able to form liquid crystalline phases, which are an intermediate between a completely amorphous system like a liquid and a highly ordered crystal. Liquid crystals have a long-range order, which is only possible if the self-assembled structure is anisotropic, like it is the case for disks and rods. [7,8]

The structure of lyotropic phases in concentrated media depends on the free energy of the self-assembled structures and can be calculated with the self-consistent mean field theory. [17,28] The basic parameters, which determine the size and shape of the self-assembled structures are the degree of polymerization N, whereas

$$N = N_A + N_B \tag{7}$$

the composition f, which means the block length ratio

$$f = \frac{N_A}{N} \tag{8}$$

and the Flory-Huggins interaction parameter χ, describing the strength of the repulsive interaction between both blocks.

The Flory-Huggins interaction parameter is dependent on the temperature and decreases with increasing temperature.

$$\chi \sim \frac{1}{T} \tag{9}$$

Phase diagrams plotting χN against the block length ratio f, as theoretically depicted in Figure 5, show an overview of the different self-assembled structures. In Figure 5, at the weak segregation limit (WSL), $\chi N = 10$, and close to the order-disorder transition (ODT), many different structures are depicted. At higher values of χN, at the strong segregation limit (SSL), the individual structures are stable and can be tailored by choosing the right block length ratio f. [6,17]

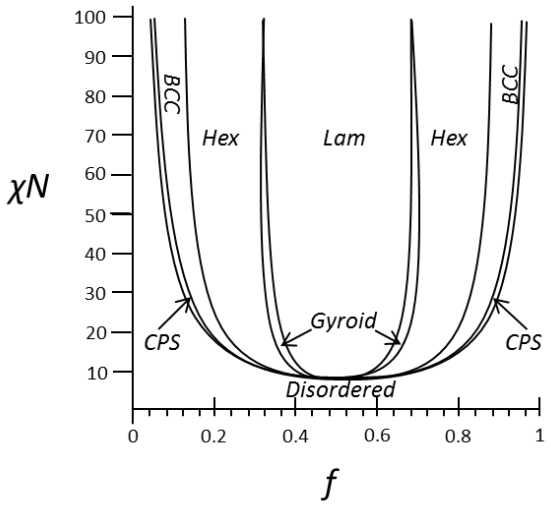

Figure 5. Illustration of an ideal phase diagram of a diblock copolymer. Adapted with permission from Förster, S., Plantenberg, T., From Self-Organizing Polymers to Nanohybrid and Biomaterials. Copyright (2002) John Wiley and Sons [17]

The domain size of such lyotropic structures or microphases is between 10 to 100 nm and depends on the radius of gyration R_g of the polymer coils. [6,8] The phase diagram in Figure 5 already shows few of the many different morphologies, which can occur during microphase separation. Hence, already for simple amphiphiles, like diblock copolymers, the phase behavior can be quite complicated. [6]

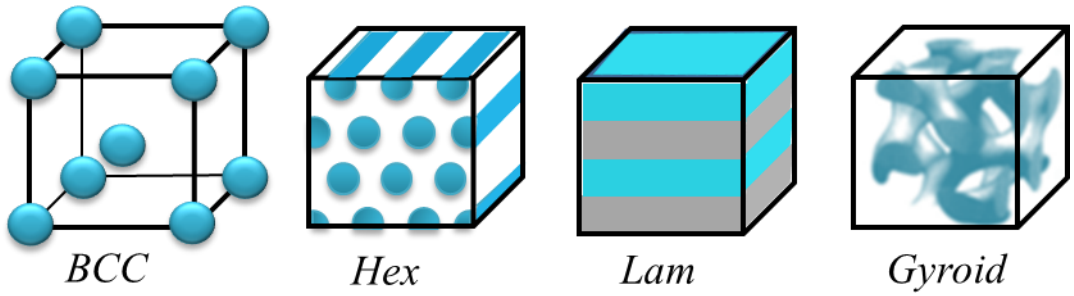

Figure 6. Scheme of classical lyotropic structures of a diblock copolymer. Adapted with permission from Förster, S., Plantenberg, T., From Self-Organizing Polymers to Nanohybrid and Biomaterials. Copyright (2002) John Wiley and Sons [17]

Common lyotropic structures are illustrated in Figure 6. There are several cubic phases, which consist of regularly packed micelles. The left cube in Figure 6 shows the body-centered cubic (BCC) structure. The second cube from left shows hexagonally ordered cylinders (Hex). The lamellar phase (Lam) is consisting of bilayers. The last cube on the right shows the gyroid structure, which is a bicontinous cubic phase. [6,7]

”It is the macromolecular architecture of the amphiphilic copolymers and the different length scales, time-scales, and levels of interaction that it entails, which makes the use of these compounds very attractive.” [18] The different length scales, which can be adjusted, are explained in the next section.

Structural Hierarchies

So far, structures of diluted and more concentrated system were discussed. The evolved structures are connected in a hierarchy, which bridges several orders of magnitude in the length scale, as shown in Figure 7.

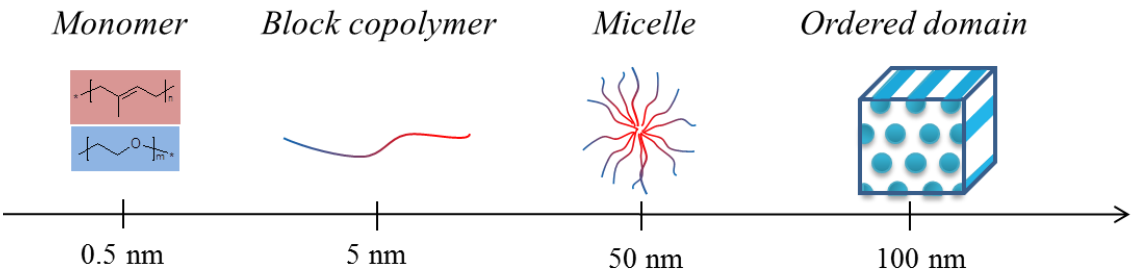

Figure 7. Hierarchy at a length scale of sub nanometer to hundreds of nanometers. Adapted with permission from Förster, S., Plantenberg, T., From Self-Organizing Polymers to Nanohybrid and Biomaterials. Copyright (2002) John Wiley and Sons [17]

The smallest parts in the hierarchy are the used monomers. In Figure 7 Poly(isoprene) and Poly(ethyleneoxide) are shown exemplarily. The monomers are then polymerized to build block copolymers. The polymerization and thus, the degree of polymerization N is dependent on the ratio of the two monomers A and B and the initiator. The second step in hierarchy is the self-assembly of the amphiphile into micelles. It is influenced by the Huggins interaction parameter χ, describing the incompatibility of the two blocks and the aggregation number Z. At higher concentration, e.g. upon solvent evaporation, lyotropic structures, like Lam, Hex or BCC, are formed by undergoing a disorder-order transition. This is dependent on the volume fraction f and the segregation parameter χN. By applying external forces like temperature or shear stress a macroscopic orientation of the lyotropic structures is possible, which leads to “single crystals”. Thus, five orders of magnitude can be adjusted during the organization of mesoscale materials. [6,18]

2.2 Microfluidics

Microfluidics (MF) is a field which deals with the transport phenomena of small volumes of fluids. Therefore, the liquids or gases are pumped through microfluidic channels which have at least one dimension in the micrometer or even in the nanometer range. Due to these small dimensions, different properties occur compared to macroscopic fluid mechanics. This can be described by the scaling laws, where the change of physical quantities is expressed by changing the size l. For example, if the size of the system is decreased, the surface forces become more dominant compared to the volume forces, as demonstrated in equation (10).

$$\frac{surface\ forces}{volume\ forces} \propto \frac{l^2}{l^3} = l^{-1} \underset{l \to 0}{\longrightarrow} \infty \tag{10}$$

Hence, with this different behavior at small length scales, microfluidics opens a field of new phenomena and research possibilities. [29,30]

Microfluidics was first mentioned by Manz in the 1990's in his paper describing a micro-total analysis system (µ-TAS). [31] However, it took more than ten years until microfluidics experienced a boom due to the demands in biology and medicine for systems simulating the behavior in small channels, e.g. blood vessels, and the interest in the behavior of fundamental processes in biology, physics and chemistry. Furthermore, the possibility to produce channels in micrometer scale range and the idea of lab-on-a-chip systems, opened the success to microfluidics. [30,32]

The origin of microfluidics can be mainly found in silicon-based microelectronics, but also molecular analysis systems, like Gel Permeation Chromatography (GPC), High Performance Liquid Chromatography (HPLC) and Capillary Electrophoresis (CE), smoothed the way for microfluidic devices, since they also manipulate little amounts of fluids. Besides the classical microfluidic chip materials, glass and silicon, polymer-based materials were developed rapidly. Lower costs and faster production of polymer-based microfluidic chips promised disposable lap-on-a-chip systems for fast diagnostics.

Given that microfluidics deals with small volumes of fluids, it leads to several advantages. First of all, only small quantities of samples or reagents are needed. This is especially benefiting if expensive, hazardous or rare liquids are investigated. In addition, microfluidic devices can be integrated, for example in biological systems. The small-sized microfluidic devices are portable and can operate parallel or in subsequent processes, e.g. lab-on-a-chip. Hence, high-throughput is possible with short analysis and reaction times. The production of microfluidic devices is cost-efficient, especially for the mostly used Poly(dimethylsiloxane) (PDMS) microfluidic chips. Furthermore, it is possible to test new chip designs within 24 hours due to rapid prototyping, which is described in chapter 2.2.1.9. But outstanding and tremendously interesting for research are the physical effects due to the small size in the micrometer range, like laminar flow, diffusion limited mixing processes, fluidic resistance, and surface tension. [33] To understand these properties and effects, the next section describes the physical fundamentals in microfluidics.

Motion of Fluids

In this work no gases were investigated and for the fluid flow no electrokinetic or capillary forces were induced. Therefore, this section mainly describes the fundamentals of pressure-driven liquids.

First, it has to be considered the way the fluid is regarded at the size range of microfluidics. Transport phenomena in fluids are described with conservation laws applied to continua. [29] The continuum hypothesis says that the macroscopic properties of the fluid behave like it is a continuous medium and not like it consists of single molecules, as it is in reality. It obviously depends on the probing volume or the analyzing method. If the probing volume is at the atomic scale, e.g. in Atomic Force Microscope (AFM) or Scanning Tunnelling Microscope (STM) measurements, spatial fluctuations due to the small number of molecules occur. This is exemplarily shown in Figure 8 for density measurements. If the probing volume increases the mesoscopic region is attained. The number of molecules is large enough and a plateau is reached, where the fluctuations are statistically small. Hence, the measured quantities are steady and reproducible. In the macroscopic region external forces can induce slight variations in the fluid.

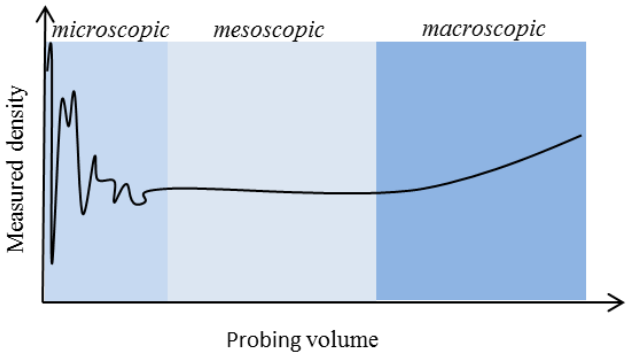

Figure 8. Scheme of the density of a fluid depending on the probing volume. Adapted with permission from Bruus, H., Theoretical Microfluidics, (2008), Oxford University Press, Batchelor, G., K., An introduction to fluid dynamics, 2nd ed, (2000) Cambridge University Press and Tabeling, P., Introduction to Microfluidics, (2010), Oxford University Press [30,34,35]

Accordingly, the fluid is not considered as single molecules but as fluid particles, where a fluid particle has a finite size on the mesoscopic length scale. Given that this size is not exactly defined, fluid mechanics works with physical properties on a per volume basis. Since in microfluidic devices the length scale is in the order of 10 µm or more, the fluid particle size for liquids is comparable small and hence, appears continuous. [30,34,35] With the continuum hypothesis of fluid particles, physical properties can be described with terms of fields, meaning their distribution in the three dimensional domain. [30]

2.2.1.1 The Navier-Stokes Equation

With the continuum hypothesis mentioned above, describing the behavior of fluids in microfluidic systems, now the equations for the transport phenomena are derived.
If one thinks of the motion of fluids in microfluidics, the Navier-Stokes equation is the first association. It can be derived from the second Newtonian law, shown in equation (11). [30,36,37]

$$\vec{F} = m \cdot \vec{a} \tag{11}$$

$\vec{F}$ is the force, $\vec{a}$, the acceleration and m, the mass. As already mentioned, due to the continuum hypothesis fluid mechanics is based on the fluid particle volume.

Hence, the second Newtonian law changes and the fluid dynamics are described with the density ρ and force densities $\overrightarrow{f_J}$.

$$\frac{\vec{F}}{V} = \vec{f_j} = \frac{m}{V} \cdot \vec{a} = \rho \frac{d\vec{v}}{dt} \tag{12}$$

There are two ways to describe the dynamics of fluids, the Eulerian description and the Lagrangian description. The Eulerian description focuses on fixed points $\vec{r}$ in space and observes the fluid flow in time at these points. In the Lagrangian description, one follows an individual fluid particle as it moves through the system, given its position vector as a function of time. Since in a fluid, there is a large amount of particles and not all information is of interest, the Eulerian description is commonly used.

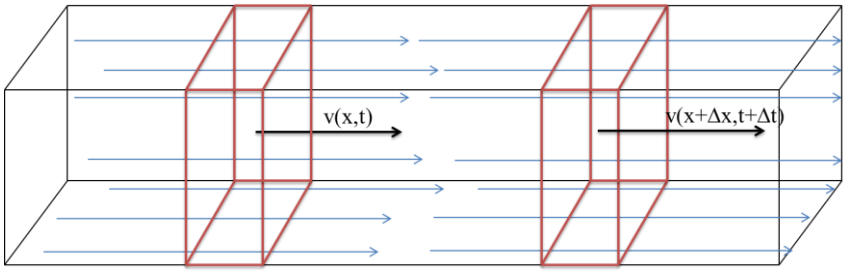

Figure 9. Illustration of a microfluidic channel with acceleration in x-direction. Adapted with permission from Bruus, H., Theoretical Microfluidics, (2008), Oxford University Press and Phillips, R., Kondev, J., Theriot, J., Physical biology of the cell; Copyright (2009) Garland Science-Books [30,38]

If we consider now the acceleration in x-direction (direction of the flow) in a microfluidic channel as shown in Figure 9, and we know that the velocity depends on space and time, it results in the momentum equation.

$$f_{j,x} = \rho \cdot \frac{dv_x}{dt} = \rho \cdot \frac{d}{dt} v_x(x(t), y(t), z(t), t) \tag{13}$$

$$f_{j,x} = \rho \cdot \left(\frac{\partial v_x}{\partial x}\bigg|_{y,z,t} \cdot \frac{dx}{dt} + \frac{\partial v_x}{\partial y}\bigg|_{x,z,t} \cdot \frac{dy}{dt} + \frac{\partial v_x}{\partial z}\bigg|_{x,y,t} \cdot \frac{dz}{dt} + \frac{\partial v_x}{\partial t}\bigg|_{x,y,z} \right) \tag{14}$$

The change of x over t is the velocity in x-direction v_x and hence, for y over t, v_y, and z over t, v_z, respectively.

$$f_{j,x} = \rho \cdot \left(\frac{\partial v_x}{\partial x}\bigg|_{y,z,t} \cdot v_x + \frac{\partial v_x}{\partial y}\bigg|_{x,z,t} \cdot v_y + \frac{\partial v_x}{\partial z}\bigg|_{x,y,t} \cdot v_z + \frac{\partial v_x}{\partial t}\bigg|_{x} \right) \tag{15}$$

In the three-dimensional domain and with

$$\vec{\nabla} = \vec{e_1}\frac{\partial}{\partial x} + \vec{e_2}\frac{\partial}{\partial y} + \vec{e_3}\frac{\partial}{\partial z} \tag{16}$$

we result in the acceleration term,

$$\vec{f_j} = \rho \cdot \frac{d\vec{v}}{dt} = \rho \cdot \left(\vec{v} \cdot \vec{\nabla}\right) \cdot \vec{v} + \frac{\partial \vec{v}}{\partial t} \tag{17}$$

The acceleration of a body, in this case the defined volume elements, is caused by forces acting on the surface (pressure and shear stress) and on the whole volume (body forces).

So far, we have derived the acceleration term on the right-hand side of the Navier-Stokes-equation (17). The individual forces acting on the fluid are described in the following section.

At each infinitesimal small volume element dV the surroundings act onto it with the pressure force $-pdV$, as shown in Figure 10.

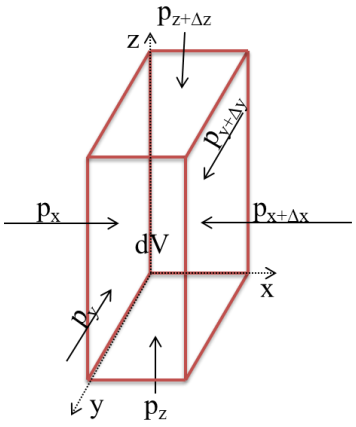

Figure 10. Schematic description of all pressure forces acting on the volume element dV. Adapted with permission from Phillips, R., Kondev, J., Theriot, J., Physical biology of the cell; Copyright (2009) Garland Science-Books [38]

We now consider the overall pressure in x-direction.

$$\delta f_x^p = p_x dydz - p_{x+\Delta x} dydz \tag{18}$$

With the Taylor series,

$$p_{x+\Delta x} \approx p_x + \frac{\partial p}{\partial x} dx \tag{19}$$

equation (18) results in

$$\delta f_x^p = -\frac{\partial p}{\partial x} dxdydz \tag{20}$$

If we now expand this into the three-dimensional domain, we obtain for the pressure force. [38,39]

$$\delta f^p = -\nabla p dV \tag{21}$$

Another force acting on the fluid is friction, caused from the viscosity of the fluid. The relation of friction and viscosity can be imagined with a simple experiment where a fluid is placed between two parallel plates, as shown in Figure 11. One plate is fixed, and the other plate is moving in x-direction with a speed $\vec{v}_z$. Therefore, a force tangent to the plate is required, which is proportional to the viscosity of the fluid, the speed $\vec{v}_z$, the surface area of the plate and inversely proportional to the distance between the two plates. [36]

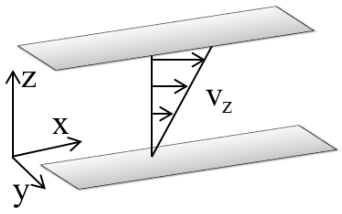

Figure 11. Scheme of a liquid between two plates, whereas the lower is fixed and the upper one is moving with v_z. Adapted with permission from Bruus, H., Theoretical Microfluidics, (2008), Oxford University Press [30]

The shear stress σ is thus the force $\vec{F}$ per area A, equal the viscosity η times the change of velocity $\vec{v}_z$ with dx.

$$\sigma = \frac{\vec{F}}{A} = \eta \frac{d\vec{v}_z}{dx} \tag{22}$$

For the microfluidic experiment we have to consider the viscous forces acting on the elemental volume.

$$\delta \vec{f}_z^{\,v} = -\eta \frac{\partial v_z(x)}{\partial x} dydz\vec{e}_z + \eta \frac{\partial v_z(x+\Delta x)}{\partial x} dydz\vec{e}_z \tag{23}$$

With the Taylor series of the second term, we get [38]

$$\delta \vec{f}_z^{\,v} = \eta \frac{\partial^2 v_z(x)}{\partial x^2} dxdydz\vec{e}_z \tag{24}$$

If we repeat this for y- and z-direction, we obtain

$$\delta f^v = (\eta \nabla^2 \vec{v} + \eta' \nabla(\nabla \cdot \vec{v}))dxdydz \tag{25}$$

Finally, the body forces f acting on the entire body of the fluid must be taken into account. Body forces are for example gravitational force, centrifugal or electrical force. [30] In general only the gravity force f^g is considered. Here, g is the gravitational constant, ρ the density and V the elemental volume.

$$df^g = \rho g dV \tag{26}$$

Summing up equations (17), (21), (25) and (26), it results in

$$-\nabla p dV + (\eta \nabla^2 \vec{v} + \eta' \nabla(\nabla \cdot \vec{v}))dxdydz + \rho g dV = \rho \left[\left(\frac{\partial \vec{v}}{\partial t} \right) + (\vec{v} \cdot \vec{\nabla})\vec{v} \right] \tag{27}$$

The continuity equation describes the conservation of mass in classical mechanics, for hydrodynamics. Here, the temporal change of a given quantity in a fluid particle volume can be described with the flux of this quantity through the surface of the volume.

$$\frac{\partial \rho}{\partial t} + \nabla \cdot (\rho \cdot \vec{v}) = 0 \tag{28}$$

If we assume an incompressible fluid, then the density ρ is constant and the mass in the fluid particle volume does not change. [37,40]

$$\frac{\partial \rho}{\partial t} = 0 \tag{29}$$

It follows, [40]

$$\nabla \cdot \vec{v} = 0 \tag{30}$$

This simplifies equation (25) to

$$\delta F^{v} = \eta \nabla^2 \vec{v}\, dV \tag{31}$$

This leads to the Navier-Stokes equation:

$$\rho \left[\frac{\partial \vec{v}}{\partial t} + \vec{v} \cdot \vec{\nabla} \cdot \vec{v} \right] = -\nabla p + \eta \nabla^2 \vec{v} + \rho g \tag{32}$$

The left-hand part of the equation is the acceleration term, whereas the right side describes the forces acting on the fluid. [40]

In microfluidic experiments usually low flow velocities are applied. Hence, the non-linear term can be neglected, resultant the linear Stokes equation (33) or in the time dependent linear Stokes equation (34) [30]

$$0 = -\nabla p + \eta \nabla^2 v + f \tag{33}$$

$$\rho \frac{\partial v}{\partial t} = -\nabla p + \eta \nabla^2 v + f \tag{34}$$

Due to the linearity of the Stokes equation and with several simplifications it is possible to obtain analytical solutions for low flow velocities (Stokes flow). [30]

2.2.1.2 No-slip Boundary Condition

The no-slip boundary condition is an assumption or restriction for the solution of the Navier-Stokes equation and describes the fluid flow at the solid liquid interface. [32,41] It says that the tangential velocity of the fluid is zero close to the channel wall, i.e. there is no relative motion of the fluid along the solid wall. [41,42] Two explanations are described for the no-slip boundary condition. On a molecular basis it is assumed that the intermolecular forces between the liquid molecules and the solid ones give a bond. The second explanation is that the solid surfaces are rough on a microscopic scale. Experiments of Pearson and Petrie with polymer melts showed that no-slip is valid for moderate velocities (shear rates) but that there is slip at high velocities. The question of what happens if fluids are not wetting the solid surface and how roughness influences the slip are discussed in many publications.[41] Furthermore, in the recent years in many papers a slip boundary condition is described. This slippage is described with the effective slip length b, which is already mentioned in the linear boundary condition of Navier in 1823. [43] However, it is concluded that the no-slip boundary condition is a good approximation for pressure driven microfluidics with channel sizes in the micrometer range. [32]

In Figure 12 the different flow profiles at different slip conditions are illustrated. The first shows the Couette flow or shear flow at no-slip condition. [43] Here, one plate is fixed and the other is pulled with a certain shearing rate. In the second image, the same experiment is assumed but with two fixed plates. There, slip occurs at the liquid-solid interface, described with the slip length b. If one assumes a perfect smooth surface of the solid, the perfect slip flow profile is assumed like in the third image.

And finally, the pressure driven flow, which is obtained for the microfluidic experiments of this thesis, is shown in the fourth image. Due to the no-slip condition at the fixed channel walls, a parabolic shaped flow arises, called Poiseuille flow.

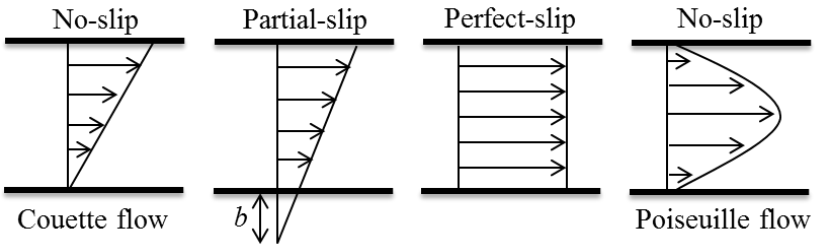

Figure 12. Chart of the different flows and slips. Adapted with permission from Bruus, H., Theoretical Microfluidics, (2008), Oxford University Press and Lauga, E., Microfluidics: The No-Slip Boundary Condition. Copyright (2007) Springer [30,43]

2.2.1.3 Pressure Driven Flow

The so called Poiseuille or Hagen-Poiseuille flow is a steady state flow induced by a pressure gradient in the microfluidic channel. It is an analytical solution of the Navier-Stokes equation. This steady state flow means, the fluid is moving in a constant speed or is at rest. Hence, the acceleration and velocities derivatives are zero.

$$\frac{\partial v}{\partial t} = 0 \tag{35}$$

If we assume gravitational force as the only external force, then equation (35) and (34) lead to the simple equation [39]

$$\nabla p = \rho g \tag{36}$$

For an incompressible fluid like water, and in the negative z-direction, the integration of eq. (36) results in

$$p(z) = p^* - \rho g z \tag{37}$$

Here, p^* is the pressure at level $z = 0$. This z-dependent part is defined with the hydrostatic pressure p_{hs}. Thus, in microfluidics p_{hs} is the only contribution of gravity and hence, the gravitational body force is cancelled by the gradient of p_{hs}.

We now consider two infinite parallel plates, as shown in Figure 13. The distance between the two parallel plates is the channel height h and the system is translation invariant in x- and y-direction. Hence, the velocity field can only depend on z.

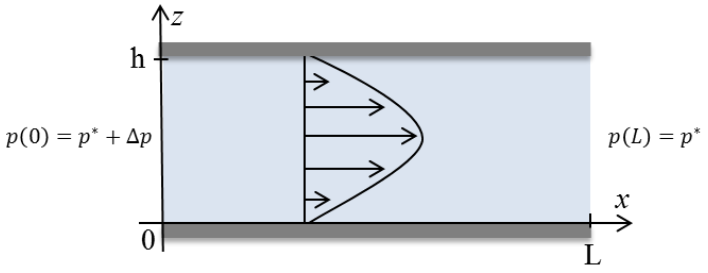

Figure 13. Pressure driven flow between two infinite parallel plates. Adapted with permission from Bruus, H., Theoretical Microfluidics, (2008), Oxford University Press [30]

The movement of the fluid between the parallel plates is induced by a pressure drop Δp in x-direction, hence, only the x-component of the velocity field is non-zero.

$$\vec{v}(\vec{r}) = v_x(z)\vec{e}_x \tag{38}$$

The pressure drop Δp is constant over the length L (Figure 13) of the channel, i.e.

$$p(0) = p^* + \Delta p \tag{39}$$

and [30]

$$p(L) = p^* \tag{40}$$

Furthermore, the steady state (eq. (35)) and the symmetry, lead to

$$(\nabla \cdot \vec{v})\vec{v} = 0 \tag{41}$$

Thus, the Navier-Stokes equation is then simplified to

$$0 = -\nabla p + \eta \nabla^2 [v_x(z)\vec{e}_x] \tag{42}$$

As already mentioned the velocity fields of y and z are zero. Hence, the pressure field only depends on x; $p(\vec{r}) = p(x)$.

$$\eta \partial_z^2 v_x(z) = \partial_x p(x) \tag{43}$$

With the boundary conditions (eq. (39),(40)) for the pressure we get

$$p(\vec{r}) = \frac{\Delta p}{L}(L - x) + p^* \tag{44}$$

This leads to the second order partial differential equation

$$\partial_z^2 v_x(z) = -\frac{\Delta p}{\eta L} \tag{45}$$

We now take into consideration the no-slip condition as described in 2.2.1.2,

$$v_x(0) = 0 \tag{46}$$

$$v_x(h) = 0 \tag{47}$$

Thus, we obtain a **parabola** solution for the velocity in x-direction.

$$v_x(z) = \frac{\Delta p}{2\eta L}(h - z)z \tag{48}$$

Finally, the flow rate Q through a section of width w is found as [30]

$$Q = \int_0^w dy \int_0^h dz \frac{\Delta p}{2\eta L}(h - z)z = \frac{h^3 w \Delta p}{12\eta L} \tag{49}$$

We consider now a cylindrical shaped channel, like in a glass capillary, with the cylindrical co-ordinates (x, r, Φ) as shown in Figure 14.

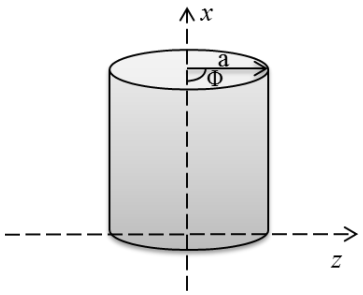

Figure 14. Cylindrical channel with radius r. Adapted with permission from Bruus, H., Theoretical Microfluidics, (2008), Oxford University Press [30]

$$\begin{aligned} x &= x \\ y &= r\,cos\Phi \\ z &= r\,sin\Phi \end{aligned} \tag{50}$$

With the orthonormal basis vectors

$$\begin{aligned} \vec{e}_x &= \vec{e}_x \\ \vec{e}_r &= +\cos\Phi\,\vec{e}_y + \sin\Phi\,\vec{e}_z \\ \vec{e}_r &= \sin\Phi\,\vec{e}_y + \cos\Phi\,\vec{e}_z \\ \nabla^2 &= \partial_x^2 + \partial_r^2 + \frac{1}{r}\partial_r + \frac{1}{r^2}\partial_\Phi^2 \end{aligned} \tag{51}$$

Again, the symmetry considerations reduce the velocity field to

$$\vec{v}(\vec{r}) = v_x(r)\vec{e}_x \tag{52}$$

leading to the differential of second order

$$\left[\partial_r^2 + \frac{1}{r}\partial_r\right] v_x(z) = -\frac{\Delta p}{\eta L} \tag{53}$$

This inhomogeneous equation can be solved by summation of the general homogeneous solution, as shown in eq. (54).

$$\begin{gathered} v_x'' + \frac{v_x'}{r} = 0 \\ v_x(r) = A + B\ ln\ r \end{gathered} \tag{54}$$

and the particular solution to the inhomogeneous equation.

$$v_x(r) = -\frac{\Delta p}{4\eta L} r^2 \tag{55}$$

With the boundary conditions

$$\begin{gathered} v_x(a) = 0 \\ v_x'(0) = 0 \end{gathered} \tag{56}$$

we get

$$v_x(r, \Phi) = -\frac{\Delta p}{4\eta L}(a^2 - r^2) \tag{57}$$

for the velocity field.

The flow rate is then,

$$Q = \int_0^{2\pi} d\Phi \int_0^a dr\, r \frac{\Delta p}{4\eta L}(a^2 - r^2) = \frac{\pi}{8}\frac{a^4}{\eta L}\Delta p \tag{58}$$

or

$$Q = \frac{\Delta p}{R} \tag{59}$$

with R as the hydraulic resistance.

$$R = \frac{8\eta L}{\pi a^4} \tag{60}$$

Thus, the resistance R is reciprocal to the fourth power of the radius of the channel. Hence, the resistance increases tremendously if the radius decreases. [30,33,36]

Besides the flow in cylindrical glass capillaries, rectangular shaped channels were used in this thesis. This rectangular shape occurs due to the fabrication method, soft lithography, which is described in chapter 2.2.1.7. We consider rectangular channels with small aspect ratio, meaning the channel height (h) is about the size of the channel width (w), but with $w > h$, as shown in Figure 15.

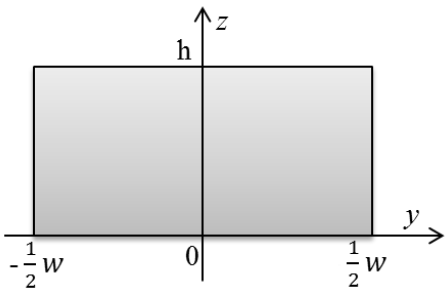

Figure 15. Cross-section of a rectangular shaped channel with height h and width w. Adapted with permission from Bruus, H., Theoretical Microfluidics, (2008), Oxford University Press [30]

Therefore, the velocity field in the rectangular channel is

$$v_x(y,z) = \frac{4h^2\Delta p}{\pi^3 \eta L} \sum_{n,odd}^{\infty} \frac{1}{n^3} \left[1 - \frac{\cosh(n\pi \frac{y}{h})}{\cosh(n\pi \frac{w}{2h})}\right] \sin\left(n\pi \frac{z}{h}\right) \tag{61}$$

And the resistance R is then, [30,33]

$$R = \frac{12\eta L}{wh^3}\left[1 - \frac{h}{w}\left(\frac{192}{\pi^5}\sum_{n=1,3,5}^{\infty}\frac{1}{n^5}tanh\left(\frac{n\pi w}{2h}\right)\right)\right]^{-1} \quad (62)$$

For further reading and the derivations of the last two equations for rectangular channels it is referred to Bruus H. *Theoretical microfluidics*; Oxford University Press: Oxford, 2008.

2.2.1.4 The Reynolds Number

The representation of a physical equation by a smaller number of dimensionless parameters simplifies the equation and furthermore provides insight to relevant physical properties. Therefore, in microfluidics many non-dimensional numbers are used to quantify physical properties. [36] The Reynolds number Re derives from the non-dimensionalization of the Navier-Stokes equation. It associates the inertial forces F_i to the viscous forces F_v.

$$Re = \frac{F_i}{F_v} = \frac{\rho D_h v}{\eta} \quad (63)$$

with

$$F_i = \rho(v \cdot \nabla)v \approx \frac{\rho v^2}{D_h} \quad (64)$$

$$F_v = \eta\nabla^2 v \approx \frac{\eta v}{{D_h}^2} \quad (65)$$

Whereas ρ is the density, D_h is the hydraulic diameter depending on the geometry of the microfluidic channel, typically in the scale of micrometers, v is the flow velocity and η is the viscosity. [33,40] For low Reynolds numbers, the viscosity has stronger influence than inertial forces leading to a laminar flow in the microfluidic channel. Whereas, at high Reynolds numbers turbulent flow occurs. The critical point at which the flow is always laminar, is usually below Re 1700 to 2300. [44]

As already mentioned in chapter 2.2.1.1 at low flow and hence, at low Reynolds number the inertial terms can be neglected. Furthermore, if we assume stationary flow ($\frac{\partial v}{\partial t} = 0$), the Stokes equation simplifies to [45]

$$\nabla p = \eta \nabla^2 v \tag{66}$$

Hence, the speed of flow is simply proportional to the forces exerted on the fluid. [45]

2.2.1.5 Diffusion and Convection

Mixing of miscible fluids with pressure driven flow in microfluidic channels can be described with convection along the microfluidic channel and diffusion transverse to the flow. Convection is the momentum transport of the bulk flow by a fluid. [46] Diffusion is mixing due to thermally induced random motion of particles with a concentration gradient in a volume. It is called Brownian motion. [30] As described in chapter 2.2.1.4, in microfluidics laminar flow dominates. Hence, due to the absence of turbulence, transverse mixing of fluid streams, which are in contact to each other, only occurs through diffusion. [33,47] Diffusion is described with the constant-step random-walk model. We assume a particle performing a number of continuous steps which are unrelated to each other. Each step i takes the same time τ and moves the same distance Δx_i with the step length l. Since the particle performs a random walk, the moved distance can be negative or positive.

$$\Delta x_i = \pm l \tag{67}$$

After the particle has executed N steps at time $t = N\tau$, the position x_N is defined by

$$x_N = \sum_{i=1}^{N} \Delta x_i \tag{68}$$

If we now consider M random walks ending at $x_N^{(j)}$, with $j = 1,2,\dots,M$, each random walk consists of N random steps $\Delta x_i^{(j)} = \pm l$.

The mean value of x_N is then,

$$\langle x_N \rangle \equiv \frac{1}{M}\sum_{j=1}^{M} x_N^{(j)} = \frac{1}{M}\sum_{j=1}^{M}\left(\sum_{i=1}^{N}\Delta x_i^{(j)}\right) = \sum_{i=1}^{N}\left(\frac{1}{M}\sum_{j=1}^{M}\Delta x_i^{(j)}\right) = \sum_{i=1}^{N}\langle \Delta x_i \rangle = 0 \qquad (69)$$

Equation (69) equals zero because the probability of stepping $+l$ or $-l$ is the same. Hence, this equation does not describe the quantity of diffusion kinematics. Therefore, the squared value of the particle displacement is calculated. For the product term different summation i, k are used.

$$\begin{aligned}\langle x_N^2 \rangle \equiv \frac{1}{M}\sum_{j=1}^{M}\left[x_N^{(j)}\right]^2 &= \frac{1}{M}\sum_{j=1}^{M}\left(\sum_{i=1}^{N}\Delta x_i^{(j)}\right)\left(\sum_{k=1}^{N}\Delta x_k^{(j)}\right) \\ &= \frac{1}{M}\sum_{j=1}^{M}\sum_{i=1}^{N}\sum_{k=1}^{N}\Delta x_i^{(j)}\,\Delta x_k^{(j)}\end{aligned} \qquad (70)$$

Now the so called diagonal terms, $k = i$, and the offdiagonal terms, $k \neq i$, are collected.

$$\langle x_N^2 \rangle = \frac{1}{M}\sum_{j=1}^{M}\left(\sum_{i=1}^{N}\left[\Delta x_i^{(j)}\right]^2 + \sum_{i=1}^{N}\sum_{k\neq i}^{N}\Delta x_i^{(j)}\,\Delta x_k^{(j)}\right) = Nl^2 + \sum_{i=1}^{N}\sum_{k\neq i}^{N}\langle \Delta x_i \Delta x_k \rangle \qquad (71)$$

Since, $k \neq i$, Δx_i and Δx_k are statistically independent. Hence, $(+l)(-l) = (-l)(+l) = -l^2$ and $(+l)(+l) = (-l)(-l) = l^2$ have the same probability and equation (71) simplifies to [30]

$$\langle x_N^2 \rangle = Nl^2 \qquad (72)$$

From equation (72) and (69) the diffusion length l_{1D} in the 1D is

$$l_{1D} \equiv \sqrt{\langle x_N^2 \rangle - \langle x_N \rangle^2} = \sqrt{N}l \qquad (73)$$

with $t = N\tau$.

$$l_{1D}(t) = \sqrt{\frac{t}{\tau}}l = \sqrt{\frac{l^2}{\tau}}t = \sqrt{2Dt} \tag{74}$$

Here, D is the diffusion coefficient, defined by

$$D \equiv \frac{l^2}{2\tau} \tag{75}$$

Whereas, τ is the time the particle needs for each single step.

Hence, the average time the particle needs to diffuse over distance l is described with the following equation [30,35]

$$t_{1D}(l) = \frac{l^2}{2D} \tag{76}$$

This shows the dependence of the time of diffusion to the distance square. Since in microfluidics the distances are small, the diffusion time is usually small. Furthermore, the diffusion time can be controlled by tuning the diffusion length, e.g. dividing into smaller streams to decrease the diffusion length. But the diffusion time is also dependent on the diffusion coefficient D and thus, many different approaches have been published in the recent years introducing chip designs with passive mixers. [30,32,35,48]

The diffusion coefficient for spherical particles in a liquid can be described with the Einstein-Stokes equation. Diffusion in a liquid must be formulated differently, because of the denser phase of the liquid compared the free environment assumed before. For the Brownian motion of spherical particles, the diffusion coefficient is

$$D = \frac{\langle v^2 \rangle}{\beta} \tag{77}$$

The friction coefficient β describing the friction the fluid applied on the particle.

It is defined as

$$\beta = \frac{6\pi r\eta}{m} \tag{78}$$

with r is the radius of the particles, m is the mass of the particles and η is the viscosity of the fluid.[35]

The energy equipartition theorem,

$$\frac{1}{2}m\langle v^2\rangle = \frac{1}{2}k_B T \tag{79}$$

with k_B is the Boltzman constant, T the absolute temperature leads to the Stokes-Einstein relation.[35,48]

$$D = \frac{k_B T}{6\pi\eta r} \tag{80}$$

As already mentioned, to obtain an equation describing the mixing conditions in a microfluidic channel we have to consider diffusion and convection. First, we only consider diffusion in x-direction, which is described in Fick's first law.

$$J_D = -D\frac{\partial c}{\partial x} \tag{81}$$

J_D is the diffusive flux and c, the concentration of the species.

Now we regard the time dependent diffusion process in a narrow cuboid of area A and length l, as shown in Figure 16.

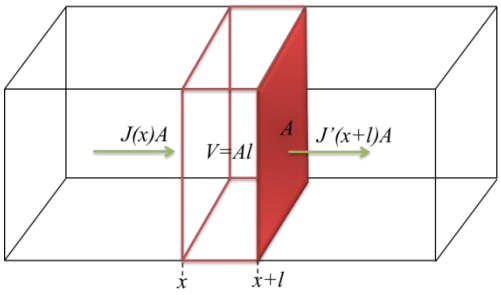

Figure 16. Scheme of a cuboid with volume V and a flux J(x) occurring due to a concentration gradient in x-direction. Adapted with permission from Bruus, H., Theoretical Microfluidics, (2008), Oxford University Press and Phillips, R., Kondev, J., Theriot, J., Physical biology of the cell; Copyright (2009) Garland Science-Books [30,38]

The number of particles diffusing into the cuboid in an infinitesimal time interval dt is $JAdt$. Therefore, the concentration c in the cuboid increases with increasing flux $J(x)$.

$$\frac{\partial c}{\partial t} = \frac{JAdt}{Aldt} = \frac{J}{l} \tag{82}$$

On the other side the particles leave the cuboid with a flux $J'(x + l)$.

$$\frac{\partial c}{\partial t} = \frac{J'Adt}{Aldt} = \frac{J'}{l} \tag{83}$$

The change of concentration per time interval is then,

$$\frac{\partial c}{\partial t} = \frac{J_D - J'_D}{l} = \frac{\left(-D\frac{\partial c}{\partial x} + D\frac{\partial c'}{\partial x}\right)}{l} = \frac{\left(-D\frac{\partial c}{\partial x} + D\frac{\partial}{\partial x}\left[c + \left(\frac{\partial c}{\partial x}\right)l\right]\right)}{l} = D\frac{\partial^2 c}{\partial x^2} \tag{84}$$

which is Fick's second law.

On the other hand, convection is the transport of particles through a flowing liquid. If we just consider convection and assume again a narrow cuboid with area A and length l, and a particle flux through this area A at the time dt due to velocity v as shown in Figure 16, then

$$J_C = \frac{cAv\Delta t}{A\Delta t} = cv \tag{85}$$

Hence, the overall change of concentration per time interval dt is the summation of equation (82) and (83). And with equation (85) it follows,

$$\frac{\partial c}{\partial t} = \frac{J_C - J'_C}{l} = \left\{c - \left[c + \left(\frac{dc}{dx}\right)l\right]\right\}\frac{v}{l} = -v\frac{\partial c}{\partial x} \tag{86}$$

Thus, the overall change of concentration in the time interval dt in a microfluidic channel can be described with the summation of convection and diffusion.[49]

$$\frac{\partial c}{\partial t} = D\frac{\partial^2 \mathrm{c}}{\partial \mathrm{x}^2} - v\frac{\partial \mathrm{c}}{\partial \mathrm{x}} \tag{87}$$

2.2.1.6 Péclet Number and Taylor Dispersion

Another dimensionless number describes the relation between convection and diffusion, the Péclet number.

$$Pe = \frac{J_C}{J_D} = \frac{\frac{v\delta c}{l}}{\frac{D\delta c}{l^2}} = \frac{vl}{D} \tag{88}$$

v is the average flow velocity, l is the characteristic size of the system and D the Diffusion coefficient. It follows, the higher the Péclet number the more diffusion is influenced by the convective flow. In liquids the diffusion coefficient D is usually on the order of $10^{-5}\ \frac{cm^2}{s}$. So, the Péclet number and the question if diffusion or convection dominates is dependent on the flow velocity v and the characteristic length l. For example, with a flow velocity of $1\ \frac{mm}{s}$ and a channel with $l = 100\ \mu m$, the $Pe \approx 100$ and convection is dominant. But If $l = 1\ \mu m$ and $v = 10\ \mu m/s$, then $Pe \approx 10^{-2}$ and diffusion dominates. [35]

The Taylor dispersion considers the convection and diffusion of a solute with concentration $c(\vec{r}, t)$ in a solution flowing with a velocity field $\vec{v}(\vec{r}, t)$ in a cylindrical channel with radius a. A steady-state Poiseuille flow $\vec{v} = v_x(r)\overrightarrow{e_x}$ is obtained. The convection-diffusion equation (87) has then the form,

$$\frac{\partial c}{\partial t} = D\left(\frac{\partial^2 c}{\partial r} + \frac{1}{r}\frac{\partial c}{\partial r} + \frac{\partial^2 \mathrm{c}}{\partial \mathrm{x}^2}\right) - v\frac{\partial \mathrm{c}}{\partial \mathrm{x}} \tag{89}$$

Figuratively, the solute is placed into the channel at $t = 0$ and the concentration gradient changes because of convection due to the applied pressure flow and diffusion due to the Brownian motion of the solute.

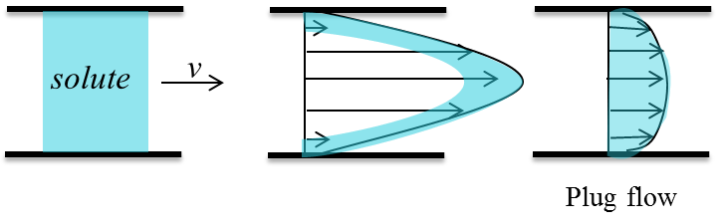

Figure 17. Left picture shows a band of solute inserted into a channel. The middle image shows the increasing parabolic profile, if diffusion is absent. The right scheme shows plug flow evolving due to diffusion and convection.

If only convection occurs the band of solute will be an increasing long parabolic profile, as shown in the middle scheme in Figure 17. Since diffusion is present, the concentration of the parabolic profile is changed. At the front of the parabolic profile, the higher concentration is in the middle of the channel. Hence, the particles diffuse towards the lower concentration at the channel walls. However, in the back of the parabolic profile the higher concentration is close to the channel walls and the particle diffuse in the middle of the channel. This leads to the so called plug flow, shown in the right scheme of Figure 17. [30] Eventually, the Taylor dispersion for stationary flow in a channel with small transverse size, takes into account diffusion and convection. This shear flow leads to an increase of the diffusivity of the considered particles. Hence, an effective diffusion constant D_{eff} is introduced, which can be described with equation (90).

$$D_{eff} \sim Pe^2 D \tag{90}$$

Summing up, mixing in microfluidic channel is described with diffusion and convection. Which one of these two dominates depends mainly on the flow velocity and the size of the system. Due to laminar flow, two miscible fluids moving next to each other form a diffusive interface which broadens as the fluids mix. In many cases this mixing is too slow and many papers have been published with channel designs trying to accelerate the mixing by size reduction or designs introducing chaotic mixing. [35]

Device Fabrication

There exist many different technologies to produce microfluidic devices. In the following, only the most established technologies or the methods used during the thesis will be explained. Lithography is one of the most powerful methods in microfabrication and can be differentiated by the used radiation, e.g. photolithography, electron-beam lithography, X-ray-lithography. With different lithographic methods, structures with sizes between 0.2 and 500 µm are possible for hard materials, like glass or silicon. For soft materials, that is polymers like PDMS or PMMA, the scale for structures ranges between 0.5 and 500 µm. [35]

Photolithography is mainly used in microfabrication, e.g. in microelectronic industry for production of microelectronic chips.

In the photolithographic process the desired micro pattern is transferred on a thin photoresist film with a printed photomask or chrome mask. Depending on whether the resist is a positive or negative resist the irradiated parts become the positive structure or negative structure. Photolithography is further differentiated between proximity lithography and projection lithography. In Proximity lithography the spatial resolution r is dependent on the Fresnel diffraction and hence, on the wavelength λ and the distance d between the mask and the photoresist.

$$r = 1.5\sqrt{\lambda d} \tag{91}$$

In Projection lithography the spatial resolution is dependent on the wavelength λ and the numerical aperture NA. [35,50,51]

$$r = \frac{\lambda}{2NA} \tag{92}$$

But photolithography has a few drawbacks. First, only two dimensional structures can be realized and that only on flat surfaces. [14] Additionally clean-room conditions are necessary for each device production. If photolithography is used to directly produce a microfluidic device and not to use the product as a master for reproduction, the devices have to be sealed in a complicated and time-consuming way. Furthermore, the used materials are fragile (glass, silicone) and expensive. [52]

Therefore, a new method was established, called soft lithography, where the used device material is a polymer, and photolithography is only used to fabricate the masters for replication. Polymers used as chip materials have several advantages, like lower costs, lower fragility and fast prototyping. [35]

2.2.1.7 Soft Lithography

The key element of soft lithography is an elastomeric block, mostly poly(dimehtylsiloxane) (PDMS) containing the desired pattern and is therefore used as stamp, mold, mask or device itself. PDMS consists of an inorganic siloxane backbone and attached organic methyl groups. The glass transition temperature is very low, which means it is liquid at room temperature, and PDMS can easily be converted into a solid polymer by cross-linking. [14] In the 1990's Whitesides and co-workers published several papers using PDMS as elastomeric mold for micrometer patterned devices, e.g. for microcontact printing and micromolding in capillaries (MIMIC). [53,54] The method described there to prepare PDMS molds is still used today, also for microfluidic chip preparation consisting of PDMS itself (e.g. as integrated capillary electrophoresis (ICE) chips). [55] First a Master for the PDMS has to be prepared, which is usually made by photolithography, described in the earlier chapter. Then, the mold, e.g. the silicon wafer with the photoresist negative structure, is placed in a Petri dish. The elastomer combined with the curing agent, e.g. SYLGARD 184 from Dow Corning Corporation, in a ratio of 10:1, is poured over the patterned master. The elastomer has to be degassed for 30 minutes, whereupon the dish is stored in the oven at 75°C for 1 to 2 hours. The hardened elastomer can then be peeled off the master. [53] The different fabrication steps during PDMS chip production is depicted in Figure 18. Compared to other methods soft lithography is a low-cost technique, which is easy to learn and apply and hence, it is accessible to a wide range of users.

Advantageous of soft lithography to photolithography is the access to quasi three-dimensional structures. Furthermore, patterns can be generated on nonplanar surfaces and many different materials can be used, which leads to different surface chemistry. [14]

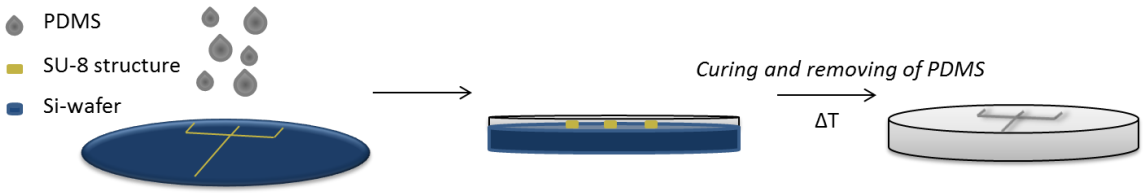

Figure 18. Description of the PDMS chip fabrication steps. Adapted with permission from Xia, Y., Whitesides, G., M., SOFT LITHOGRAPHY. Copyright (1998), Annual Reviews [14]

The success of PDMS as chip material, especially in soft lithography, is due to several advantages. It is a soft elastomer with low surface energy. Hence, PDMS can be used for pumps or membranes and is easily removed from the substrate (e.g. silicon wafer) or mold. However, it is sufficiently rigid that the replica maintains its structure. It is durable, which means it can be used several times. Furthermore, PDMS is hydrophobic and does not swell due to humidity. It is permeable to gas and has good thermal stability up to ~186 °C. The isotropic and homogeneous PDMS is optically transparent (~300 nm) and the interfacial properties of PDMS can be changed readily by modifying the prepolymers or by treatment with oxygen plasma. [14] Plasma treatment is used to change the surface properties of PDMS from hydrophobic to hydrophilic. [35] But the hydrophilic character changes back to hydrophobic in 45 minutes. If the channels are filled with a liquid like water, it stays hydrophilic for at least 80 minutes. [52,56] The structured side of a MF-chip has to be bonded to close the channels molded in the PDMS. Therefore, plasma is also used to bond two microfluidic chip halves or chip half and glass slide together. Thus, a surface oxidation via plasma of the PDMS surface is necessary. Thereby, at the surface of the PDMS, methyl groups are oxidized and a layer with silanol-groups (Si-OH) arises. Bringing two plasma treated parts, like PDMS-PDMS, PDMS-glass or PDMS-silicon, together seals them irreversibly, by forming covalent (Si-O-Si) bonds through condensation. [35,52]

However, PDMS has also several drawbacks. PDMS is not resistant to most organic solvents and swells if it gets in contact. It shrinks by 1% upon curing, which changes the original designed sizes. Furthermore, the softness of PDMS limits the aspect ratio, which means the ratio of the width to the height. This and further problems, which have to be considered during the device design, is described in detail in chapter 0. [14]

Besides, soft lithography or molding, two more methods are popular for the fabrication of polymer based micro-patterns, casting or hot embossing and microinjection. Microinjection is the injection of a hot, liquid polymer into a mold, cooling it down and removing the negative of the mold shape. Microinjection was not used during the thesis and thus, is not explained any further. All of these three methods are replication methods. [35]

2.2.1.8 Hot Embossing

Another used method for microfluidic device fabrication is hot embossing. This micromolding technique uses thermoplastic polymers to imprint structures at elevated temperatures. Used polymers are e.g. PMMA, PC, PI, PE, PVC, PEEK, which are heated above their glass transition temperature T_g and then are pressed into a mold with a pressure of tens of bars. Hence, a mold with the desired microstructure is needed, which are usually fabricated via etching, LIGA (Lithografie, Galvanoformung, Abformung) or CNC (Computerized Numerical Control)-machining. The molds have to withstand the applied pressure and the high temperatures and are usually made of metal or silicon. Hot embossing has a good accuracy in the order of tens of nanometers. Further advantages are the low costs, the easy production and the possibility to obtain high aspect ratios under certain conditions. It can be tuned to a high throughput process, but compared to the hot injection method, the fabrication time takes relatively long. [35,51,57,58]

2.2.1.9 Rapid Prototyping

Fast prototyping is a feature of soft lithography. It describes the design, production and testing of a new device within 24 hours, as depicted in Figure 19. Whitesides et al. reported the fast prototyping process in 1996, whereas a new PDMS stamp design was printed on a transparent polymer with a commercially available laser-assisted image setting system. These patterned polymer films were then used as mask for 1:1 projection photolithography. The whole procedure from designing the structured device until receiving the final product was realized in about 7 hours. The PDMS stamps were produced with the already known methods like microcontact printing, micromolding in capillaries and microtransfer molding. [50,53,54,59]

By stacking different masks on top of each other in a certain way, new patterns have been generated, which were not realizable with only one mask. The smallest feasible feature was about 20 µm limited by the resolution of the image setting system. [50]

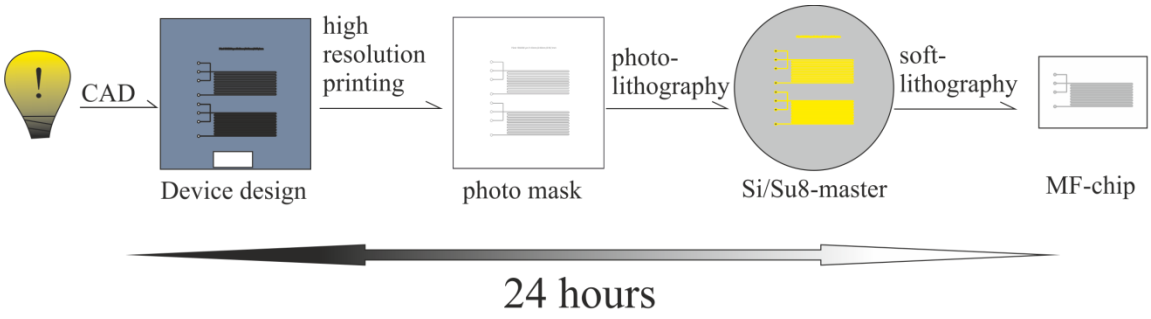

Figure 19. Illustration of the rapid prototyping process; beginning with the idea of the device design on the left to the completed microfluidic chip on the right. Adapted with permission from Xia, Y., Whitesides, G., M., SOFT LITHOGRAPHY. Copyright (1998), Annual Reviews and Qin, D., Xia, Y., Whitesides, G., M., Rapid prototyping of complex structures with feature sizes larger than 20 µm. Copyright (1996), John Wiley and Sons and Duffy, D., C., McDonald, J.,C., Schueller, O., J., A., Rapid Prototyping of Microfluidic Systems in Poly(dimethylsiloxane), Copyright (1998), American Chemical Society.[14,50,52]

Besides the benefit to receive a newly designed device in 24 hours, rapid prototyping has several more advantages. The used masks are printed transparencies. They are produced within hours and are much less expensive than chrome masks, commonly used in photolithography. Compared to etching in silicon the variety of patterns is much larger using a photoresist. Eventually, every orientation and form can be realized in the limits of the resolution. [35,52]

2.3 Small Angle X-ray Scattering

Small angle X-ray scattering (SAXS) is a well-known method for analyzing the structure of colloids and soft matter. [60,61] X-rays are electromagnetic waves with wavelength of 0.01 to 10 nm, which is much smaller than the wavelength of visible light. [8,61] In X-ray diffraction (XRD), where e.g. inorganic crystals are analyzed, the observed lattice spacing is of the same order of magnitude as the employed wavelength and thus, the diffraction angle θ is large. To observe larger structures, such as polymers or other mesoscale materials, smaller angles θ are needed. This is due to the inverse relation of the lattice distance r and the diffraction angle θ, described by Braggs law (Eq. (96)(49)), which is derived in the next section. [61,62]

Physical Fundamentals of Small Angle X-ray Scattering

When X-rays pass a sample, the photons interact with the electrons of the sample atoms. A part of the X-rays is absorbed, a part is passing through the sample and a part will be scattered. The absorption of X-rays expels electrons, leaving undesired holes in the atom shells. Hence, these holes must be refilled either by emitting another electron (Auger effect) or by rearranging the electrons. This rearrangements lead to radiation of light with a different wavelength than the incident X-rays. [62]

Scattering is distinguished by Compton scattering and Thomson scattering. The incoherent Compton scattering occurs when a photon hits an electron and is bounced away. Though, the photon loses a part of its energy to the electron and radiates with a different wavelength and with no phase relationship with the incident radiation. Thus, it does not comprise structural information and is obtained as background scattering. Furthermore, for scattering at small angles, Compton scattering is small and can be neglected. [63] More interesting for the structural analysis is the Thomson scattering. Here, the photon hits a strongly bonded electron. No energy is transferred to the electron, but it starts to oscillate with the same frequency as the incoming X-rays. Given that, also adjacent strongly bonded electrons are hit by photons, they all oscillate synchronous with the same frequency and hence, radiate coherent spherical waves. These coherent waves can interfere with each other and show interference patterns with the structural information of the sample. Since the scattering is elastic and the waves are coherent, they are summed up.

Therefore, their amplitude can only differ by the phase. This means the waves can be constructive, destructive or in between, depending on the relative position of the electrons. [62] The fundamental equation for interference pattern in crystallography is described by Braggs law. It depicts diffraction as a function of the distance $|\vec{r}|$ between two atoms and the scattering angle θ, as shown in Figure 20.

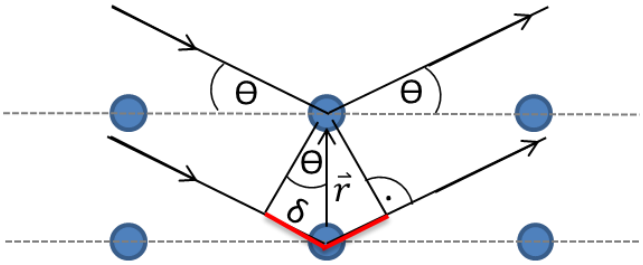

Figure 20. Scheme of X-ray diffraction at two atoms positioned at distance $\vec{r}$. Adapted with permission from Stribeck, N., X-ray scattering of soft matter, Copyright (2007), Springer, Glatter, O., Kratky, O., Small angle x-ray scattering, Copyright (1982) Elsevier* and Guinier A., X-ray diffraction, Dover, Copyright (1963).[60–62]

If we consider the scattering at two atoms, we can see from Figure 20, that the path the light takes for the upper atom is different to the path for the lower atom. This path difference is highlighted in red. Hence, simple geometry for right triangle shows that,

$$\delta = r \cdot \sin\theta \tag{93}$$

and the path difference Δδ (red line) is δ times two. Consequential,

$$\Delta\delta = 2\delta = 2r \cdot \sin\theta \tag{94}$$

If the scattered or diffracted waves are constructive, the path difference $\Delta\delta$ is the multiple integer n of the wavelength λ.

$$\Delta\delta = n \cdot \lambda \tag{95}$$

Hence, Braggs law is [64]

$$n \cdot \lambda = 2r \cdot \sin\theta \tag{96}$$

*This article was published in Small angle x-ray scattering, Glatter, O., Kratky, O., Chapter 2, p. 19, Copyright Elsevier (1982).

In contrast to crystallography, in small angle X-ray scattering different considerations have to be made, than the analyzation of diffraction patterns by lattice distances. [62] Figure 21 shows a simplified schematic graphic of an X-ray scattering experiment at two atoms A and B.

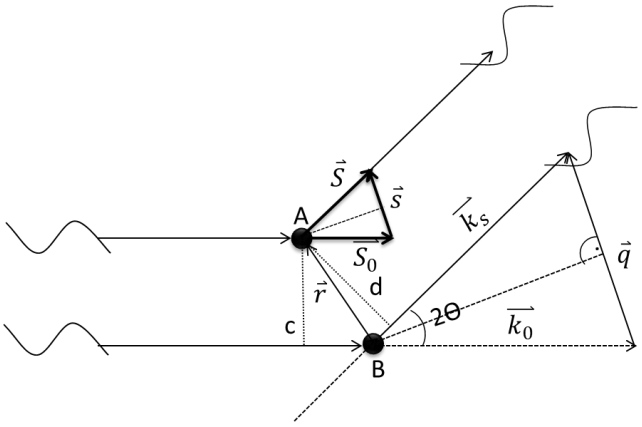

Figure 21. Scattering by two atoms A and B at distance $\vec{r}$. Adapted with permission from Glatter, O., Kratky, O., Small angle x-ray scattering, Copyright (1982) Elsevier* and Guinier A. *X-ray diffraction*; Dover, Copyright (1963). [60,62]

Hence, A and B are two scattering points, which are positioned at a certain distance shown with the vector $\vec{r}$. The path length of the incident X-rays is longer for atom *B* than for atom *A*. Hence, the path difference is

$$\Delta\delta = cB + Bd \tag{97}$$

c and *d* are the projections of *A* on the rays passing *B*. S_0 is the unit vector for the incident rays and *S* is the scattered rays unit vector. It shows,

$$cB = S_0 AB \tag{98}$$

$$Bd = -SAB \tag{99}$$

*This article was published in Small angle x-ray scattering, Glatter, O., Kratky, O., Chapter 2, p. 19, Copyright Elsevier (1982).

With $\vec{r}$ as the distance between AB, the path difference is

$$\Delta\delta = AB\left(\vec{S}_0 - \vec{S}\right) = -\vec{r}\,(\vec{S} - \vec{S}_0) \tag{100}$$

$\vec{s}$ is defined as the difference between the incident X-rays and the scattered ones and is always perpendicular to the angle bisector of $\vec{S}$ and $\vec{S}_0$.[62]

$$\vec{s} = \vec{S} - \vec{S}_0 \tag{101}$$

The wave vectors are defined as

$$\vec{k}_0 = \frac{2\pi}{\lambda}\vec{S}_0\,;\ \vec{k}_s = \frac{2\pi}{\lambda}\vec{S} \tag{102}$$

In elastic scattering the absolute value of $\left|\vec{k}_0\right| = \left|\vec{k}_s\right|$. [8]

$$\vec{k} = \left|\vec{k}_0\right| = \left|\vec{k}_s\right| = \frac{2\pi}{\lambda} \tag{103}$$

The phase difference φ is the wave number k times the path difference $\Delta\delta$. [8] Therefore, from equation (100) and (103) it follows,

$$\varphi = \frac{2\pi\Delta\delta}{\lambda} = -2\pi r\frac{\left(\vec{S} - \vec{S}_0\right)}{\lambda} = -2\pi\vec{r}\cdot\frac{\vec{s}}{\lambda} \tag{104}$$

The scattering vector $\vec{q}$ is introduced [61]

$$\vec{s} = \frac{\vec{q}}{2\pi} \tag{105}$$

Scattering vector $\vec{q}$ is defined as the difference of the scattered wave vector $\overrightarrow{k_s}$ and the incident wave vector $\overrightarrow{k_0}$.

$$\vec{q} = \overrightarrow{k_s} - \overrightarrow{k_0} \tag{106}$$

Considering Figure 21, simple geometry shows,

$$\frac{\vec{q}}{\overrightarrow{k_s}} = \sin(2\theta) \tag{107}$$

Hence, with equation (107) and (103) $\vec{q}$ has the magnitude,

$$\vec{q} = \left| q \right| = \frac{4\pi}{\lambda} \sin\theta \tag{108}$$

The scattering vector is useful since a diffraction peak of a measured sample appears at a certain q –value independent of the wavelength, whereas its scattering angle will change with λ. [8]

The phase shift is then,

$$\varphi = -\vec{q}\vec{r} = -\frac{4\pi}{\lambda}\vec{r} \cdot sin\theta \tag{109}$$

This equation shows like the Bragg equation (96) the reciprocal relation between the size or particle distance $\vec{r}$ and the scattering angle θ. Hence, at small angles, large structures are observed and vice versa. Furthermore, in diffraction experiments the used wavelength is usually at the size of the observable structures. But colloidal systems are much larger than the wavelength of X-rays and are observed due to this relation. [60]

So far, we have introduced with a simplified approach, the inverse relation of particle size and the scattering angle θ, as well as the scattering vector $\vec{q}$. Now, we have to consider the calculation of the scattering curve.

In the listed equations the electron scattering intensity and amplitude is taken to be of magnitude 1. As already mentioned, the scattered waves are coherent and hence, the amplitudes are added. [60]

The amplitude of secondary waves is usually presented with the complex form

$$A(\vec{q}) = \sum_{j=1}^{N} b_j(\vec{q})\, e^{i\varphi} = \sum_{j=1}^{N} b_j(\vec{q})\, e^{-i\vec{q}\vec{r}} \tag{110}$$

b is the "scattering length", which is a constant getting greater with stronger interaction between the incident wave and the scattered point. [65]

$$b = b_e Z \tag{111}$$

with b_e as the scattering length of electrons and Z as number of electrons in the atom.

For electrons the scattering length is the Thomson radius or electron radius.

$$b_e \approx \frac{e^2}{4\pi m \varepsilon_0 c^2} = 2.82x10^{-15}\, m \tag{112}$$

c is the speed of light, m the mass of the electron and ε_0 is the permittivity of free space. Hence, for small angle X-ray scattering particles are described only by the local density of electrons. [63,66]

Now the amplitude is not accessible by summing up all secondary waves, because there are too many electrons and it is not possible to localize a single electron. Therefore, the electron density must be introduced, which is the number of electrons per unit volume $\rho(\vec{r})dV$.

The summation in equation (110) can then be replaced by integration over the whole illuminated volume at position $\vec{r}$.

$$A(\vec{q}) = \iiint dV \cdot \rho(\vec{r}) e^{-i\vec{q}\vec{r}} \tag{113}$$

The amplitude A of diffraction at a certain direction $\vec{q}$ is thus obtained by Fourier transformation of the electron density.

In a scattering experiment not the amplitude is measurably but the intensity. The intensity is obtained by the square modulus of the amplitude or with the conjugate complex A*. Hence, an inversion of the Fourier transform to obtain the electron density is not possible, because the phase information is lost. This is known as the phase problem. However, the intensity I($\vec{q}$) is derived with the Fourier transform of equation (113) considering only the relative distance ($\vec{r}_1 - \vec{r}_2$) for every pair of points. [60]

$$I(\vec{q}) = |A^2| = AA^* = \iiint \iiint dV_1 dV_2 \rho(\vec{r}_1)\rho(\vec{r}_2) e^{-i\vec{q}(\vec{r}_1 - \vec{r}_2)} \tag{114}$$

This double integration is calculated in two separated steps. In the first step the convolution square or auto-correlation is used to summarize all pairs of equal relative distance. [60]

$$\tilde{\rho}^2(\vec{r}) \equiv \iiint dV_1 \rho(\vec{r}_1)\rho(\vec{r}_2) \tag{115}$$

with

$$\vec{r} = (\vec{r}_1 - \vec{r}_2) = constant \tag{116}$$

Here, we introduce the fictitious space C, where every electron pair with a relative distance $\vec{r}$ can be described by a point. The density of the points is given by $\tilde{\rho}^2(\vec{r})$, also called the electron density distribution. Every pair is counted twice ($\vec{r}, -\vec{r}$), thus the distribution in the C space must have a center of symmetry.

The second step is to integrate over all relative distances including the phase factor $e^{-i\vec{q}\vec{r}}$. This is the integration over the C-space, which is the Fourier transform again. [60]

$$I(\vec{q}) = \iiint dV \tilde{\rho}^2(\vec{r}) e^{-i\vec{q}\vec{r}} \tag{117}$$

Thus, the intensity distribution in the reciprocal space or $\vec{q}$ is only determined by the structure of the object, expressed with the auto-correlation function $\tilde{\rho}^2(\vec{r})$. In turn $\tilde{\rho}^2(\vec{r})$ can be derived from $I(\vec{q})$ with the inverse Fourier transform

$$\tilde{\rho}^2(\vec{r}) = \left(\frac{1}{2\pi}\right)^3 \iiint dq_x dq_y dq_z I(\vec{q}) e^{i\vec{q}\vec{r}} \tag{118}$$

For small angle scattering of colloidal systems several assumptions can be made to simplify the mentioned equations. First, the investigated system is statistically isotropic and second, there is no long-range order of the particles. The isotropic system leads to the simplification that the distribution $\tilde{\rho}^2(\vec{r})$ in the C-space is only dependent on the magnitude of the distance $\vec{r}$.

Hence, the phase factor $e^{-i\vec{q}\vec{r}}$ can be replaced by the average $\langle\,\rangle$, taken over all directions $\vec{r}$ derived by Debye. [63]

$$\langle e^{-i\vec{q}\vec{r}} \rangle = \frac{\sin qr}{qr} \tag{119}$$

Due to the missing long-range order, respective electron densities at a large distance are independent and are replaced by the mean value $\bar{\rho}$. Therefore, the density can be expressed with the mean density and the density fluctuations $\Delta\rho$.

$$\rho = \Delta\rho + \bar{\rho} \tag{120}$$

The mean value does not contain any information, which means with constant values along the whole volume, the volume acts like a blank object. Hence, not the electron density distribution gives the information about the structure but the electron density fluctuations. Thus, the contrast can also be negative. With equation (117) it results in

$$I(\vec{q}) = \iiint dV \Delta\rho(\vec{r}) e^{-i\vec{q}\vec{r}} \tag{121}$$

From equation (115) and (120) it follows

$$\Delta\rho^2 = (\widetilde{\rho - \bar{\rho}})^2 = \tilde{\rho}^2 - V\bar{\rho}^2 = V\gamma(r) \tag{122}$$

with $V\bar{\rho}^2$ as a constant value for the autocorrelation at large distances $\vec{r}$ and $\gamma(r)$ as the correlation function [60]

The Correlation Function

The already mentioned correlation function $\gamma(\vec{r})$ was introduced by Debye and Bueche in 1949 describing the average of two fluctuations at a certain distance. [67] The electron density of particles has to be different to the electron density of the surrounding medium to detect scattering. This difference in electron density leads to fluctuations. [60,68]

We consider a system with two points situated at a distance $\vec{r}$ with their respective electron density fluctuations $\Delta\rho_1$ und $\Delta\rho_2$.Then the correlation function $\gamma(r)$ is defined with

$$\gamma(\vec{r}) = \langle \Delta\rho_1(\vec{r}) \cdot \Delta\rho_2(-\vec{r}) \rangle \tag{123}$$

The average depends on $\vec{r}$, so if $\vec{r} = 0$

$$\gamma(\vec{r} = 0) = \langle \Delta\rho^2 \rangle \tag{124}$$

and if $\vec{r}$ is very large $\Delta\rho_1; \Delta\rho_2$ vary independently and therefore,[60]

$$\gamma(\vec{r} = \infty) \to 0 \tag{125}$$

Since our assumptions predict there is no long-range order, the final value 0 is reached within a finite range. In addition, with equation (117) and (119), it follows

$$I(q) = V \int_0^\infty 4\pi r^2 dr \cdot \gamma(r) \frac{\sin qr}{qr} \tag{126}$$

By inverse Fourier transform the correlation function can be derived.

$$V\gamma(\vec{r}) = \frac{1}{2\pi^2}\int_0^\infty q^2 dq \cdot I(q)\frac{\sin qr}{qr} \tag{127}$$

If $q = 0$ and $r = 0$ then $\gamma(\vec{r}) = 1$ and the Debye factor $\frac{\sin qr}{qr}$ is 0, which leads to the equation

$$I(0) = V\int_0^\infty 4\pi r^2 dr \cdot \gamma(r) \tag{128}$$

This means if $q = 0$, then all secondary waves are in phase, so it might be expected that $I(0)$ is equal to the square of total number of electrons irradiated volume V. This is not observable because $I(q)$ cannot be measured in the full regime $0 < q < \infty$. [60,63] It can be considered that every electron of the volume V acts in coherence only with a surrounding region, as defined by $\gamma(\vec{r})$.

It also follows,

$$V\gamma(0) = \frac{1}{2\pi^2}\int_0^\infty q^2 dq \cdot I(q) = V\langle\Delta\rho^2\rangle \tag{129}$$

Equation (129) shows that the integral of intensity is directly related to the mean square fluctuation of electron density. However, it is independent of the structure.

The integral in equation (129) is called “invariant” Q, because also if parts of the system are deformed or shifted, the value has to stay the same. [60,63]

$$Q = \int_0^\infty q^2 dq \cdot I(q) \tag{130}$$

To summarize, the following sketch illustrates the relations between the mentioned parameters and operations. It is called the “magic square of scattering”. [61]

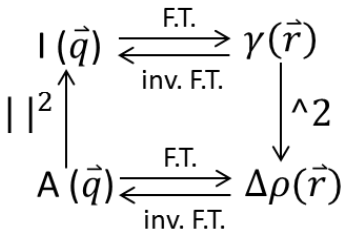

Figure 22. The "magic square" shows the relations of the different parameters. Adapted with permission from Stribeck, N., X-ray scattering of soft matter, Copyright (2007), Springer. [61]

The scattering amplitude $A(\vec{q})$ and the electron density fluctuations $\Delta\rho$ are connected by the Fourier transformation. The scattering intensity $I(\vec{q})$ is the Fourier transform of the auto-correlation function $\gamma(\vec{r})$ averaged over all directions in space. The correlation function is the square of the density fluctuations and the intensity is the mean square of the amplitude. [63]

Form Factor

Due to the phase problem, meaning the loss of the phase information, it is impossible to obtain the electron density in real space from the measured scattering pattern. Hence, it is necessary to use models with calculated intensities and compare them with the measured intensity. [69]

First, we assume a diluted system where the particles are distant and thus, uncorrelated. Therefore, only one particle can be considered. The scattered intensity of all illuminated particles is summed up. For an inhomogeneous particle of a certain orientation the normalized amplitude is,

$$a(\vec{q}) = \int_{V_{Part}} \rho(\vec{r}) e^{-i\vec{q}\vec{r}}\, d\vec{r} \tag{131}$$

It follows,

$$I_{Part}(\vec{q}) = a(\vec{q})a^*(\vec{q}) = V_{Part}^2 P(\vec{q}) \tag{132}$$

whereas $P(\vec{q})$ is the form factor.

From equation (114) it follows,

$$P(\vec{q}) = \frac{1}{V_{Part}^2} \iint_{V_{Part}} \rho(\overrightarrow{r_1})\rho(\overrightarrow{r_2})\, e^{-i\vec{q}(\overrightarrow{r_1}-\overrightarrow{r_2})} d\overrightarrow{r_1} d\overrightarrow{r_2} \tag{133}$$

If the system contains N identical particles in a volume V, the intensity per unit volume $I_m(\vec{q})$ is

$$I_m(\vec{q}) = \frac{N}{V} V_{Part}^2 P(\vec{q}) \tag{134}$$

The form factor can also be calculated via the correlation function by taking the Fourier transform of it. [63] This is not described here and for further information it is referred to [63].

A concrete example for the calculation of the form factor is for a homogeneous spherical particle. Since the system is homogeneous, the electron density fluctuations are angular independent.

$$I(q) = (\Delta\rho^2) V^2 P(q) \tag{135}$$

With conversion to spherical polar-co-ordinates,

$$P(q) = \left[\frac{3}{(qR)^3}(\sin qR - qR\cos qR)\right]^2 \tag{136}$$

the equation leads to

$$I(q) = (\Delta\rho^2) V^2 \left[\frac{3}{(qR)^3}(\sin qR - qR\cos qR)\right]^2 \tag{137}$$

Where R is the sphere´s radius and the form factor is the square of the Bessel function of the order $\left(\frac{3}{2}\right) j_{3/2}(qR)$. With zeros at $qR = 4.49, 7.73\ldots$, the size of the sphere from the scattering function can be estimated. [63]

Structure Factor

So far, we assumed a dilute and isotropic system, but if the concentration increases interparticular relations have to be taken into count. We consider the simple case of N identical spherical particles, which are correlated in space. The system then can be seen as one large composite particle, with the single spheres as subparticles.

$$I(q) = NI_0P(q)S(q) \tag{138}$$

$NI_0P(q)$ is the scattering of N single spheres and $S(q)$ is called the structure factor describing the effect of positional correlations of the particles. It follows,

$$S(q) = 1 + \frac{N}{V}4\pi \int_0^\infty [c(r) - 1]\, r^2 \frac{\sin(qr)}{(qr)}\, dr \tag{139}$$

with $c(r)$ as the pair correlation function.

The multiplication of the form factor $P(q)$with the structure factor $S(q)$ leads to changes of the scattering curve, mainly at low q-values. [60,63] A more precise description of the employed calculations for the structure and form factor is given in the next chapter.

Analyzation of Measured Scattering Patterns

For particles with non-spherical shapes the calculation of the intensity is carried out with numerical methods. [60] During the thesis the software S*catter* was used to calculate fits to the corresponding measured small angle X-ray scattering patterns. This software uses closed analytical expressions based on decoupling approximation for the numerical calculations of 1D, 2D and 3D structures and structural imperfections.[70]

It is assumed a two-phase system with scattering length b_1 and b_2 and the volume fractions ϕ_1 and $\phi_2 = 1 - \phi_1$. For monodisperse particles located at the exact lattice points it holds,

$$I(\vec{q}) = (b_1 - b_2)^2 \rho_N A^2(\vec{q}) S(\vec{q}) \tag{140}$$

with $\rho_N = \frac{N}{V}$ as the number density of the particles, $A(\vec{q})$ as the scattering amplitude and $S(\vec{q})$ as the structure or lattice factor, which describes the spatial distribution of the particles. If the particles are not located at the exact lattice points, the probability of these displacements can be described by a Gaussian function.

It follows [70]

$$I(\vec{q}) = (b_1 - b_2)^2 \rho_N \left[A^2(\vec{q})\left(1 - G(\vec{q})\right) + A^2(\vec{q}) G(\vec{q}) S(\vec{q}) \right] \qquad (141)$$

$G(\vec{q})$ is the Debye-Waller factor, describing the lattice distortion by thermal movement. [61]
$G(\vec{q})S(\vec{q})$ specifies the decay of intensity of the Bragg peaks due to displacement.
$1 - G(\vec{q})$ describes the following increase of the diffuse scattering. [70]

It is now exemplarily shown the calculation for cylinders with length L and cross-sectional radius R. From equation (141) it follows,

$$I(\vec{q}) = (b_1 - b_2)^2 \rho_N \left[\langle A^2(\vec{q}, \vec{R}, \vec{L}) \rangle_{L,R} + \langle A(\vec{q}, \vec{R}, \vec{L}) \rangle_{L,R}^2 G(\vec{q}) (S(\vec{q}) - 1) \right] \qquad (142)$$

with $\langle\ \rangle_{L,R}$ as the average over the length and radius distributions. If the particles are monodisperse, then

$$\langle A^2(\vec{q}, \vec{R}, \vec{L}) \rangle_{L,R} = \langle A(\vec{q}, \vec{R}, \vec{L}) \rangle_{L,R}^2 = A^2(\vec{q}, \vec{R}, \vec{L}) \qquad (143)$$

which results again in equation (141).

For anisometric particles like cylinders, the spatial orientation has to be taken into account. Therefore, vectors $\vec{L} = L\vec{l_{\parallel}}$ and $\vec{R} = R\vec{l_{\perp}}$ are introduced, with $\vec{l_{\parallel}}$ and $\vec{l_{\perp}}$ as the unit vectors in direction of the cylinder axis and normal to it. These unit vectors and the all used parameters for the different shapes are illustrated in Figure 23.

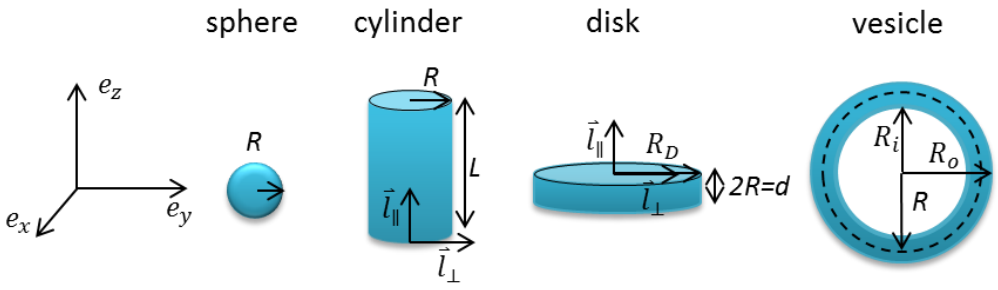

Figure 23. Scheme of the different structures and their characteristic parameters used in *Scatter* software. Adapted with permission from Förster, S. Fischer, S., Zielske, K., Schellbach, C., Sztucki, M, Lindner, P., Perlich, J., Calculation of scattering-patterns of ordered nano- and mesoscale materials, Copyright (2011), Elsevier [70]

The scattering intensity is, besides the orientational distribution of the particles, also affected by the orientational distribution of the unit cells, which influence the structure factor $S(\vec{q})$. Therefore, the reciprocal lattice vector $\vec{g}$ is introduced, for the orientation of the unit cells and the average over the oritational distribution is calculated $\langle\ \rangle_{or}$.

$$I(\vec{q}) = (b_1 - b_2)^2 \rho_N \big[\langle\langle A^2(\vec{q},\vec{R},\vec{L})\rangle_{L,R} - \langle A(\vec{q},\vec{R},\vec{L})\rangle_{L,R}^2 G(\vec{q},\vec{g}) + \langle A(\vec{q},\vec{R},\vec{L})\rangle_{L,R}^2 G(\vec{q},\vec{g}) S(\overrightarrow{q},\vec{g})\rangle_{or}\big] \tag{144}$$

This exact calculation can be simplified if the structure factor is sufficiently peaked and if the domains are sufficiently oriented, which is described further in [70,71]. In nano- and mesoscale materials, the lattice structure can be divided into large number of ordered domains, in which the particles are oriented. Thus, the orientational average of the product of the form factor and structure factor can be factorized,

$$\langle\langle A(\vec{q},\vec{R},\vec{L})\rangle_{L,R}^2 G(\vec{q},\vec{g}) S(\overrightarrow{q},\vec{g})\rangle_{or} = \langle\langle A(\vec{q},\vec{R},\vec{L})\rangle_{L,R}^2\rangle_{or} \langle G(\vec{q},\vec{g}) S(\overrightarrow{q},\vec{g})_{or}\rangle \tag{145}$$

It is further assumed that the Debye-Waller factor is isotropic, it follows

$$\langle G(\vec{q},\vec{g}) S(\overrightarrow{q},\vec{g})\rangle_{or} = G(\vec{q},\vec{g}) \langle S(\overrightarrow{q},\vec{g})\rangle_{or} \tag{146}$$

Then, from equation(144) and(146) it follows,

$$I(\vec{q}) = (b_1 - b_2)^2 \rho_N \langle\langle A^2(\vec{q},\vec{R},\vec{L})\rangle_{L,R}\rangle_{or} \left[1 + \frac{\langle\langle A(\vec{q},\vec{L},\vec{R})\rangle_{L,R}^2\rangle_{or}}{\langle\langle A^2(\vec{q},\vec{L},\vec{R}\rangle_{L,R}\rangle_{or}} (\langle S(\overrightarrow{q},\vec{g})\rangle_{or} - 1) G(\vec{q},\vec{g})\right] \tag{147}$$

with

$$\beta(\vec{q},\vec{L},\vec{R}) = \frac{\langle\langle A(\vec{q},\vec{L},\vec{R})\rangle_{L,R}^2\rangle_{or}}{\langle\langle A^2(\vec{q},\vec{L},\vec{R}\rangle_{L,R}\rangle_{or}} \tag{148}$$

and $P(\vec{q},\vec{L},\vec{R})$ as the form factor.

$$P(\vec{q},\vec{L},\vec{R}) = \langle A^2(\vec{q},\vec{R},\vec{L})\rangle_{L,R} \tag{149}$$

It follows,

$$I(\vec{q}) = (b_1 - b_2)^2 \rho_N \langle P(\vec{q},\vec{L},\vec{R})\rangle_{or}\left[1 + \beta(\vec{q},\vec{L},\vec{R})(\langle S(\vec{q},\vec{g})\rangle_{or} - 1)G(\vec{q},\vec{g})\right] \tag{150}$$

In equation (150) the effect of the particles (form factor, β) and of the lattice (structure factor, Debye-Waller factor) on the scattered intensity is considered. Equation (150) is used for the calculation of scattering patterns in the software *Scatter*.

For simple geometries like a homogeneous sphere, the form factor is already present in equation (136). For more complicated shapes the form factor can be divided into the contribution parallel or perpendicular to the structure axis. The isotropic form factors $P(\vec{q},\vec{L},\vec{R})$ have the asymptotes.

$$\lim_{q\to\infty} q^4 P(q) = P_{d\infty} \tag{151}$$

With the Porod's law it is obtained the following relation,

$$V \lim_{q\to\infty} q^4 I(q) = 2\pi(b_1 - b_2)^2 S_V \tag{152}$$

with S_V as the surface area per volume.

For diluted isotropic systems of volume V, the structure factor $S(\vec{q}) = 1$ and with equation (140) it follows

$$VI(\vec{q}) = (b_1 - b_2)^2 N P(\vec{q}) \tag{153}$$

With $N = 1$ equation (153) and (152) lead to

$$V_{dp}(b_1 - b_2)^2 P_{d\infty} = 2\pi(b_1 - b_2)^2 S_V \tag{154}$$

where V_{dp} is the volume of the particle. [70]

To obtain the calculation of the illustrated structures in Figure 23, it is referred to [70] for the summarized form factors and the corresponding parallel and perpendicular contributions, the Porod asymptotes $P_{d\infty}$, as well as the volumes of the structures.

During the thesis various lattice types were calculated with *Scatter* and compared with the measured scattering patterns. Therefore, the calculations for the structure factor have to be considered. The structure factor for an ideal undistorted structure is expressed with

$$S(\vec{q}, \vec{g}) = \frac{(2\pi)^3}{n v_d} \sum_{\substack{hkl=-\infty \\ (hkl)\neq(000)}}^{\infty} f_{hkl}^2 L_{hkl}\,(\vec{q}, \vec{g}_{hkl}) \tag{155}$$

hkl are the Miller indices, deriving from crystallography and characterize the crystallographic directions and distances. [64] Furthermore, n is the number of particles in the unit cell, f_{hkl} is the structure factor of the unit cell, v_d is the volume ($d = 3$), surface ($d = 2$) or long-period ($d = 1$) of the d-dimensional unit cell, $\vec{g}_{hkl}$ are the reciprocal lattice vectors and $L_{hkl}(\vec{q}, \vec{g}_{hkl})$ is a normalized peak shape function.

In equation (155) all values of the Miller indices are added except for $(hkl) = (000)$, which assures that the invariant Q is given by,

$$(2\pi)^{-3} V \int I(\vec{q}) d\vec{q} = Q = \phi_1(1 - \phi_1) \tag{156}$$

With the term $-\phi_1^2$ it ensures the consistency with Porod's law described in equation (152).

Thus, with the limit of $q \to 0$ the density fluctuations are,

$$\lim_{q \to 0} \frac{\langle N^2 \rangle - \langle N \rangle^2}{V} \tag{157}$$

As already mentioned, particles often are not located at the exact lattice points. Such disorders have to be taken into account. For translational disorder with statistically independent displacement of the particles from the lattice points, a Gaussian lattice point distribution with zero mean and a relative mean square displacement σ_α^2 is considered.

$$G(q) = exp[\sigma_\alpha^2 \bar{\alpha}^2 q^2] \tag{158}$$

Here, $G(q)$ is the already introduced Debye-Waller factor and $\bar{\alpha}$ is the next nearest distance to adjacent particles. [70] All calculation patterns for the used lattice types are listed in [70], to which should be referred for detailed information.

Experimental Set-up

Small angle X-ray scattering (SAXS) with the miniaturized X-ray optics and the third-generation synchrotrons has become a promising method for analysis of fast kinetics. As described in the introduction small beamsizes influences directly the temporal resolution of the Microfluidic-SAXS-experiment. The high brilliance of the third-generation synchrotrons enables short exposure times. Furthermore, SAXS is an accurate, non-destructive method with needs of small sample volume. During the thesis SAXS measurements were performed at Deutsches Elektronen-Synchrotron (DESY), at European Synchrotron Radiation Facility (ESRF) and at the in-house rotating anode Ganesha, SAXSLAB.

Synchrotrons like DESY or ESRF are working with storage rings. There, electrons or positrons are accelerated from few MeV to GeV. Moving charged particles emit electromagnetic radiation if an electrical or magnetic force applies on them. The particles run through the storage ring million times and emit radiation tangentially to the ring. [61,69] At DESY the PETRA III storage ring for X-rays is the most brilliant one in the world with a length of 2.3 km. [72] Also the ESRF has a source of the third generation with a beam energy of 6 GeV and a beam intensity of 200 mA. The storage ring has a length of 844.4 m and is the most powerful and stable source in Europe. [73]

The in-house X-ray measurements were performed with a rotating anode, Rigaku Micromax 007 HF. The used detector is a Pilatus 300K from DECTRIS. The set-up allows different sample detector distances, as well as a microfocus of about 100 µm, depending on the scattering intensity and the sample detector distance.

A representative SAXS experiment set-up is shown in Figure 24 and consists of an X-ray source, e.g. copper anode with a wavelength of 0.15418 nm (CuK_α), a collimation system (e.g. slits), the sample and the detector. The set-up used in this thesis is a transmission set-up, where the sample and detector are located perpendicular to the incident X-ray beam. [61,74]

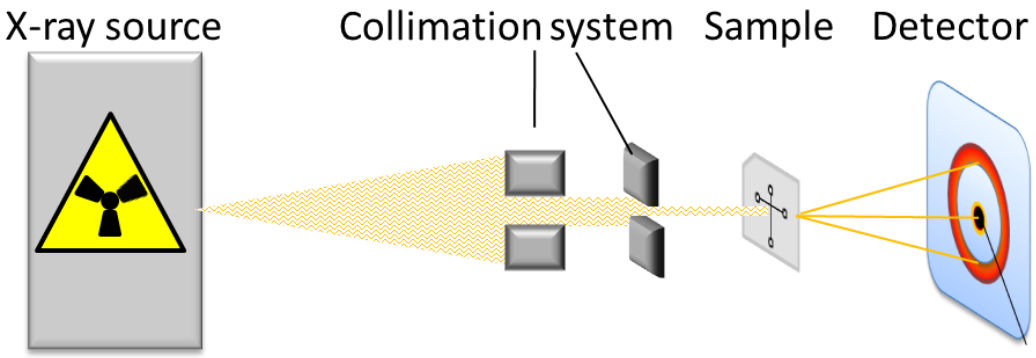

Figure 24. Set-up of small angle X-ray scattering (SAXS) experiment with a source generating X-rays. The collimation system adjusts the beamsize and a microfluidic chip includes the sample. The detector records the characteristic scattering patterns of the sample. Adapted with permission from Stribeck, N., X-ray scattering of soft matter, Copyright (2007), Springer and Lindner, P., Zemb, T., Neutrons, X-rays and Light: Scattering Methods Applied to Soft condensed Matter, Copyright Elsevier (2002)*. [61,63]

* This article was published in Neutrons, X-rays and Light: Scattering Methods Applied to Soft condensed Matter, Book ISBN: 0-444-51122-9, Lindner, Zemb, Chapter: Introduction to Scattering Experiments, Page 5, Copyright Elsevier (2002)

2.4 Further Characterization Methods

Microscopy

Microscopy is a field to visualize small structures, which cannot be resolved with the naked eye. The minimum resolvable detail of any microscope is dependent on the wavelength of the light and the numerical aperture (NA) of the microscope. It is defined with the Rayleigh criterion [75,76]

$$\delta = \frac{0.61\lambda}{\mu \sin \beta} \tag{159}$$

Here δ is the minimal resolvable distance, λ is the wavelength, μ is the refractive index of the material and β is the semi-angle of collection of the magnifying lenses.μ $sin\beta$ is also called the numerical aperture (NA) of the optical system. [75] The image of an ideal point is blurred and is described as an airy disc. The Rayleigh criterion says that two discs must be separated by at least their radius in order to be resolved. In Figure 25 the application area of the different microscopes and the structures observable at the characteristic length scales are illustrated.

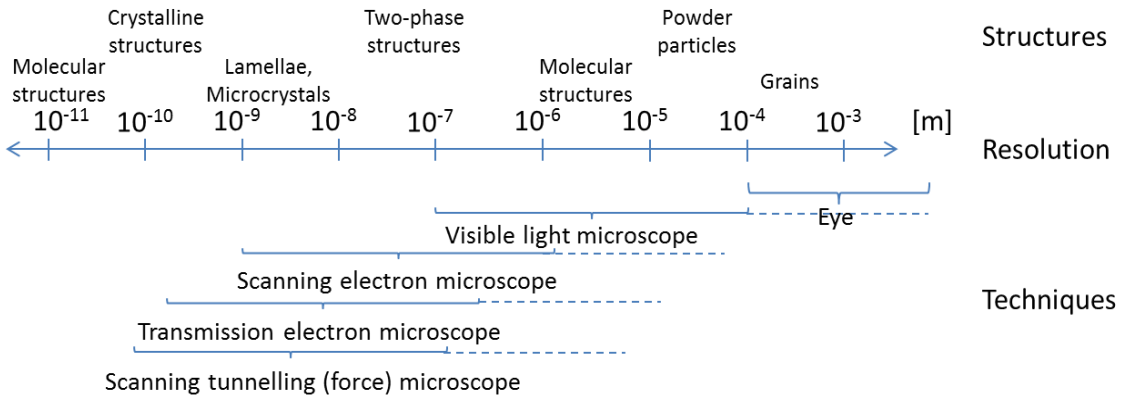

Figure 25. Length scale with the different analytical methods and their minimum resolution. Adapted with permission from Michler, G., H., Electron microscopy of polymers, Copyright (2008), Springer [77]

Figure 25 shows that with electron microscopy even crystalline structures can be investigated. De Broglie defined the wave like behavior of electrons with

$$\lambda = \frac{h}{p} \tag{160}$$

λ is the wavelength, h the Planck's constant, p is the magnitude of the particle momentum $\vec{p}$.

Taken into account relativistic effects this leads to equation (161) with e is the charge of the electron, m_0 the rest mass of the electron, c the velocity of light in vacuum and V the accelerating voltage. [77]

$$\lambda = h\left[2eVm_0 + \left(\frac{eV}{c}\right)^2\right]^{-\frac{1}{2}} \tag{161}$$

Equation (161) shows the relation of the accelerating voltage to the wavelength of the electrons.

Confocal Laser Scanning Microscopy (CLSM)

The main advantage of confocal laser scanning microscopy is that out of focus blur is barred from the images. Furthermore, the application of lasers as a point source to excite fluorophores allows the illumination of only small sample regions. Hence, three-dimensional images are available by serial non-invasive optical sectioning through the sample. [78]

So called fluorophores are molecules which can emit fluorescence light after excitation. Fluorescence is the emission of light, nanoseconds later than the adsorption of light, which is usually of shorter wavelength (Stokes shift). Before the adsorption of light, fluorophores are in the ground state S_0. If photons are hitting the atoms of the fluorophores, they absorb the photon energy, which can change their electronic, vibrational or rotational states. The uptake of energy can cause an electron to move to a more distanced orbital from the nucleus and the fluorophore is then in an excited state S_1, S_2. By molecular vibration or fluorescence emission the fluorophore returns to the ground state.

If outer electrons are raised to a new orbital, they are excited to the triplet states (T), which is then followed by reversal of the spin. Thus, the pair of electrons is now parallel, which is forbidden by quantum theory. This intersystem crossing between singlet to triplet states is unlikely but occurs especially, if the triplet state vibrational energy levels overlap with the lowest energy level in S_1. This leads to phosphorescence, which weakens fluorescence as it removes molecules from the illuminated volume. Phosphorescence can also cause irreversible bleaching and phototoxicity. [79]

The confocal laser scanning microscope set-up is illustrated in Figure 26. A laser, which serves as point light source, emits light of a certain wavelength. The emitted light (blue) is directed by a dichromatic mirror toward rotating mirrors, which are directing the light through lenses onto the sample. The laser light interacts with the sample and excites fluorochrome molecules in the focal plane of the sample. The fluorescent light (green) is directed with the same objectives and mirrors through a pinhole, which excludes all out of focus light. The remaining fluorescent light is then measured by the detector, usually a photomultiplier tube.[76,78,80]

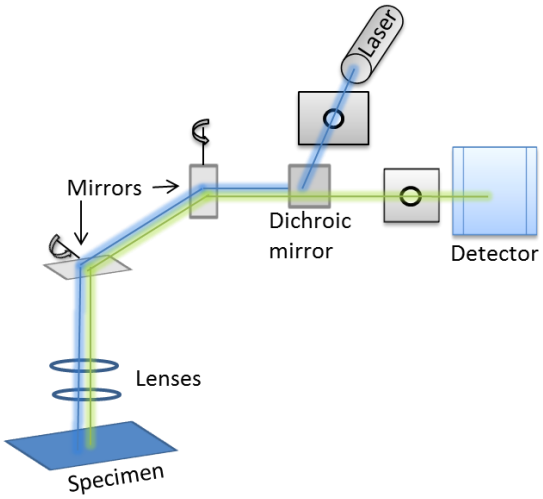

Figure 26. Scheme of the set-up of a confocal laser scanning microscope. Adapted with permission from Prasad, V., Semwogerere, D., Weeks, E.,R., Confocal microscopy of colloids, Copyright (2007), Journal of Physics : Condensed Matter.[76]

Hence, the point by point illumination by the laser and the exclusion of out of focus light from the detector with the pinhole leads to the advantages of the CLSM. Figure 27 compares simplified the imaging of confocal laser scanning microscope with a conventional optical microscope (OM). Usually the same objectives are used for illumination and detection as shown in Figure 26.

In conventional optical microscopy a large area of the specimen is illuminated by the light source transmitting information of many points in the sample. Furthermore, also the out of focus illuminated sample points are detected. In CLSM the point source allows illumination of small areas of the specimen. In addition, out-of-plane illuminated sample points are furthermore blocked by the pinhole or confocal imaging aperture, leading to high contrast and sharpness of the image. [76,78]

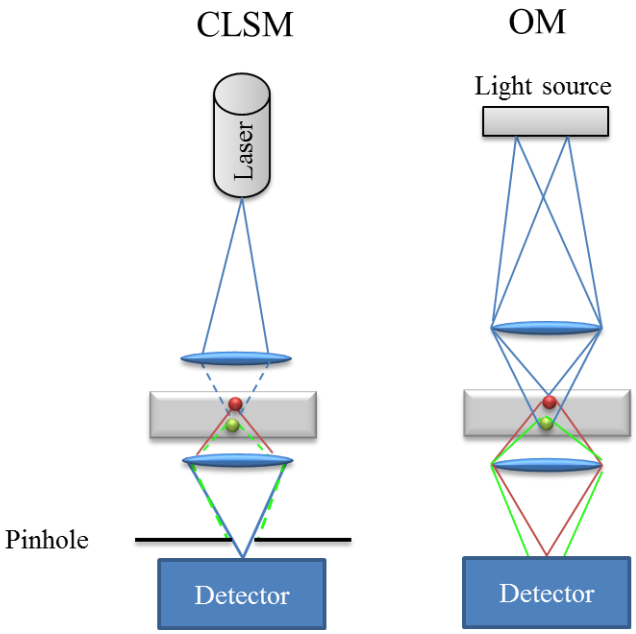

Figure 27. Pathway of the light in confocal laser scanning microscope (CLSM) and optical microscope (OM) Adapted with permission from Michler, G., H., Electron microscopy of polymers, Copyright (2008), Springer [77]

Cryogenic Transmission Electron Microscopy (Cryo-TEM)

Light microscopy has limited image resolution due to the wavelength of the visible light (~400-700 nm). Hence, electron microscopy was developed to overcome these limits since electrons have smaller wavelength (see equation (160)). [75,81] Up-to-date TEMs can analyze over a large spatial range, which is from the atomic scale < 1 nm up to micrometer and beyond. [75] If electrons hit a thin sample many secondary processes occur shown in Figure 28. For very thin samples, most of the electrons do not interact with the sample and are called transmitted electrons. Scattering of electrons can be classified into elastic and inelastic scattering. [82]

If the electrons are scattered at the nucleus without loss of energy but with a change of their direction, it is elastic scattering. This is the most important interaction for imaging electron microscopy causing image contrast. Inelastic scattering is used for analytical electron microscopy. Therefore, electrons are scattered by the electrons of the atomic shell of the sample and hence lose energy. [77,82] Transmission electron microscopy is the complementary technique to small angle X-ray scattering.[83]

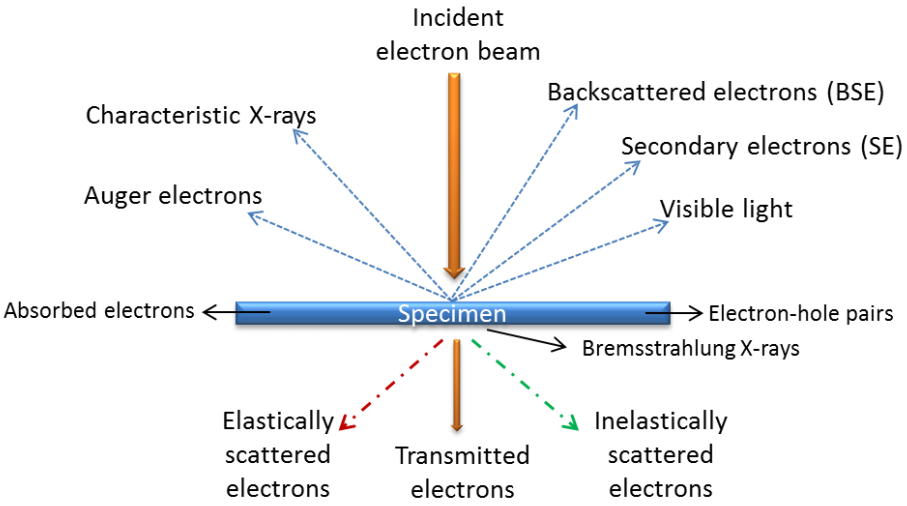

Figure 28. Secondary processes occurring when electron beam hit the sample. Adapted with permission from Williams, D., B., Carter, C., B., The Transmission Electron Microscope, Copyright (2009), Springer and Shindo, D., Oikawa, T., Analytical electron microscopy for materials science, Copyright (2002), Springer.[75,82]

In Figure 29 a basic transmission electron microscope is illustrated. The electron gun on top of the TEM yields the cathode generating electrons. These electrons are then accelerated to the anode forming a crossover. There are different types of electron guns characterizing the electron beam. It is differentiated between thermionic emission guns and field emission guns. For thermionic guns tungsten hairpin filaments or LaB_6 single crystals are used as electron sources. LaB_6 cathodes have a longer lifetime and higher brightness than tungsten tips but are more sensitive to thermal changes and need better vacuum. The emitted electrons are accelerated in the acceleration tube (anode) and pass the Wehnelt electrode, which has a higher negative potential than the cathode. It restricts the electron emission and also focuses the electrons to a crossover. Field emission guns (FEGs) are using quantum tunneling by electron extraction to achieve an electron beam.

Two anodes are used to first extract the electrons from the cathode and second to accelerate them. FEGs generate electrons with higher brightness and higher coherence than thermionic guns.[77,82] There are cold field emission guns and thermal emission guns. Both are using fine cathode tips, usually a tungsten tip. Cold FEGs have better performance characteristics but the thermal FEG has less emission noise and a stable emission current.

The next part of the microscope is the illumination system. There, the electrons are focused and transferred to the sample. In doing so the beam is usually converged and focused with at least two condenser systems. The first condenser lens is stronger and decreases the gun crossover to and image of 1 µm in diameter.

Then, the second weaker lens projects the image onto the sample plane. Depending on the purpose of the TEM further lenses are incorporated. The image-forming system yields the sample holder with the specimen and objective lenses, which forms images when electrons pass through the specimen. The objective lens consists of lens coils, a magnetic circuit and a polepiece, which shape determines the optical properties of the lens. Various aberrations occur during electron microscope measurement, amongst others spherical and chromatic aberration and astigmatism. A spherical aberration from the objective lense is determined with the spherical aberration coefficient C_S. Chromatic aberration occurs due to variation in the current for objective lens excitation and changes the varies the focal length. It is taken into account with the chromatic aberration coefficient C_C. Astigmatism occurs because of inhomogeneities of the pole-pieces, elliptical pole-piece bores, charging effects in the bore or the aperture diaphragm form contamination. It is corrected by quadrupole lenses, so called stigmators. The magnifying lens system consists of the intermediate and projector lenses. Magnification and hence change of the focal length, is made by changing the strength of the magnetic field in the magnetic lens.

The final part of the transmission electron microscope is the image acquisition with the viewing screen, usually equipped with a binocular for focusing the images, and the camera chamber, where the images are recorded. [77 82]

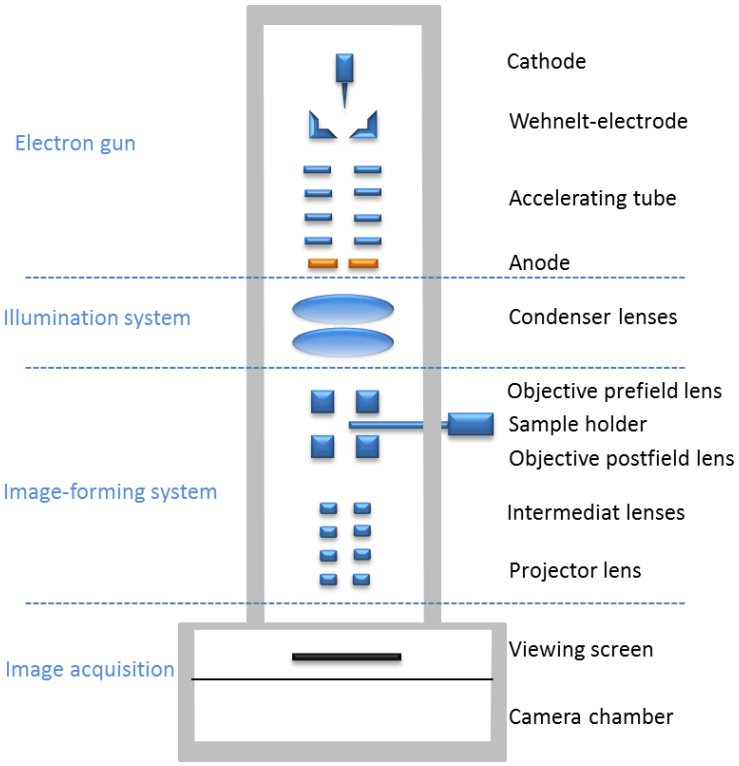

Figure 29. Scheme of a basic transmission electron microscope. Adapted with permission from Michler, G., H., Electron microscopy of polymers, Copyright (2008), Springer [77]

For Cryo-TEM measurements the sample is dropped on a supporting grid, frozen and measured at cryogenic temperatures. The freezing of the sample has to be very fast to minimize the contamination with water crystals. The vitrified sample is brought into the vacuum chamber of the TEM, which is cooled with liquid nitrogen, and recorded.[83,84]

3 Experiments

3.1 Small Angle X-ray Scattering

SAXS measurements were performed at the Deutsches Elektronen-Synchrotron (DESY) in Hamburg and at the European Synchrotron Radiation Facility (ERSF) in Grenoble. At DESY all experiments were performed at the P03, Micro- and Nanofocus X-ray Scattering (MiNaXS) beamline at the PETRA III storage ring. The measurements at the ESRF in Grenoble were made at the ID13 microfocus beamline. Furthermore, SAXS measurements were performed at the in-house rotating anode Ganesha (SAXSLAB), equipped with a rotating anode (Rigaku Micromax 007 HF).

3.2 Confocal Laser Scanning Microscopy

The measured CLSM images shown in this work were all measured with TCS SP8, equipped with an inverse DMI 6000B Microscope, from Leica. The scans were carried out with precise x-, y-, z-stage movements, carrying the specimen. With a variable confocal aperture (pinhole), the quality of the measured images could be enhanced.

3.3 Cryogenic Transmission Electron Microscopy

The Cryo-TEM measurements were performed with LEO EM922 Omega TEM from Zeiss with an accelerating voltage of 200 kV. Magnification of 80 to 100000x is possible with a lateral resolution of <0.24 nm. The samples were dropped on a lacey grid and rapidly frozen in liquid ethane. Therefore, the controlled environmental vitrification system (CEVS) was used to control the temperature and humidity during preparation. [85,86]

3.4 COMSOL Multiphysics

In microfluidics the fluid dynamics are expressed with partial differential equations, e.g. Navier-Stokes equation. These equations can be solved numerically with computational fluid dynamics (CFD) by various methods, like finite difference, finite volume, finite element and spectral methods. [87] The finite-element method (FEM) uses portioned simple functions defined on a small element. This leads to an approximation of the exact solution. It is then estimated how far it is from fulfilling the exact equations. The FEM shows superior performance compared to other methods like the finite difference method (FDM) and needs better computer memory.[88,89] Simulations using FEM in this thesis were performed with COMSOL Multiphysics software (v 5.0).

4 Results and Discussion

4.1 Materials for Microfluidic Devices

A microfluidic device material must fulfil specific criteria based on the desired purpose of the device. The three most important requirements of the microfluidic device material are solvent stability, fabrication as well as specific optical properties depicted in Figure 30.

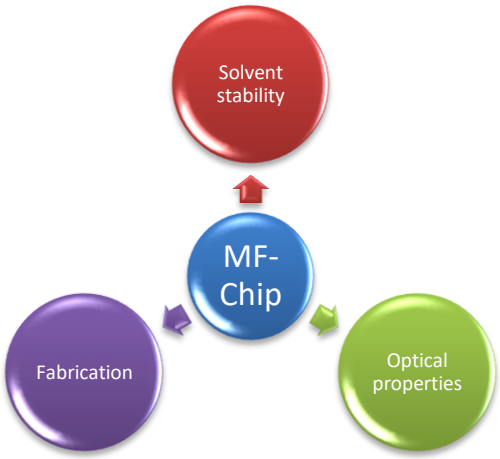

Figure 30. Requirements for microfluidic device material.

Solvent Resistant Chip Materials

As microfluidics deals with the manipulation of liquids, the chip material has to be resistant to the used solvent. Especially organic solvents cause swelling or dissolution of oligomers of the standard used chip materials. [90] Figure 31 shows the swelling of a PDMS microfluidic device with Tetrahydrofuran (THF). The left image shows the channel cross with no THF in the MF chip. The black bars show the channel walls. In the right image THF is pumped into the microfluidic chip for five minutes. The swelling of the PDMS leads to deformation of the channel design. The dashed lines show the original channel wall distance.

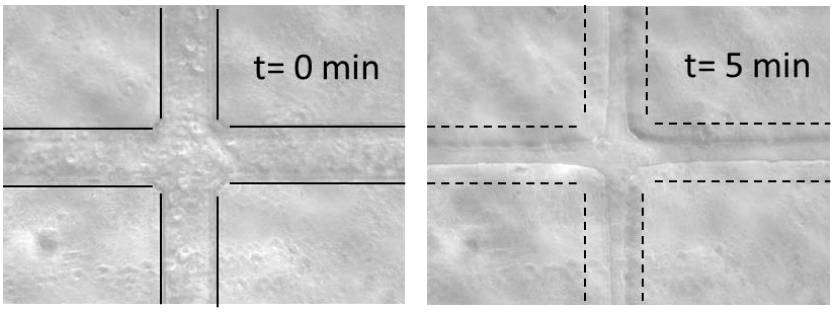

Figure 31. Light microscope images of a PDMS microfluidic device at the channel cross. Left: Channel cross with no penetration of THF. Right: THF pumped into the MF chip for 5 minutes, causes swelling of the PDMS material and change in the channel geometry.

The change of the channel geometry disturbs investigations in the MF device. Especially in kinetic studies, where the time scale of the reaction is dependent on the channel geometry, the investigation is falsified.

With two different methods several materials were tested against their resistance to different organic solvents. In the first method, the solvent was pumped through the completed MF chip based on the particular material, whereas changes of the channel geometry were observed under the optical microscope. The second approach was to put pieces of the material into a vial together with the organic solvent and to follow the changing of the material, like swelling or dissolving. The outcome of these two methods is summarized in Table 2.

Table 2. Resistant test of various polymers and the corresponding solvents. x: dissolution or swelling of the material, o: no change observed, -: not tested

Polymer / Solvent	PDMS	NOA 81	THV815 GZ	THV610 AZ	THV500 GZ	TVH221	ET6235	HTE-1705Z
THF	x	x	x	o	o	x	a	x
Toluene	x	x	x	o	o	o	o	o
Chloroform	x	x	x	o	o	o	o	o
Dioxane	x	x	x	o	o	o	o	o
Acetone	o	o	x	x	o	x	o	o
Octadecene	o	o	x	o	o	o	o	o

Polymer / Solvent	PS	PMMA	TOPAS 8007/6013	Bendlay	SIFEL	SU8 50
THF	x	x	x	x	o	o
Toluene	x	o	x	x	o	o
Chloroform	x	x	x	x	o	o
Dioxane	x	x	o	x	o	o
Acetone	x	x	o	x	o	-
Octadecene	o	o	x	o	-	-

It has to be mentioned that for the tests of the Norland Optical Adhesive (NOA) 81 with toluene, PDMS with dioxane and for HTE1705Z with THF the changes were small and the solvents can be used in combination with the material depending on the application. In literature swelling tests of PDMS with dioxane are indicated with a moderate solubility. [91] For example, a swelling was observed while floating a NOA 81 MF chip with toluene although the swelling degree was little for a long period of time. Optical microscope images of this experiment are shown in Figure 32.

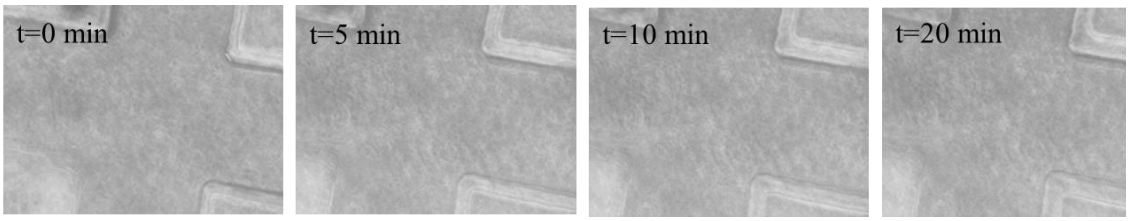

Figure 32. Optical microscope images of toluene pumped through NOA81 MF chip after 0 min, 5 min, 10 min and 20 min.

Publications listing the swelling ratio of PDMS or SIFEL with non-polar solvents are using equation (162).

$$S = \frac{D}{D_0} \tag{162}$$

The calculated swelling ratio S compares the length of the polymer in the solvent D and the length of the dry polymer D_0. If the swelling ratio S is 1 there is no swelling of the polymer with the solvent. For further information it is referred to [90,91].

SIFEL2610 is a fluorinated polymer distributed by Shin-Etsu. In Figure 33 the chemical structure of SIFEL is illustrated. [91]

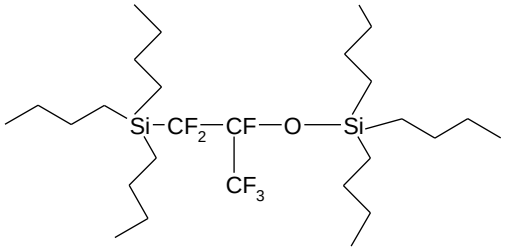

Figure 33. Chemical structure of SIFEL. Adapted with permission from Maltezos, G., Gracia, E., Gomez, F., A., Vyawhare, S., van Dam, R., Michael, chen, Y., Scherer, a., Design and fabrication of chemically robust three-dimensional microfluidic valves. Copyright (2007), Royal Society of Chemistry. [91]

It is liquid at room temperature and hardens at elevated temperatures. SIFEL2610 is stable to all our tested organic solvents and is therefore suitable for experiments realized in organic solvents. The chip fabrication is more time consuming than the PDMS chip production, but fast prototyping can still be realized due to the similar procedure to PDMS.

SIFEL2610 is a turbid elastomer with a certain background scattering in SAXS measurements. To minimize the background scattering and to analyze also samples with low scattering intensity a combination of a glass-capillary with a SIFEL2610 microfluidic chip was developed. Hence, the defined mixing of the reagents is realized in the SIFEL-microfluidic chip part and the SAXS measurements are made in the glass-capillary region with the low background scattering. Furthermore, due to the no-slip boundary conditions described in chapter 2.2.1.2, a three-dimensional design was investigated to avoid wall contact of the reactants with the channel walls.

In the thesis also different THVs purchased from 3M (Dyneon) were tested. THVs are fluorothermoplastics consisting of blended tetrafluoro ethylene, hexafluoro propylene and vinylidene. [92] The THV microfluidic chips were fabricated via hot embossing, introduced in chapter 2.2.1.8.

Optical Properties of Chip Materials

Depending on the application, the optical properties have to be considered by choosing the adequate chip material. The most commonly used analysis method is microscopy. Hence, optical properties, like transparency of the chip material, should allow microscopic investigation. Furthermore, for diffraction methods like small angle X-ray scattering the background scattering should be low and the material should withstand X-radiation. Therefore, many different device materials were tested with the in-house rotating anode. The intensities in Figure 34 und Figure 35 were multiplied with various factors for plotting the numerous curves. In Figure 34 the different materials were measured with a closer detector position to the sample than in Figure 35. Beam stops of either 2 mm or 4 mm in size (x- and y-direction) were used.

Most of the tested materials at the short detector sample distance (Figure 34) show a peak at high q-values (dashed curves). This limits their usage for SAXS measurements of small particles, e.g. kinetic investigations of nanoparticle's nucleation and growth. The solid curves point out the materials with a flat scattering curve and hence, low background scattering at the q-values 0.06 nm^{-1} to 1.1 nm^{-1}.

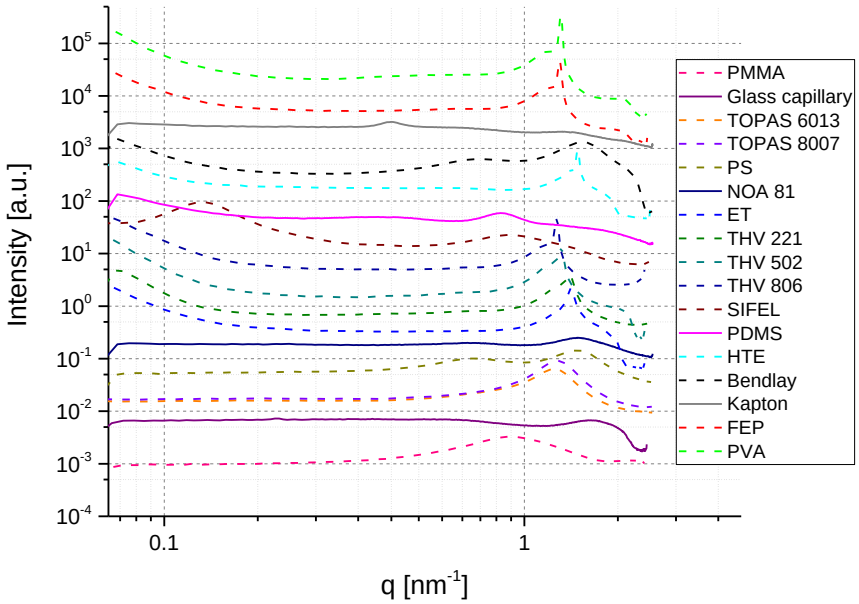

Figure 34. SAXS measurements of all tested materials in configuration 1.

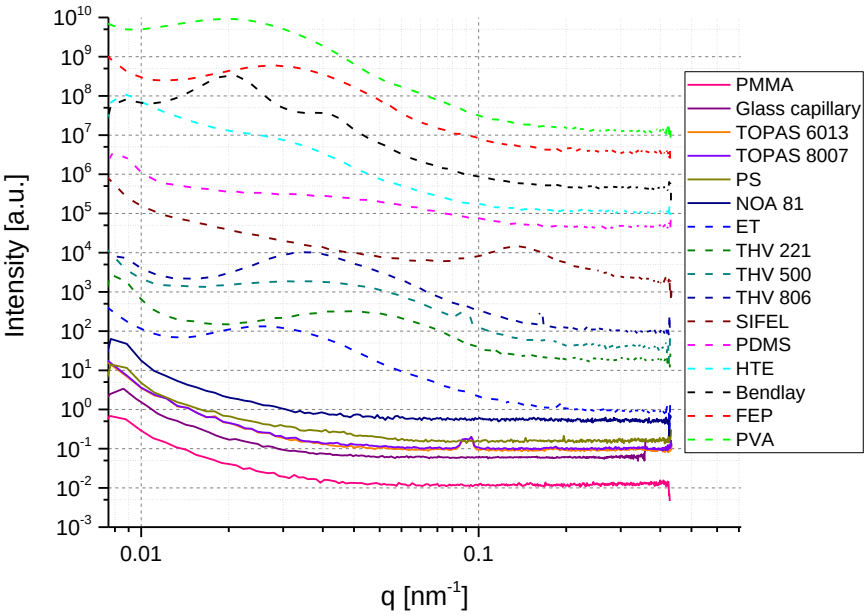

Figure 35. SAXS measurements of all tested materials in configuration 3.

In Figure 35, SAXS measurements of the different chip materials were performed at a larger distance between the sample and the detector. The dashed curves have a large peak at low q-values, which hinder the analyzation of larger particles. Consequently, for large objects PMMA, TOPAS, PS, NOA 81 are convenient for SAXS measurements in the microfluidic chip. For small particles Kapton®, PDMS, NOA 81 are appropriate for microfluidic chip materials. For comparison, the scattering curves for glass capillaries with 1 mm outer diameter and a wall thickness of 0.01 mm are also shown in Figure 35 (purple curve).

Besides the background scattering of the material and the solvent stability, the ease of production is also relevant. The most commonly used microfluidic chip fabrication methods are soft-lithography (2.2.1.7) and hot embossing (2.2.1.8). The success of these two methods arises from the fast and easy production process.

Furthermore, the desired microfluidic chip has to be reproducible and should be adaptable to many different channel designs. Rapid prototyping as described in 2.2.1.9 is a great advantage for testing new microfluidic chip designs. In combination with COMSOL, the time and effort to design, test and produce suitable microfluidic chips is reduced to a minimum. During the thesis many different microfluidic channel designs, and chip materials were used to achieve various properties. PDMS was mainly used for water based systems, since the resistance to organic solvents is limited. Optical properties, i.e. the clear and transparent appearance, favor PDMS for microscopic application, like Confocal Laser Scanning Microscopy (CLSM). In SAXS experiments the scattering of PDMS is relatively high, for which very thin or hybrid chips need to be used. However, the elastomeric properties make the thin PDMS very unstable and difficult for handling.

Thus, for water based solutions and *in-situ* small angle X-ray studies, Norland Optical Adhesive (NOA) 81 was used. With this UV-light curable adhesive, it is possible to produce very thin microfluidic chips, as the hardened material is very stiff. Due to a chip thickness of about 400 nm, the background scattering of the chip material could be minimized. Another advantage is the fast production of the NOA based chip. In less than ten minutes it is possible to obtain a complete microfluidic device. However, the chip material is unstable to most of the organic solvents (Table 2) and at high intensity synchrotron radiation beam damage can occur in the chip material. Consequently, the application is limited to mainly water based experiments and the exposure dose has to be minimized.

Another used chip material is THV of different composition. The chips were produced *via* hot embossing. This device material is resistant to many organic solvents. Yet, the chip production is time-consuming, since the heating and cooling of the material to emboss the chip design takes several minutes. Due to the fact that the alignment for bonding of at least two structured sheets is tedious, it is very difficult to achieve three-dimensional chip designs.

The last used chip material is SIFEL2610 purchased from Shin-Etsu. SIFEL is resistant to all tested organic solvents and cures under heat. It is produced by layering until the desired thickness is obtained. For stabilization PDMS is cured on top of SIFEL. Since only the first few layers, i.e. the part which is in contact with solvents, consists of SIFEL, the volumetric major part consists of the relatively cheap PDMS. SIFEL is slightly turbid and has a peak in SAXS at ~0.015 nm^{-1}. Furthermore, the PDMS part used for stabilization impairs the background scattering. Therefore, in this thesis a new three-dimensional chip design in SIFEL with a glass capillary as the continuing main channel was developed. In the SIFEL-PDMS chip part the mixing of the reactants is controlled, whereas the thin walled glass capillary represents the part of the chip where the SAXS measurement is carried out.

The three-dimensional design was used to avoid wall contact of the reactants, as the no slip boundary condition leads to sticking of the particles to the channel walls. Furthermore, a buffer stream separates the two reactants, which enables to control the mixing position or contact point of the reactants in the microfluidic channel or in the glass capillary. For this three-dimensional design both chip halves are structured and have to be bonded in an accurate way.

Microfluidic Device Design

The design of microfluidic devices is in general very variable. Due to rapid prototyping and flow simulation (COMSOL) many different designs for various applications can be realized. The limitation is usually the fabrication of the microfluidic chip. Micromolding for PDMS or SIFEL allows precise and close structures and even three-dimensional chip designs.

A further problem occurs due to the elastomeric properties of SIFEL2610 and PDMS. This softness limits the aspect ratio of the device design. The aspect ratio

$$aspect\ ratio = \frac{h}{w} \tag{163}$$

is defined by the width w and the height h of the structure, but also the distance d between different structures has to be considered. If the aspect ratio is too high or too low the polymer will deform leading to sagging or pairing of the individual structure elements as shown in Figure 36. In literature for PDMS an aspect ratio of 0.2 to 2 is suggested to avoid deformation in the structure. [14,93]

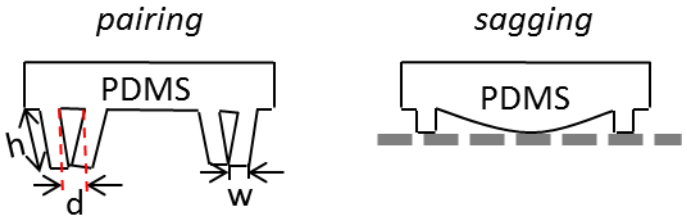

Figure 36. Scheme of sagging and pairing at too high and too low aspect ratio. Adapted with permission from Xia, Y., Whitesides, G., M., SOFT LITHOGRAPHY. Copyright (1998), Annual Reviews [14]

Different device designs were used during the thesis. The first used chip design yielded a perpendicular channel cross with three inlets, a long meander and one outlet. This chip design allows a two-dimensional hydrodynamic flow focusing as shown in Figure 37. One reactant is pumped in from the main channel (MC) and is then focused by another reactant flowing from the two side channels (SC). A long meander allows the investigating over a long period of time, because of a long retention time of the reactants in the chip. At the same time the microfluidic chip size is kept small.

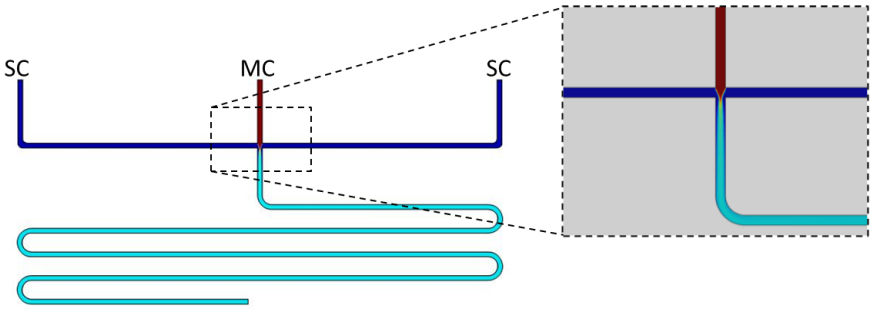

Figure 37. Concentration simulation (COMSOL) of the microfluidic chip with a two-dimensional hydrodynamic focusing of the reactant flowing from the main channel (MC) by the two solutions coming from the side channels (SC).

4.2 Vesicle Formation Pathways Under Very Fast and Very Slow Formation Conditions

Introduction

In many industrial relevant mixing and formulation processes the mixing times are very short, and can be in the range of the molecular relaxation times. This could lead to the formation of non-equilibrium structures, which may be trapped during the course of the mixing process. This is of relevance even for small-molecule surfactant formulations, because structural rearrangements on the micellar and vesicular level can be surprisingly slow.

In particular the evolution of vesicles from micellar structures fall in this category. Depending on the preparation method, vesicle formation can proceed via different topological pathways and can occur on different time scales. Unilamellar vesicles as the simplest of all vesicular structures can be prepared by different methods, including extrusion of multilamellar vesicles or lamellar phases, lamellar phase unbinding by dilution, shear or sonication, or by mixing stoichiometric ratios of cationic and anionic surfactant solutions. The latter method often produces quite narrow disperse catanionic vesicles in the 100-nm range, which is useful for many applications, but it depends critically on the mixing conditions and its time scale.

Mixtures of cationic and anionic surfactant systems have a strong tendency to precipitate at equimolar mixing ratios. This is much less pronounced for mixtures of anionic and zwitterionic surfactants because of the reduced electrostatic attraction. These also form vesicular systems, especially for the case of zwitterionic hydrocarbon and anionic fluorocarbon surfactants. A particularly well investigated system consists of the anionic surfactant lithium perfluorooctanoate (LPFO) and the zwitterionic surfactant tetradecyldimethylamine oxide (TDMAO). LPFO forms spherical micelles in dilute solution, while TDMAO forms cylindrical micelles. The vesicle formation of these surfactants has been investigated by Gradzielski et al. [94,95] They demonstrated that upon mixing vesicles are formed over a broad range of TDMAO mixing ratios.

In the vesicles both surfactants form mixed bilayers, because the attractive charges overcompensate the immiscibility of the hydro- and fluorocarbons. Kinetic studies revealed that immediately after mixing, disk-like micelles are formed, which grow and eventually close into vesicles over a large range of time scales from milliseconds to minutes. [96–98]

These experiments were performed using stopped-flow mixing techniques, which are widely used to induce rapid concentration changes to trigger fast chemical reactions, structural changes in proteins, surfactant self-assembly and nucleation and growth processes. Recent progress in microfluidic device engineering have made also fast continuous-flow mixing experiments possible, which enable in-situ investigations of fast mixing processes also for complex and viscous fluids. [99] Fast mixing is possible by using hydrodynamic flow-focusing devices, which focus a stream of reactants using two orthogonal streams from side channels through a mixing cross downstream into a reaction channel, where a reaction or a structural change takes place. As fluid flow in microchannels is laminar, even at high flow rates, interdiffusion is the only mixing processes and well-defined steep stationary concentration gradients are established. Under stationary laminar flow conditions, different times after mixing can be mapped downstream onto different positions in the microchannel. The temporal resolution then is given by the spatial resolution of the detection technique and the flow-rate in the experiment, and is not set by the temporal resolution of the detection technique.

Similar to microfluidics, X-ray optics has considerably advanced in recent years. It has become possible to focus X-ray beams to micrometer spot sizes, at dedicated synchrotron beamlines even reaching sub-micron dimensions. This enables high resolution microbeam X-ray diffraction experiments to follow the local structural evolutions in microfluidic channels. The combination of both methods then allows one to follow fast structural changes with high spatial and temporal resolution. Fast, even sub-millisecond protein folding kinetics could be followed using this technique. Recently, this technique was also applied to study flow-reorientation of anisotropic colloids in narrow microchannels.

To investigate catanionic vesicle formation at early, intermediate and late stages of structure formation in-situ over time scales from milliseconds to days, we used a combination of continuous flow microfluidics and capillary interdiffusion combined with micro-focus small-angle X-ray scattering and cryo-transmission electron microscopy.

Materials and Methods

Preparation of microfluidic devices. The microfluidic chip material based on a UV curable polymer, NOA81 (Norland Products Incorporated). Details of the chip preparation are described in the supporting information. The microchannel downstream of the channel cross has a width of x=182 µm, a height of h=100 µm, and a length of l≈86 mm. A sketch of the device is shown in Figure 38.

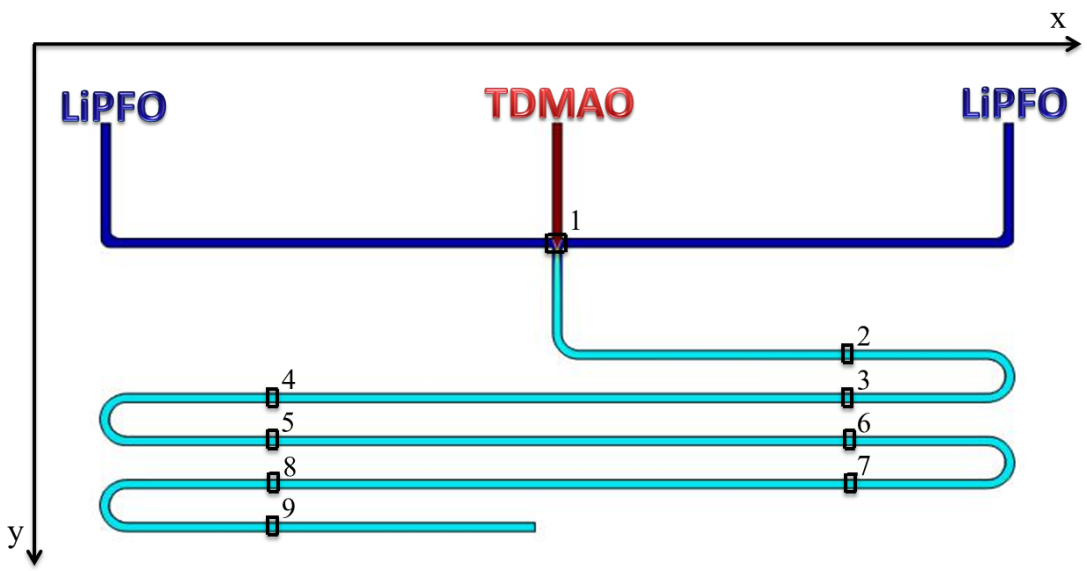

Figure 38. Sketch of the microfluidic device and the analyzed positions (1-9) along the channel. TDMAO is pumped into the main channel, which is hydrodynamically focused by LFPO from both side channels.

Sample Preparation. Tetradecyldimethylamine oxide (TDMAO) was used as received from Sigma Aldrich. Lithium perfluorooctanoate (LPFO) was synthesized via saponification. Both surfactants were then dissolved in water at concentrations of 50 mM and 100 mM.

Small-angle X-ray scattering. The experiments were performed at the microfocus beamline ID13 of the European Synchrotron Research Facility (ESRF), Grenoble, France. The beam diameter was adjusted to 3 µm in x- direction and 4 µm in y-direction with a wavelength of λ=0.095 nm. As a detector a FReLoN camera with 2000 x 2000 pixels cooled to -15 °C [100] and a sample-detector distance of 0.288 m was used. The beam was scanned over the stationary concentration gradient that develops in the microchannel upon mixing. For the measurements we used NOA-based microfluidic devices to meet the requirements for high X-ray transmission.

The in-house glass capillary measurements were performed at a GANESHA (SAXSLAB) small-angle X-ray scattering setup equipped with a microfocus rotating anode (Rigaku Micromax 007 HF) and a Pilatus 300K detector (DECTRIS). The X-ray beam (λ = 0.154 nm) was focused to 100 µm for the scanning experiment. The used sample to detector distance was ~0.3 m.

Microfluidic/SAXS experiment. The gas-tight syringes (Hamilton) were set up in a high-precision syringe pump (NEMESYS, Cetoni GmbH) and connected via PE tubing (Scientific Commodities Inc.) with the microfluidic chip. The background measurements were performed prior to the experiments with pure water in the microfluidic channel under quiescent conditions. The background was measured for 0.2 seconds. All presented scattering curves in this report are background-subtracted.

At the ID13 beamline, the alignment of the microfluidic chip in the environment of the beamline was monitored with a microscope camera, which showed the approximate position of the X-ray beam. With this procedure the motor position corresponding to the beam penetrating the channel walls could be identified as well as the positions for the channel cross. To ensure that the whole chip was scanned, a larger area than the actual chip dimension was measured.

To align the capillary in the sample environment of the GANESHA set-up, the pin-diode intensity in front of the detector was monitored while moving the capillary through the beam path. The motor positions corresponding to positioning the X-ray beam in the center of the capillary could be followed by a decreasing beam intensity measured at the diode due to increasing capillary material in the beam path.

Afterwards the flow rates were set to 100 µl/h for the main channel (TDMAO) and 100 µl/h for both side channels (LPFO). Figure 40 shows the scanning regions of the X-ray measurements along the microfluidic channel. The first scanning region (1) was within the channel mixing cross. Subsequent scanning regions were located downstream in the outlet channel (2-9).

Static SAXS capillary experiment. A glass capillary (Ø 1 mm, Müller&Müller OHG Glasbläserei, Germany) was filled with ca. $\sim 0.02\ ml$ of a 100 mM LPFO micellar solution and then carefully topped with the same amount of a 100 mM TDMAO micellar solution to achieve a visible interface between both solutions. The structural evolution at the interface was then followed over 10 days. Here, a detector distance of ~0.3 mm was chosen. The beam spotsize was set to approximately 100 µm. The integration time for each sample measurement was 10 minutes. The background measurement, which was carried out with solely water in a separate capillary, had an integration time of 40 minutes.

Cryogenic Transmission Electron Microscopy (Cryo-TEM). For the Cryo-TEM measurements 2µl of the solution exiting the microfluidic chip were dropped onto a lacey carbon filmed copper grid (Science Services). Subsequently, most liquid was removed with blotting paper. The specimen was vitrified by rapid immersion in liquid ethane at its freezing point in a controlled environmental vitrification system (CEVS) (Zeiss Cryobox, Zeiss Microscopy GmbH). After shock freezing, the sample was inserted into a cryotransfer holder (CT3500, Gatan) and transferred to a Zeiss/LEO EM922 Omega EFTEM (Zeiss Microscopy GmbH). The TEM was operated at an acceleration voltage of 200 kV. Zero-loss filtered micrographs (DE=0 eV) were taken under reduced dose conditions (100–1000 e/nm^2). All images were registered digitally by a bottom-mounted slow-scan CCD camera system (Ultrascan 1000, Gatan) combined and processed with a digital imaging processing system (Digital Micrograph GMS 1.9, Gatan).

Results and Discussion

Micellar structures under static conditions

Prior to the kinetic experiments, the micellar structure of the pure LPFO solution containing spherical micelles and the pure TDMAO solution containing cylindrical micelles were characterized by small-angle X-ray scattering (SAXS) under quiescent conditions in a capillary at a concentration of 100 mM. This concentration is larger than the critical micelle concentration of TDMAO ($CMC = 0.12\,mM$) and of LPFO ($CMC = 0.31\,mM$). The measured scattering curves are shown in Figure 39. For the LPFO solution we observe a pronounced maximum at $q^* = 0.85\,nm^{-1}$ corresponding to a length scale of $d^* = \frac{2\pi}{q} = 7.4\,nm$, which corresponds to the intermicellar distance. The higher scattering intensity compared to TDMAO is due to the fluorinated alkyl chains which provide large SAXS-contrast. At $q \approx 3\,nm^{-1}$ we observe the first minimum of the form factor oscillation, corresponding to a micellar radius of $R \approx 1.5\,nm$. The scattering curve measured for the TDMAO-solution shows a q^{-1}-scaling at low q, characteristic for cylindrical micelles, with a weak form factor minimum at $q \approx 3\,nm^{-1}$. A quantitative analysis by fitting the experimental scattering curves to theoretical models for polydisperse spheres, using a Percus-Yevick structure factor, and for cylinders yields values of $R = 1.4\,nm$ for the spherical LPFO-micelles and a cross-sectional radius of $R = 1.5\,nm$ and a length of $L = 18.3\,nm$ for the cylindrical TDMAO micelles. These values are in good agreement with the values determined by Gradzielski *et al.* [94] for these surfactant systems at lower concentrations.

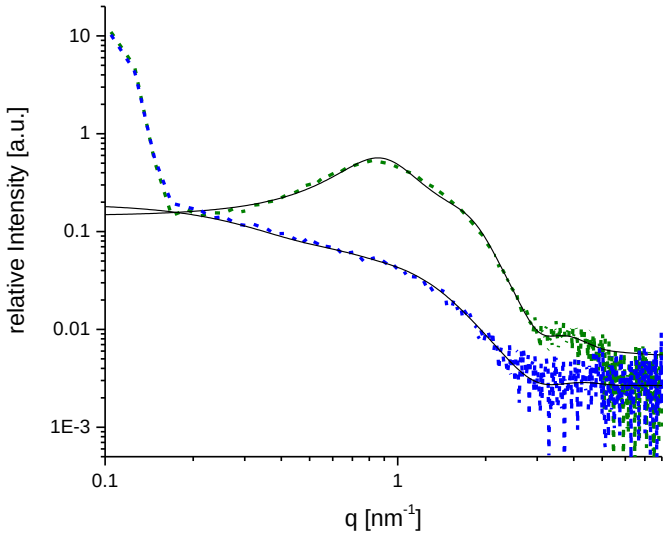

Figure 39. SAXS curves of 100 mM LPFO/H_2O (green) and 100 mM TDMAO/H_2O (blue) measured in a glass capillary of 1 mm outer radius and a wall thickness of 0.01 mm.

Microfluidic microfocus synchrotron SAXS

The very early stages of the interdiffusion and structure formation process were studied by continuous flow microfluidic flow-focusing experiments. The corresponding experiment with the layout of the microfluidic channels is shown in Figure 38. A stream of a TDMAO cylindrical micelle solution is hydrodynamically focused with two solutions of LPFO spherical micelles into a mixing channel. In the mixing cross and the mixing channel this establishes a well-defined, stationary and at the beginning of the mixing process very steep concentration gradient between the two micellar streams, leading to very fast mixing on time scales of milliseconds.

The microfluidic channels had a width of $w = 182\ \mu m$ and a height of $h = 100\ \mu m$. The volumetric flow in the central and focusing channels were typically $Q = 100\ \mu l/h$, corresponding to mean flow velocities of $v = \frac{Q}{wh} = 1.5\ mm/s$. In the outlet channel the velocity is three time this value, i.e. $v = 4.5\ mm/s$. The developing structures in the microfluidic channels were monitored using raster-scanning with a microfocus X-ray beam with 10 x 10 μm^2 spot size to measure the SAXS-patterns at each position.

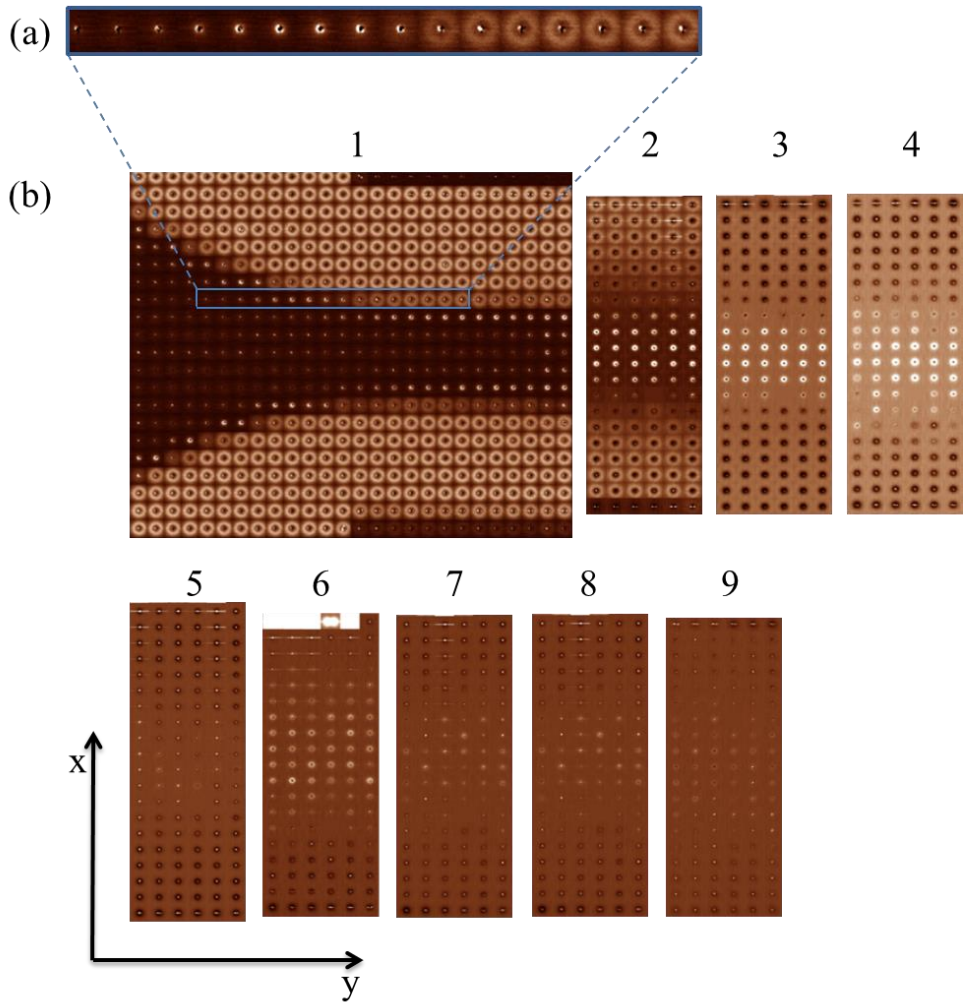

Figure 40. (a) Detail: Evolution of structures across the interface of the two solutions; (b) Overview of scattering images measured across the microfluidic channel; number each position from 1–9 scanned in y- and x-line.

Figure 40 (b) shows the measured scattering patterns at each of the measured positions in the mixing cross, where the TDMAO- and LPFO micellar solutions make first contact, and in the subsequent downstream scanning regions, numbered from 1-9 as in Figure 38. The characteristic Debye-Scherrer ring of the LPFO micellar solution, similar the LPFO-scattering curve in Figure 39, is observed in the upper and lower part of the entrance channel and of the reaction channel. The TDMAO micellar solution shows a much weaker, featureless scattering pattern. The location of the two focusing LPFO-streams and the central TDMAO-stream can be well recognized from the measured scattering patterns.

In Figure 40 (a) the scattering patterns developing across the interface of the two micellar solutions are shown in more detail. Each scattering pattern corresponds to a 10 x 10 μm^2 area within the microfluidic channel.

From the left, we observe for the first five positions a very weak scattering pattern, corresponding to the weakly scattering TDMAO-solution. At position 6, and more visible at the subsequent positions 7-9, we observe a pronounced low-*q* scattering corresponding to the emergence of larger structures, much larger than the spherical LPFO- and cylindrical TDMAO-micelles. At position 10 we observe a very weak Debye-Scherrer ring, becoming more intense at the subsequent positions 11-16, but not changing its position. This shows that in the interfacial region a new structure is emerging, as the corresponding scattering pattern with its pronounced low-*q* upturn is very different from the scattering curves measured for the adjacent LPFO- and TDMAO-streams. The mapping of different mixing times to different positions in the channel is in this case of great advantage to follow and understand fast structural evolution.

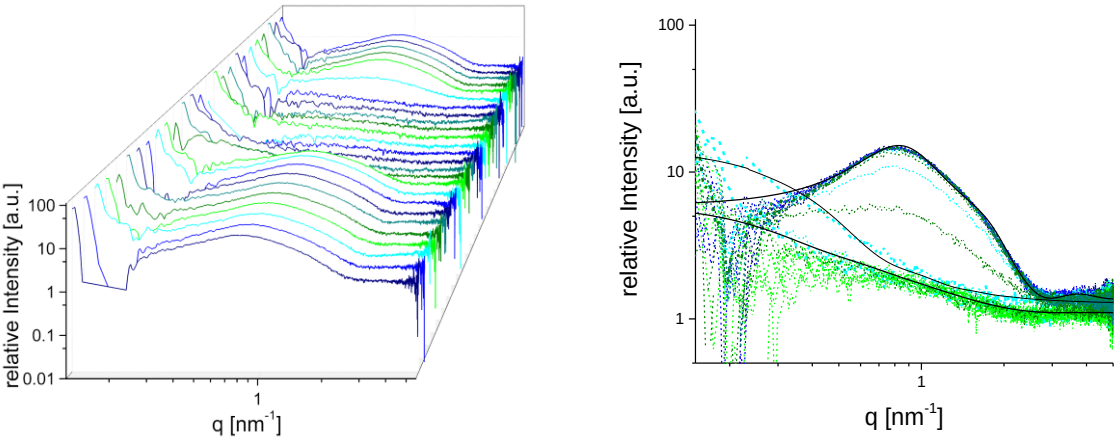

Figure 41. Both graphs show all SAXS measurements of one-line scan along y-direction at the microfluidic channel cross. A concentration of 100 mM and a flow velocity of 100 µl/h for each solution was used. Left: Parallel stacking of adjacent measurements, showing the symmetric flow focusing of TDMAO with LPFO in the channel cross. Right: Plot shows the three different structures occurring in the channel cross, i.e. spherical micelles, cylindrical micelles and the evolved disk-like structures (intermediate). The black solid curves show the corresponding fit curves for each structure.

For further analysis, the scattering patterns were radially averaged to obtain the corresponding scattering curves. Figure 41 shows the sequence of scattering curves when scanning across the mixing cross in *y*-direction, i.e. perpendicular to the flow direction. The scattering curves in the front of the stack plot in Figure 41 (left), showing a pronounced and broad maximum, correspond to the LPFO-micellar stream.

In the subsequent narrow interfacial region scattering curves with a pronounced low-*q* scattering are observed, followed by the weakly scattering TDMAO-solution. Further backwards in the stack plot, again the interfacial region is crossed, with the developing scattering peak of the LPFO-solution.

In Figure 41(right) the scattering curves displayed in Figure 41(left) are plotted on top of each other, such that the structural development in the interfacial becomes more apparent. Starting from the LPFO-solution we observe the decrease of the peak intensity, where the peak position stays constant. Subsequently scattering curves with a high low-q intensity are observed, until the weakly scattering TDMAO-solution is reached.

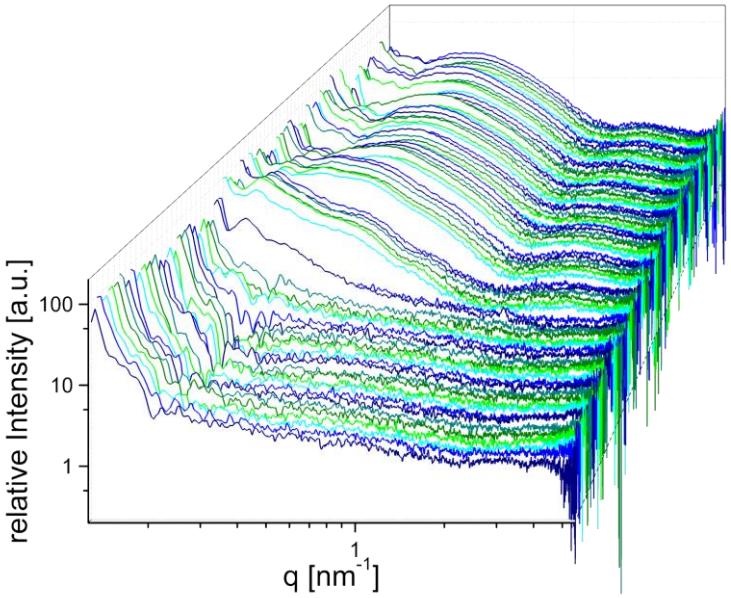

Figure 42. SAXS measurements of one line in x-direction for all 9 positions, starting in the middle of the channel cross (cylindrical micelles). A concentration of 100 mM and flow velocities of 100 µl/h each were used.

Figure 42 shows a stack plot of measured scattering curves in *x*-direction, downstream into the mixing channel. We observe the same evolution of the scattering curves when crossing the interface of the LPFO- and the TDMAO-stream, which is indicated in Figure 40 (a).

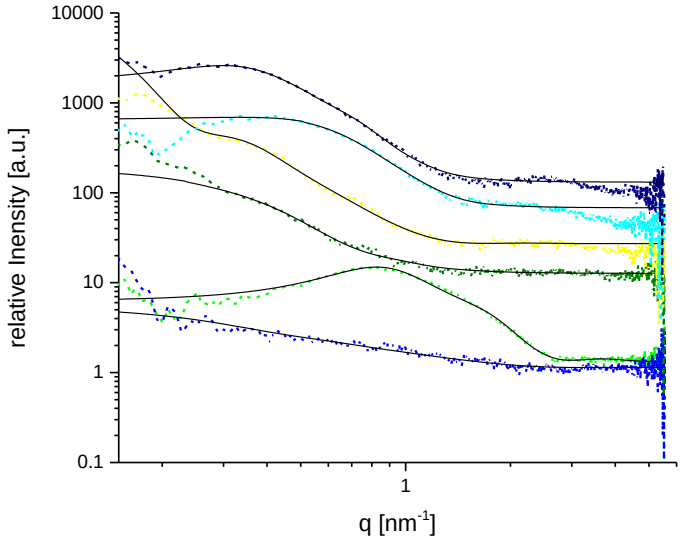

Figure 43. SAXS measurements downstream the NOA-microfluidic chip show the structural evolution of 100 mM TDMAO and 100 mM LPFO solutions with 100 µl/h flow each. The black solid lines show the corresponding fits to the original and intermediate downstream structures.

For further analysis, selected scattering patterns from the different scanning regions were radially averaged and plotted as shown in Figure 43. From the bottom upwards, the first three scattering curves correspond to the pure TDMAO-cylindrical micelles with a weak characteristic q^{-1}-scattering, the second corresponds to the pure LPFO-spherical micelles exhibiting the Debye-Scherrer ring, and third to the first transient structure with the strong low-q upturn. The scattering curve could not be described by particles with spherical, cylindrical or vesicular shape. It could be best fitted to a disk-like micellar structure.

For quantitative determination of the micellar structures, the scattering curves were fitted to analytical expressions for the form factor and structure factor. The first scattering curve from the TDMAO-micelles could be fitted to the form factor of polydisperse cylinders, yielding a cross-sectional radius of 1.49 nm and a length of 18.3 nm. The second scattering curve of the LPFO-micelles could be well fitted to the form factor of polydisperse spheres with a Percus-Yevick (PY) structure factor indicating liquid-like order. We determined a radius of 1.39 nm and an effective radius from the PY-structure factor of 3.0 nm, in agreement with the static measurements shown in Fig. 2. The third scattering curve could be best fitted to the form factor of a disk-like micelle, yielding a disk diameter of $d_D = 4.0$ nm with a lateral radius of 7.5 nm. These values are in good agreement with previous measurements of more dilute solutions. [94]

Further downstream, we observe the development of a shoulder at $q = 0.3$ nm^{-1}, developing into a weak maximum at $q = 0.4$ nm^{-1} which subsequently shifts to lower q. All subsequent scattering curves could best be described with the form factor of disk-like micelles, showing a weak maximum corresponding to the intermicellar distance. The fit parameters for the scattering curves are all summarized in Table 3.

Table 3. Fit parameters corresponding to the SAXS curves in Figure 43. The first line belongs to the first curve, the second line belongs to the second curve et cetera. The mesh numbers correspond to the mesh-scan numbers in Figure 40.

Mesh	c_{eff}	R_{eff} [nm]	R_c [nm]	d/2 [nm]	R [nm]	L [nm]	R_i	R_o
1	0.2	3.3	1.6					
1				2.0	5.6			
1			1.2			16.6		
2							12.1	15.9
5	0.1	4.7		2.0	2.6			
8	0.1	8.0		2.9	2.5			

Experimental and kinetic time scales

From the measured scattering curves, we observe that immediately after first contact of the LPFO- and TDMAO-streams, large micellar aggregates are formed – corresponding to a pronounced low-q scattering - concomitant with the formation of disk-like structures, as apparent from the intermediate and high q-scattering. In the following we will estimate the time resolution of the experiment and compare it to the time of the first appearance of the micellar aggregates and the disk-like micellar structures.

As the structural changes are very fast and already start upon first contact of the LPFO- and TDMAO-streams in the mixing cross, the simple relation between time, position and mean flow velocity, cannot be used to compute the time-position relation, since in the channel cross the velocity varies along the streamlines. Therefore, the time-position relation is calculated within the Lagrangian frame of reference, considering the time that a fluid element travels downstream on its streamline. For the specific case of mixing the LPFO- and TDMAO-streams, we are particularly interested in the streamline of first contact that starts at point “E”, indicated in Figure 44, which is located at the corner of the entrance channel and the upper focusing channel.

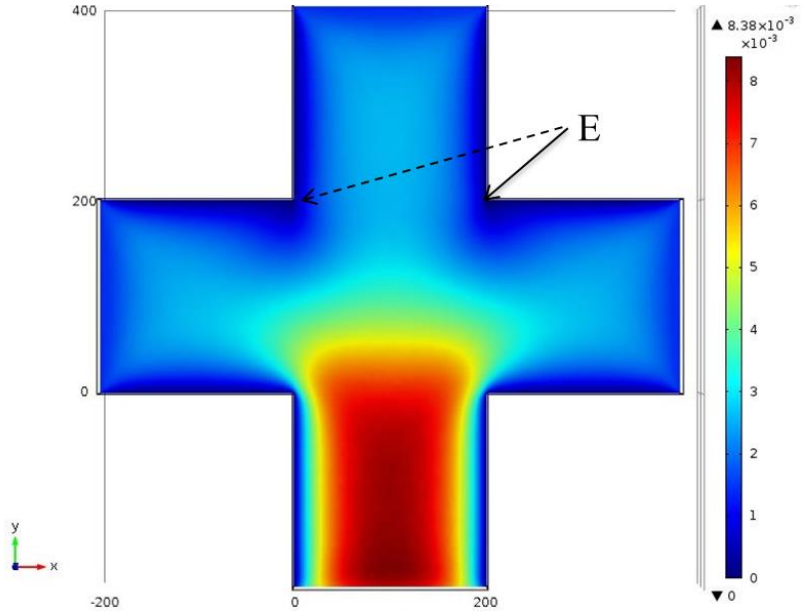

Figure 44. COMSOL velocity simulation of a microfluidic chip with 200 µm width, 100 µm height and a perpendicular channel cross. The starting flow rates are 100 µl/h for each inlet. The unit of the color scale bar is [m/s]. Point "E" indicates the first contact of TDMAO and LPFO. The Field was calculated for the mid-plane in vertical direction.

To obtain the time-position relation for this streamline, we computed the velocity field in the channel cross and the adjacent channels using 3D computational fluid dynamics (CFD) simulations (COMSOL) assuming Newtonian conditions and using the volumetric flow rates that were used in the experiment. The finite elements were set to a size of 10 µm, equal to the spot size of the scanning SAXS-experiment. The calculated velocity field is shown in Figure 44. We observe that the parabolic velocity profiles of the streams that merge into the channel cross, first develop into a more complex profile, which then again evolves into a parabolic velocity profile downstream in the mixing channel. The time-position relation of a fluid element starting from point "E" and moving along its streamline is calculated as

$$t(s) = \int_0^S \frac{1}{v(s')} ds' \approx \Delta x \sum_i \frac{1}{v(i)} \tag{164}$$

where the integral is taken over the path S of the streamline and is approximated by a sum over the finite volume elements V_i with dimension $\Delta x = 10\mu m$ along this path.

Figure 45 shows an overlay of the streamline onto the scanned positions as shown in Figure 40, where the pixels that were considered along the path in the integration are marked. We observe that the interface of the micellar streams exactly follows the streamline.

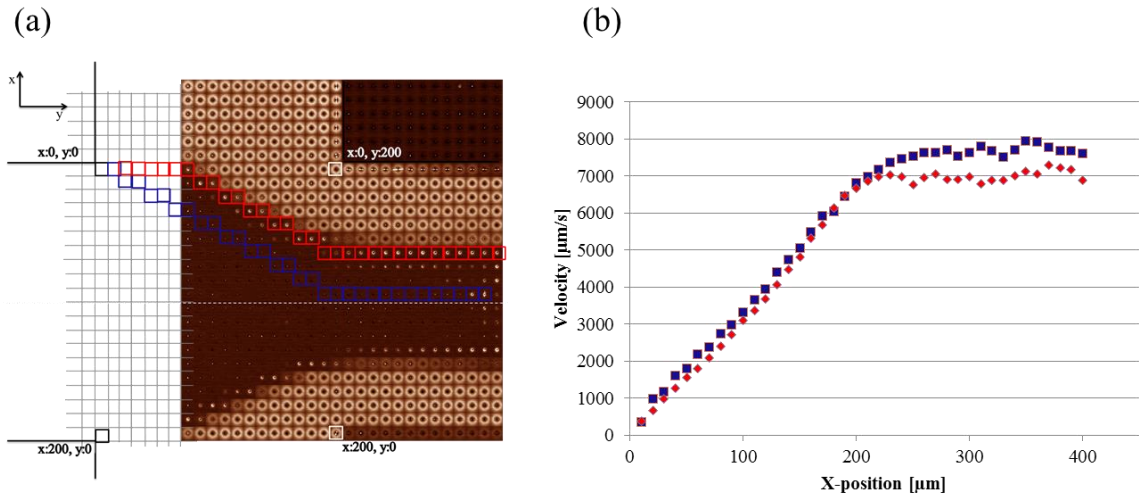

Figure 45. (a) Scanned lines (blue and red) in the calculation of mixing times, and (b) the corresponding calculated velocities as function of channel downstream position x.

When computing the $t(s)$-curve from Eq. (169), we found that its values critically depend on the velocity in the first finite volume element V_1 adjacent to the wall at point "E". Because stick boundary conditions were applied in the CFD simulation, the velocity of the fluid in the first volume element is very small, and thus the fluid residence time very large, approaching infinity in direct contact to the wall. To illustrate this for our 10 µm size volume elements shown in Figure 45 the mean velocity of the first volume element V_1 is $v_1 = 2$ µm/s, whereas the mean velocities of the next and its subsequent volume elements along the streamline are much larger, i.e. $v_2 = 345$ µm/s and $v_3 = 988$ µm/s, respectively. This indicates that convective mass transport in the first volume element is very small, and may be comparable or even smaller than diffusive mass transport.

A quantitative comparison can be made by considering the Péclet-number for each volume element, which is given by $Pe_1 = \frac{\Delta x v_i}{D}$. For $Pe \gg 1$, convective mass transport dominates over diffusive mass transport. For these calculations we need to specify the value of the diffusion coefficient D, for which we used the value corresponding to the spherical LPFO-micelles, as they are the micellar species with the highest diffusivity.

We used a value of $D = 10^{10}$ m²/s, as calculated from the Stokes-Einstein relation $D = \frac{k_B T}{6\pi\eta R_h}$ using the viscosity of water ($\eta = 0.001\,Pas$), a temperature of 25°C and a hydrodynamic radius of $R_h = 1.5$ nm, which is of the order of the micellar core radius $R_c = 1.4$ nm as determined in our experiments. Accordingly, the Péclet-numbers in the first volume elements have values of $Pe_1 = 0.2, Pe_2 = 34.6, Pe_3 = 98.8, \ldots$, showing that diffusive transport dominates in the first volume element, adjacent to the wall, whereas convective transport dominates in all successive volume elements along the streamline. Accordingly, micelles exit the first volume element by diffusion, which complicates the calculation of the time-position function.

We note that the complication of having two fast reacting streams in first contact at a channel wall is a particular disadvantage of simple 2D-flow focusing designs. This problem has been solved by recent 3D-flow focusing designs that include buffer streams which separate the two reacting streams until they reach the center of the downstream mixing channel, where a much more homogeneous velocity profile has developed, sufficiently separated from the microchannel walls. However, this channel design is more complicated to fabricate and we are currently in the progress to fabricate such mixing channels. As simple 2D-flow focusing designs are and will be further used due to their much simpler fabrication, we in the following provide further guidelines to construct the time-position function for their case.

To proceed with the analysis, we plotted the fluid velocities v_i in each volume element V_i along the streamline as shown in Figure 45 (b) as a function of the downstream x-position. We observe that the velocity increases nearly linearly until the reaches a plateau value at the beginning of the downstream mixing channel, i.e. at $x = w = 182$ µm, with a value of $\bar{v} = 7.8$ mm/s. Thus, in the mixing cross we can approximate the convective fluid velocity $v_{con}(x)$ with $v_{con} = \frac{\bar{v}x}{w}$, which is linearly increasing with increasing position x. The convective fluid velocity can be compared to the diffusive velocity given by $v_{diff} = \frac{2D}{x}$, which decreases with increasing distance x. Thus, there exists a distance x^*, beyond which convective motion becomes faster than diffusive motion, i.e. $v_{con} > v_{diff}$, which can be calculated as $x^* = \sqrt{\frac{2wD}{\bar{v}}} = 2$ µm, which corresponds to a diffusion time $t^* = \frac{(x^*)^2}{2D} \approx 20$ ms.

This is of the order of the first convective time scale, which is set by the experimental resolution $\Delta x = 10$ µm and the value v_2, and given by $\Delta t = \frac{\Delta x}{v_2} = 29$ ms. As $t^* \approx \Delta t$, we have derived a consistent description of the local fluid motion near the channel for our experiment. We thus approximate the first point of the time-position function as $t_1 = t^*$, and take the velocities v_i in all subsequent volume elements V_i to calculate the time-position function along the streamline starting from point "E" over the complete first scanning grid as shown in Figure 45 (a). The last point with a value $t_{400} = 120$ ms corresponds to the residence time of a fluid element in the first scanning grid. The longest time scale at the end of the last scanning grid is given by 2 seconds.

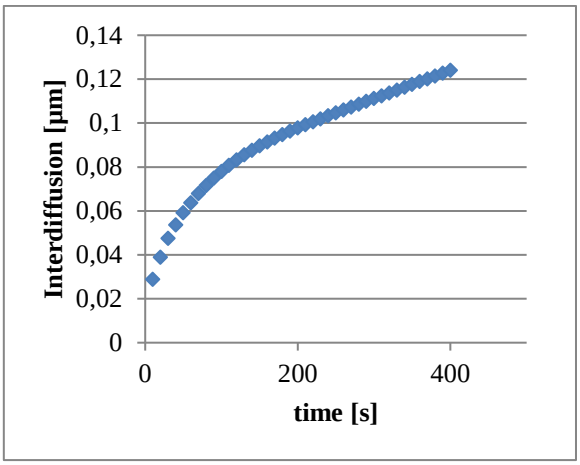

Figure 46. Elapsed time along the streamline, i.e. channel position (left) and interdiffusion across the interface at the corresponding time, assuming 10^{-9} m^2/s as the diffusion coefficient. It shows that interdiffusion across adjacent 10 x 10 micron pixels becomes significant already in the channel cross, but across two pixels only downstream the reaction channel.

We thus cover time scales of 30–120 ms along the streamline of first contact of the LPFO- and TDMAO micellar streams. During this time the spherical LPFO-micelles diffuse over a distance of $x = \sqrt{2Dt} \approx 5$ µm, which well corresponds to the abrupt change of the scattering patterns of adjacent scanning regions where the broad Debye-Scherrer ring observed for the LPFO-micellar solutions suddenly evolves into pronounced, featureless low-q scattering due to the formation of micellar aggregates. As the time scale of first changes of the micellar structure are the same as the experimental time resolution, we conclude that the corresponding structural change is diffusion-limited.

Even in a faster experiment with 5-fold stream velocity (see below) having a time resolution of $t^* \approx 5\,ms$ we observe the fast structural process occurring simultaneously to interdiffusion time scale. This is in agreement with the observations of Gradzielski. [96] We observed the formation of disk-like micelles with the deadtime of the stopped-flow experiment, which was ~5 ms.

Capillary counter diffusion

Capillary counter diffusion has become standard method in protein crystallization, where two solutions, one containing the protein, the other containing the crystallization agent, are brought into contact within a capillary. The slow and controlled interdiffusion of the two solutions results in a controlled nucleation and growth of protein crystals. [101] This technique can also be applied for kinetic studies, where e.g. interdiffusion of two liquids can be monitored, such as for molten metals. [102,103] To our knowledge, capillary interdiffusion has not yet been applied to study the interdiffusion of molecules in solution.

As capillary counter diffusion experiments do not involve convective motion, interdiffusion and related kinetic processes can be followed over time scales from minutes to days. Faster time scales are difficult to study, as the two interdiffusing liquids have to be carefully broad into contact without convection, which is difficult on a sub-100 μm scale.

Here we applied capillary interdiffusion to investigate structural changes that occur during interdiffusion of LPFO- and TDMAO-micellar solutions. This corresponds to the microfluidic mixing experiment, but allowing one to monitor much longer time scales. For this experiment we used long vertically positioned capillaries, where the upper and lower halves are filled with the two solutions, which are in contact in the middle of the capillary. This is known as the “long capillary technique” which has been used to study interdiffusion in liquid metals using capillaries that are 5–20 cm long. For liquid metal interdiffusion studies the method can be combined with X-ray imaging to obtain the interdiffusion coefficient from the measured concentration profiles along the capillary.

If diffusion occurs only along the vertical z-axis of the capillary across the interface between the two solutions, the development of the concentration profile of the components obeys Ficks's second law

$$\frac{\partial c(z,t)}{\partial t} = D\frac{\partial^2 c(z,t)}{\partial z^2} \tag{165}$$

where $c(z,t)$ is the concentration of solvents or surfactants along the capillary direction z after a time t, and D the diffusion coefficient of the components. For the initial condition of the two solutions brought in contact in the middle of the capillary at $z = 0$, this equation can be solved analytically to obtain

$$c(z,t) = \frac{c}{2}\left(1 - erf\left[\frac{z}{\sqrt{4Dt}}\right]\right) \tag{166}$$

with $erf(z)$ the error function, and z the position along the axis of the capillary. Assuming a micellar diffusion coefficient of the order of $D = 10^{-10}$ m²/s, we can use equation (166) to calculate the temporal evolution of the concentration gradient as shown in Figure 47.

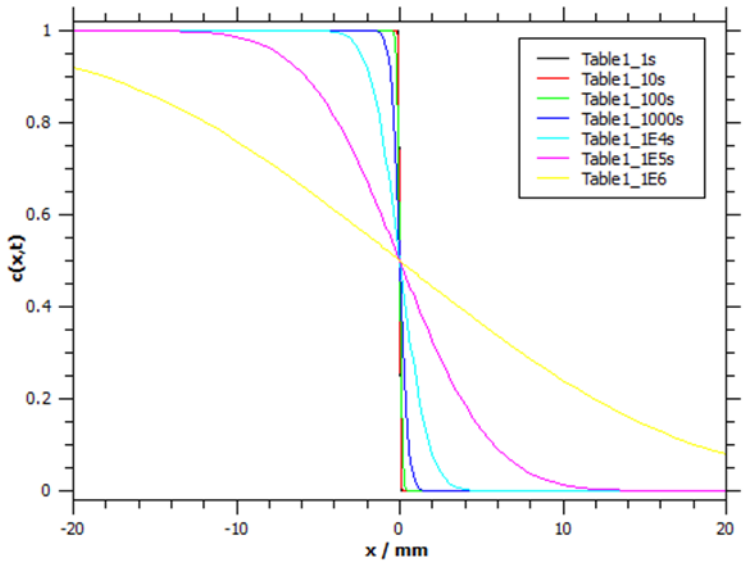

Figure 47. Concentration profile $c(z,t)$ calculated from Eq. (166) for times from 1 second up to 10^6 seconds corresponding to 12 days. Noticeable concentration changes at distances of ca. 0.5 mm from the interfaces are occurring between 100-1000 seconds, i.e. between ca. 1 minute and 10 minutes, which corresponds to the time scale of the SAXS capillary experiments.

For the experiment, a solution of 100 mM LPFO was carefully topped with a solution of 100 mM TDMAO in a 1 mm diameter capillary (length: 8 cm). The LPFO-solution was chosen as the bottom layer because LPFO has a higher density (1.922 g/ml) compared to TDMAO (0.897 g/ml), thus avoiding gravitation-induced convection. The vertically positioned capillary was then aligned in the X-ray beam such that the beam transects the capillary at ca. 0.5 mm below the interface ($z = -0.5\,mm$) of the two solutions. Thus, initially the pure LPFO solution with spherical micelles is observed, which upon contact and interdiffusion with the TDMAO cylindrical micelles structurally changes. The X-ray beam was focused to a spot size of 100 µm to illuminate an as small as possible scattering volume in the concentration gradient. SAXS-measurements were performed on time scales from 1 min to 10 days to follow the structural evolution upon interdiffusion.

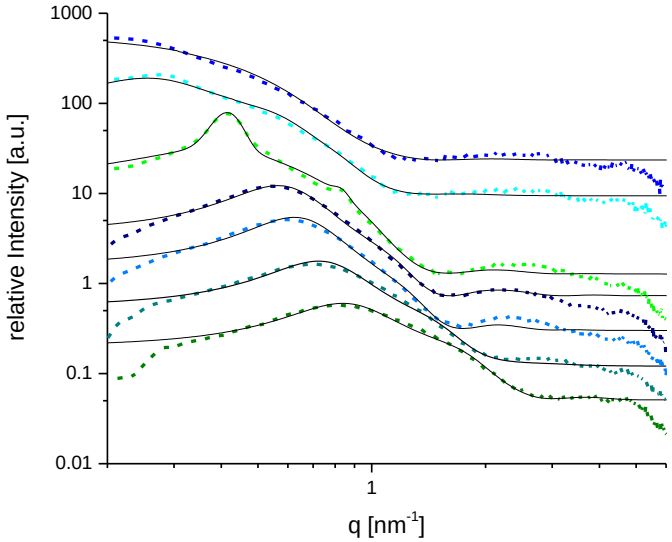

Figure 48. SAXS-curves measured at z = -0.5 mm for different times upon interdiffusion. We observe a structural evolution from spherical micelles to disk-like micelles.

Figure 48 shows the measured SAXS-curves during the capillary interdiffusion experiment. The first measured scattering curve corresponds to the pure LPFO-micellar solution directly adjacent to the interface. It shows a broad maximum at $q^* = 0.85$ nm^{-1}, which with time shifts to smaller q, developing a sharp peak at $q^* = 0.45$ nm^{-1} with a second order reflection ($q_2^* = 0.90$ nm^{-1}) which subsequently broadens, shifts to lower q and develops into a shoulder at $q^* = 0.20$ nm^{-1}.

The initial set of scattering curves could be well fitted to growing spherical micelles showing a Percus-Yevick structure factor which indicates liquid-like order. The subsequent set of scattering curves can be fitted to disk-like and lamellar structures, which are further diluted.

Structural evolution

To provide a simple model and to rationalize the structural evolution during mixing spherical LPFO-micelles with cylindrical TDMAO-micelles, we first consider the geometrical constraints set by the surfactant molecules in terms of their molecular weight M, their density ρ and their molecular volume $v = \frac{M}{\rho N_L}$. The alkyl chain length L_c (in nm) is calculated from the number of carbon atoms N_c of the surfactant alkyl chain as $L_c = 0.125\ N_c$. The relation between aggregation number Z and the size of spherical, cylindrical and disk-like micelles is given by

$$Z = \begin{cases} \dfrac{4\pi R^3}{3v} & \text{for spheres} \\ \dfrac{\pi R^2 L}{v} & \text{for cylinders} \\ \dfrac{\pi R_D^2 d_D}{v} & \text{for disks} \end{cases} \tag{167}$$

where R is the radius of the spherical micelle or the cross-sectional radius of the cylindrical micelle, L the length of the cylindrical micelle, R_D the lateral radius of a disk-like micelle, and d_D the thickness of a disk-like micelle. The values of M, v, L_c and Z are summarized in Table 4.

For a given aggregation number, the intermicellar distance can then be calculated as

$$d^* = \left(\frac{Z}{cN_L}\right)^{1/3} \tag{168}$$

This assumes an isotropic three-dimensional micellar distribution, which for anisotropic cylindrical and disk-like micelle implies that their concentration is smaller or at most is around the overlap concentration c^*, which for the present investigations is well fulfilled except for a narrow time-range of the structural evolution, where dilute lamellar phases are observed. For concentrations around c^*, a peak in the scattering intensity is expected, whose position can be related to the intermicellar distance via $q^* = \frac{2\pi}{d^*}$. In Table 4, the values d^* and q^* are also calculated for a 1:1 mixture of LPFO and TDMAO. For the calculations we assumed a radius of the spherical LPFO-micelles of $R = 1.4$ nm, a cross-sectional radius $R = 1.5$ nm for the cylindrical TDMAO-micelles having a length of $L = 18$ nm as determined from the scattering curves in Figure 48. We observe that the radius of the spherical LPFO-micelles is smaller than the contour length of the C8-alkyl chains, which indicates a quite dense, compacted structure. The larger cross-sectional diameter observed for the cylindrical TDMAO-micelles indicates, that part of the zwitterionic head group has a similar electron density as the alkyl chains, and is therefore observed as a part of the micellar core in the SAXS-experiment. All values of d^* and q^* are also summarized in Table 4.

Table 4. Structural parameters of the LPFO-, TDMAO and mixed micelles

	LPFO (C8)	**TDMAO (C14)**	**1:1 Mix**	**1TDMAO +*n*=1,2,3,8.5 LPFO**	**Disk fusion *N*=2,4**
shape	Sphere	Cylinder	Disk		
M [g/mol]	420.0	257.5			
ρ [g/ml]	1.922	0.897			
v [nm^3]	0.36	0.48	0.42		
L_c [nm]	1.75	1.00			
R, d_D [nm]	1.39	1.49	4.0	4.0	4.0
L, R_D [nm]		18	8	3.1, 3.3, 3.5, 4.2	5.9, 8.4
Z	31	263	1920		
d* [nm]	8.0	16.3		17, 17.5, 18, 20.6	26, 33
q* [nm^{-1}]	0.78	0.38		0.37, 0.36, 0.35, 0.31	0.24, 0.19
Q_{exp}	0.85			MF: ~0.3 (late, weak) Cp: 0.85 – 0.45 – 0.20	

From these basic structural considerations, we would expect the spherical LPFO-micelles to show a peak at $q^* = 0.78$ nm^{-1} (Table 4), which is in good agreement with the observed value of $q^* = 0.85$ nm^{-1}. The calculated aggregation number of $Z = 31$ is also in good agreement with values published in literature [96]. For the cylindrical TDMAO-micelles somewhat larger values for the cross-sectional radius (1.5-1.8 nm) with similar lengths ((15 nm) have been reported in literature. For further calculations we will keep the value of 1.49 nm, as it could be determined with good precision from the position of the first form factor minimum (Figure 48).

According to Table 4, for the TDMAO-cylindrical micelles we could expect a peak in the corresponding scattering curve at $q^* = 0.38$ nm^{-1}. In the experiment, however, a maximum in the scattered intensity is not observed.

This is likely due to the negative scattering contrast of core with respect to the shell, which effectively suppresses the scattering intensity at low q, where the peak is expected. We further observe that the intermicellar distance $d^* = 16$ nm is of the order of the cylinder length ($L = 18$ nm), such that the concentration of cylindrical micelles is around the overlap concentration c^*.

For the very first aggregation steps it could be conceived that subsequently $n = 1, 2, \ldots$ spherical LPFO-micelles fuse with a cylindrical TDMAO-micelle in discrete steps to form a disk-like micelle. From the known aggregation numbers of the micelles, we could then calculate for the subsequent fusion steps the corresponding disk radii R_D, the distances d^*, and the peak positions q^* using Eq. ((167)(168)). These values are given in Table 4, calculated for a disk thickness of $d_D = 4.0$ nm, which was determined experimentally. The case $n = 8.5$ would correspond to an exact 1:1 stochiometry of LPFO- and TDMAO-surfactants. Disks could subsequently fuse via attach at their periphery to grow further. The calculated values for $N = 2$ and $N = 4$ fused disks are also given in Table 4.

We observe that for the beginning $n = 1 \ldots 8.5$ sphere-cylinder fusion values for the disk radii would be in a range of $R_D = 3.1 \ldots 4.2$ nm, with subsequent disk fusion for $N = 2 \ldots 4$ further increasing to $R_D = 5.9 \ldots 8.4$ nm. The smallest disk observed in the fast microfluidic experiment, detected immediately after mixing, has a disk radius of $R_D = 7.5$ nm, which is already in the regime of the first disk-fusion events.

With increasing disk aggregation number in the dilute concentration regime, where $c < c^*$, the lateral disk radius increases faster than the distance between adjacent disks, i.e. $d^* \sim Z^{1/3}$ and $R_D \sim Z^{1/2}$, such that the growth reduces c^* leading to the onset of disk-disk correlations leading to a peak in the scattering curve. These peaks would be in range of $q^* = 0.37 \ldots 0.31$ nm^{-1} for the first fusion events, and for the subsequent disk fusion regime in a range of $q^* = 0.24 \ldots 0.19$ nm^{-1}. Indeed, in the fast microfluidic experiment we observe a weak shoulder at $q^* \sim 0.3\ nm^{-1}$(see Figure 43) which would correspond to the first fused disk states. In the slow capillary interdiffusion experiment we observe a clear first order peak at $q^* \sim 0.4$ nm^{-1} with a second-order reflection, which would correspond to very small disk-like structures.

Comparison of fast and slow structural evolution

When comparing the structural evolution in the fast microfluidic to the slow capillary counter diffusion experiment, we observe a pronounced difference. As shown in Figure 48 we observe in the capillary experiment that the peak, which at first corresponds to the pure spherical LPFO-micelles with a value of $q^* \sim 0.85$ nm^{-1} continuously shifts to lower q, and then develops into a quite narrow peak at $q \sim 0.4$ nm^{-1} with a second order reflection. It subsequently shifts to lower q-values and broadens. In the fast microfluidic mixing experiment the position of the peak, corresponding to the LPFO spherical micelles $q^* \sim 0.85$ nm^{-1}, remains constant while its intensity decreases until the peak disappears. At later times a shoulder in the scattering curve at around $q^* \sim 0.3$ nm^{-1} appears. This shoulder then evolves into a quite featureless scattering curve.

This indicates different structural pathways for the formation of disk-like micelles in both experiments. In the microfluidic channel within the narrow interfacial region of ca. 50 µm all spherical LPFO- and cylindrical TDMAO-micelles instantaneously fuse to form disk-like micelles with a 1:1 stoichiometric composition. As the TDMAO micelles are integrated into the spherical LPFO-micelles, the scattering contrast rapidly decreases and a pronounced low-q scattering develops due to extended micellar interconnections resulting from the cylindrical TDMAO-micelles. Subsequently, the disk-like micelles grow by fusion and develop larger lateral dimensions, such that lamellar correlations develop, with a new peak developing at $q^* \sim 0.3$ nm^{-1}.

In the capillary interdiffusion experiment, at the $z = -0.5$ mm position, non-stoichiometric, LPFO-rich compact micelles are formed by the fusion of TDMAO cylindrical strands with pure LPFO-micelles. As the micellar aggregation number gradually increases, the intermicellar distances increases causing the gradual shift of the scattering peak. Eventually, also disk-like micelles with 1:1 stoichiometry and large lateral dimensions develop, indicated by the development of equidistant lamellar peaks at $q \sim 0.4$ nm^{-1}. The structural pathway observed in the capillary interdiffusion experiment may also occur on the microfluidic flow-focusing experiment, but at much later time-scales and much further away from the interface of the LPFO- and TDMAO-streams.

Cryo-Transmission electron microscopy

To capture the final state of the structural evolution we performed cryo-transmission electron microscopy (cryo-TEM). The solution collected at the exit of the microfluidic chip was vitrified at the following day by fast immersion in liquid ethane at its melting point. Vitrified specimens were then imaged at 200 kV under cryo-conditions. The recorded images of the solution structures are shown in Figure 49. We observe unilamellar and occasionally multi-lamellar vesicles with diameters between 50 and 200 nm, in some cases even up to 500 nm. The vesicle bilayer thickness is 1.9 nm. The interlamellar distance of the multi-lamellar vesicles of 20.3 nm, is in good agreement with the observed shoulder at $q \sim 0.3$ nm^{-1} in the fast microfluidic experiment.

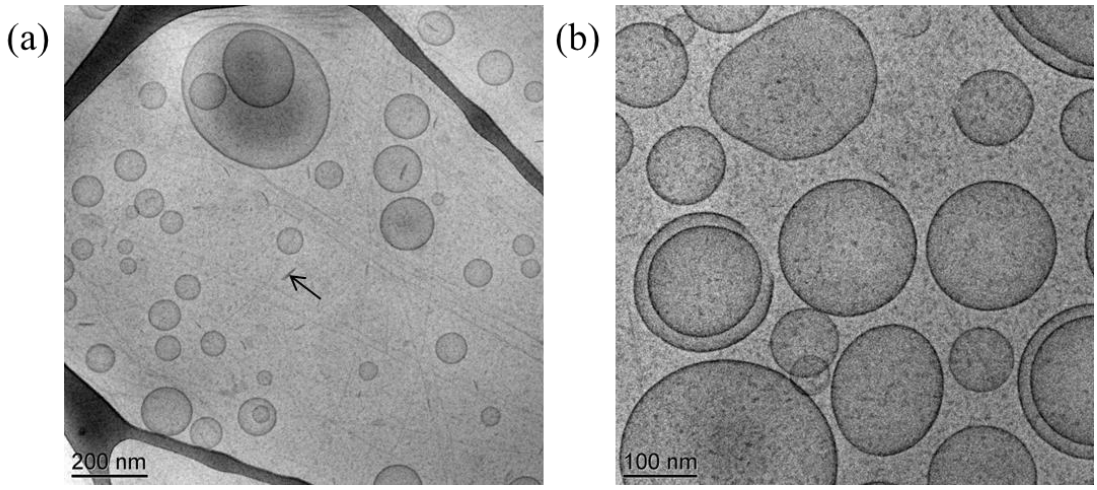

Figure 49. Cryo-TEM images of a 100 mM TDMAO/LPFO mixture prepared in microfluidic chip and measured 1d after preparation. Cryo-TEM shows single- and multi-wall vesicles with bilayer thickness (thick dark) of 1.9 nm and an interlamellar distance of 20.3 nm.

As indicated by the arrow in Figure 49 (a), we also observe disk-like micelles. They have lateral dimensions of 12.5 nm and a thickness of 3.9 nm, which is in good agreement with experiments. This indicates that the vesicle bilayers have intercalated structures, whereas the disks have extended chain bilayer structures.

Conclusions

The temporal evolution of vesicles from micellar structures is followed on time scales from milliseconds to hours using microfluidic flow focusing and capillary interdiffusion experiments coupled with small angle X-ray scattering (SAXS). The particular case of vesicle formation from mixtures of anionic spherical lithium perfluorooctanoate (LPFO) micelles and zwitterionic cylindrical tetradecyldimethylamine oxide (TDMAO) micelles was investigated as a reference system with fast kinetics to investigate the versatility of both interdiffusion experiments. We observe the very fast formation of large-scale structures evolving into disk-like micelles on millisecond time scales, which eventually form vesicular structures on much longer time scales. We found the pathway of vesicle formation to be different for the fast microfluidic flow focusing and the slow capillary interdiffusion experiment.

4.3 Solvent Resistant Microfluidic-Hybrid-Chip for Three-Dimensional Hydrodynamic Flow Focusing

Introduction

The investigation of kinetics for chemical, physical or biochemical reactions is essential to understand and control reactions like protein folding or self-assembly of amphiphilic block copolymers. [99,104,105] Microfluidics offers many advantages for the investigation of reaction kinetics. Besides the little demand of sample volume and the diffusion controlled mixing, due to low Reynolds number, the conversion of the reaction time scale to the length scale along the microfluidic channel, is one of the most significant benefits. [2,40,52] It enables to adjust the temporal resolution as well as the residence time of the particles in the microfluidic chip by changing the flow rate, which is especially advantageous for fast kinetic processes. [99,106] However, it is commonly known that due to the no-slip boundary condition with the parabolic flow profile of pressure driven flow, the flow velocity is close to zero at the channel walls. [32] This distorts the kinetics of reactions. Thus, it is fundamental to achieve a flow where the reactants or particles are away from the microfluidic channel walls, which can be achieved by three-dimensional hydrodynamic flow focusing.

Two-dimensional hydrodynamic focusing is widely used in microfluidics. Austin et al. introduced hydrodynamic focusing to obtain a very thin stream focused by two sheathing streams. Hereby, a reagent or particles flowing in the main channel are focused from two side channels to obtain a stream of adjustable thickness. The thickness of the reagent stream influences the mixing time, since due to laminar flow in microfluidics, only diffusive mixing occurs.[107] This simple channel design, mainly consisting of one channel cross and a single layer device, has the drawback of lacking vertical focusing.

Furthermore, the most commonly used microfluidic device material is PDMS, which swells in contact with most organic solvents.[90,92,108] Since many synthesis or reactions are performed with organic solvents, this is a real drawback. There have been several attempts to use different solvent resistant materials or to coat the PDMS microfluidic channels with solvent stable coatings. Glass coating is a fast and easy method to cover the channel walls, but the rigid thin glass film often has cracks or breaks.

Fluorinated polymers, like THV (3M, Dyneon) or Teflon-, and polyimide based devices are fabricated via hot embossing or lamination techniques.[92,109–111] Hot embossing has a good accuracy performance but this method hinders a three dimensional design with two structured chip halves, because the two chip halves have to be aligned for bonding.

We developed a new chip design where all reacting streams are separated from the channel walls to avoid premixing. With an additional layer separating the reagent streams from each other we are able to adjust the mixing point. Furthermore, we used perfluoropolyether to fabricate solvent resistant microfluidic devices. The fabrication steps are similar to the standard PDMS micromolding process and therefore, easy and fast. In addition, we inserted a glass capillary to the leaving channel to achieve low background scattering for diffraction methods like e.g. small angle X-ray scattering. This chip design leads to parallel flowing reagent streams, which has the advantage of better spatial resolution than conventional concentric flow.

Results and Discussion

4.3.1.1 Flow and Device Design

In microfluidics the no-slip boundary conditions leads to a velocity close to zero at the channel walls. Reactions with reagents or products which stick to the channel wall change the reaction conditions and destroy the steady state flow in microfluidic devices. Hence, by introducing protective layers in the microfluidic chip design, wall contact of the reagents could be avoided. Protective layers were already mentioned by Pollack et al (2006) to avoid premixing.[106] In contrast to the sheathing side channels, additional sheathing streams on top and bottom of reagents were introduced, which allows not only horizontal but also vertical focusing. Besides the mentioned layers to avoid wall contact, a buffer layer between the two reagents streams to control the mixing point of the solutions was induced. Figure 50 shows a section of the mixing element of the device design with the two channel crosses. The two reagent streams A and B are distanced from the top and bottom wall, resulting in a stacking of protective layer- reagent stream -protective layer. At the first channel cross the A and B stacked streams are separated with a buffer stream flowing centrically between them.

At the second channel cross the incoming streams are additionally distanced from the right and left channel walls. This results in two completely separated streams, where the reagents have no wall contact and the mixing point of stream A and B is dependent on the ratio of the flow velocity between them and the middle buffer stream.

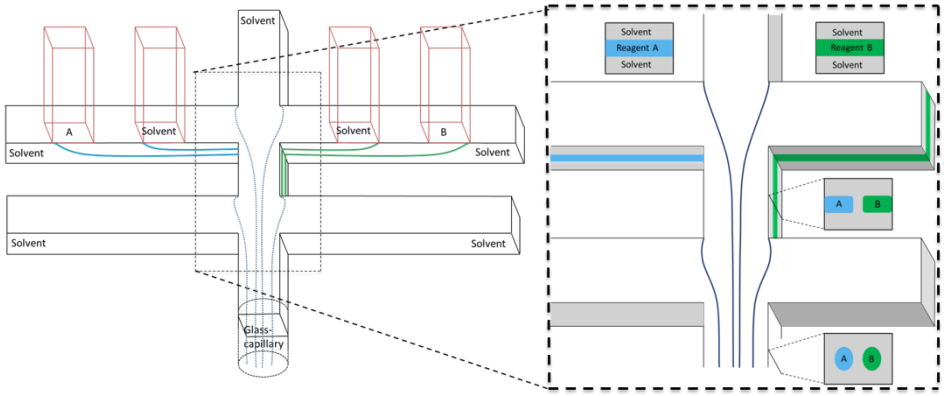

Figure 50. Left: Section of the device design. The red colored channels are from the upper structured chip half and the black lined channels are on the lower chip half. Right: Magnification of the two channel crosses with the different protective and buffer layers, resulting in two separated streams.

To the best of our knowledge two parallel flowing streams containing reagents have not been reported so far. Three dimensional flow focusing results mostly in concentric flow.[105,112–115] This means a reactant A is surrounded by B, whereas B can be a reactant or sheathing streams. Hence, for concentric flow, the diffusive layer during mixing broadens in the direction of the beam. Thus, the investigation of a system e.g. in terms of the structure evolution in self-assembly processes shows an average of all different evolved structures at one measured position depending on the scattered volume. With our new device design, it is possible to follow the different structures separately since reactant A and B are flowing separated by a buffer stream and the structure evolution can be followed spatially resolved (Figure 51). Therefore, with a small enough X-ray beam, as provided at synchrotron facilities, a scan in y-direction of the microfluidic device shows the different structure stages of e.g. a self-assembly process.

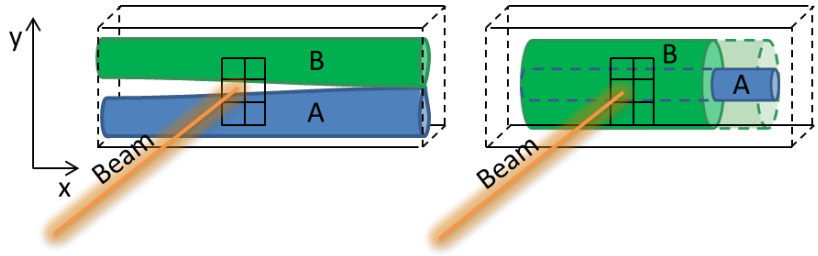

(169)

Figure 51. The left image shows the two separated streams of our chip design. Here the different structure stages can be followed due to the spatial separation. The right image shows the concentric sheath flow, where the different structures are not separately detectable due to the sheathing reagents.

4.3.1.2 Device Fabrication

Our new hybrid microfluidic device comprises several advantages. First, the device fabrication is simple and similar to the standard PDMS micromolding. Furthermore, rapid prototyping is also possible for the SIFEL-Hybrid Chip since the master fabrication is identical to the photolithographic process of the PDMS master production. The fabrication steps are similar to the procedure described by Kreutzer et al (2011) but with slight changes depicted later.[116] The used chip material, SIFEL2610 (Shin-Etsu), a perfluoropolyether with silicone crosslinking groups, is resistant to most organic solvents.[117] To minimize costs, only thin layers of SIFEL were used to cover the device structure. For stabilization of the microfluidic device, PDMS was added on top of the with SIFEL covered masters. In Figure 52 the left image shows a SEM measurement of a cut SIFEL-PDMS chip. The blue line separates the two individual chip halves and shows one channel in the upper and one in the lower half. The PDMS and the SIFEL part can be clearly distinguished, showing that the channels are completely build-up of perfluoropolyether. Additionally, the chip material is reusable because the channels can be cleaned with appropriate solvents.

To achieve a three-dimensional chip design, we used two structured chip halves and aligned them face to face. Mostly, this alignment step is tedious since the alignment has to be very accurate. With our new chip design, the alignment is quick and easy as the overlapping parts are small and can withstand a certain error.

For low background scattering of the microfluidic chip, we added a glass capillary to the outlet of the chip (Figure 52, right). Reactions in the microfluidic channel are translated from time to space, which means the reaction evolution proceeds along the channel.

Since we are able to adjust the mixing point of the two reagents with the middle buffer layer, we can delay this mixing point to a position in the glass capillary where background scattering is much lower than in the SIFEL-PDMS part of the microfluidic device.

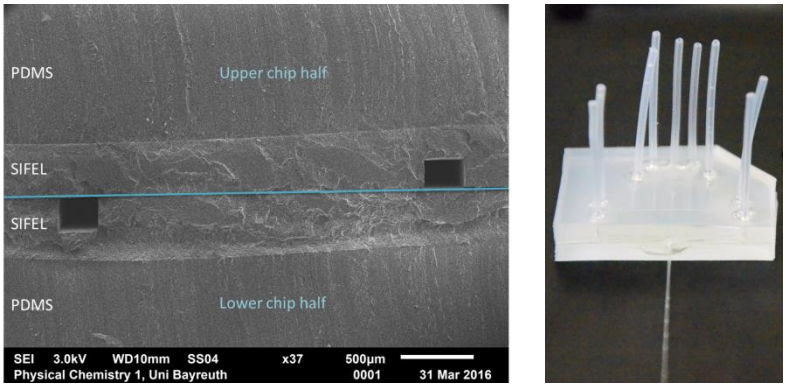

Figure 52. Left: SEM image shows the two structured chip halves with the SIFEL layer containing the channel design and the stabilizing PDMS on top. Right: SIFEL-PDMS device with inserted glass capillary.

4.3.1.3 Flow Control

We performed several confocal laser scanning microscopy (CLSM) measurements to investigate the flow in our new microfluidic device. Therefore, we used Fluorescein and Rhodamine B to dye the different streams.

Figure 53 shows the CLSM images of the SIFEL-hybrid device. The left picture shows the lateral hydrodynamic focusing of the solvent-reagent-solvent stacked streams at the second channel cross. It shows that both stacked streams are separated in the middle by the buffer stream. The right CLSM image in Figure 53 shows the flow in the glass capillary. The two reagent streams (green) are flowing separately in the middle of the glass capillary with no contact to the glass walls (blue).

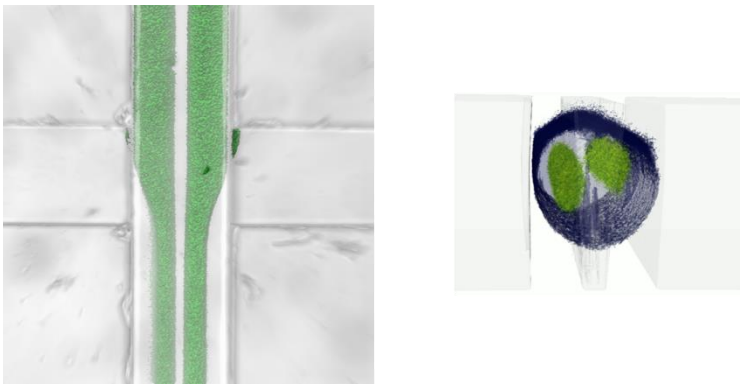

Figure 53. CLSM of the flow of fluorescein and rhodamine b in the SIFEL-hybrid chip. The left image shows the hydrodynamic focusing at the second channel cross. The right picture shows the two separated streams flowing in the glass capillary.

In a further experiment we used Ca-Green, a Ca^{2+} sensitive dye, to determine the contact point of reagent A (here Ca-Green) and B (Ca^{2+}) at different flow rates. We used the in Pollack et al (2006) described procedure with higher concentration of the stock solutions, as due to the sheathing streams the reagents are diluted in the microfluidic channel lately. Therefore, we prepared a buffer solution of 25 mM MOPS, 0.1 mM EGTA and 150 mM KCl. For better results we added 5 µM Cascade blue. Then, Ca-Green (CG5N) with a concentration of 20 µM and 10 mM $CaCl_2$ were individually dissolved in the puffer solution. The Ca-Green and the $CaCl_2$ solution are reagent streams A and B (Figure 50) and for the remaining sheathing and buffer streams the buffer solution without Cascade blue was used. Figure 54 shows a CLSM image of this system with flow rates of 500 µl/h for the reagent streams A and B. The middle buffer stream has a velocity of 100 µl/h and the remaining sheathing streams have a flow rate of 63 µl/h. The increase of fluorescence intensity marked with the green arrow in Figure 54 shows clearly the reaction of Ca-Green and Ca^{2+}.

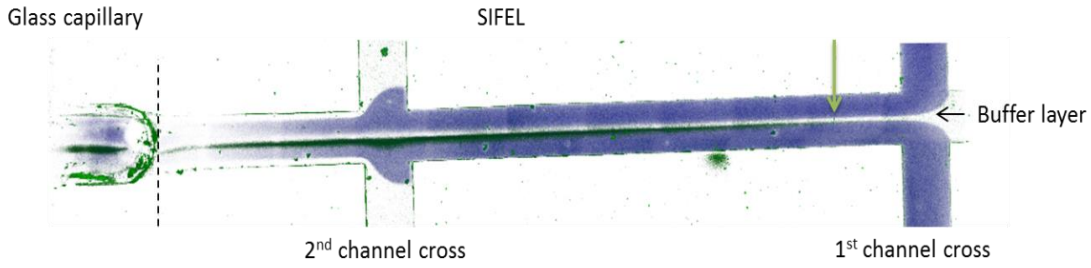

Figure 54. CLSM image of the SIFEL hybrid chip with Ca-green, $CaCl_2$ and Cascade blue in buffer solution with flow rates AB 500 µl/h, middle buffer stream 100 µl/h, remaining streams 63 µl/h.

4.3.1.4 Application

This new SIFEL-hybrid chip was used to analyze the self-assembly process of poly(isoprene)-*(b)*-poly(ethylene glycol) block copolymer (PI_{70}-(*b*)-PEG_{60}). Therefore, 20 wt% of the block copolymer was dissolved in 1,4-dioxane and was pumped into the microfluidic device (reagent stream A). Dioxane serves as sheathing and buffer streams, whereas water as reagent is stream B. The structure evolution was followed by small angle X-ray scattering. As mentioned above with our flow of two separated streams, which mix only by diffusion, the structure evolution can be followed in x-direction, which means along the channel, and in y-direction. In Figure 55 two series of measurements in y-direction are shown at two different x-positions in the microfluidic device. The first image (a) in Figure 55 shows the measurements at an earlier stage of the self-assembly process. The distance between adjacent measurements were 15 µm and were limited by the x-ray beam size of x = 15 µm and y = 20 µm. Six measurements are depicted to demonstrate the structure progress in y-direction. The scan starts at a position of the dioxane sheathing stream showing no form or structure peaks. At the next displayed curve the dissolved block-copolymer in dioxane shows a broad peak, which can be fitted with a structure factor given by Leibler.[118] The y-scan proceeds towards the water stream showing the evolving FCC structure factor.

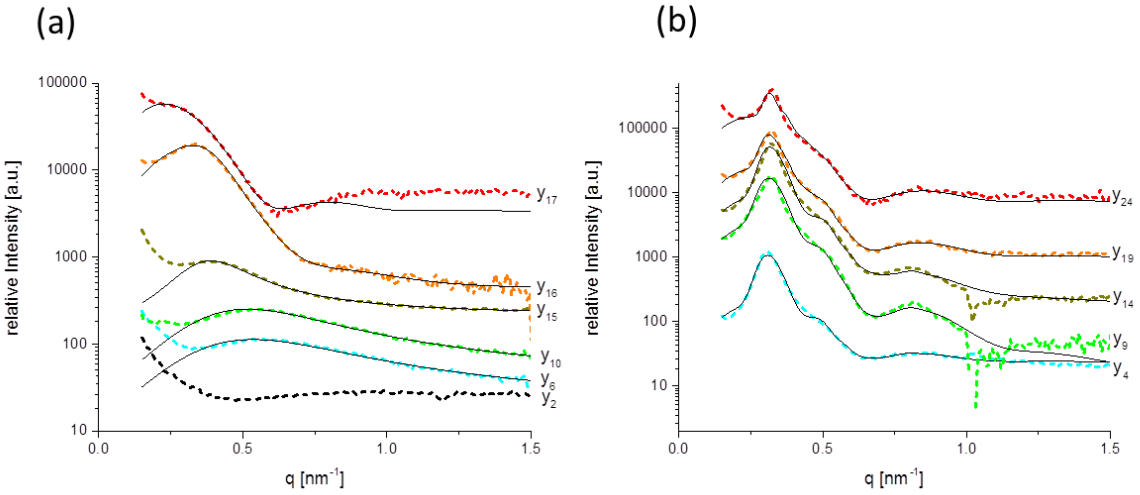

Figure 55. (a) Y-scan at position 1 of SIFEL-cap-chip measurements at flow rates A, B 1500 µl/h, middle buffer stream 500 µl/h and remaining streams 6*100 µl/h. The step width for each measured point was 15 µm. (b) y-scan at position 8 at flow rates A, B 1500 µl/h, middle buffer stream 500 µl/h and remaining streams 6*100 µl/h.

The later point in the microfluidic channel is shown in Figure 55 (b). All curves show the now more pronounced FCC structure factor for all measured positions. Five of the measured points at this x-position are depicted here. This points out, there is homogeneous mixing over the whole channel width. We also measured the same poly(isoprene)-(*b*)-poly(ethylene glycol) block copolymer in solvent resistant microfluidic devices based on THV or polyimide. Besides the elaborate fabrication and the difficulties to fabricate three-dimensional designs, the background scattering of these microfluidic devices is still higher even with very thin chips. In Figure 56 we compare a small angle X-ray scattering measurement at the DESY synchrotron beamline P03 of 20 wt% PI-(*b*)-PEG in polyimide based microfluidic device (blue curve) to 20 wt% PI-(*b*)-PEG in SIFEL-hybrid chip (red curve).

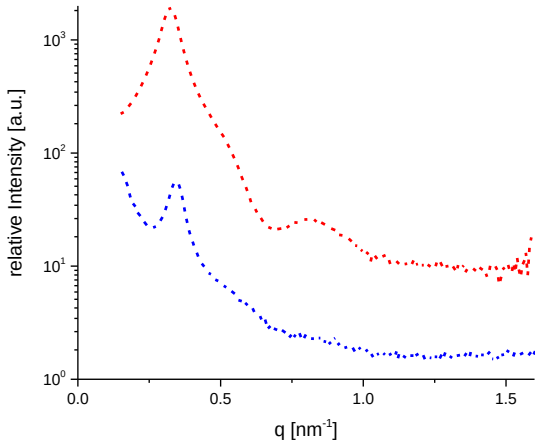

Figure 56. Comparison of two measurements analyzing the self-assembly process of 20 wt% PI-(*b*)-PEO in polyimide chip device (blue curve) and SIFEL-hybrid chip (red curve).

Both measurement show the final FCC structure but the measurement of the SIFEL-hybrid chip shows more intense peaks of the structure factor and a more pronounced form factor oscillation.

Experimental

Materials and Methods

Device fabrication procedure. For the SIFEL-hybrid-chip production a master with the negative structure was fabricated initially. Therefore, photolithography was used, which is a well-established procedure for PDMS masters. In the second step the silicon-wafer, yielding the structure, was coated with trichloroperfluorooctylacid (Sigma Aldrich) for easy removal of SIFEL from the silicon-master afterwards. To achieve this coating, the structured silicon-wafers and an open vial with few milliliters of trichloroperfluorooctylacid was placed in a desiccator for one hour. Under vacuum the trifluoroperfluorooctylacid cover the silicon-wafer, which was subsequently heated in the oven at 120 °C for 2 hours. In the next step SIFEL was brought on top of the structured and coated wafer (~ 4.5 g per wafer). Then, the first layer of SIFEL was spin-coated on the silicon-wafer. It is important to make a layer by layer procedure of a thin SIFEL layer to avoid wrinkling during the drying process. The first layer is then baked in the oven at 72 °C for several hours. The right moment to spin-coat the next layer is when the earlier layer is solid but still sticky. This guarantees, that the first layer is not flowing off the wafer at the next spin-coating step, but is still merging with the next SIFEL layer. The baking time depends on the SIFEL layer thickness. These steps have to be repeated until the desired thickness is achieved, which is usually when the whole structure is covered with SIFEL. In the next step PDMS is poured over the with SIFEL covered Si-wafer, degassed and then bake in the oven at 75 °C for at least one hour. This realizes a stable microfluidic chip without wasting to much expensive SIFEL. The SIFEL-PDMS chip halves are removed from the silicon-wafer and cut to the right size. Wholes for the tubings are punched in at desired positions for the in- and outlets. Then, to bond the two halves together, one half is coated with liquid SIFEL. Therefore, 20 wt% SIFEL is mixed with 1,3-bis(trifluoromethyl)benzene and spin-coated onto a clean silicon-wafer. One of the cleaned chip halves is then pressed on the coated wafer. For the bonding of the 3D-chip design, the two halves have to be aligned under the microscope to achieve the right orientation. The two halves are then clamped together between two glass slides and baked in the oven for one day at 75 °C.

Finally, the tubings and the glass capillary are connected to the SIFEL-chip. The chip is cut in such a way that the main channel is open at the end. Here the glass capillary with an outer diameter of 0.3 mm and wall thickness of 0.01 mm is adjusted to the channel with a channel width of ~ 0.29 mm.

Eventually, the glass capillary is inserted into the device main channel for 1-2 millimeter and if necessary clued with a two-component epoxy-clue. The glass-capillary was previously laser cut at both sides to get a straight glass-tube with two openings.

Small angle X-ray scattering. The illustrated measurements were performed at the P03 MiNaXs beamline, PETRA III at DESY/HASYLAB, Hamburg. The SIFEL-chip measurements were all performed in one session with a beamsize of 15 µm in x-direction and 20 µm in y-direction and a wavelength of $\lambda = 0.0957$ nm. The measurement in the polyimide device was performed with a beamsize of 31 µm in x-direction and 22 µm in y-direction and a wavelength of $\lambda = 0.1088$ nm.

Conclusion

We revealed a new microfluidic device design for three-dimensional flow focusing. Besides the usage of sheathing streams to avoid wall contact of the reagents, an additional buffer layer between the two reagent streams allowed us to adjust the temporal resolution of our measurements, as well as the retention time of the sample in the microfluidic device. The used perfluoropolyether, SIFEL 2610, is resistant to organic solvents and is easily fabricated due to the similar PDMS micromolding procedure. Furthermore, the new chip design led to a parallel flow of the reagents, which allowed an excellent spatial resolution in matters of analyzing methods like small angle X-ray scattering (SAXS). We proved the parallel flow by confocal laser scanning microscopy (CLSM) measurements, where two completely separated streams can be observed in the capillary. Furthermore, the streams are in no contact with the channel or capillary walls. Additionally, we followed the reaction of Ca^{2+} with Ca-green in the microfluidic channel with CLSM. It shows the laminar flow and the diffusion limited mixing, since the fluorescence arises in the middle of the channel between the two reagent streams.

Thus, this chip design is suitable for kinetic studies because the reaction is not disturbed by the stay of particles at the channel walls. Especially the inserted glass capillary enables low background scattering of the microfluidic device.

The improvement was pointed out by the comparison of SAXS measurements in a thin polyimide microfluidic chip with the new SIFEL-hybrid chip. Furthermore, we investigated the fast self-assembly process of Poly(isoprene)-(*b*)-poly(ethylene glycol) block copolymer. We showed that with the parallel reagent stream not only the structural evolution along the main channel can be followed but also the evolution perpendicular to this.

4.4 Self-assembly of Block Copolymers via Micellar Intermediate States into Vesicles on Time Scales from Milliseconds to Days

Introduction

Amphiphilic block copolymers in solution can self-assemble into a variety of micellar and vesicular structures, depending on their relative block lengths and block chemistries. [119] This allows one to tune self-assembly to prepare well-defined structures with good control of size and topology for a variety of different applications in materials [120] and life science. [17]

The methods that are used to prepare block copolymer assemblies often differ and have to be adapted to the specific block copolymer/solvent system. In the simplest case the block copolymers can be directly dissolved in the solvent to form the desired structure. However, in most cases this method fails, because the block copolymer forms undesired partially solvated, ill-defined structures or does not dissolve at all. This problem is avoided by dissolving the block copolymer in a good solvent for both polymer blocks. This solution is subsequently mixed with or dialyzed into a selective solvent, mostly water, which induces self-assembly to obtain the targeted structure. The obtained structure may indeed be the expected equilibrium structure, but could also represent a morphology which was trapped during the preparation process, and represents a metastable non-equilibrium state.

It is thus important to monitor the actual structural evolution during solvent mixing. Here it becomes essential to consider the time scales of mixing and self-assembly. The mixing time depends on the mixing procedure. Generally, mixing of two liquids firstly involves convection, e.g. by stirring, to intersperse and break down the fluid volumes of each liquid to micrometer dimensions, on which length scale interdiffusion becomes effective to eventually homogenize the solution on a molecular scale. The time scales of convection and interdiffusion must then be compared and adjusted to the time scales of self-assembly.

The mixing process can be simplified and made more efficient if liquid streams of micrometer dimensions are mixed. Then convection is not needed, and interdiffusion is the only relevant mixing process. With the advent of microfluidic technology, micrometer scale mixing is possible with a choice of many different channel designs. [48]

In microchannels flow is characterized by low Reynolds numbers and is laminar such that very well-defined mixing conditions can be realized. A simple and versatile continuous mixing design is based on flow-focusing, [107] where a central stream (e.g. the block copolymer solution) is focused with two side streams (e.g. the selective solvent) to micrometer width in a downstream mixing channel. The time a solvent molecule needs to diffuse across the width w of the focused central stream is the mixing time, which e.g. for a focused stream width of $w = 10$ µm is ca. 50 milliseconds, becoming much smaller for smaller stream widths.

With respect to block copolymer solution mixing, flow-focusing establishes a well-defined stationary concentration gradient across the two solvents streams. Within this concentration gradient the block copolymer self-assembles. Each position x downstream the microfluidic mixing channel is then related to a certain polymer/solvent composition and a certain time t after first contact of the two liquids. Thus, the time-evolution of the self-assembly process is mapped onto different positions along the mixing channel. The structural evolution at each position can then be monitored by scattering, spectroscopy or microscopy techniques. The achievable time resolution depends only on the spatial resolution Δx of the technique and the flow velocity v as $\Delta t = \frac{\Delta x}{v}$. With typical flow velocities of the order of $v = 10$ mm/s and spot sizes of $\Delta x = 10$ µm this then results in a time resolution of ~1 millisecond. The maximum detectable time t_{max} is given by the residence time of the fluids in the mixing channel as $t_{max} = \frac{L}{v}$, such that for typical lengths of L~5 cm maximum time scales of t_{max}~5 seconds can be assessed.

Flow-focusing mixing experiments combined with synchrotron SAXS have first been developed to study fast protein folding with down to microsecond resolution. [121,122] It has only recently been applied to study the structural evolution of other molecular structures. We demonstrated that this method can be used successfully to investigate the kinetics of amphiphile self-assembly, where we studied the formation of micellar lyotropic phases using polyimide based flow focusing devices.[99] Polyimide is highly transparent to X-rays, but allows one to realize only simple channel designs like two-dimensional (2D) flow-focusing where the central channel is focused with two side streams. To avoid wall-contact of the mixing streams, which for 2D-focusing occurs on the bottom and ceiling of the mixing channel, and to avoid premixing in the channel junction, three-dimensional (3D) focusing devices employing a buffer layer have been realized. [106,123]

For the present study we developed a new three-dimensional hybrid focusing device. It 3D-focuses and locates the polymer and the water stream adjacent to each other, separated by a buffer stream. The streams are additionally separated from the channel walls by sheath streams and focused into an X-ray transparent thin glass capillary as the mixing channel, where high-quality SAXS-data can be recorded.

Using classical 2D-polyimide flow-focusing, the newly developed 3D-hybrid device and a capillary interdiffusion experiment, we investigated the self-assembly pathway of an amphiphilic block copolymer during solvent mixing on time scales from milliseconds to days. We show that the block copolymer, which forms vesicles in water as its equilibrium structure, upon solvent mixing into water structurally evolves via spherical and cylindrical micellar transient structures into, eventually, vesicles.

Materials and Methods

Microfluidic chip preparation.

For the *in-situ* mixing SAXS experiments we used two different microfluidic devices, a polyimide chip with a simple 2D channel design which has been used previously, [99] and a newly developed SIFEL-capillary hybrid chip with a 3D-focusing/buffer layout.

Polyimide device: The polyimide device is made of three different types of commercial available polyimide films. The channels are cut into the films with laser cutting. The explicit preparation of these microfluidic devices is described elsewhere. [99] These microfluidic chips have a low background scattering in SAXS experiments and are resistant to most organic solvents. Figure 57 shows the simple polyimide chip design with three inlets and one outlet and a perpendicular channel cross. The dimension of the channels is 110 µm in width, 115 µm in height and 31 mm length from the channel cross to the channel outlet.

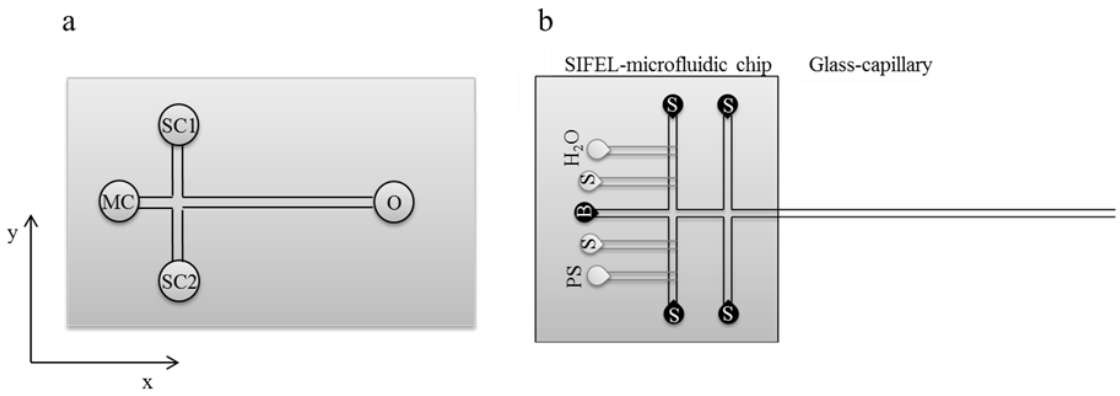

Figure 57. Scheme of (a) the polyimide microfluidic chip with the three inlets (MC, SC1, SC2), the perpendicular channel cross and the outlet (O), and (b) the SIFEL-capillary hybrid chip with the 3-dimensional design. The four bright gray colored inlets are imprinted into the bottom chip side and the five black inlets into the upper chip side.

SIFEL-device: SIFEL is a solvent-resistant perfluoropolymer material (Shin-Etsu SIFEL2610), which consists of a perfluoropolyether backbone with reactive silicone end-groups which can be cured under similar conditions as PDMS (Sylgard). [116,124,125] For this chip both chip sides are structured and are bonded together to achieve a 3D-focusing design. The design is schematically shown in Figure 57 (b), where grey channels belong to the bottom chip side and the black channels are molded into the upper chip side.

The device has nine inlets and one outlet. Seven inlets are used as buffers (B, dioxane), to separate the reactants from the channel walls and to modify the starting point of the reaction with a buffer stream in the middle between the polymer solution (PS) and water stream (H_2O). The outlet is connected to a glass capillary where the reaction can be followed via SAXS. Figure 58 shows the different streams in the channel flow, where fluorescein and rhodamine B are used to show the two still separated focused streams in the glass capillary to prove the 3D-focusing/buffer stream design.

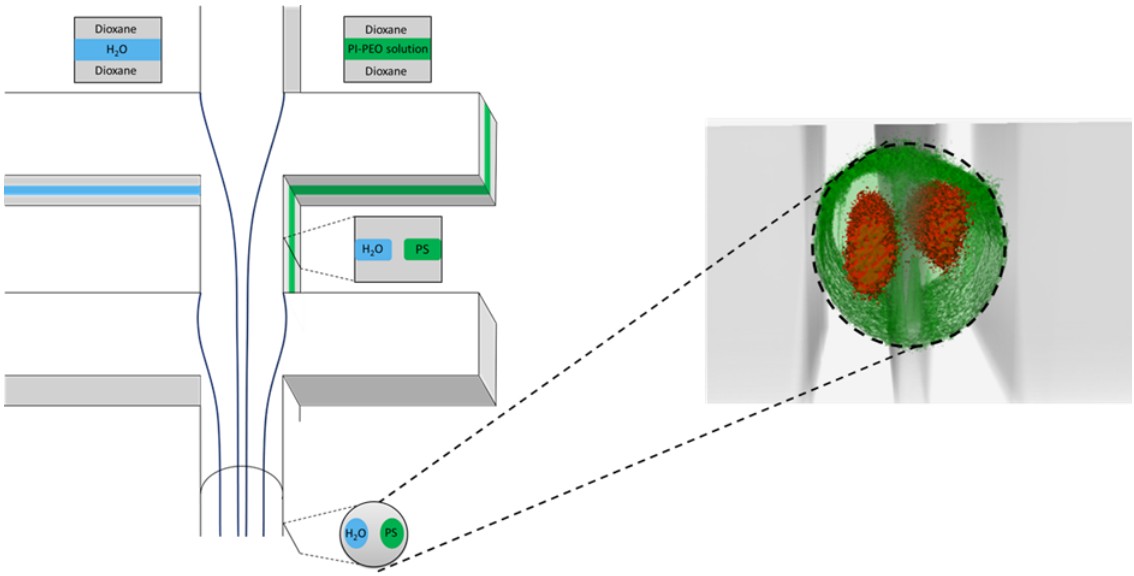

Figure 58. Scheme of the SIFEL 3D-channel design (left) and confocal laser scanning microscopy image (right) of a cross-section of the glass capillary, showing two rhodamine B streams in the capillary of a SIFEL-capillary chip, still separated by the buffer layer.

Sample Preparation. For the SAXS measurements a poly(isoprene)-(*b*)-poly(ethylene glycol) block copolymer was used with a molecular weight of $M_w = 7411$ g/mol and block lengths of 70 and 60 monomer units respectively. The polydispersity of PI_{70}-(*b*)-PEG_{60} is M_w/M_n = 1.08. The polymer was synthesized via sequential living anionic polymerization in THF. First the poly(isoprene) block was synthesized. Therefore, the polymerization of the purified isoprene was initiated with *s*-BuLi. The reaction was terminated with dried ethylene oxide (EO). The PI-OH homopolymer was then activated with DPMK, and then ethylene oxide was condensed into the PI/THF solution. After polymerization the living polymer anions were reacted with acetic acid, and the polymer subsequently precipitated in cold acetone and dried to constant weight. For the experiments, the block copolymer was dissolved in 1,4-dioxane.

Small angle X-ray scattering. All experiments were performed at the PETRA III MiNaXs Beamline P03 at DESY/HASYLAB or at the in-house rotating anode setup, GANESHA (SAXSLAB). For the measurements in the polyimide device at PETRA III, the beam size was 31 µm in *x*-direction and 22 µm in *y*-direction and had a wavelength of λ = 0.1088 nm.

For the SAXS measurements with the SIFEL-glass-capillary microfluidic chip at PETRA III the wavelength was λ= 0.957 nm and the beam size was 25 µm in *x*-direction and 15 µm in *y*-direction. For detection a Pilatus 1M or 300K (DECTRIS) was used with a pixel size of 172 µm x 172 µm. The sample was placed at a distance of 3.53 m - 4 m to the detector between which an evacuated tube was positioned. The microfluidic chip or the glass capillary was positioned with precision motors in x-, y-, z-direction.

The in-house measurements were performed at GANESHA (SAXSLAB), a small angle X-ray scattering setup equipped with a microfocus rotating anode (Rigaku Micromax 007 HF) and a Pilatus 300K detector (DECTRIS). The X-ray beam (λ = 0.154 nm) was focused to 100 µm for the scanning experiments.

Microfluidic/SAXS experiment. The inlets and outlets of the microfluidic chip were connected *via* PE-tubings (Scientific Commodities Inc.) to gas-tight syringes (Hamilton). The syringes were driven by high-precision syringe pumps (NEMESYS, Cetoni GmbH) to provide a constant flow of the solution in the microfluidic device.

Results and Discussion

4.4.1.1 Experiments in a 2D-Polyimide Microfluidic Device

The first set of experiments on PI_{70}-(*b*)-PEG_{60} block copolymer assembly was made in a conventional 2D-focusing polyimide microfluidic device. A 20 wt% PI_{70}-(*b*)-PEG_{60}/dioxane solution was pumped into the main channel (MC) and dynamically focused with water from both side channels (SC). The used flow rates were 100 µl/h in the main channel and 400 µl/h for each side channel. SAXS measurements were performed in *x*-direction downstream along the microfluidic channel and in *y*-direction across the channel. The presented SAXS curves in Figure 59 show the structural evolution in *x*-direction in the center of the channel. Positions x_1 and x_2 are located before the mixing cross, where only polymer/dioxane solution is present. All other curves show with increasing position number an increasing distance from the channel cross after mixing.

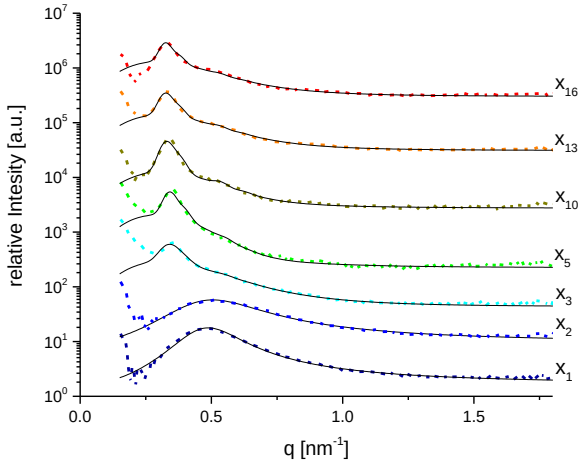

Figure 59. SAXS measurements of 20 wt% PI_{70}-(*b*)-PEG_{60}/dioxane in a polyimide microfluidic device along the downstream direction, after mixing with water. The evolution from a broad peak indicating weak segregation into a well-defined Bragg peak at lower *q*, indicating the formation of an ordered lyotropic micellar phase, is clearly visible.

The scattering curves measured at the first two positions x_1 and x_2 in the main channel show a broad peak at $q = 0.5$ nm^{-1} ($d = 2\pi/q = 13$ nm). This indicates that already in pure dioxane there is a weak microphase separation. The scattering curves can be fitted to a structure factor given by Leibler [118] for the case of weak segregation, with

$$S(q) = \frac{N}{F(x) - 2\chi N} \tag{170}$$

where χ is the Flory-Huggins interaction parameter, characterizing the effective interaction between both monomer groups, N the degree of polymerization, and the function

$$F(x) = \frac{g\,(1,x)}{g(f,x)g(1-f,x) - \frac{1}{4}[g(1,x) - g(f,x) - g(1-f,x)]^2} \tag{171}$$

with $x = qR_g$, $R_g$being the radius of gyration, f the fraction of monomer A in the AB-block copolymer, and $g(f,x)$ being the Debye function given by

$$g(f,x) = \frac{2(fx + e^{-fk} - 1)}{x^2} \tag{172}$$

When fitting Eq. (170) to the experimental data, the degree of polymerization N and the volume fraction f where set to fixed values of $N = 130$ and $f = 0.5$ to reduce the number of adjustable parameters. The values of the chi-parameter, χ, and the radius of gyration, R_g, where then adjusted to obtain the best fit to the measured scattering curves. The main feature of the Leibler structure factor is a maximum at a q-value, which is directly related to the value of R_g. The determined values of the chi-parameter are in a range of $0.04 \leq \chi \leq 0.07$. The corresponding segregation parameter χN thus has values in a range of $5.2 \leq \chi \leq 9.1$, which is characteristic for the weak segregation regime ($\chi < 10$). In the following we only consider the radius of gyration obtained from the fits to Eq. (170), as it is of relevance for the structural evolution of the polymer chains during self-assembly. A complete Table of fit parameters is provided in the Supporting Information (Table S1).

Already at position x_3, which is the first position after the mixing cross, we observe a pronounced shift of the peak to lower $q = 0.3$ nm^{-1} ($d = 21$ nm) with a smaller peak width and a weak shoulder. This indicates an increasing segregation with the formation of micelles, which develop an ordered structure. Further downstream, at positions x_5, x_{10}, x_{13}, and x_{16}, the measured peaks further gain in intensity, but do not shift further to lower q.

For a quantitative analysis, the scattering curves were fitted to an analytical expression describing the scattered intensity of ordered structure. [70,71]

$$I(q) = (b_1 - b_2)^2 \rho_N \langle P(q) \rangle S(q) \tag{173}$$

where the b_J are the contrast factors of micelles and solvent, ρ_N is the number density of the micelles, and $P(q)$ is the form factor of the micellar core, assumed to have a spherical shape. $\langle \dots \rangle$ denotes the average over the particle size distribution, for which a Schulz-Zimm distribution is used. The sphere form factor is given by

$$P(q) = \frac{9}{(qR)^6} [\sin(qR) - qR\cos(qR)]^2 \tag{174}$$

The structure factor $S(q)$, which describes the spatial arrangement of the micelles, is given by

$$S(q) = \frac{(2\pi)^3}{n_n v} \sum_{h,k,l} f_{hkl}^2 L_{hkl}(q, g_{hkl}) \tag{175}$$

where n_n is the number of micelles per unit cell ($n_n = 4$ for FCC), v the unit cell volume, *hkl* the Miller indices, L_{hkl} the peak shape function, and g_{hkl} the reciprocal lattice vector.

Fits to Eq. (173) yield the space group (in our case: Fm3m), the unit cell dimension a, the mean crystalline domain size Δ, the mean displacement δ of the micelles from the ideal lattice points (Debye-Waller factor), the mean micellar core radius R_c, and the polydispersity of the micelles.

All scattering curves measured at positions x_5, x_{10}, x_{13}, and x_{16} could be fitted to Eq. (173) assuming an FCC-lattice with a lattice constant in the range of $a \sim 31 - 33$ nm and a micellar core radius of $R_c = 6.7$ nm. The mean displacement of the micelles from the ideal lattice point is on average ca. $\delta = 4 - 5$ nm, a typical range for lyotropic liquid crystals. The fits to the Leibler structure factor (Eq. (170) and the FCC-lattice (Eq. (173)) describe the scattering curves very well in the relevant *q*-range for $q > 0.2$ nm^{-1} and are shown by the straight lines in Figure 59.

To relate the channel position to a time after mixing, we take the *x*-position at the beginning of the channel cross as the starting point of the mixing between polymer/dioxane solution and water. Then the time after mixing t can be calculated from the channel positions as

$$t = \frac{\mathrm{w} \cdot \mathrm{h} \cdot \mathrm{x}}{\mathrm{Q}} \tag{176}$$

where w is the channel width, h is the channel height, and Q the volumetric flow rate. Since the distances in x are larger than the channel dimensions (w, h), we assume that a well-defined parabolic flow profile has developed already at position x_3, and that we can take the mean velocity to calculate the time after mixing. The positions and calculated times after mixing, together with the measured values of R_g, R_c, a, and Δ are summarized in Table 5.

Table 5. Fit parameters for SAXS measurements of 20 wt% PI_{70}-(*b*)-PEG_{60}/dioxane in polyimide microfluidic device. Δx is the channel position with respect to the beginning of the channel cross, Δt the corresponding time after mixing, R_g the radius of gyration, a the unit cell size, Δ the domain size, and $R_c$the micellar core radius.

Position	Δx [mm]	Δt [s]	R_g [nm]	a [nm]	Δ [nm]	R_c [nm]
1	-0.87	-0.246	4.0			
2	-0.27	-0.119	3.9			
3	0.33	0.017		31.1	77	6.7
5	1.53	0.078		31.3	105	6.7
10	4.53	0.229		32.6	100	6.7
13	6.33	0.320		32.9	104	6.7
16	8.13	0.411		32.9	115	6.7

We observe that already after 17 milliseconds (see Table 5) micelles have formed that are assembling on an FCC-lattice. Further downstream, the lattice becomes more and more ordered until after 320 ms no more structural changes are observed. The time of 17 ms is of the order of the interdiffusion time across the central stream. The interdiffusion time can be estimated from the width of the focused central stream w_f, which can be calculated from the flow rate ratios as

$$w_f = \frac{Q_{PD}}{Q_{S1} + Q_{PD} + Q_{S2}} w_c \tag{177}$$

With the volumetric flow rates $Q_{PD} = 100$ µl/h, $Q_{S1} = Q_{S2} = 400$ µl/h and $w_c = 110$ µm, we calculate $w_f = 12$ µm. The time of a solvent to diffuse from both sides of the central stream to its center, i.e. over a distance $\frac{w_f}{2}$, is given by

$$t_D = \frac{w_f^2}{8D} = 18\, ms \tag{178}$$

which is in good agreement with the estimated value of 17 ms, using for the solvent diffusion coefficient a typical value of $D = 10^{-9}$ m²/s. This clearly shows that the formation of the micelles is diffusion controlled.

4.4.1.2 Experiments in SIFEL Microfluidic Device

Polyimide microfluidic chips have been established as solvent-resistant and X-ray transparent microfluidic chips [126] capable to host 2D-flow focusing channel designs. The disadvantage of a 2D-design, where the focused stream is still in contact with the ceiling and the floor of the microchannel, can be overcome with a 3D-focusing design, which is, however, difficult to realize in polyimide chip materials. In order to realize 3D-focusing designs with buffer layers to additionally have a well-defined onset of mixing we used SIFEL as a chip material. SIFEL is optically and X-ray transparent, but has the disadvantage of having a higher X-ray scattering background. Therefore, we constructed a hybrid chip consisting of a SIFEL chip with 3D-focusing and implemented buffer layer, where the mixing channel immediately enters into a thin-walled glass capillary used for X-ray experiments. The hybrid chip thus combines state-of-the-art 3D-mixing/buffer design in SIFEL with X-ray capability. To capture the earliest mixing events, the onset of mixing is located downstream at the beginning of the X-ray capillary *via* adjustment of the buffer stream flow velocity.

With the SIFEL-capillary-chip the downstream structural evolution of 20 wt% PI_{70}-(*b*)-PEG_{60}/dioxane solutions after mixing with water was followed at different channel flow rates in the glass capillary. Compared to the polyimide chip with *x*-positions up to 8 mm, limited by the length of the microfluidic chip, the SIFEL hybrid chips allow to measure positions up to x= 43 mm, limited only by the length of the capillary.

For our first study we used flow rates of $Q_w = 1500$ µl/h for the water stream, $Q_{PD} = 1500$ µl/h for central the polymer/dioxan stream, $Q_B = 750$ µl/h for the dioxane buffer stream, and $Q_S = 100$ µl/h for the outer sheath streams. We first measured the scattering curves after the mixing point perpendicular to the flow direction (*y*-scan) to verify that the polymer/dioxane and water streams are focused into the center of the capillary, separated from the wall by sheath streams.

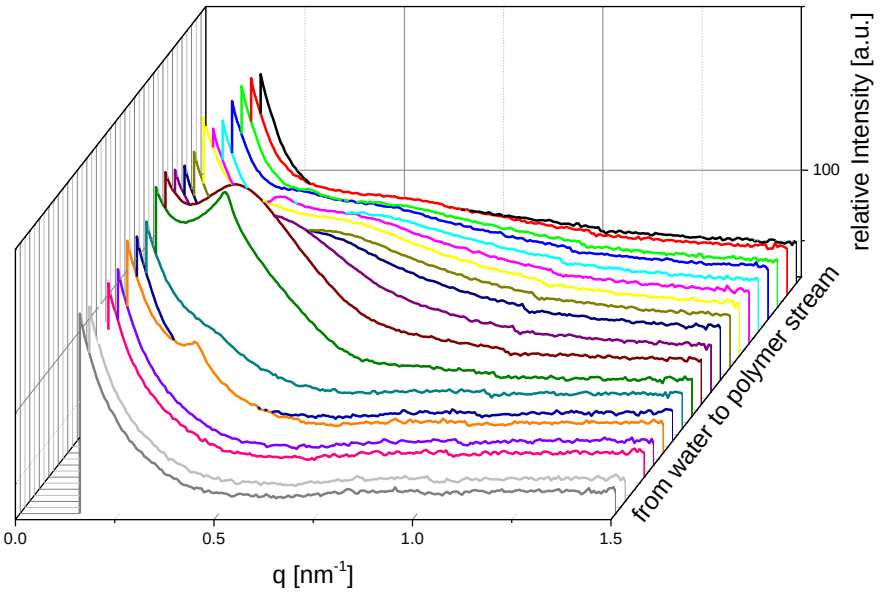

Figure 60. *Y*-scan through the glass capillary with a step width of 15 µm, with SAXS-curves measured at the corresponding positions. In the experiment a 20 wt% PI_{70}-(*b*)-PEG_{60}/dioxane solution was investigated at flow rates of 1500 µl/h for water and the polymer solution, 750 µl/h for the middle dioxane buffer stream and 100 µl/h for the sheath streams. The evolution of ordered micellar structures in the center of the capillary can be well observed.

Figure 60 shows the measured scattering curves across the glass capillary in *y*-direction with a scanning step width of $\Delta y = 15$ µm. Beginning from the front, we first observe featureless scattering curves characteristic for the pure solvent sheath flows. Further towards the center we observe the development of Bragg-peaks, characteristic for the formation of the ordered lyotropic micellar phase by interdiffusion with water. Towards the back we observe the broad peak at lower *q*-values corresponding to the pure, weakly segregated polymer/dioxane solution. At the back of the capillary we again observe featureless scattering curves, as expected from the pure solvent sheath streams. For the following experiments we used the central *y*-position to scan along the *x*-direction downstream the capillary.

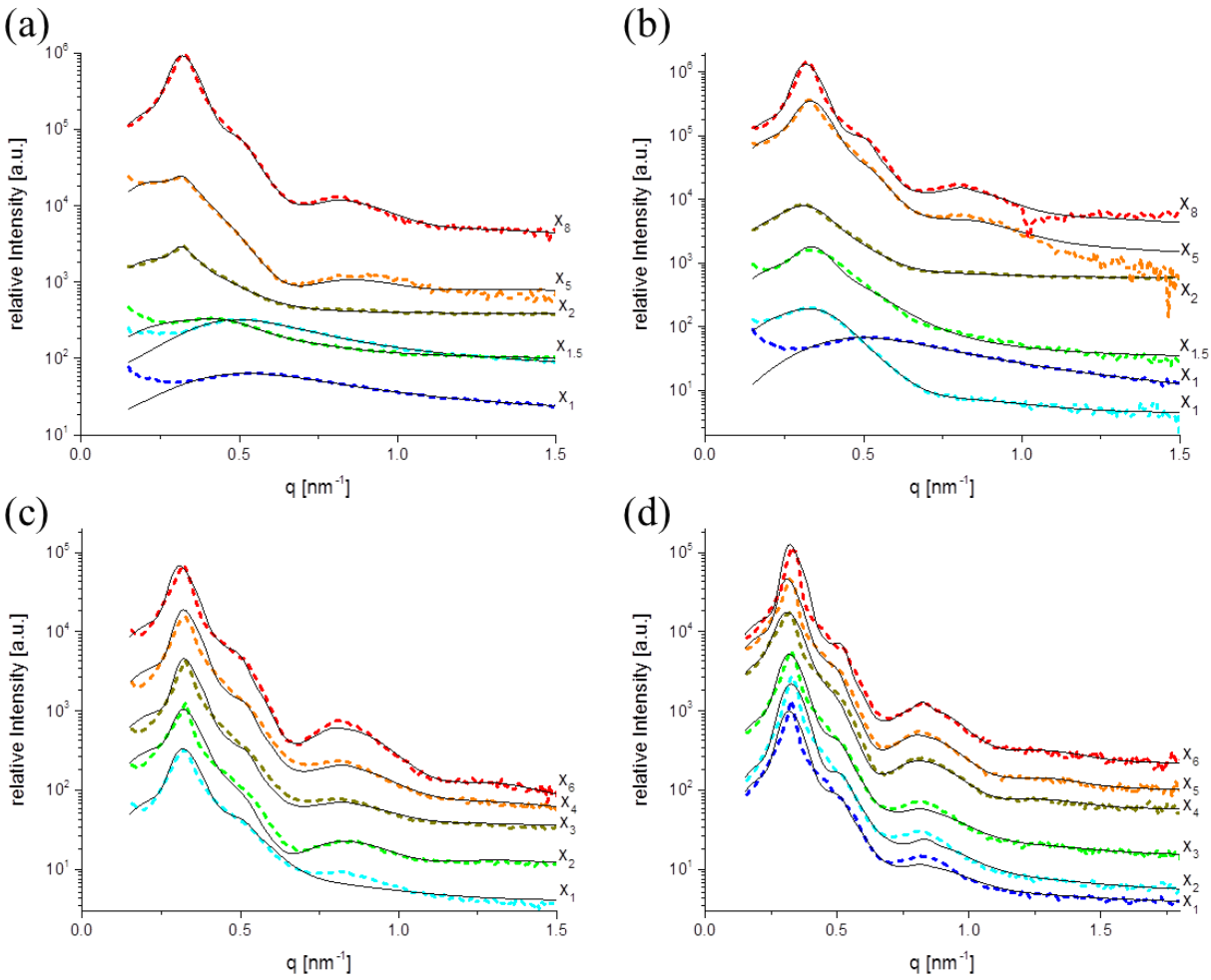

Figure 61. SAXS curves of 20 wt% PI_{70}-(*b*)-PEG_{60}/dioxane measured downstream in *x*-direction in the SIFEL-capillary microfluidic device with flow rates of (a):1500 µl/h for water and polymer solution (W/PS), 750 µl/h for the middle dioxane buffer stream (M) and 100 µl/h for the remaining buffer streams (R); (b):1500 µl/h (W/PS), 500 µl/h (M) and 100 µl/h (R); (c):1000 µl/h (W/PS), 400 µl/h (M) and 63 µl/h (R); (d):1000 µl/h (W/PS), 200 µl/h (M) stream and 63 µl/h (R). The structural evolution from the weakly segregated polymer/dioxane solution to the ordered, strongly segregated lyotropic liquid crystalline micellar phase can be clearly observed.

The scattering curves measured at different downstream positions x in the glass capillary are shown in Figure 61 for different flow rates. In the first experiment shown in Figure 61 (a) we used flow rates of $Q_w = 1500$ µl/h for the water stream, $Q_{PD} = 1500$ µl/h for the polymer/dioxane stream, $Q_B = 750$ µl/h for the central stream, and $Q_S = 100$ µl/h for the outer sheath streams, as in the y-scan experiment (Figure 60).

As for the polyimide chip, we observe at the first two positions x_1 and $x_{1.5}$ in the capillary a broad peak at $q = 0.5$ nm^{-1} ($d = 13$ nm). As discussed above, this indicates weak microphase segregation in the pure polymer/dioxane solution. The scattering curves can be fitted to a structure factor given by Leibler (Eq. (170)) yielding a chi-parameter, which increases downstream from $\chi = 0.037$ to $\chi = 0.051$. Starting at position x_2 we observe a narrow peak shifted to $q = 0.3$ nm^{-1} ($d = 21$ nm) with a weak shoulder, which shows that the interdiffusion with water has caused stronger segregation leading to the formation of micelles, which start to arrange in an ordered structure. Further downstream we observe the evolution of scattering curves with narrowed Bragg peaks, higher order reflections and form factor oscillations indicative of well-ordered lyotropic micellar phase morphologies. This shows the advantage of using hybrid chips with X-ray transparent glass capillaries that have very low X-ray background such that low-intensity features of the scattering curves such as the form factor oscillations at high *q* can be well resolved.

4.4.1.3 Determination of the Mixing Point

The 3D buffer stream design produces a well-defined point of mixing, located at the beginning of the glass capillary. This onset point can, in principle, be determined by fast reference reactions that produce a fluorescent species such as calcium green. [127] We found, however, that the mixing point determined with this method was systematically located upstream the actual mixing point in our polymer/dioxane/water experiments. We therefore used the following method to determine the onset of mixing for our series of experiments.

We observe from the experiment in Figure 61 (a) that interdiffusion commences between positions $x_{1.5}$and x_2, which allows one to determine the mixing point x_0 and the time after mixing t for different flow rates. Similar to the calculation of the diffusional mixing in the polyimide chip, we consider the diffusional mixing of the polymer/dioxane and water stream across the buffer stream. The buffer stream width after the first focusing is given by [107]

$$w_{B1} = \frac{Q_B}{Q_{PD} + Q_B + Q_W + 4Q_S} w_{cap} \tag{179}$$

where Q_B is the volumetric flow rate of the buffer layer, Q_{PD} of the polymer/dioxane stream, Q_W of the water stream, and Q_S of the sheath flow. w_{cap} is the width of the capillary.

With

$$Q_1 = Q_{PD} + Q_B + Q_W + 2Q_S \tag{180}$$

being the total flow rate after the first focusing, the buffer stream width after the second focusing can be calculated as

$$w_{B2} = \frac{Q_1}{Q_1 + 2Q_S} w_{B1} \tag{181}$$

which under our experimental conditions is only slightly smaller than the width after the first focusing step. The flow rate in the capillary is given by

$$v_{cap} = \frac{Q_1 + 2Q_S}{\pi R_{cap}^2} \tag{182}$$

As in Eq. (178), the time to diffuse half across the buffer layer is

$$t_D = \frac{w_{B2}^2}{8D_S} \tag{183}$$

during which there is a downstream motion over the distance $x_D = v_{cap} t_D$. As this calculation neglects the effect of different diffusivities of the solvents (dioxane, water) and the polymer across the buffer layer, we introduce a factor α such that $w_B = \alpha w_{B2}$ describes the effective width of the buffer layer, with the diffusion time given by

$$t_D = \frac{(\alpha w_{B2})^2}{8D_S} \tag{184}$$

From experiments at different flow velocities, we obtain a very reasonable value of $\alpha = 1.5$ for our experimental setup, from which the width of the buffer layer at different flow velocities and the different times after mixing can be calculated. From the given volumetric flow rates Q, the inner width of the capillary ($R_c = 140$ µm) and the diffusion coefficient of the solvent ($D = 10^{-9}$ m²/s) we then calculate the width of the buffer layer, the flow velocity v, and the mixing position x_0.

These values are summarized for all experiments in Table 6. Using different total flow rates and different flow rate ratios we can access different time scales in the microfluidic experiment from milliseconds to up to 3 seconds.

As seen in Figure 61 (a), for the first time a micellar peak can be observed at position x_2, which corresponds to a time of 10 ms after mixing. Further downstream, at position x_5, which corresponds to 0.77 s after mixing, a pronounced form factor oscillation with the first minimum at $q = 0.6$ nm^{-1} has developed. This shows that at this time the micellar core is already strongly segregated, forming a sharp interface. Finally, at position x_8 ($\Delta t = 1.5$ s), a second weak maximum and an indication of a second formfactor minimum is observed, signaling further ordering and development of narrow disperse, highly segregated micellar cores. The scattering curves of the ordered structures can be well fitted to an FCC-lattice with lattice constant and core radii listed in Table 7. All fits are indicated by straight lines in Figure 61.

Table 6. Volumetric flow rates of the water stream Q_W, the polymer/dioxane stream Q_{PD}, the buffer stream Q_B, the 6 sheath streams Q_S, the total flow rate Q_{total}, the calculated widths w_{B1} and w_{B2} of the buffer layer according Eqs. (179) and (181), then mean flow velocity v, the diffusion time t_D across the buffer layer, and x_0-position for the four different flow-focusing experiments #1 - #4 in the 3D-SIFEL capillary hybrid chip.

Experiment no.	**#1**	**#2**	**#3**	**#4**
Q_W [µl/h]	1500	1500	1500	1000
Q_{PD} [µl/h]	1500	1500	1500	1000
Q_B [µl/h]	750	500	200	400
Q_S [µl/h]	100	100	63	63
Q_{total} [µl/h]	4350	4100	3578	2778
w_{B1} [µm]	51	36	16	42
w_{B2} [µm]	48	34	16	40
v [mm/s]	19.6	18.5	16.1	12.5
t_D [s]	0.66	0.33	0.07	0.46
x_0 [mm]	12.9	6.1	1.1	5.7

Table 7. Positions Δx, times after mixing Δt, fitted radius of gyration R_g, unit cell size a, ordered domain size Δ, and micellar core radius R_c as determined by SAXS-experiments of 20 wt% PI_{70}-(*b*)-PEG_{60}/dioxane in a SIFEL-capillary microfluidic device at different flow rates.

time	Δx [mm]	Δt [s]	R_g [nm]	*a* [nm]	D [nm]	R_c [nm]
#1: Q_W = 1500 µl/h, Q_{PD} = 1500 µl/h, Q_B = 750 µl/h, Q_S = 100 µl/h						
x1	8.0	-0.25	4.0			
x1.1	10.5	-0.12	3.9	21.1	35	6.2
x2	13.0	0.01		33.3	101	6.7
x5	28.0	0.77		32.7	97	6.8
x8	43.0	1.54		33.6	80	7.1
#2: Q_W = 1500 µl/h, Q_{PD} = 1500 µl/h, Q_B = 500 µl/h, Q_S = 100 µl/h						
x1	8.0	0.11	3.9	26.2	33	6.8
x1.1	10.5	0.24		30.8	61	6.9
x2	13.0	0.38		30.6	42	7.1
x5	28.0	1.19		31.7	67	7.2
x8	43.0	2.00		34.0	85	7.3
#3: Q_W = 1500 µl/h, Q_{PD} = 1500 µl/h, Q_B = 200 µl/h, Q_S = 63 µl/h						
x1	13.4	0.76		33.9	82	7.1
x2	18.4	1.07		33.1	74	7.1
x3	23.4	1.38		33.7	78	7.2
x4	28.4	1.69		34.2	70	7.2
x5	33.4	2.00		34.6	95	7.2
x6	38.4	2.31		33.6	106	7.1
#4: Q_W = 1000 µl/h, Q_{PD} = 1000 µl/h, Q_B = 400 µl/h, Q_S = 63 µl/h						
x1	13.4	0.61		33.7	84	6.9
x2	18.4	1.01		33.3	90	7
x3	23.4	1.41		33.3	102	7.1
x4	28.4	1.81		33.5	97	7.1
x5	33.4	2.21				
x6	38.4	2.61		34.9	97	7.1

From the set of experiments shown in Figure 61 (a), we observe that the initial segregation into a micellar structure is very fast and diffusion-limited. The micelles then arrange into an ordered structure within the first second. The scattering curves subsequently develop higher order reflections and form factor oscillations characteristic for strongly segregated, well-ordered structures.

By adjusting the flow rates of the individual streams, we were able to access different time spans after mixing. Figure 61 (b) shows the set of scattering curves measured downstream for flow rates of $Q_W = 1500$ µl/h, $Q_{PD} = 1500$ µl/h, $Q_B = 500$ µl/h, and $Q_S = 100$ µl/h, thus accessing later stages of structural evolution in more detail. We observe at the latest time a well-developed first-order Bragg-peak with the development of a second order reflection. Figure 61 (c) shows a set of scattering curves measured for still lower buffer and sheath stream velocities ($Q_B = 500$ µl/h, $Q_S = 100$ µl/h), showing still later stages of structural evolution. With an overall decrease of the flow rates, shown in Figure 61 (d), we can access a broader time span, where finally structures with many higher order reflections and many form factor oscillations in the scattering curves can be observed.

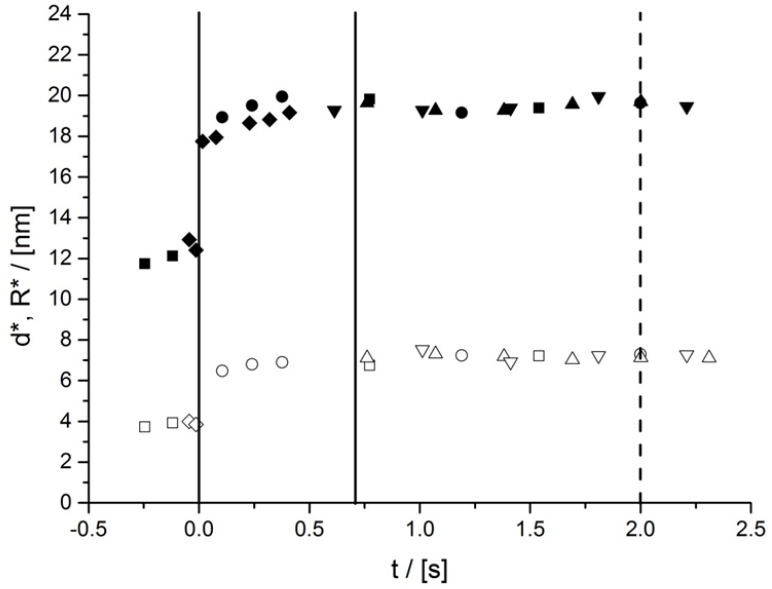

Figure 62. Temporal evolution of the block copolymer and micellar radii R^* and the characteristic distance d^* as a function of time after mixing. Micelle formation occurs within the first 10 milliseconds. Within 0.7 seconds the micelles arrange on an ordered lattice, with the maximum order of the resulting lyotropic liquid crystalline phase reached after 2 seconds.

The structural evolution as measured from all experiments is summarized in Figure 62. Here we plot the characteristic distance $d^* = \frac{2\pi}{q^*}$ and the characteristic radius $R^* = R_g, R_c$ as a function of time after mixing. d^* is derived from the peak position, and thus can be given both for the weak segregation case, where we measure a Leibler-type structure factor (Eq. (170)), and the strongly segregated ordered case, where we observe Bragg peaks from an FCC structure (Eq. (173)). Also, the choice of R^* allows to provide a polymer chain dimension for both cases.

As observed in Figure 62, the characteristic dimension R^* of the block copolymers is ca. 4 nm in the weak segregation regime before mixing, and increases to 7 nm within 0.7 seconds which corresponds to the stretching of the polymer chains under strong segregation conditions to locate the PI-(*b*)-PEO block connection at the interface and homogeneously fill the micellar core/shell structure. The characteristic distance d^* increases similar from ca. 12 nm in the weak segregation regime before mixing, to 20 nm within the first 0.7 seconds. As a characteristic parameter for the development of a well-ordered structure we could also consider the domain size, which increases from ca. 40 nm to 100 nm, albeit with a much greater variation as it is derived from the peak width, which is also affected by shear effects (see Table S 1-Table S 5 in the supporting information).

The time scales are in good agreement with a previous continuous flow mixing experiment, where the development of block copolymer micellar structures was also diffusion-limited, occurring on time scales within 25 milliseconds, with the ordered lyotropic phase structure evolving over 1.1 seconds, the longest time scale that could be covered with the setup. [99]

4.4.1.4 Capillary Interdiffusion Experiments

The interesting feature of the PI_{70}-(*b*)-PEG_{60} block copolymer used for the present study is the fact, that in water it is expected to form vesicles, based on the relative block lengths of the block copolymer, where the fraction of the hydrophilic PEG-block is only 0.46. Vesicle formation is not observed during the first milliseconds and seconds after mixing, where well-defined spherical micelles are found. The spherical micelles thus appear to be a transient structure, which evolves into other structures at later stages of the self-assembly process. We thus performed capillary mixing experiments, which access longer time scales.

For these experiments a 20 wt% polymer/dioxane solution was filled into a vertically positioned, 1 mm diameter glass capillary and water was carefully placed on top of the solution avoiding convection. As the polymer/dioxane solution ($\rho\,(dioxane) = 1.03$ g/cm^3) has a slightly higher density compared to water ($\rho\,(water) = 1.00$ g/cm^3), this avoids convection during the experiment.

With time a concentration gradient along the capillary is developing caused by interdiffusion of the two solutions. This is analogous to the interdiffusion of both solutions in the microfluidic setup, but occurring on much longer time scales. In our case, the structures evolving along the concentration gradient were followed by vertically scanning the capillary after a waiting time of one hour. A comparison of the structural evolution during fast interdiffusion in the microfluidic chip and slow interdiffusion in the capillary would provide insight into possibly different kinetic pathways and intermediate states.

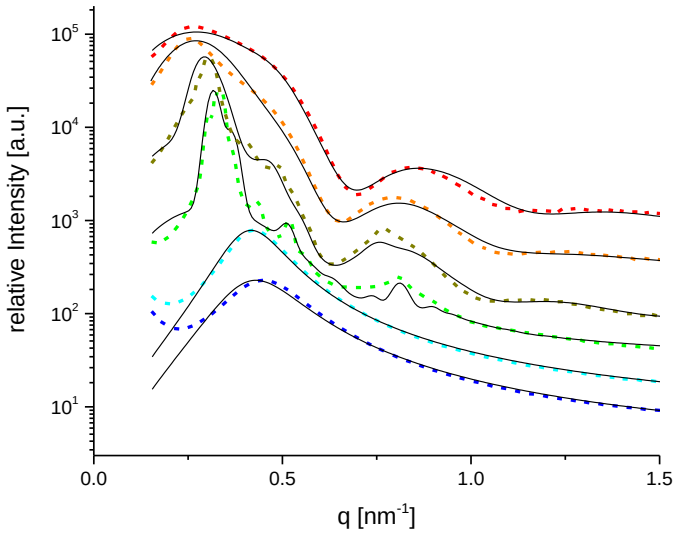

Figure 63. SAXS-curves measured along a vertical concentration gradient of a 20 wt% PI_{70}-(*b*)-PEG_{60}/dioxane and water in a vertical glass capillary. The concentration scan starts at the polymer rich phase (bottom) and proceeds towards the water rich phase (top). A development of an ordered structure and the subsequent decrease of the micellar core diameter, as indicated by the shift of the formfactor minimum to higher q-values can be observed.

For the concentration gradient measurements in the capillary the first measured point was located below the interface in the polymer solution region. The next points were scanned upwards along the capillary into the water phase with 1 mm step width and measurement time of 10 seconds.

The structural evolution can be followed by the measured SAXS-curves that are shown in Figure 63. The first two scattering curves show a broad peak that can be fitted to the Leibler structure factor (Eq. (170)). The peak position at $q = 0.4$ nm^{-1} corresponds well to the measured scattering curves in the fast interdiffusion experiments. The third scattering curve shows a well-developed, highly ordered FCC-lattice with 5 higher order reflections and pronounced form factor oscillations.

Further, at higher water content, the peak broadens and shifts to lower q, whereas the form factor oscillations shift to higher q. Still the formfactor oscillations can be well described by assuming a spherical structure, however with a decreasing core radius.

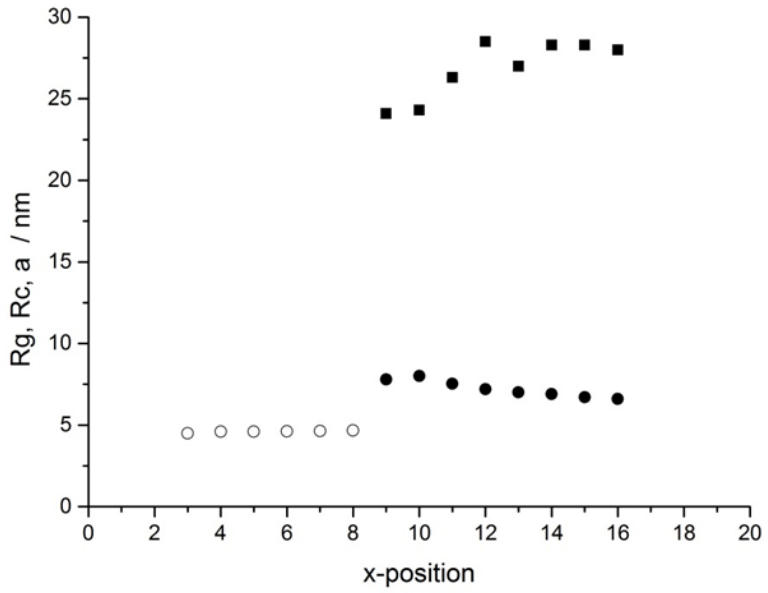

Figure 64. Evolution of the polymer radius of gyration R_g (○), the micellar core radius R_c (●) and the unit cell dimension a (■) along the concentration gradient in the vertically aligned capillary from the dioxane-rich into the water-rich phase.

The results obtained from fits the measured scattering curves are summarized in Table S 6 in the Supporting Information and are shown in Figure 64. We observe that with increasing water content the FCC-lattice swells, and the radius of the micelles decreases from 8.0 nm to 6.6 nm due to effusion of dioxane into the water phase and stronger segregation.

4.4.1.5 Cryo-Transmission Electron Microscopy (cryo-TEM)

The slow vertical capillary interdiffusion experiments already indicate that still after one hour the micelles have spherical shape. To study the structural evolution over longer time periods, we used cryo-transmission electron microscopy (cryo-TEM).

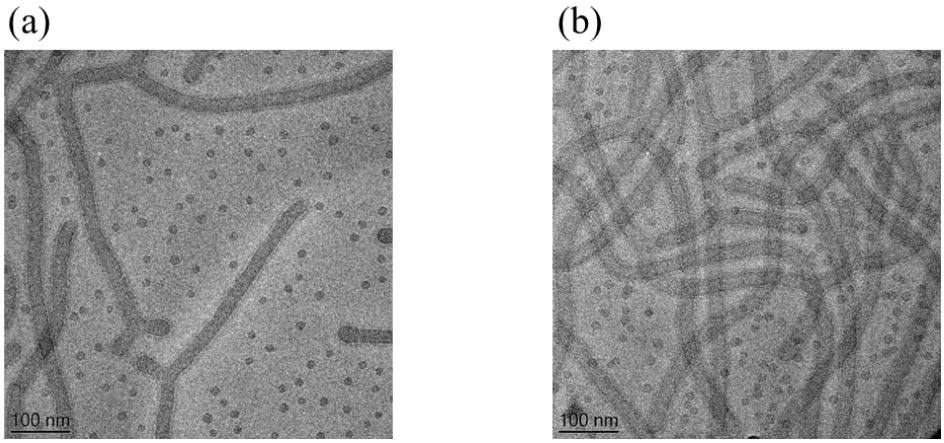

Figure 65. Cryo-TEM images of 20 wt% PI_{70}-(*b*)-PEG_{60}/dioxane/water solution collected after mixing in microfluidic chip. A coexistence of small spherical micelles and larger diameter cylindrical micelles can be observed.

Figure 65 shows cryo-TEM images of the polymer/dioxane/water mixtures that were collected after the fast mixing experiments in the microfluidic chip and measured one day later. We now, after a much longer time, observe a coexistence of small spherical micelles and larger diameter cylindrical micelles. The spherical micelles have a core radius of 6.8 nm, which is in very good agreement with the radii determined from the SAXS-experiments (see Figure 64). The cross-sectional diameter of the cylindrical micelles is 26.7 nm and thus much larger than expected, as the cross-sectional diameter is usually smaller than the diameter of the corresponding spherical micelles [128]. This indicates that the effusion of dioxane leads to very compacted micellar cores.

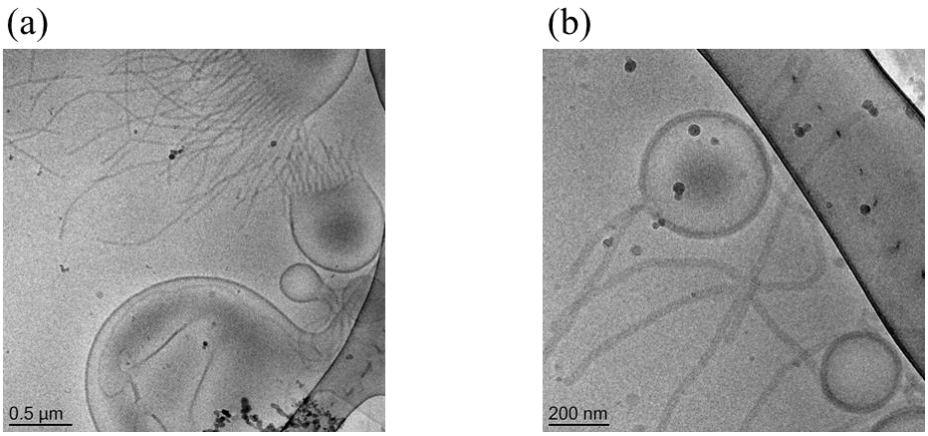

Figure 66. Cryo-TEM images of 20 wt% PI-(*b*)-PEO after reverse phase evaporation. We observe a coexistence of cylindrical micelles and vesicles together with intermediate structures.

Finally, we compared the dioxane/water-mixing experiment with a phase transfer experiment, where the block copolymer is dissolved in chloroform, which is covered with a water layer. After evaporation of the chloroform phase at 60 °C for three days, the aqueous phase contained the self-assembled block copolymer structures, which were imaged by cryo-TEM and which we expected to correspond to the final equilibrium vesicular structure of the block copolymer. As shown by the cryo-TEM images in Figure 66, we observe a coexistence of cylindrical micelles and vesicles and many intermediate structures such structures similar to "jellyfishes". The measured double layer thickness of the vesicles is 27.6 nm, and the thickness of the cylindrical micelles is 30.7 nm, and thus only slightly larger compared to the cylindrical micelles in Figure 65. Details of the arrangement of the cylindrical micelles in the "jellyfish" intermediates indicate the adjacent cylindrical micelles fuse into the vesicle bilayer.

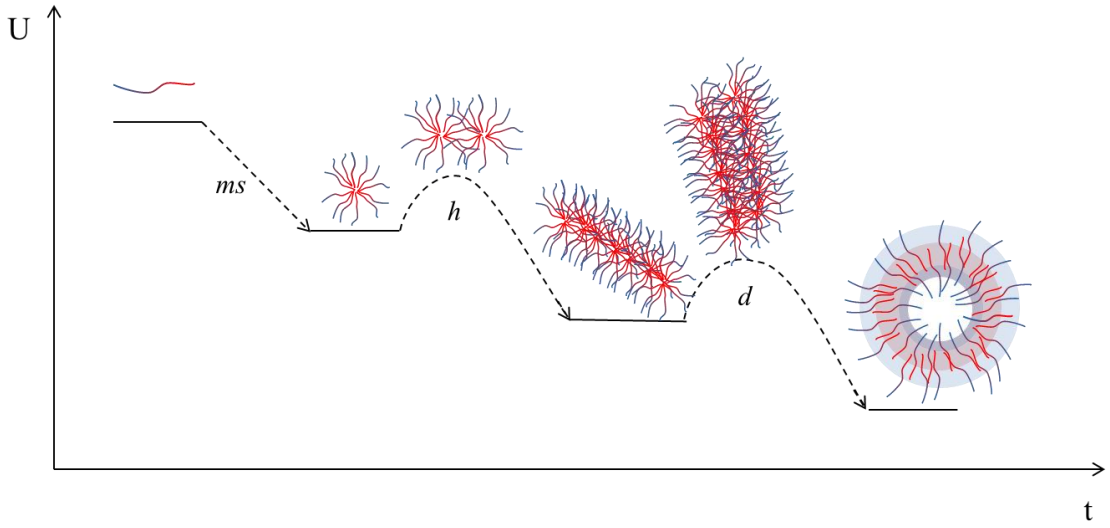

Figure 67. Scheme of the structural evolution from single block copolymers into spherical micelles, cylindrical micelles and vesicles with the corresponding time scales (milliseconds, hours, days), as observed by selective solvent-induced self-assembly. Whereas the assembly into micelles is very fast and transport-limited, the formation of cylindrical micelles and bilayers requires micellar fusion, which occurs on much longer time scales.

We thus observe the formation of different micellar intermediate structures along the structural pathway from single block copolymer chains to vesicles during selective solvent mixing as schematically shown in Figure 67. The first assembly step from single block copolymers to micelles is very fast and only limited by the translational diffusion of the block copolymer chains, thus occurring on time scales of a few milliseconds. The subsequent arrangement into a well-ordered liquid crystalline lattice occurs on time-scales of several hundred milliseconds, which is of the order of typical relaxation time of lyotropic block copolymer phases. The subsequent structural development into cylindrical structures occurs on time scales of hours to days, and involves micellar fusion, which has to overcome the steric stabilization barrier of the micellar shell. The next step involves the fusion of the cylindrical micelles into vesicles, where again the steric stabilization barrier has to be overcome and thus long time scales are involved, as time scales are related exponentially, i.e. as $\tau \sim exp\left[\frac{E}{kT}\right]$ to the activation energy, which is of the order of the steric repulsion energy of the spherical and cylindrical micellar shells.

Conclusion

We investigated in-situ the structural evolution during selective solvent-induced block copolymer self-assembly via micellar intermediate states into vesicles. Self-assembly was induced by mixing a solution of the block copolymer in a common solvent, dioxane, with water as a selective solvent. This corresponds to the most common preparation procedure for block copolymer assemblies. Mixing by interdiffusion, occurring on time scales of milliseconds to seconds was studied by microfluidic flow-focusing in combination with in-situ microfocus SAXS. It shows that micelle formation is very fast and diffusion-limited. The subsequent structural arrangement into an ordered liquid crystalline phase occurs on time scales of several hundred milliseconds to seconds. On longer time scales the micellar cores more strongly segregate and shrink by effusion of dioxane, which could be studied by capillary interdiffusion. The structural evolution over time scales of hours to days could be followed by cryo-TEM. On these time scales spherical micelles fuse into cylindrical micelles, which further fuse into vesicle bilayers. The study provides insights not only on the self-assembly pathways of block copolymers into vesicles, but also on the related time-scales and intermediate structures.

4.5 Kinetic Studies of Biocompatible PEG-(*b*)-PLA Block Copolymers

Introduction

Since block copolymers find application in pharmaceutical, cosmetic or food industries, as mentioned in chapter 0, biocompatible and biodegradable block copolymers are of increasing importance and interest. Due to the amphiphilic properties of the block copolymers, they can order to structures like micelles or vesicles. These structures can be loaded with e.g. drugs, colorings and flavors. The micelles or vesicles should then carry the active agents to the desired position where due to a trigger the actives are released. [27,129] Poly(ethylene glycol)-(*b*)-poly(lactic acid) (PEG-(*b*)-PLA) is an example for biocompatible block copolymers. The PEG block is thereby the hydrophilic part with low toxicity. PEG is widely used in the cosmetic industry. It is flexible, resistant to immunological recognition, there is no combination with proteins, and it is biocompatible. Furthermore, PEG has the advantage to resist opsonisation, an antibody reaction. The hydrophobic PLA block is biodegradable and also nontoxic. It hydrolyses into hydroxyl-carboxylic acid through ester bond cleavage, which is then metabolized into water and carbon dioxide. Besides the biodegradability PLA has good mechanical strength and low immunity. The disadvantages are the long degradation time, the low drug loading of polar drugs, and the weak hydrophilicity. Thus, the combination of PEG with PLA by polymerization leads to better drug loading, improved hydrophilicity and a higher degradation rate, as well as crystallization. At low concentration PEG-(*b*)-PLA is nontoxic and not accumulative in vivo because the degradation products can be eliminated by the kidney or enter the tricarboxylic acid cycle. [130]

The PEG-(*b*)-PLA block copolymer has an amphiphilic character and thus can undergo self-assembly. Especially, vesicles are of interest since due to their double layer also lipophilic substances can be encapsulated, as explained in chapter 2.1.1.1. An example where PEG-(*b*)-PLA is used to produce vesicles was published by Weitz et al.. There, a microfluidic device is generating a double emulsion forming uniform PEG-(*b*)-PLA vesicles. The release of an active is then triggered by the application of a large osmotic pressure difference.

However, the production of stable and tailored self-assembly structures is tedious and thus, the investigation of the underlying kinetic process is important to adjust such structures for further applications. [27,130]

In this thesis two different poly(ethylene glycol)-(*b*)-poly(lactic acid) block copolymers were used. The first PEG-(*b*)-PLA has a molecular weight of Mw_1=48927 g/mol and block lengths of 217 and 532 monomer units respectively. The polydispersity of PEG_{217}-(*b*)-PLA_{532} is Mw/Mn=1.06. The second investigated PEG-(*b*)-PLA has a molecular weight of Mw_2=13506 g/mol with block lengths of 84 and 130 monomer units respectively and Mw/Mn=1.08. The block copolymers were synthesized *via* sequential living anionic polymerization. Before the investigation of the polymer kinetics in the microfluidic channel the PEG-(*b*)-PLA block co-polymers were dissolved in 1,4-dioxane to maintain various wt%/wt solution.

For the kinetic studies a microfluidic device was brought into a small angle X-ray scattering set-up. The SAXS experiments were either performed at the PETRA III, MiNaXs Beamline P03 at DESY/HASYLAB or at the in-house rotating anode Ganesha, SAXSLAB. For the continuous flow measurements, the SIFEL-capillary-hybrid chip was used, described in chapter 4.2. At PETRA III the experiments were carried out with a wavelength of λ= 0.957 nm and a beam size of 25 µm in x-direction and 15 µm in y-direction. For detection a Pilatus 1M or 300K (DECTRIS) was used with a pixel size of 172 µm by 172 µm. The sample to detector distance was varied between 3.53 m to 4 m. In between an evacuated tube was placed. Different motors allowed positioning of the microfluidic chip or the glass capillary in x-, y-, z-direction. The in-house SAXS set-up Ganesha is equipped with a microfocus rotating anode (Rigaku Micromax 007 HF) and a Pilatus 300K detector (DECTRIS). The X-ray beam has a wavelength of λ = 0.154 nm was focused to 100 µm for the scanning experiments.

The inlets and outlets of the SIFEL-capillary-hybrid chip for three-dimensional hydrodynamic flow focusing, were connected with PE-tubings (Scientific Commodities Inc.) to gas-tight syringes (Hamilton). The syringes were adjusted to high-precision syringe pumps (NEMESYS, Cetoni GmbH) to provide a constant pressure driven flow of the solution in the microfluidic device.

The different SAXS measurements of PEG-(*b*)-PLA can be divided into capillary and microfluidic experiments. Whereas the capillary experiments can be differentiated between concentration scans and time scans. The microfluidic experiments vary in different flow rates and flow ratios.

Results and Discussion

4.5.1.1 Experiments in the Microfluidic Device

The used microfluidic device is a combination of a microfluidic channel design and a glass-capillary. This combines two advantages, the defined mixing in the microfluidic device and the low background of thin walled ($\sim 10\,\mu m$) glass-capillaries in SAXS experiments.

We tested different flow rates to achieve different measurable timescales in the microfluidic device. For a higher total flow rate, earlier stages of the self-assembly process can be observed, but with a shorter residence time in the microfluidic chip and vice versa. Also, the middle buffer stream between the water and the polymer stream highly influences the first contact of the two reactants. The higher the flow rate ratio between the streams of polymer and water to the buffer layer $\frac{\mathrm{PS+H2O}}{M}$, the thinner is the buffer layer and the water/polymer molecules need less time to interdiffuse, due to the smaller diffusion length.

The device design is already illustrated in Figure 50 and described in chapter 4.2. The used PEG-(*b*)-PLA/dioxane solution (inlet A) had a concentration of 20 wt% and was always pumped with the same flow rate as water (inlet B). With the middle buffer stream the reactant (A) and (B) are separated and thus, the mixing position in the channel was adjusted. The other seven sheathing layers were used to keep the reactants off the channel walls. Their flow velocity influenced the residence time and the overall flow rate, as well as the stream geometry of the polymer and the water streams.

The first chip measurement had an overall flow rate of 3200 µl/h. The flow rate ratio of stream PEG_{84}-(b)-PLA_{130}/dioxane and H_2O (1000 µl/h each) to the separating middle stream (500 µl/h) was 4:1. The obtained SAXS data in Figure 68 (b) show, that for the first two measured positions (x_1 and $x_{1.5}$) no features in the scattering curves are observed. Only at the last position (x_4) a pronounced shoulder at $q = 0.16\,nm^{-1}$ ($d = 39\,nm$) occurs. The peak was fitted to the structure factor of hexagonally packed cylinders (HEX lattice) and the fitted parameters are shown in Table 8. For all HEX lattice and cylinder fits, for the cylinder length only a lower limit could be specified, since

$$L > \frac{2\pi}{q_{min}} \tag{185}$$

Figure 68 (a) shows the y-scan at position 4 indicating the unperturbed laminar stream in the channel. From the fifth curve a weak Bragg-peak indicates the ordering of the cylindrical micelles due to the interdiffusion with water. The peak weakens towards the polymer stream and diminishes finally.

The PEG-(*b*)-PLA/dioxane solution, as well as dioxane and water, show no scattering features in the SAXS-curves. Hence, the first curves in the front can be attributed to each of the three solutions. However, due to the fact that water molecules are much smaller compared to the polymer molecules and the diffusion coefficient is dependent on the radius of the molecule (Eq. (80)), it is assumed that water diffuses faster and thus, that the curves in the y-scan with the Bragg peaks are slightly more located in the former polymer stream region and the most intensive peaks are located towards the water stream. Therefore, the y-scan started in the outer dioxane sheathing stream, proceeded towards the water stream and then, reached the buffer- and the polymer stream before it ended again in an outer dioxane sheathing stream. Since in Figure 68 (a) a Bragg peak is obtained in the middle of the y-scan, water (and polymer) molecules have interdiffused the buffer layer and caused an ordering of the polymer.

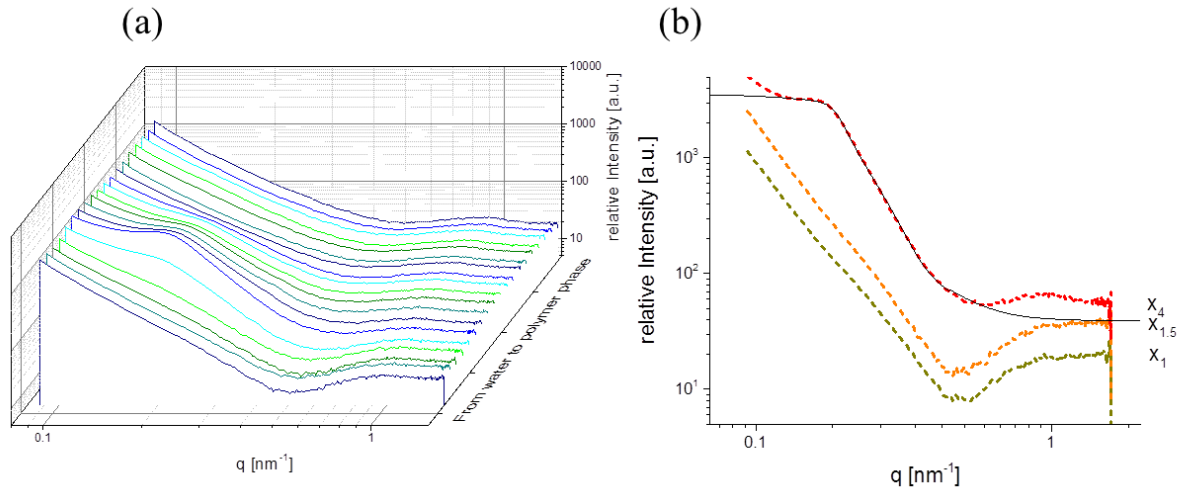

Figure 68. SAXS measurement in microfluidic device with a concentration of 20 wt% and flow rates of PEG_{84}-(*b*)-PLA_{130}/dioxane/H_2O: 1000 µl/h, middle buffer stream: 500 µl/h and remaining buffer streams: 100 µl/h. (a) shows the y-scan at Position 4 and (b) the single selected scattering curves at Position 1, 1.5 and 4.

Table 8. Fit values of Figure 68 (b).

Position	a [nm]	Δ [nm]	displ. [nm]	R_c [nm]
4	38.8	55.6	8.4	11.1

For the second chip measurement the flow rates of stream PEG_{84}-(*b*)-PLA_{130}/dioxane and H_2O were kept at 1000 µl/h. However, the middle buffer stream had a lower flow rate (400 µl/h) than in the previous measurement. Therefore, the ratio of stream A and B to the buffer stream is 5:1. The remaining sheathing streams are also slower with flow rates of 63 µl/h. Thus, the total flow rate is 2841 µl/h. Because of the slower total flow rate and the higher ratio of the A and B streams to the middle buffer stream, the start of the reaction is shifted towards earlier positions in the capillary. All analyzed positions show a more evolved or later state in the structural evolution.

In Figure 69 different y-scans at position 1 (a), 5 (b) and 6 (c) are shown. The first position (a) shows a weak shoulder in the middle of the scattering curve, indicating the beginning of the self-assembly. The later positions five (b) and six (c) show a more pronounced peak characteristic for the formation of an ordered lyotropic phase.

The featureless curves before and after the described curves belong to the polymer/dioxane solution, the pure water, the buffer and sheathing streams, as described before. In (d) single curves for each position are shown for clarification. These measurements were fitted with hexagonally packed cylinders with radii of 14 nm and a slight increase of the unit cell dimension *a*, as listed in Table 9.

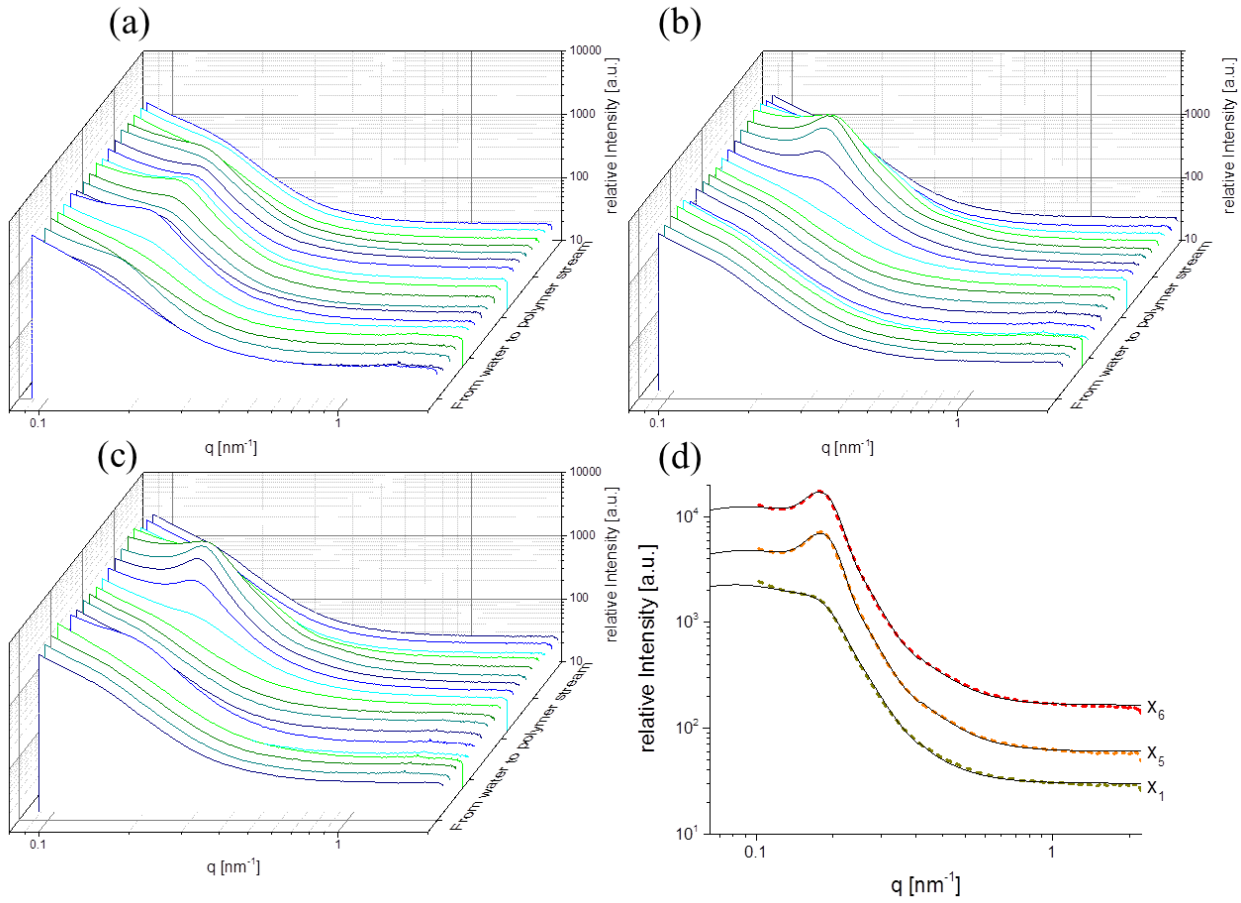

Figure 69. Microfluidic chip experiment with flow rates of 20 wt% PEG_{84}-(*b*)-PLA_{130}/dioxane /H_2O: 1000 µl/h, middle buffer stream: 400 µl/h, remaining streams: 63 µl/h at x-Position 1 (a), 5 (b) and 6 (c) and the selection of the most pronounced curves of each position in (d).

Table 9. Fit values of Figure 69 (d).

Position	a [nm]	Δ [nm]	displ. [nm]	R_c [nm]
1	38.8	101.0	12.6	14.0
5	39.6	122.0	9.0	14.0
6	39.9	123.0	9.3	14.0

The third measurement in the microfluidic device had the lowest total flow rate of 2541 µl/h. Furthermore, the middle buffer stream flow rate was decreased to 100 µl/h. The flow rate ratio of stream PEG_{84}-(*b*)-PLA_{130}/dioxane and H_2O to this buffer stream is 20:1. In Figure 70 (a) the y-scan of position 4 is exemplarily shown. The polymer solution and the water inlet were interchanged compared to the measurements before.

Thus, the y-scan started in the sheathing stream, proceeded towards the polymer solution followed by the buffer and water streams and ended again in dioxane sheathing stream. The first sheathing stream was not included in the y-scan, such that the first curves in (a) show already the evolved Bragg peak. Throughout all measured positions a Bragg peak was observed as summarized in Figure 70 (b). The parameters for the hexagonal lattice fits are listed in Table 10. The core radius remains at R_c~13 nm and the lattice constant a increases towards later positions in the microfluidic channel.

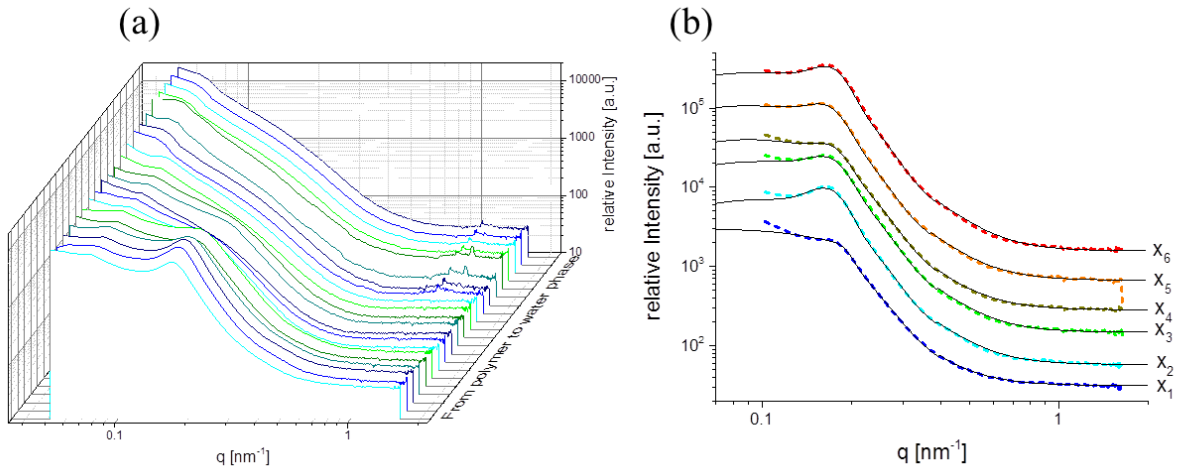

Figure 70. 20 wt% PEG_{84}-(b)-PLA_{130}/dioxane in microfluidic chip with flow rates of polymer solution/H_2O: 1000 [µl/h] each, middle buffer stream: 100 [µl/h], and remaining sheathing streams: 63 [µl/h]. (a) shows a y-scan at position 4 and (b) show selected curves from x-position 1 to 6.

Table 10. Fit values of Figure 70 (b).

Position	a [nm]	Δ [nm]	displ. [nm]	R_c [nm]
1	37.8	70.5	9.2	12.6
2	39.1	103.0	9.6	12.8
3	38.5	99.4	10.4	12.8
4	38.5	111.0	12.0	12.8
5	40.9	78.2	8.8	13.2
6	40.9	76.5	8.4	13.0

Further microfluidic kinetic experiments were made with the larger molecular weight PEG_{217}-(*b*)-PLA_{532} with similar flow velocities and ratios as for the short chain PEG-(*b*)-PLA, which is exemplarily shown in Figure 71. A fast formation of cylindrical micelles was observed, but no further structural evolution took place, indicating a slower self-assembly process due to the larger block copolymer lengths. Therefore, time dependent measurements were realized by analyzing the diffusion in a glass capillary, which is described in the next chapter.

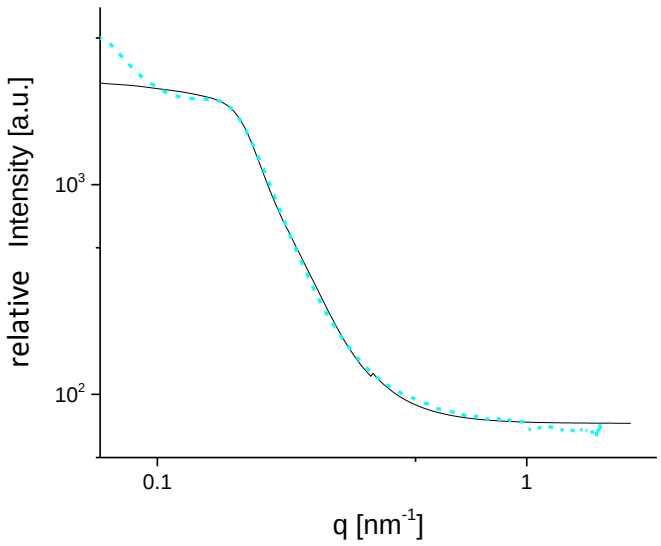

Figure 71. SAXS measurement of the 20 wt% PEG_{217}-(*b*)-PLA_{532}/dioxane in the SIFEL-capillary hybrid chip with flow velocities of 1000 µl/h for the 20 wt% PEG_{217}-(*b*)-PLA_{532}/dioxane and water stream each, 200 µl/h for the buffer stream and 63 µl/h for the remaining sheathing streams.

4.5.1.2 Experiments in the Glass Capillary

Time dependent measurements of PEG_{217}-(*b*)-PLA_{532}

Since the SAXS measurements of the microfluidic experiments with the larger PEG_{217}-(*b*)-PLA_{532} block copolymer showed no structural evolution, the time dependent measurements were realized with a slow capillary time scan. During the time scan measurements, the X-ray beam always hit the same point of the sample, close to the polymer/water interface, located slightly more in the polymer region. This was realized by filling 20 wt% of the polymer/dioxane solution in a capillary and adding water on top.

Then, the capillary was aligned vertically into the X-ray beam. The structural changes due to diffusion were measured over periods of several hours. Compared to the diffusion experiment in the microfluidic chip, this diffusion experiment is slower since the diffusion length is longer.

The time scan for 20 wt% PEG_{217}-(*b*)-PLA_{532} started after 5 minutes and 23 seconds and ended after 19 hours and 53 seconds. Each measurement took 10 minutes. The respective time for the measured points after preparation of the capillary (dead time) was calculated and is listed in Table 11. The measured core radius increased over time from 12 nm to 14 nm, as well as the lattice constant a.

The last red scattering curve in Figure 72 can also be fitted with a vesicle form factor (black dashed curve) with a double layer thickness of 18.3 nm and an outer radius of 42 nm.

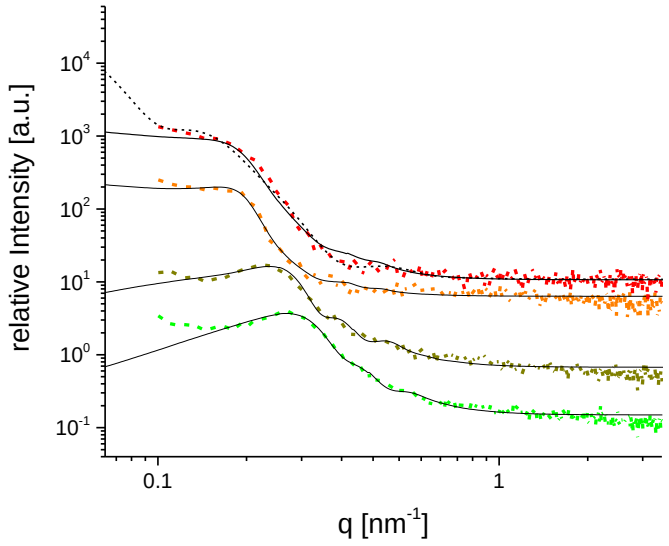

Figure 72. Time scan of 20 wt% PEG_{217}-(*b*)-PLA_{532} /dioxane in 1 mm glass capillary.

Table 11. Fit parameters of the time scan of 20 wt% PEG_{217}-(*b*)-PLA_{532} /dioxane in Figure 72

Measurement	time [min]	a [nm]	Δ [nm]	displ. [nm]	R_c [nm]
t_1	5.38	20.7	44.6	0.9	12.0
t_{37}	388	24.0	55.2	2.1	13.4
t_{54}	710	40.9	54.7	1.0	14.0
t_{100}	1193	41.6	43.4	1.6	13.9

Concentration gradient capillary measurements

So far, the kinetic experiments of PEG_{84}-(b)-PLA_{130} in the microfluidic channel revealed the formation of cylindrical micelles with a low degree of order during the self-assembly process. It was shown that the core radius increases during the reaction in the flow, as well as the unit cell dimension a. The time dependent capillary measurement for the large PEG_{217}-(*b*)-PLA_{532} diblock copolymer also showed a structural pathway over cylindrical micelles with a low degree of hexagonal ordering. Since for both block copolymers a final formation of vesicles is expected, due to the block length fractions of 0.39 for the PEG-block of PEG_{84}-(b)-PLA_{130} and 0.29 for the PEG-block of PEG_{217}-(*b*)-PLA_{532}, capillary concentration experiments were performed to obtain further information.

For the concentration gradient capillary experiments the PEG-(*b*)-PLA/dioxane solution of varied concentrations (20, 30, 40 wt%) were filled into the glass capillary and on top carefully water was located, to avoid convection. Then, the capillary was aligned vertically into the SAXS set-up. For all concentration scans, except for the 20 wt% PEG_{217}-(*b*)-PLA_{532} scan, the first measured point was slightly below the polymer solution/water interface, more in the polymer/dioxane region. The next points were scanned upwards the capillary into the water phase. The 20 wt% PEG_{217}-(*b*)-PLA_{532} concentration scan started in the water rich phase close to the interface and scanned towards the polymer/dioxane richer phase.

PEG_{84}-(b)-PLA_{130}

For the concentration scan of 20 wt% PEG_{84}-(*b*)-PLA_{130}/ dioxane topped with water, a step width of 500 µm was applied. Some of the performed measurements are depicted in Figure 73 (a). The measured curves, z_2, z_3, z_7, show a Bragg peak at $q \approx 0.16\ nm^{-1}$ ($d \approx 39\ nm$) and a weak form factor oscillation. All four curves were fitted to a hexagonal lattice, whereas the last red dashed curve z_{10}, shows less features. This is reflected in the lower mean crystalline domain size Δ compared to the other plotted curves, and is due to the dilution of the cylinders in water. In Table 12 the step width d of the respective measurement to the starting measurement point and the fitted parameters are listed. The core radius R_c decreases from 13.5 nm to 11.2 nm towards the water rich phase, which can be explained with the stronger segregation of the cylindrical micelles by effusion of dioxane into the water rich region.

The core radius for the 30 wt% and 40 wt% capillary measurements show an increase of the core radius, which can be explained with the higher possible uptake of dioxane due to the higher polymer concentration. The lattice constant a is of the same size for the first three measurements and increases in the last measurement due to the dilution in the water phase.

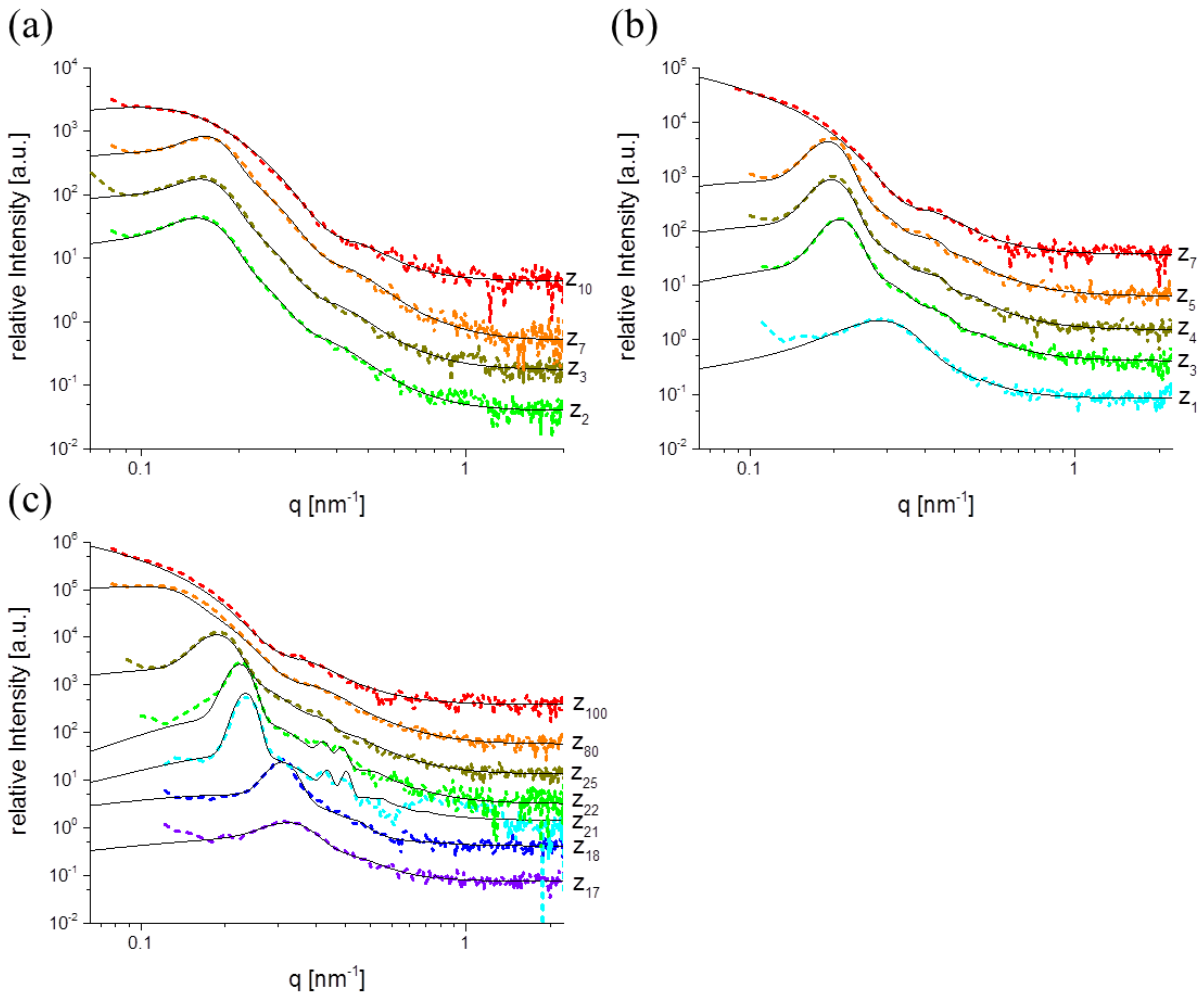

Figure 73. Concentration scan of (a) 20 wt%, (b) 30 wt% and (c) 40 wt% PEG_{84}-(*b*)-PLA_{130}/dioxane with water in 1 mm glass capillary of 10 µm wall thickness.

Table 12. Fit values for the 20 wt% PEG_{84}-PLA_{130}/dioxane /water SAXS measurements in a 1 mm glass capillary (d=10 µm) shown in Figure 73 (a).

Measurement	d [mm]	a [nm]	Δ [nm]	displ. [nm]	R_c [nm]
z_2	0.50	41.5	88.6	7.9	13.5
z_3	2.50	41.2	97.0	9.1	12.9
z_7	3.00	41.0	104.0	9.6	11.9
z_{10}	4.50	44.2	42.4	8.0	11.2

For the 30 wt%/wt PEG_{84}-(*b*)-PLA_{130}/ dioxane concentration scan a 100 µm step width was applied. Some selected curves are shown in Figure 73 (b) and the corresponding fit parameters are specified in Table 13. The first depicted bright blue curve in (b) shows a broad peak indicating weak segregation in the dioxane rich phase. All measurements of the 30 wt% PEG_{84}-(*b*)-PLA_{130}/ dioxane concentration scan were fitted to a hexagonal lattice, except the last red dashed curve, which was fitted to a cylinder form factor. The core radius increases from 9.8 nm to 14.2 nm. The consecutive measured curves (z_3, z_4, z_5) show a Bragg peak shifting from $q \approx 0.19\, nm^{-1}$ ($d \approx 33\, nm$) to $q \approx 0.18\, nm^{-1}$ ($d \approx 35\, nm$), as well as a weak from factor oscillation. This indicates that the diffusion of water led to stronger segregation. The formed cylinders start to order, which is increasing upwards in the capillary, towards the water region. However, the last shown curve z_7 has no higher order reflections and only a weak form factor oscillation at. This is again due to the dilution of the cylinders in the water rich phase.

Table 13. Fit values for the SAXS measurements of 30 wt% PEG_{84}-PLA_{130}/dioxane /water; in Figure 73 (b).

Measurement	d [mm]	R_c [nm]	a [nm]	Δ [nm]	displ. [nm]	R_c [nm]
z_1	0.00		22.7	41.9	1.8	9.8
z_3	0.20		35.8	115.0	2.2	13.8
z_4	0.30		37.7	114.0	3.4	13.8
z_5	0.40		38.6	116.0	4.3	13.9
z_7	0.60	14.2				

The 40 wt% PEG_{84}-(*b*)-PLA_{130}/dioxane solution in the concentration scan also undergoes an ordering into hexagonally packed cylinders, followed by dilution in the water rich phase and therefore, the loss of the order. The fits to a cylinder form factor and a hexagonal lattice show the increase of the core radius from 6.2 nm to 16.4 nm, which spans a large radius size range of the cylinders. This is due to the larger measured range of $d_{max} = 7.9\, mm$ compared to the $d_{max} = 0.6\, mm$ and $d_{max} = 4.5\, mm$ ranges of 30 wt% and 20 wt% respectively. The measurements z_{21}-z_{80} show narrow Bragg peaks, whereas z_{21} and z_{22} additionally have 3 higher order reflections. This higher order indicates well-ordered lyotropic phases of cylindrical micelles. The fits for the depicted measurements with HEX lattice or cylinder are listed in Table 14.

Table 14. Fit values for the 40 wt% PEG_{84}-PLA_{130}/dioxane/water SAXS measurements, shown in Figure 73 (c).

Measurement	d [mm]	R_c [nm]	a [nm]	Δ [nm]	displ. [nm]	R_c [nm]
z_{17}	1.60		22.9	53.5	4.8	6.2
z_{18}	1.70		25.8	98.5	4.3	6.9
z_{21}	2.00		34.7	160.0	1.0	13.5
z_{22}	2.10		39.1	98.3	0.01	13.2
z_{25}	2.40		39.0	117.0	3.9	14.6
z_{80}	7.90		52.7	125.0	17.3	15.1
z_{100}	9.90	16.4				

PEG_{217}-(b)-PLA_{532}

For the second used block copolymer, PEG_{217}-(*b*)-PLA_{532}, the 20 wt% concentration scan also reveals the formation of cylindrical particles at the polymer solution/water interface. The step width between the adjacent measured points was 250 µm and the scan started slightly more in the water rich region and led towards the polymer solution. The curves show a Bragg peak at $q \approx 0.20\, nm^{-1}$ ($d \approx 31\, nm$) and a weak oscillation for the measurements z_{17} and z_{19}. All curves were fitted to a hexagonal lattice and the obtained values are summarized in Table 15. The core radius increases from 11.0 nm in the polymer rich phase to 13.2 nm in the water region. The lattice constant increases with higher water content, as well as the curves show less features.

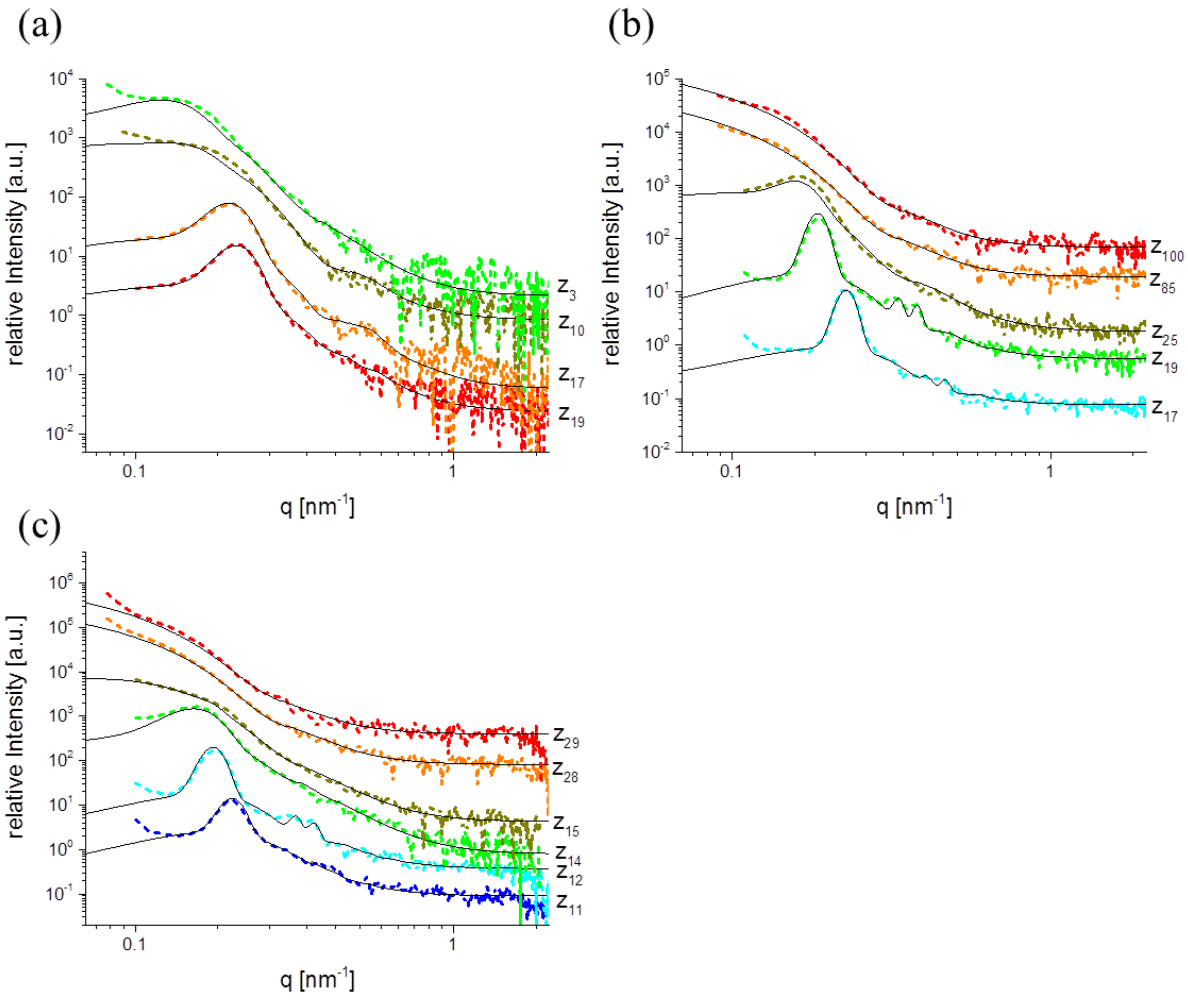

Figure 74. Concentration scan of (a) 20 wt%, (b) 30 wt% and (c) 40 wt% PEG_{217}-(*b*)-PLA_{532}/dioxane with water in 1 mm capillary with 10 µm wall thickness.

Table 15. Fit values of the 20 wt% PEG_{217}-(*b*)-PLA_{532}/dioxane with water SAXS measurements in a 1 mm capillary, shown in Figure 74 (a).

Measurement	d [mm]	a [nm]	Δ [nm]	displ. [nm]	Rc [nm]
z_{19}	5.00	32.1	90.8	4.1	11.0
z_{17}	4.00	33.8	89.8	5.1	10.7
z_{10}	2.25	44.9	293.0	21.4	10.3
z_{3}	0.50	47.1	81.0	10.9	13.2

The concentration scan with 30 wt% PEG_{217}-(*b*)-PLA_{532}, starts in the polymer region and proceeds towards the water region. The evolution is from hexagonally packed cylinders with reflections of the third order to dilute cylinders in the water region.

The higher order peaks indicate a well-ordered lyotropic phase. The cylinder radius increases from 11.9 nm to 15.0 nm along the scan to the water phase. The step width was 100 µm for adjoining measurements.

Table 16. Fit values of the 30 wt% PEG_{217}-(*b*)-PLA_{532}/dioxane/water SAXS measurements, shown in Figure 74 (b).

Measurement	d [mm]	R_c [nm]	a (nm):	Δ (nm):	displ. (nm):	Rc (nm):
z_{17}	1.60		31.0	172.0	1.4	11.9
z_{19}	1.90		37.9	199.0	1.1	14.9
z_{25}	2.40		41.0	112.0	9.2	13.4
z_{85}	8.40	14.5				
z_{100}	9.90	15.0				

For 40 wt% the evolution is similar to the concentration scan of the 30 wt% PEG_{217}-(*b*)-PLA_{532}/dioxane-water capillary. First the cylinders arrange hexagonally and then due to the higher water contain disorder. The cylinders radii grow from 14 nm to 17.3 nm. The step width was 500 µm between adjacent measurements.

Table 17. Fit values of 40 wt% PEG_{217}-(*b*)-PLA_{532} /dioxane Figure 74.

Measurement	d [mm]	R_c [nm]	a [nm]	Δ [nm]	displ. [nm]	R_c [nm]
z_{11}	5.00		34.6	154.0	1.4	14.0
z_{12}	5.50		39.6	178.0	1.2	15.7
z_{14}	6.50		40.7	89.0	4.5	15.4
z_{15}	7.00		39.6	184.0	16.8	15.1
z_{28}	13.50	16.5				
z_{29}	14.00	17.3				

To give an overview of the discussed results for the self-assembly process of PEG-(*b*)-PLA, the fit values of the core radius R_c and the lattice constant a are summarized in the following graphs. In Figure 75 the three microfluidic chip measurements of 20 wt% PEG_{84}-(*b*)-PLA_{130} are combined. a and R_c are plotted against Δd_A, which is the distance between the second channel cross and the measured position in the capillary. The Δd_A values for all three chip measurements of 20 wt% PEG_{84}-(*b*)-PLA_{130}/dioxane are listed in Table 18.

Table 18. Δd_A values of microfluidic chip measurements of A: [PEG_{84}-(*b*)-PLA_{130}/dioxane/H_2O: 1000 µl/h, middle buffer stream: 500 µl/h and remaining buffer streams: 100 µl/h], B: [PEG_{84}-(*b*)-PLA_{130}/dioxane /H_2O: 1000 µl/h, middle buffer stream: 400 µl/h, remaining streams: 63 µl/h], C: Polymer solution/H_2O: 1000 µl/h each, middle buffer stream: 100 µl/h, and remaining sheathing streams: 63 µl/h]

	A			**B**			**C**					
Position	1	1.5	4	1	5	6	1	2	3	4	5	6
Δd_A [mm]	8.03	10.53	28.03	13.41	33.41	38.41	13.41	18.41	23.41	28.41	33.41	38.41

The positions Δd_A in Figure 75 should only be compared to the different measured positions of one flow rate ratio, as the mixing and thus the self-assembly process is also dependent on the total flow rate and the flow rate ratios. However, Figure 75 demonstrates that for all measurements the core radius of the cylinder undergoes only minimum changes and also the lattice constant only increases slightly. This indicates that the self-assembly process starts with a fast formation of cylindrical micelles but the ordering and further structural changes like the formation of vesicles is slow and thus, is not observable from these microfluidic kinetic experiments.

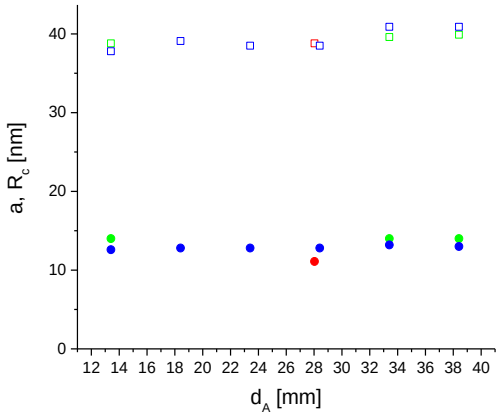

Figure 75. Structural evolution of 20 wt% PEG_{84}-(*b*)-PLA_{130} in the MF-chip. The different experiments (A/B: 1000 µl/h, M: 500 µl/h and B: 100 µl/h (red), A/B: 1000 µl/h, M: 400 µl/h and B: 63 µl/h (green), A/B: 1000 µl/h, M: 100 µl/h and B: 63 µl/h (blue) are plotted against the respective distance from the second channel cross to the measurement position. The unit cell dimension a (hollow squares) as well as the core radius R_c (spheres) are depicted.

Furthermore, all concentration gradient capillary measurements of both PEG-(*b*)-PLA block copolymers are represented in Figure 76.

The upper three graphs belong to the lower molecular weight PEG_{84}-(*b*)-PLA_{130} block copolymer and the lower three graphs showing the different concentrations of the higher molecular weight PEG_{217}-(*b*)-PLA_{532} block copolymer. All graphs, except the first red graph in the upper line, show an increase of the core radius R_c (filled spheres) and an increase of the unit cell dimension a (hollow squares) as the scan proceeds from the polymer solution rich phase towards the water rich phase. The first upper graph belongs to the 20 wt% PEG_{84}-(*b*)-PLA_{130} capillary scan, whereas the core radius decreases due to the stronger segregation in the water phase. The rightmost graph (dark blue) in the upper line summarizes the fits for the 40 wt% PEG_{84}-(*b*)-PLA_{130} capillary scan. The last two $R_c$values belong to diluted cylinder fits and thus, no unit cell dimension values were obtained.

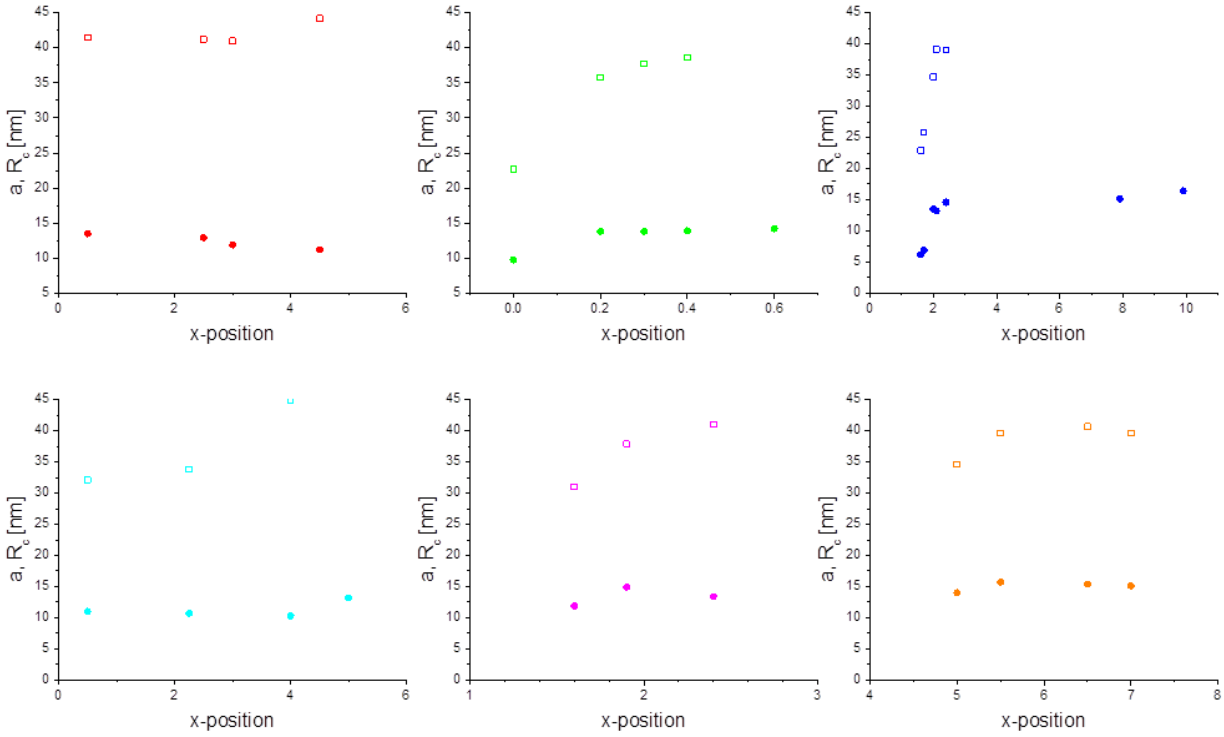

Figure 76. Summary of the fitted values for both PEG-(*b*)-PLA block copolymers in the capillary concentration scans. The first row shows the unit cell dimension a (hollow square) and the core radius R_c (sphere) of the PEG_{84}-(*b*)-PLA_{130} whereas red is the 20 wt%, green the 30 wt%, and dark blue the 40 wt% scan. In the second row the PEG_{217}-(*b*)-PLA_{532} concentration scan with the different concentrations (20 wt% bright blue, 30 wt% magenta, 40 wt% orange) and also for a and R_c is illustrated.

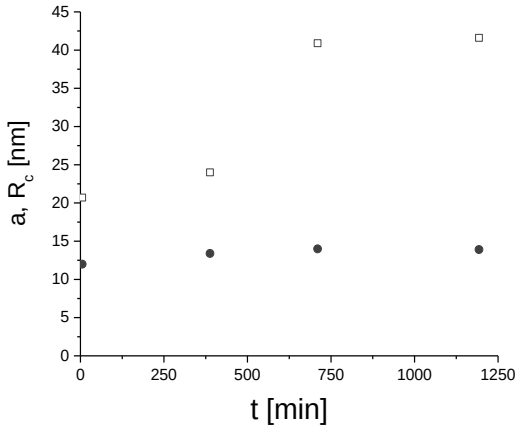

Figure 77. Outline of the 20 wt% PEG_{217}-(*b*)-PLA_{532} time dependent SAXS measurements.

The time dependent SAXS measurements of 20 wt% PEG_{217}-(*b*)-PLA_{532} in a 1 mm glass capillary are summarized in Figure 77. The time scan shows a more intense increase of the unit cell dimension compared to the previous discussed results. This is due to the long time range at, which this measurement was performed. However, the core radius of the cylindrical micelles only increases little from 10 nm to 14 nm.

All measurements show that PEG-(*b*)-PLA block copolymer undergo a self-assembly to cylindrical micelles. The microfluidic chip measurements demonstrate that this micelle formation is a fast reaction. The capillary concentration measurements depict that on longer time scales the cylinder order into a hexagonal lattice, which becomes more pronounced at higher concentrations.

4.5.1.3 Cryogenic Transmission Electron Microscopy Measurements

Both PEG-(b)-PLA block copolymers are expected to form vesicles because of the relative block length, with a shorter hydrophilic PEG-block. The fraction for the PEG-block of PEG_{84}-(b)-PLA_{130} is 0.39 and for PEG_{217}-(*b*)-PLA_{532} it is 0.29. Therefore, the conventional reverse phase evaporation method for vesicle preparation was used, to obtain longer time periods and analyzed it with cryo-TEM. Therefore, the samples were dropped onto a lacey TEM grid and immediately vitrified in liquid ethane. This procedure was performed in a controlled environmental vitrification system (CEVS). The shock frozen sample was brought with a cryo transfer holder into the LEO EM922 Omega TEM (Zeiss). The acceleration voltage of the EM922 Omega is 200 kV.

PEG_{84}-(*b*)-PLA_{130}

For cryo-TEM measurements the PEG_{84}-(*b*)-PLA_{130} polymer was dissolved in chloroform. Then, water was added and the solution was stirred and heated at 60 °C for three days. An opening in the sample vial lid allowed chloroform to evaporate slowly. The cryo-TEM images of the reverse phase evaporation samples were taken after filtration with a membrane filter.

The images in Figure 78 show the self-assembled structures after phase evaporation of PEG_{84}-(*b*)-PLA_{130}. Besides spherical micelles, with an average radius of 24.69 nm, also small vesicles (red arrows) and giant “jellyfish” like structures are found. The thickness of the cylindrical arms is 24.66 nm, which is in good agreement with the obtained radius in the capillary experiment. The double layer of the vesicles has an average thickness of 18.11 nm.

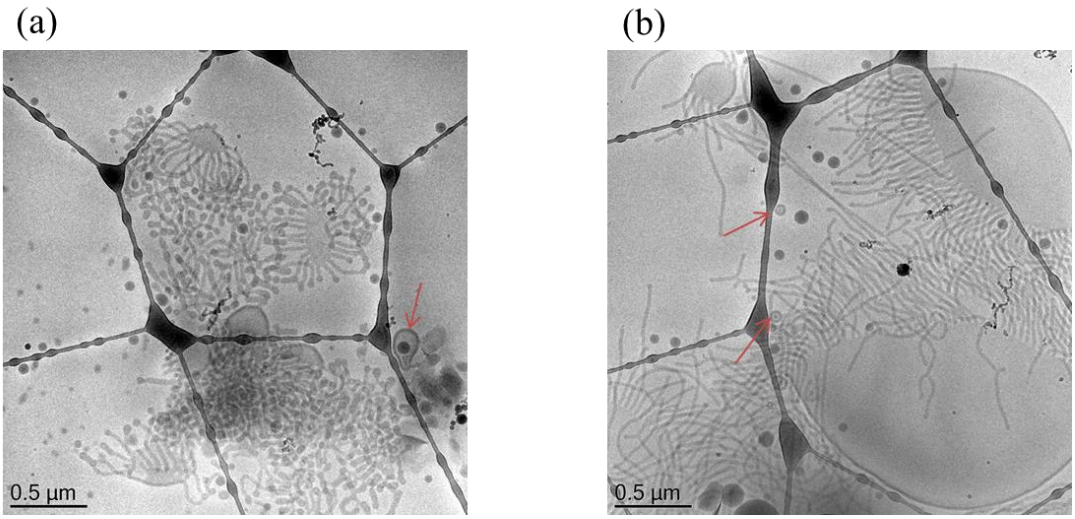

Figure 78. Cryo-TEM images of PEG_{84}-(*b*)-PLA_{130} after reverse phase evaporation.

PEG_{217}-(*b*)-PLA_{532}

The PEG_{217}-(*b*)-PLA_{532} block-co-polymer was also analyzed with Cryo-TEM. The sample was prepared with reverse phase evaporation as described above.

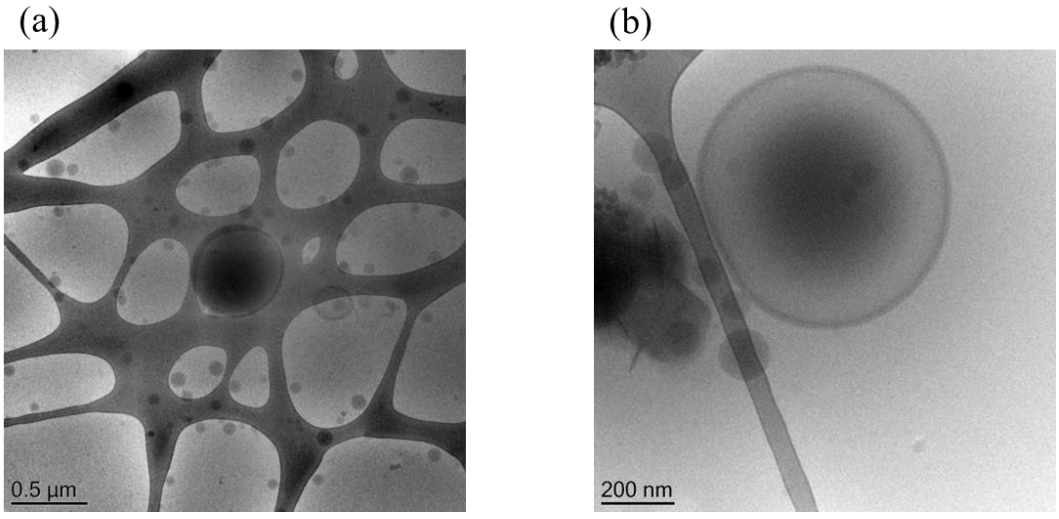

Figure 79. Cryo-TEM of PEG_{217}-(*b*)-PLA_{532} after reverse phase evaporation.

The filtrated sample, shown in Figure 79 (a) and (b), contained micelles of different sizes and few vesicles. Also, the unfiltered sample was analyzed in cryo-TEM to make sure that the large vesicles were filtered out. The non-filtered sample of PEG_{217}-(*b*)-PLA_{532} also shows micelles of different sizes, more vesicles and cylindrical micelles.

The analyzed spheres of the filtrated sample show size variations from 16.49 nm to 66.80 nm of radius. The average spherical radius is 34.16 nm. The vesicle double layer has an average thickness of 18.78 nm, which is in good agreement with the thickness obtained from the time dependent capillary measurement.

Conclusion

The kinetics of the self-assembly process of biocompatible PEG-(*b*)-PLA block copolymers of two different molecular weights were investigated. With the microfluidic chip experiments, the fast self-assembly of the block copolymer into cylindrical micelles was shown. Longer timescale investigations were possible with time dependent capillary measurements or with concentration gradient capillary measurements. For the larger molecular weight PEG_{217}-(*b*)-PLA_{532} the time dependent experiment in the capillary showed a structural evolution from cylindrical micelles to eventually vesicles, which could be followed over 19 hours. Concentration gradient measurements in the glass capillary showed the slight growth of the core radius of the cylindrical micelles for scans proceeding from the polymer/dioxane phase to the water phase. The lattice constant also increased in this scanning direction. Compared to the time dependent capillary measurement, the lattice constant increased only little, which indicates the slow evolution of vesicles. Cryo-TEM measurements of the reverse phase evaporation preparation method were made for both PEG-(*b*)-PLA block copolymers. They confirmed the expected formation of vesicles. PEG_{84}-(*b*)-PLA_{130} showed a coexistence of spherical and cylindrical micelles, as well as giant “jellyfish” like structures and small vesicles. The obtained values for the thickness of the cylinders were in good agreement with the SAXS measurements. For the larger PEG_{217}-(*b*)-PLA_{532} only few vesicles were obtained besides spherical micelles of various sizes.

5 Conclusion and Outlook

In this dissertation different microfluidic device materials were tested against solvent resistance and their possible application in small angle X-ray scattering. For different analyzed self-assembly systems either NOA81 based chips were fabricated for water based systems or if organic solvents like dioxane or THF were applied, perfluorinated chips like THV or SIFEL were used. The microfluidic chips were then applied to analyze self-assembly processes *in-situ* with SAXS.

First, the structural evolution of two surfactants (LPFO, TDMAO) with concentrations above their CMC was investigated. For the continuous flow measurements, a simple chip design with a perpendicular channel cross and a long meander was used. At the high brilliance synchrotron beamline with its small beam dimension of x= 3 µm and y= 4 µm, a raster scanning of the NOA81 based chip with a width of $\sim 200\ \mu m$ could be performed, getting a spot size of 10 µm x 10 µm. This revealed, that already at first contact of LPFO and TDMAO a new structure assembled. At the interface in the channel mixing cross, the cylindrical micelles (TDMAO) and the spherical micelles (LPFO) fuse to form disk-like micelles. Simulations and calculations showed that the disk formation is a diffusion limited process and that the disk-like micelles fuse with a 1:1 stoichiometric composition of the LPFO spherical micelles and the TDMAO cylindrical micelles. The disks grow further via fusion and develop a larger lateral dimension, which results in a lamellar correlation. Furthermore, experiments in the glass capillary with LPFO at the bottom and TDMAO on top were investigated to observe a larger time scale. The capillary interdiffusion experiment was performed over ten days. The measurements indicated a different structural pathway compared to the fast microfluidic experiment. In the capillary experiment the original LPFO sphere peak shifted to lower q-values. Then, the peak narrowed and showed a second order reflection, before it broadened with further shifting to lower q-values. In the microfluidic experiment the sphere peak stayed constant and only the intensity decreased. At later stages a shoulder at $q^{*}{\sim}0.3\ nm^{-1}$ was observed until finally a featureless scattering curve was measured. Consequently, both pathways show the formation of disk-like micelles, whereas the slow capillary experiment showed first the formation of non-stoichiometric and LPFO-rich micelles.

The aggregation number of the micelles increased and thus, the intermicellar distances increased as well, leading to a gradual shift of the scattering peak. Eventually, disk-like micelles with 1:1 stoichiometry and large lateral dimensions developed and showed an equidistant lamellar peak at $q = 0.4\,nm^{-1}$. Finally, the solution mixed in the microfluidic chip was collected and measured with cryo-TEM. The cryo-TEM images showed uni- and multilamellar vesicles with interlamellar distances in agreement with the measured SAXS data and disks with sizes comparable with the SAXS experiments. Furthermore, the calculations and simulations showed the disadvantage of the two-dimensional chip design, due to the no-slip-boundary condition in microfluidics.

Thereupon, a more sophisticated channel design was developed for the analyzation of two different diblock copolymers, considering the no-slip boundary condition in microfluidic chips. Therefore, a 3D flow focusing device was designed with six sheathing streams avoiding wall contact of the reagents with the channel walls. For the realization of the 3D flow focusing two chip halves had to be structured and aligned. In extension of the main channel a glass capillary was located, which led to a hybrid chip with low background scattering in SAXS, due to the thin walled glass capillary. An additional buffer stream between the reagents A and B allowed the adjustment of the mixing position in the channel. Since the mixing is only diffusive the buffer stream thickness limits the diffusion time. Consequently, the start of the reaction could be transferred to a position in the glass capillary. The used solvent for the kinetics investigation of the diblock copolymers was dioxane. Hence, a solvent resistant chip material was needed, e.g. a perfluorinated polymer. SIFEL was chosen over THV because of the easier fabrication of three-dimensional MF devices. Furthermore, the new chip design led to a parallel flow of the two reactants. This parallel flow has a better spatial resolution in SAXS y-scans, than concentrically flowing streams. This improved spatial resolution was demonstrated with SAXS measurements vertical to the channel flow. The two single reagent streams and the reaction progress at each point in the vertical direction (y-scan) could be followed. The flow was proofed with CLSM. In the microfluidic hybrid chip the reagents stream A, a Ca^{2+} buffer solution, and stream B, Ca-Green, a Ca^{2+} sensitive dye showing increasing fluorescence in presence of Ca^{2+}were mixed. In the remaining streams a buffer solution was pumped in. Eventually, SAXS measurements proofed the enhanced measurement quality of the SIFEL-glass-capillary-hybrid chip compared to the thin polyimide based devices.

The new developed and tested chip design was then used to investigate the self-assembly process of the PI_{70}-(*b*)-PEO_{60} block copolymer. Microfluidic chip measurements of different flow rate ratios and total flow rates revealed the formation of spherical micelles in the first 10 milliseconds after mixing. The micelles started to order in a face centered cubic (FCC) lattice after 0.77 s and the FCC-lattice got more pronounced with the evolution of the reaction. The SIFEL-glass-capillary-hybrid chip was compared to continuous flow measurements in a polyimide based microfluidic chip. The structural evolution to spherical micelles in the polyimide chip was comparable, but the hybrid chip showed an enhanced quality of the SAXS measurements with the appearance of higher order reflections. Furthermore, capillary concentration scan SAXS measurements of 20 wt% PI_{70}-(*b*)-PEO_{60}/dioxane showed a longer period of the self-assembly process. An evolution from a weak segregated Leibler peak in the dioxane phase to a highly ordered FCC-lattice and the disorder due to dilution in the water phase was observed. Eventually, cryo-TEM measurement of the collected sample after mixing in the microfluidic channel and samples, prepared with reverse phase evaporation, showed the coexistence of spherical micelles, cylindrical micelles, vesicles and "jellyfish"-like intermediate structures.

Finally, the self-assembly kinetics of two PEG-(*b*)-PLA block copolymers with different molecular weights were studied. Microfluidic continuous flow experiments showed the fast evolution of cylindrical micelles. For the PEG-(*b*)-PLA block copolymer with lower molecular weight different flow rates and flow rate ratios were analyzed and showed only a slight increase of the core radius, as well as of the lattice constant. Since the PEG-(*b*)-PLA block copolymer with the higher molecular weight showed no change in the microfluidic experiments, an additional time dependent capillary experiment was performed. The capillary time scan showed an evolution from cylindrical micelles to vesicles over 19 hours. For the investigation of longer time scales concentration gradient SAXS measurements in the capillary were carried out. For the SAXS measurements of the PEG_{217}-(*b*)-PLA_{532} block copolymer in the glass capillary, an increase of the core radius and the unit cell dimension for all concentrations (20 wt%, 30 wt%, 40 wt%) was observed. The PEG_{84}-(*b*)-PLA_{130} block copolymer SAXS measurements in the glass capillary also showed an increase of the lattice constant for all measurements, but the core radius only increased for the 30 wt% and 40 wt% PEG_{84}-(*b*)-PLA_{130}/dioxane solution due to interdiffusion with water.

The 20 wt% PEG_{84}-(*b*)-PLA_{130}/dioxane/water capillary scan showed a slight decrease of the core radius, due to the effusion of dioxane into the water phase and thus, a stronger segregation of the micellar core. Cryo-TEM measurements showed the coexistence of spherical and cylindrical micelles, as well as the expected appearance of vesicles, due to the block length ratio of the block copolymer.

In this work it was shown that microfluidics combined with small angle X-ray scattering is a powerful method to analyze fast reactions and to follow structural evolutions over different time spans. However, the method was not pushed to its limits. With a small beamsize as realized at microfocus beamlines at synchrotron facilities and with higher flow rates, temporal resolutions in the sub-millisecond region can be obtained. Furthermore, new chip designs can improve the quality of the SAXS measurements for weak scattering sample. Due to the needed sheathing streams the sample is diluted, which can lead to a weak scattering intensity.

References

(1) Kunz, W., Kellermeier, M. Materials science. Beyond biomineralization. *Science (New York, N.Y.)* **2009**, *323*, 344–345.

(2) Polte, J., Erler, R., Thünemann, A. F., Sokolov, S., Ahner, T. T., Rademann, K., Emmerling, F., Kraehnert, R. Nucleation and Growth of Gold Nanoparticles Studied viain situ Small Angle X-ray Scattering at Millisecond Time Resolution. *ACS Nano* **2010**, *4*, 1076–1082.

(3) Antonietti, M., Ozin, G. A. Promises and Problems of Mesoscale Materials Chemistry or Why Meso? *Chem. Eur. J.* **2004**, *10*, 28–41.

(4) Philp, D., Stoddart, J. F. Self-Assembly in Natural and Unnatural Systems. *Angew. Chem. Int. Ed. Engl.* **1996**, *35*, 1154–1196.

(5) Whitesides, G. M. Self-Assembly at All Scales. *Science* **2002**, *295*, 2418–2421.

(6) Stephan Förster, Markus Antonietti. Amphiphilic Block Copolymers in Structure-Controlled Nanomaterial Hybrids. *Advanced Materials* **1998**, 195–217.

(7) Kronberg B., Holmberg K., Lindman B. *Surface chemistry of surfactants and polymers*; Wiley: Chichester, West Sussex, 2014.

(8) mHamley I. W. *Introduction to soft matter: Synthetic and biological self-assembling materials*; John Wiley & Sons: Chichester, England, Hoboken, NJ, 2007.

(9) Schacher, F. H., Rupar, P. A., Manners, I. Funktionale Blockcopolymere: Nanostrukturierte Materialien mit neuen Anwendungsmöglichkeiten. *Angew. Chem.* **2012**, *124*, 8020–8044.

(10) Blanazs, A., Armes, S. P., Ryan, A. J. Self-Assembled Block Copolymer Aggregates: From Micelles to Vesicles and their Biological Applications. *Macromolecular rapid communications* **2009**, *30*, 267–277.

(11) Abetz V., Ed. *Block Copolymers II*; Springer-Verlag: Berlin/Heidelberg, 2005.

(12) Bates, F. S., Fredrickson, G. H. Block Copolymer Thermodynamics: Theory and Experiment. *Annu. Rev. Phys. Chem.* **1990**, *41*, 525–557.

(13) Lombardo, D., Kiselev, M. A., Magazù, S., Calandra, P. Amphiphiles Self-Assembly: Basic Concepts and Future Perspectives of Supramolecular Approaches. *Advances in Condensed Matter Physics* **2015**, *2015*, 1–22.

(14) Xia, Y., Whitesides, G. M. SOFT LITHOGRAPHY. *Annu. Rev. Mater. Sci.* **1998**, *28*, 153–184.

(15) Fredrickson, G. H., BATES, F. S. Dynamics of Block Copolymers: Theory and Experiment. *Annu. Rev. Mater. Sci.* **1996**, *26*, 501–550.

(16) Leibler, L. Theory of Microphase Separation in Block Copolymers. *Macromolecules* **1980**, *13*, 1602–1617.

(17) Förster, S., Plantenberg, T. From Self-Organizing Polymers to Nanohybrid and Biomaterials. *Angewandte Chemie* **2002**, 688–714.

(18) Förster, S., Antonietti, M. Amphiphilic Block Copolymers in Structure- Controlled Nanomaterial Hybrids. *Adv. Mater.* **1998**, 195–217.

(19) Nagarajan, R., Ruckenstein, E. Theory of surfactant self-assembly: a predictive molecular thermodynamic approach. *Langmuir* **1991**, *7*, 2934–2969.

(20) Israelachvili, J. N., Mitchell, D. J., Ninham, B. W. Theory of self-assembly of hydrocarbon amphiphiles into micelles and bilayers. *J. Chem. Soc., Faraday Trans. 2* **1976**, *72*, 1525.

(21) Antonietti, M., Förster, S. Vesicles and Liposomes: A Self-Assembly Principle Beyond Lipids. *Adv. Mater.* **2003**, *15*, 1323–1333.

(22) Israelachvili J. N. *Intermolecular and surface forces*, 3rd ed.; Academic Press: Burlington, MA, 2011.

(23) Zhang, L., Eisenberg, A. Multiple Morphologies of "Crew-Cut" Aggregates of Polystyrene-b-poly(acrylic acid) Block Copolymers. *Science (New York, N.Y.)* **1995**, *268*, 1728–1731.

(24) Du, J., O'Reilly, R. K. Advances and challenges in smart and functional polymer vesicles. *Soft Matter* **2009**, *5*, 3544.

(25) Yamamoto, S., Maruyama, Y., Hyodo, S.-a. Dissipative particle dynamics study of spontaneous vesicle formation of amphiphilic molecules. *J. Chem. Phys.* **2002**, *116*, 5842.

(26) He, X., Schmid, F. Dynamics of Spontaneous Vesicle Formation in Dilute Solutions of Amphiphilic Diblock Copolymers. *Macromolecules* **2006**, *39*, 2654–2662.

(27) Shum, H. C., Kim, J.-W., Weitz, D. A. Microfluidic fabrication of monodisperse biocompatible and biodegradable polymersomes with controlled permeability. *Journal of the American Chemical Society* **2008**, *130*, 9543–9549.

(28) Matsen, M. W., BATES, F. S. Unifying Weak- and Strong-Segregation Block Copolymer Theories. *Macromolecules* **1996**, *29*, 1091–1098.

(29) Kleinstreuer C. *Theory*; John Wiley & Sons, Inc, 2013. http://onlinelibrary.wiley.com/doi/10.1002/9781118749890.ch1/pdf.

(30) Bruus H. *Theoretical microfluidics*; Oxford University Press: Oxford, 2008.

(31) Manz, A., Verpoorte, E., Raymond, D. E., Effenhauser, C. S., Burggraf, N., Widmer, H. M. µ-TAS: Miniaturized Total Chemical Analysis Systems. In *Micro Total Analysis Systems: Proceedings of the [mu]TAS '94 Workshop, held at MESA Research Institute, University of Twente, the Netherlands, 21-22 November 1994*; Berg, A., Bergveld, P., Eds.; Springer Netherlands; Imprint; Springer: Dordrecht, 1995, pp. 5–27.

(32) Stone, H. A., Stroock, A. D., Ajdari, A. ENGINEERING FLOWS IN SMALL DEVICES. *Annual Review of Fluid Mechanics* **2004**, *36*, 381–411.

(33) Beebe, D. J., Mensing, G. A., Walker, G. M. Physics and Applications of Microfluidics in Biology. *Annu. Rev. Biomed. Eng.* **2002**, *4*, 261–286.

(34) Batchelor G. K. *An introduction to fluid dynamics,* 2nd ed.; Cambridge University Press: Cambridge, U.K., New York, NY, 1999.

(35) Tabeling P. *Introduction to microfluidics*; Oxford University Press: Oxford, New York, 2010.

(36) Kumacheva E., Garstecki P. *Microfluidic reactors for polymer particles*; Wiley: Hoboken, N.J., 2011.

(37) Kirby B. J. *Micro- and nanoscale fluid mechanics: Transport in microfluidic devices*; Cambridge Univ. Press: Cambridge, 2010.

(38) Phillips, R., Kondev, J., Theriot, J., *Physical biology of the cell;* Garland Science Books, 2009.

(39) Rathakrishnan E. *Fluid mechanics: An introduction,* 3rd ed.; PHI Learning: New Delhi, 2012.

(40) Squires, T. M., Quake, S. R. Microfluidics: Fluid physics at the nanoliter scale. *Rev. Mod. Phys.* **2005**, *77*, 977–1026.

(41) Richardson, S. On the no-slip boundary condition. *J. Fluid Mech.* **1973**, *59*, 707.

(42) Bocquet, L., Barrat, J.-L. Hydrodynamic boundary conditions and correlation functions of confined fluids. *Phys. Rev. Lett.* **1993**, *70*, 2726–2729.

(43) Lauga, E., Brenner, M., Stone, H. Microfluidics: The No-Slip Boundary Condition. In *Springer handbook of experimental fluid mechanics*; Tropea, C., Yarin, A. L., Foss, J. F., Eds.; Springer Science+Business Media: Berlin, 2007, pp. 1219–1240.

(44) Avila, K., Moxey, D., Lozar, A. de, Avila, M., Barkley, D., Hof, B. The onset of turbulence in pipe flow. *Science (New York, N.Y.)* **2011**, *333*, 192–196.

(45) Brody, J. P., Yager, P., Goldstein, R. E., Austin, R. H. Biotechnology at low Reynolds numbers. *Biophysical Journal* **1996**, *71*, 3430–3441.

(46) Bird R. B., Stewart W. E., Lightfoot E. N. *Transport phenomena*, 2nd ed.; J. Wiley: New York, 2007.

(47) Atencia, J., Beebe, D. J. Controlled microfluidic interfaces. *Nature* **2005**, *437*, 648–655.

(48) Capretto, L., Cheng, W., Hill, M., Zhang, X. Micromixing Within Microfluidic Devices. In *Microfluidics: Technologies and applications*; Lin, B., Basuray, S., Eds.; Springer: Berlin, New York, 2011; Vols. 304, pp. 27–68.

(49) Atkins P. W., Paula J. de. *Physikalische Chemie*, 4th ed.; Wiley-VCH: Weinheim, 2006.

(50) Qin, D., Xia, Y., Whitesides, G. M. Rapid prototyping of complex structures with feature sizes larger than 20 ?: M. *Adv. Mater.* **1996**, *8*, 917–919.

(51) Nguyen N.-T. *Mikrofluidik: Entwurf, Herstellung und Charakterisierung ; mit 12 Tabellen und 37 Beispielen*, 1st ed.; Teubner: Stuttgart, Leipzig, Wiesbaden, 2004.

(52) Duffy, D. C., McDonald, J. C., Schueller, Olivier J. A., Whitesides, G. M. Rapid Prototyping of Microfluidic Systems in Poly(dimethylsiloxane). *Anal. Chem.* **1998**, *70*, 4974–4984.

(53) Wilbur, J. L., Kumar, A., Kim, E., Whitesides, G. M. Microfabrication by microcontact printing of self-assembled monolayers. *Adv. Mater.* **1994**, *6*, 600–604.

(54) Kim, E., Xia, Y., Whitesides, G. M. Micromolding in Capillaries: Applications in Materials Science. *J. Am. Chem. Soc.* **1996**, *118*, 5722–5731.

(55) Qi, S., Liu, X., Ford, S., Barrows, J., Thomas, G., Kelly, K., McCandless, A., Lian, K., Goettert, J., Soper, S. A. Microfluidic devices fabricated in poly(methyl methacrylate) using hot-embossing with integrated sampling capillary and fiber optics for fluorescence detection. *Lab Chip* **2002**, *2*, 88.

(56) Morra, M., Occhiello, E., Marola, R., Garbassi, F., Humphrey, P., Johnson, D. On the aging of oxygen plasma-treated polydimethylsiloxane surfaces. *Journal of Colloid and Interface Science* **1990**, *137*, 11–24.

(57) Heckele, M., Bacher, W., Müller, K. D. Hot embossing - The molding technique for plastic microstructures. *Microsystem Technologies* **1998**, *4*, 122–124.

(58) Becker, H., Heim, U. Hot embossing as a method for the fabrication of polymer high aspect ratio structures. *Sensors and Actuators A: Physical* **2000**, *83*, 130–135.

(59) Zhao, X.-M., Xia, Y., Whitesides, G. M. Fabrication of three-dimensional micro-structures: Microtransfer molding. *Adv. Mater.* **1996**, *8*, 837–840.
(60) Glatter O., Ed. *Small angle X-ray scattering*, 2nd ed.; Acad. Pr: London, 1983.
(61) Stribeck N. *X-ray scattering of soft matter*; Springer: Berlin, New York, 2007.
(62) Guinier A. *X-ray diffraction* ; Dover: New York, 1963.
(63) Lindner P., Zemb T. *Neutrons, X-rays, and light: Scattering methods applied to soft condensed matter*, 1st ed.; Elsevier: Amsterdam, Boston, 2002.
(64) Lifshin E. *X-ray characterization of materials*; Wiley-VCH: Weinheim, New York, 1999.
(65) Svergun D. I., Feĭgin L. A., Taylor G. W. *Structure analysis by small-angle x-ray and neutron scattering*; Plenum Press: New York, 1987.
(66) Brumberger H. *Modern aspects of small-angle scattering*; Kluwer Academic Publishers: Dordrecht, Boston, 1995.
(67) Debye, P., Bueche, A. M. Scattering by an Inhomogeneous Solid. *J. Appl. Phys.* **1949**, *20*, 518.
(68) Dulle M. *Incorporation of Internally Self AssembledParticles into Polymeric Layer by Layer Systems and other Advanced Materials*: Graz, 2012.
(69) Falta J., Möller T. *Forschung mit Synchrotronstrahlung: Eine Einführung in die Grundlagen und Anwendungen*; Vieweg+Teubner Verlag, 2010.
(70) Förster, S., Fischer, S., Zielske, K., Schellbach, C., Sztucki, M., Lindner, P., Perlich, J. Calculation of scattering-patterns of ordered nano- and mesoscale materials. *Advances in Colloid and Interface Science* **2011**, *163*, 53–83.
(71) Förster, S., Timmann, A., Konrad, M., Schellbach, C., Meyer, A., Funari, S. S., Mulvaney, P., Knott, R. Scattering curves of ordered mesoscopic materials. *The journal of physical chemistry. B* **2005**, *109*, 1347–1360.
(72) Deutsches Elektronen-Synchrotron DESY. *PETRA III*. http://petra3.desy.de/. Accessed 17 June 2016.
(73) *Accelerators*. http://www.esrf.eu/Accelerators/Accelerators. Accessed 17 June 2016.
(74) Zeinolebadi A. *In-situ Small-Angle X-ray Scattering Investigation of Transient Nanostructure of Multi-phase Polymer Materials Under Mechanical Deformation*; Springer Berlin Heidelberg: Berlin, Heidelberg, 2013.
(75) Williams D. B., Carter C. B. *Transmission electron microscopy: A textbook for materials science*, 2nd ed.; Springer: New York, 2009.

(76) Prasad, V., Semwogerere, D., Weeks, E. R. Confocal microscopy of colloids. *J. Phys.: Condens. Matter* **2007**, *19*, 113102.

(77) Michler G. H. *Electron Microscopy of Polymers*; Springer Berlin Heidelberg, 2008.

(78) Sheppard C., Shotton D. *Confocal laser scanning microscopy*; BIOS Scientific Publishers; Springer: Oxford, UK, New York, NY, USA, 1997.

(79) Lichtman, J. W., Conchello, J.-A. Fluorescence microscopy. *Nature methods* **2005**, *2*, 910–919.

(80) Webb, R. H. Confocal optical microscopy. *Rep. Prog. Phys.* **1996**, *59*, 427–471.

(81) Milne, J. L. S., Borgnia, M. J., Bartesaghi, A., Tran, E. E. H., Earl, L. A., Schauder, D. M., Lengyel, J., Pierson, J., Patwardhan, A., Subramaniam, S. Cryo-electron microscopy - a primer for the non-microscopist. *FEBS J* **2013**, *280*, 28–45.

(82) Shindō D., Oikawa T. *Analytical electron microscopy for materials science*; Springer: Tokyo, Berlin, 2002.

(83) Thomas S., Shanks R., Chandrasekharakurup S. *Design and applications of nanostructured polymer blends and nanocomposite systems*; William Andrew: Oxford, UK, 2015.

(84) Kuehlbrandt, W. Cryo-EM enters a new era. *eLife* **2014**, *3*, e01963.

(85) Frederik, P. M., Sommerdijk, N. Spatial and temporal resolution in cryo-electron microscopy—A scope for nano-chemistry. *Current Opinion in Colloid & Interface Science* **2005**, *10*, 245–249.

(86) Design & Programming 2008/2009: Stephanie S. Roth. *Elektronenmikroskopie*, 2009. http://www.bimf.uni-bayreuth.de/de/facilities/electron_microscopy/index.html. Accessed 21 June 2016.

(87) Wesseling P. *Principles of Computational Fluid Dynamics*; Springer Berlin Heidelberg: Berlin, Heidelberg, 2001.

(88) Geschke O., Klank H., Tellemann P. *Microsystem engineering of lab-on-a-chip devices*; Wiley-VCH: Weinheim, 2004.

(89) Chung T. J. *Computational fluid dynamics*, 2nd ed.; Cambridge University Press: Cambridge, New York, 2010.

(90) Lee, J. N., Park, C., Whitesides, G. M. Solvent Compatibility of Poly(dimethylsiloxane)-Based Microfluidic Devices. *Anal. Chem.* **2003**, *75*, 6544–6554.

(91) Maltezos, G., Garcia, E., Hanrahan, G., Gomez, F. A., Vyawhare, S., van Dam, R. Michael, Chen, Y., Scherer, A. Design and fabrication of chemically robust three-dimensional microfluidic valves. *Lab Chip* **2007**, *7*, 1209.

(92) Begolo, S., Colas, G., Viovy, J.-L., Malaquin, L. New family of fluorinated polymer chips for droplet and organic solvent microfluidics. *Lab Chip* **2011**, *11*, 508.

(93) Delamarche, E., Schmid, H., Michel, B., Biebuyck, H. Stability of molded polydimethylsiloxane microstructures. *Adv. Mater.* **1997**, *9*, 741–746.

(94) Bressel, K., Prevost, S., Appavou, M.-S., Tiersch, B., Koetz, J., Gradzielski, M. Phase behaviour and structure of zwitanionic mixtures of perfluorocarboxylates and tetradecyldimethylamine oxide—dependence on chain length of the perfluoro surfactant. *Soft Matter* **2011**, *7*, 11232.

(95) Bressel K. *Controlling vesicle systems by amphiphilic copolymers*; Technische Universität Berlin, 2014.

(96) Weiss, T., Narayanan, T., Wolf, C., Gradzielski, M., Panine, P., Finet, S., Helsby, W. Dynamics of the Self-Assembly of Unilamellar Vesicles. *Phys. Rev. Lett.* **2005**, *94*.

(97) Weiss, T. M., Narayanan, T., Gradzielski, M. Dynamics of Spontaneous Vesicle Formation in Fluorocarbon and Hydrocarbon Surfactant Mixtures. *Langmuir* **2008**, *24*, 3759–3766.

(98) Gummel, J., Sztucki, M., Narayanan, T., Gradzielski, M. Concentration dependent pathways in spontaneous self-assembly of unilamellar vesicles. *Soft Matter* **2011**, *7*, 5731.

(99) With, S., Trebbin, M., Bartz, Christian B. A., Neuber, C., Dulle, M., Yu, S., Roth, S. V., Schmidt, H.-W., Förster, S. Fast Diffusion-Limited Lyotropic Phase Transitions Studied in Situ Using Continuous Flow Microfluidics/Microfocus-SAXS. *Langmuir* **2014**, *30*, 12494–12502.

(100) ESRF. *FReLoN*. http://www.esrf.eu/Instrumentation/DetectorsAndElectronics/frelon. Accessed 28 July 2016.

(101) Ng, J. D., Gavira, J. A., García-Ruíz, J. M. Protein crystallization by capillary counterdiffusion for applied crystallographic structure determination. *Journal of Structural Biology* **2003**, *142*, 218–231.

(102) Griesche, A., Zhang, B., Solorzano, E., Garcia-Moreno, F. Note: X-ray radiography for measuring chemical diffusion in metallic melts. *The Review of scientific instruments* **2010**, *81*, 56104.

(103) Ujihara, T., Fujiwara, K., Sazaki, G., Usami, N., Nakajima, K. New method for measurement of interdiffusion coefficient in high temperature solutions based on Fick's first law. *Journal of Crystal Growth* **2002**, *241*, 387–394.

(104) Hood, R. R., DeVoe, D. L., Atencia, J., Vreeland, W. N., Omiatek, D. M. A facile route to the synthesis of monodisperse nanoscale liposomes using 3D microfluidic hydrodynamic focusing in a concentric capillary array. *Lab on a chip* **2014**, *14*, 2403–2409.

(105) Gambin, Y., Simonnet, C., VanDelinder, V., Deniz, A., Groisman, A. Ultrafast microfluidic mixer with three-dimensional flow focusing for studies of biochemical kinetics. *Lab Chip* **2010**, *10*, 598–609.

(106) Park, H. Y., Qiu, X., Rhoades, E., Korlach, J., Kwok, L. W., Zipfel, W. R., Webb, W. W., Pollack, L. Achieving uniform mixing in a microfluidic device: hydrodynamic focusing prior to mixing. *Analytical chemistry* **2006**, *78*, 4465–4473.

(107) Knight, J. B., Vishwanath, A., Brody, J. P., Austin, R. H. Hydrodynamic Focusing on a Silicon Chip: Mixing Nanoliters in Microseconds. *Phys. Rev. Lett.* **1998**, *80*, 3863–3866.

(108) Lee, J. N., Park, C., Whitesides, G. M. Solvent compatibility of poly(dimethylsiloxane)-based microfluidic devices. *Analytical chemistry* **2003**, *75*, 6544–6554.

(109) Abate, A. R., Lee, D., Do, T., Holtze, C., Weitz, D. A. Glass coating for PDMS microfluidic channels by sol–gel methods. *Lab Chip* **2008**, *8*, 516.

(110) Barrett, R., Faucon, M., Lopez, J., Cristobal, G., Destremaut, F., Dodge, A., Guillot, P., Laval, P., Masselon, C., Salmon, J.-B. X-ray microfocussing combined with microfluidics for on-chip X-ray scattering measurements. *Lab on a chip* **2006**, *6*, 494–499.

(111) Ren, K., Dai, W., Zhou, J., Su, J., Wu, H. Whole-Teflon microfluidic chips. *Proceedings of the National Academy of Sciences* **2011**, *108*, 8162–8166.

(112) Chang, C.-C., Huang, Z.-X., Yang, R.-J. Three-dimensional hydrodynamic focusing in two-layer polydimethylsiloxane (PDMS) microchannels. *J. Micromech. Microeng.* **2007**, *17*, 1479–1486.

(113) Sundararajan, N., Pio, M. S., Lee, L. P., Berlin, A. A. Three-Dimensional Hydrodynamic Focusing in Polydimethylsiloxane (PDMS) Microchannels. *J. Microelectromech. Syst.* **2004**, *13*, 559–567.

(114) Mao, X., Waldeisen, J. R., Juluri, B. K., Huang, T. J. Hydrodynamically tunable optofluidic cylindrical microlens. *Lab on a chip* **2007**, *7*, 1303–1308.

(115) Tripathi, S., Kumar, A., Bala Varun Kumar, Y. V., Agrawal, A. Three-dimensional hydrodynamic flow focusing of dye, particles and cells in a microfluidic device by employing two bends of opposite curvature. *Microfluid Nanofluid* **2016**, *20*.

(116) Renckens, Theodorus J. A., Janeliunas, D., van Vliet, H., van Esch, Jan H., Mul, G., Kreutzer, M. T. Micromolding of solvent resistant microfluidic devices. *Lab Chip* **2011**, *11*, 2035.

(117) Unger, M. A. Monolithic Microfabricated Valves and Pumps by Multilayer Soft Lithography. *Science* **2000**, *288*, 113–116.

(118) Leibler, L. Theory of Microphase Separation in Block Copolymers. *Macromolecules* **1980**, *13*, 1602–1617.

(119) Hamley I. W. *The physics of block copolymers*; Oxford University Press: Oxford, New York, 1998.

(120) Förster S. *Amphiphilic Block Copolymers for Templating Applications*; Springer Berlin Heidelberg, 2003.

(121) Pollack, L., Tate, M. W., Darnton, N. C., Knight, J. B., Gruner, S. M., Eaton, W. A., Austin, R. H. Compactness of the denatured state of a fast-folding protein measured by submillisecond small-angle x-ray scattering. *Proceedings of the National Academy of Sciences* **1999**, *96*, 10115–10117.

(122) Wunderlich, B., Nettels, D., Benke, S., Clark, J., Weidner, S., Hofmann, H., Pfeil, S. H., Schuler, B. Microfluidic mixer designed for performing single-molecule kinetics with confocal detection on timescales from milliseconds to minutes. *Nature protocols* **2013**, *8*, 1459–1474.

(123) Simonnet, C., Groisman, A. Chaotic mixing in a steady flow in a microchannel. *Physical review letters* **2005**, *94*, 134501.

(124) Devaraju, Naga Sai Gopi Krishna, Unger, M. A. Multilayer soft lithography of perfluoropolyether based elastomer for microfluidic device fabrication. *Lab on a chip* **2011**, *11*, 1962–1967.

(125) Goyal, S., Desai, A. V., Lewis, R. W., Ranganathan, D. R., Li, H., Zeng, D., Reichert, D. E., Kenis, P. J. A. Thiolene and SIFEL-based Microfluidic Platforms for Liquid-Liquid Extraction. *Sensors and actuators. B, Chemical* **2014**, *190*, 634–644.

(126) Otten, A., Köster, S., Struth, B., Snigirev, A., Pfohl, T. Microfluidics of soft matter investigated by small-angle X-ray scattering. *Journal of synchrotron radiation* **2005**, *12*, 745–750.

(127) Park, H. Y., Kim, S. A., Korlach, J., Rhoades, E., Kwok, L. W., Zipfel, W. R., Waxham, M. N., Webb, W. W., Pollack, L. Conformational changes of calmodulin upon Ca2+ binding studied with a microfluidic mixer. *Proceedings of the National Academy of Sciences of the United States of America* **2008**, *105*, 542–547.

(128) Förster, S., Berton, B., Hentze, H.-P., Krämer, E., Antonietti, M., Lindner, P. Lyotropic Phase Morphologies of Amphiphilic Block Copolymers. *Macromolecules* **2001**, *34*, 4610–4623.

(129) Discher, D. E. Polymer Vesicles. *Science* **2002**, *297*, 967–973.

(130) Xiao, R. Z., Zeng, Z. W., Zhou, G. L., Wang, J. J., Li, F. Z., Wang, A. M. Recent advances in PEG-PLA block copolymer nanoparticles. *International journal of nanomedicine* **2010**, *5*, 1057–1065.

Appendix

A) Supplementary Information

NOA microfluidic chip preparation

The microfluidic device was prepared with UV- light curable Norland Optical Adhesive (NOA 81). Therefore, PDMS Masters with the negative device structure was made via soft lithography. The liquid NOA was poured over the PDMS Master. For little background scattering of the microfluidic device, the analyzable part of the device was prepared as thin as possible. However, inlets and outlets of the devices had to remain thicker (at least 2-3 mm) for proper adjustment of the tubings. Therefore, the channel cross and its leaving channel was covered by a blank PDMS so that the liquid NOA is thinned to a height of the structured part of ~200 µm. The PDMS-NOA-PDMS stacking was then cured under UV light for five minutes. To cover the cured channels another PDMS-NOA-PDMS stack with unstructured PDMS was prepared and cured for one minutes. Afterwards, the two NOA parts were removed from their PDMS Masters, bonded together and cured again under UV light for five minutes. Thereafter, PE-tubings were connected to the inlets and outlets of the channels and clued on it to prevent leaking of the floating liquids.

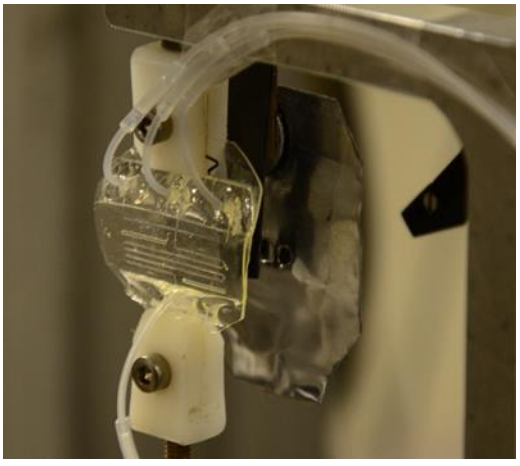

Figure S 1. Photo of the NOA-chip with connected tubings in the sample holder for the SAXS set-up.

Table S 1. Fit data for SAXS measurements of 20 wt% PI_{70}-*b*-PEG_{60}/dioxane in polyimide microfluidic device.

Position	N	f	X	R_g [nm]	a [nm]	Δ [nm]	displ. [nm]	R_c [nm]
1	131	0.498	0.0727	3.99				
2	130	0.500	0.0660	3.85				
3					31.10	76.40	4.61	6.72
5					31.30	105.00	4.53	6.72
10					32.60	100.00	3.74	6.72
13					32.90	104.00	4.59	6.72
16					32.90	115.00	5.05	6.72

Table S 2. Fit data for SAXS measurements of 20 wt% PI_{70}-*b*-PEG_{60}/dioxane in SIFEL-capillary microfluidic device with flow rates of 1500 µl/h for water and polymer solution, 750 µl/h for the middle dioxane buffer stream and 100 µl/h for the remaining buffer streams.

Position	N	f	χ	R_g [nm]	a [nm]	Δ [nm]	displ. [nm]	R_c [nm]
1	131	0.498	0.0370	3.73				
1.5	131	0.498	0.0514	3.92	21.10	35.20	4.30	6.24
2					33.30	101.00	6.64	6.68
5					32.70	97.30	7.39	6.78
8					33.60	79.50	3.58	7.10

Table S 3. Fit data for SAXS measurements of 20 wt% PI_{70}-*b*-PEG_{60}/dioxane in SIFEL-capillary microfluidic device with flow rates of 1500 µl/h for water and polymer solution, 500 µl/h for the middle dioxane buffer stream and 100 µl/h for the remaining buffer streams.

Position	N	f	X	R_g [nm]	a [nm]	Δ [nm]	displ. [nm]	R_c [nm]
1	131	0.498	0.0414	3.93	26.20	33.40	4.76	6.82
1.5					30.80	60.70	4.82	6.93
2					30.60	41.60	4.96	7.08
5					31.70	66.50	3.81	7.21
8					34.00	84.70	3.15	7.31

Table S 4. Fit data for SAXS measurements of 20 wt% PI_{70}-*b*-PEG_{60}/dioxane in SIFEL-capillary microfluidic device with flow rates of 1000 µl/h for water and polymer solution, 400 µl/h for the middle dioxane buffer stream and 63 µl/h for the remaining buffer streams

Position	a [nm]	Δ [nm]	displ. [nm]	Rc [nm]
1	33.70	84.00	3.92	6.93
2	33.30	90.20	4.54	7.00
3	33.30	102.00	3.82	7.14
4	33.50	97.30	3.67	7.14
6	34.90	96.50	3.91	7.10

Table S 5. Fits for SAXS measurements of 20 wt% PI_{70}-b-PEG_{60}/dioxane in SIFEL-capillary microfluidic device with flow rates of 1000 µl/h for water and polymer solution, 200 µl/h for the middle dioxane buffer stream and 63 µl/h for the remaining buffer streams

Position	a [nm]	Δ [nm]	displ. [nm]	Rc [nm]
1	33.90	81.60	3.23	7.05
2	33.10	73.70	2.55	7.14
3	33.70	78.30	3.29	7.15
4	34.20	69.50	4.01	7.15
5	34.60	94.70	3.92	7.15
6	33.60	106.00	3.02	7.12

Table S 6. Fit data for SAXS measurements of 20 wt% PI_{70}-*b*-PEG_{60}/dioxane in glass capillary of 1 mm diameter.

Position	N	f	X	R_g [nm]	a [nm]	Δ [nm]	displ. [nm]	R_c [nm]
3	131	0.498	0.0717	4.53				
4	130	0.500	0.0740	4.60				
5	130	0.500	0.0740	4.60				
6	130	0.498	0.0748	4.61				
7	130	0.498	0.0755	4.64				
8	131	0.499	0.0753	4.66				
9					24.10	126.00	1.35	7.82
10					24.30	113.00	1.44	8.04
11					26.30	107.00	2.86	7.53
12					28.50	50.40	4.07	7.20
13					27.00	36.80	3.91	7.03
14					28.30	41.40	4.18	6.89
15					28.30	33.80	3.04	6.74
16					28.00	36.20	3.40	6.63

B) List of Abbreviations

µ

µ-TAS *Micro-Total Analysis System*

A

AFM *Atomic Force Microscope*

B

BCC *Body-Centered Cubic*

C

CE *Capillary Electrophoresis*
CLSM *Confocal Laser Scanning Microscopy*
CMC *Critical Micelle Concentration*
CNC *Computerized Numerical Control*
cryo-TEM *Cryogenic Transmission Electron Microscopy*

D

Da *Dalton*
DESY *Deutsches Elektronen-Synchrotron*
DLS *Dynamic Light Scattering*
DNA *Deoxyribonucleic acid*

E

ERSF *European Synchrotron Radiation Facility*

F

FDM *Finite Difference Method*
FEM *Finite-Element Method*

G

GISAXS *Grazing Incidence Small Angle X-ray Scattering*
GPC *Gel Permeation Chromatography*

H

Hex *Hexagonally orderd cylinders*
HPLC *High Performance Liquid Chromatography*

I

ICE *Integrated Capillary Electrophoresis*

L

Lam *Lamellar phase*
LIGA *Lithografie, Galvanoformung, Abformung*

M

MC *Main Channel*
MF *Microfluidic/Microfluidics*
MIMIC *Micromolding In Capillaries*
MiNaXS *Micro- and Nanofocus X-ray Scattering*

N

NA *Numerical Aperture*
nm *nanometer*
NOA *Norland Optical Adhesive*

O

O *Oxygen*
ODT *Order-Disorder Transition*
OM *Optical Microscope*

P

PC *Poly(carbonate)*
PDMS *Poly(dimethylsiloxane)*
PE *Poly(ethylene)*
PEEK *Poly(ether ether ketone)*
PEG *Poly(ethylene glycol)*
PI *Poly(isoprene)*
PLA *Poly(lactic acid)*
PMMA *Poly(methyl methacrylate)*
PVC *Poly(vinyl chloride)*

S

SAXS *Small Angle X-ray Scattering*
SC *Side Channel*
SEM *Scanning Electron Microscopy*
Si *Silicon*
SSL *Strong Segragation Limit*
STM *Scanning Tunnelling Microscope*

T

TEM *Transmission Electron Microscopy*
THF *Tetrahydrofuran*

U

UV *Ultraviolet*

W

WSL *Weak SegregationLimit*

X

XRD *X-ray Diffraction*

C) List of Figures

Figure 1. Schematic section of a microfluidic device described in chapter 4.2 with the second channel cross, where two separated streams are focused. The reaction progress of growing micelles forming a hexagonal ordering is schematically shown, demonstrating the transformation of the time scale to the length scale along the channel. 2

Figure 2. Illustration of the different self- assembly monomers: a surfactant with the blue head group and the red tail and various block copolymers where different colors show the different blocks. Adapted with permission from Blanazs, A., Armes, S.P., Ryan, A.J., Self-Assembled Block Copolymer Aggregates: From Micelles to Vesicles and their Biological Applications. Copyright (2009) John Wiley and Sons and from Schacher, F.H.,Rupar, P.A., Manners, I., Funktionale Blockcopolymere: nanostrukturierte Materialien mit neuen Anwendungsmöglichkeiten. Copyright (2012) John Wiley and Sons [9,10] 5

Figure 3. Illustration of the self-assembly of amphiphiles like diblock copolymers or surfactants at low concentration. Adapted with permission from Blanazs, A., Armes, S.P., Ryan, A.J., Self-Assembled Block Copolymer Aggregates: From Micelles to Vesicles and their Biological Applications. Copyright (2009) John Wiley and Sons and from Nagarajan, R., Ruckenstein, E., Theory of surfactant self-assembly: a predictive molecular thermodynamic approach. Copyright (1991) American Chemical Society.[10,19] 7

Figure 4. Scheme of the structure determination of block copolymers. Adapted with permission from Antonietti, M., Förster, S., Vesicles and Liposomes: A Self-Assembly Principle Beyond Lipids. Copyright (2003) John Wiley and Sons [21] 8

Figure 5. Illustration of an ideal phase diagram of a diblock copolymer. Adapted with permission from Förster, S., Plantenberg, T., From Self-Organizing Polymers to Nanohybrid and Biomaterials. Copyright (2002) John Wiley and Sons [17] 12

Figure 6. Scheme of classical lyotropic structures of a diblock copolymer. Adapted with permission from Förster, S., Plantenberg, T., From Self-Organizing Polymers to Nanohybrid and Biomaterials. Copyright (2002) John Wiley and Sons [17] 13

Figure 7. Hierarchy at a length scale of sub nanometer to hundreds of nanometers. Adapted with permission from Förster, S., Plantenberg, T., From Self-Organizing Polymers to Nanohybrid and Biomaterials. Copyright (2002) John Wiley and Sons [17] 14

Figure 8. Scheme of the density of a fluid depending on the probing volume. Adapted with permission from Bruus, H., Theoretical Microfluidics, (2008), Oxford University Press, Batchelor, G., K., An introduction to fluid dynamics, 2nd ed, (2000) Cambridge University Press and Tabeling, P., Introduction to Microfluidics, (2010), Oxford University Press [30,34,35] 17

Figure 9. Illustration of a microfluidic channel with acceleration in x-direction. Adapted with permission from Bruus, H., Theoretical Microfluidics, (2008), Oxford University Press and Phillips, R., Kondev, J., Theriot, J., Physical biology of the cell; Copyright (2009) Garland Science-Books [30,38] 18

Figure 10. Schematic description of all pressure forces acting on the volume element dV. Adapted with permission from Phillips, R., Kondev, J., Theriot, J., Physical biology of the cell; Copyright (2009) Garland Science-Books [38] 19

Figure 11. Scheme of a liquid between two plates, whereas the lower is fixed and the upper one is moving with vz. Adapted with permission from Bruus, H., Theoretical Microfluidics, (2008), Oxford University Press [30] 20

Figure 12. Chart of the different flows and slips. Adapted with permission from Bruus, H., Theoretical Microfluidics, (2008), Oxford University Press and Lauga, E., Microfluidics: The No-Slip Boundary Condition. Copyright (2007) Springer [30,43] 24

Figure 13. Pressure driven flow between two infinite parallel plates. Adapted with permission from Bruus, H., Theoretical Microfluidics, (2008), Oxford University Press [30] 25

Figure 14. Cylindrical channel with radius r. Adapted with permission from Bruus, H., Theoretical Microfluidics, (2008), Oxford University Press [30] 27

Figure 15. Cross-section of a rectangular shaped channel with height h and width w. Adapted with permission from Bruus, H., Theoretical Microfluidics, (2008), Oxford University Press [30] 29

Figure 16. Scheme of a cuboid with volume V and a flux J(x) occurring due to a concentration gradient in x-direction. Adapted with permission from Bruus, H., Theoretical Microfluidics, (2008), Oxford University Press and Phillips, R., Kondev, J., Theriot, J., Physical biology of the cell; Copyright (2009) Garland Science-Books [30,38] 34

Figure 17. Left picture shows a band of solute inserted into a channel. The middle image shows the increasing parabolic profile, if diffusion is absent. The right scheme shows plug flow evolving due to diffusion and convection. 37

Figure 18. Description of the PDMS chip fabrication steps. Adapted with permission from Xia, Y., Whitesides, G., M., SOFT LITHOGRAPHY. Copyright (1998), Annual Reviews [14] 40

Figure 19. Illustration of the rapid prototyping process; beginning with the idea of the device design on the left to the completed microfluidic chip on the right. Adapted with permission from Xia, Y., Whitesides, G., M., SOFT LITHOGRAPHY. Copyright (1998), Annual Reviews and Qin, D., Xia, Y., Whitesides, G., M., Rapid prototyping of complex structures with feature sizes larger than 20 μm. Copyright (1996), John Wiley and Sons and Duffy, D., C., McDonald, J.,C., Schueller, O., J., A., Rapid Prototyping of Microfluidic Systems in Poly(dimethylsiloxane), Copyright (1998), American Chemical Society.[14,50,52] 42

Figure 20. Scheme of X-ray diffraction at two atoms positioned at distance r. Adapted with permission from Stribeck, N., X-ray scattering of soft matter, Copyright (2007), Springer, Glatter, O., Kratky, O., Small angle x-ray scattering, Copyright (1982) Elsevier* and Guinier A., X-ray diffraction, Dover, Copyright (1963).[60–62] 44

Figure 21. Scattering by two atoms A and B at distance r. Adapted with permission from Glatter, O., Kratky, O., Small angle x-ray scattering, Copyright (1982) Elsevier* and Guinier A. X-ray diffraction; Dover, Copyright (1963). [60,62] 45

Figure 22. The “magic square” shows the relations of the different parameters. Adapted with permission from Stribeck, N., X-ray scattering of soft matter, Copyright (2007), Springer. [61] 53

Figure 23. Scheme of the different structures and their characteristic parameters used in Scatter software. Adapted with permission from Förster, S. Fischer, S., Zielske, K., Schellbach, C., Sztucki, M, Lindner, P., Perlich, J., Calculation of scattering-patterns of ordered nano- and mesoscale materials, Copyright (2011), Elsevier [70] 56

Figure 24. Set-up of small angle X-ray scattering (SAXS) experiment with a source generating X-rays. The collimation system adjusts the beamsize and a microfluidic chip includes the sample. The

detector records the characteristic scattering patterns of the sample. Adapted with permission from Stribeck, N., X-ray scattering of soft matter, Copyright (2007), Springer and Lindner, P., Zemb, T., Neutrons, X-rays and Light: Scattering Methods Applied to Soft condensed Matter, Copyright Elsevier (2002)*. [61,63] 61

Figure 25. Length scale with the different analytical methods and their minimum resolution. Adapted with permission from Michler, G., H., Electron microscopy of polymers, Copyright (2008), Springer [77] 62

Figure 26. Scheme of the set-up of a confocal laser scanning microscope. Adapted with permission from Prasad, V., Semwogerere, D., Weeks, E.,R., Confocal microscopy of colloids, Copyright (2007), Journal of Physics : Condensed Matter.[76] 64

Figure 27. Pathway of the light in confocal laser scanning microscope (CLSM) and optical microscope (OM) Adapted with permission from Michler, G., H., Electron microscopy of polymers, Copyright (2008), Springer [77] 65

Figure 28. Secondary processes occurring when electron beam hit the sample. Adapted with permission from Williams, D., B., Carter, C., B., The Transmission Electron Microscope, Copyright (2009), Springer and Shindo, D., Oikawa, T., Analytical electron microscopy for materials science, Copyright (2002), Springer.[75,82] 66

Figure 29. Scheme of a basic transmission electron microscope. Adapted with permission from Michler, G., H., Electron microscopy of polymers, Copyright (2008), Springer [77] 68

Figure 30. Requirements for microfluidic device material. 71

Figure 31. Light microscope images of a PDMS microfluidic device at the channel cross. Left: Channel cross with no penetration of THF. Right: THF pumped into the MF chip for 5 minutes, causes swelling of the PDMS material and change in the channel geometry. 72

Figure 32. Optical microscope images of toluene pumped through NOA81 MF chip after 0 min, 5 min, 10 min and 20 min. 73

Figure 33. Chemical structure of SIFEL. Adapted with permission from Maltezos, G., Gracia, E., Gomez, F., A., Vyawhare, S., van Dam, R., Michael, chen, Y., Scherer, a., Design and fabrication of chemically robust three-dimensional microfluidic valves. Copyright (2007), Royal Society of Chemistry. [91] 74

Figure 34. SAXS measurements of all tested materials in configuration 1. 76

Figure 35. SAXS measurements of all tested materials in configuration 3. 76

Figure 36. Scheme of sagging and pairing at too high and too low aspect ratio. Adapted with permission from Xia, Y., Whitesides, G., M., SOFT LITHOGRAPHY. Copyright (1998), Annual Reviews [14] 79

Figure 37. Concentration simulation (COMSOL) of the microfluidic chip with a two-dimensional hydrodynamic focusing of the reactant flowing from the main channel (MC) by the two solutions coming from the side channels (SC). 80

Figure 38. Sketch of the microfluidic device and the analyzed positions (1-9) along the channel. TDMAO is pumped into the main channel, which is hydrodynamically focused by LFPO from both side channels. 83

Figure 39. SAXS curves of 100 mM LPFO/H_2O (green) and 100 mM TDMAO/H_2O (blue) measured in a glass capillary of 1 mm outer radius and a wall thickness of 0.01 mm. 87

Figure 40. (a) Detail: Evolution of structures across the interface of the two solutions; (b) Overview of scattering images measured across the microfluidic channel; number each position from 1–9 scanned in y- and x-line. 88

Figure 41. Both graphs show all SAXS measurements of one-line scan along y-direction at the microfluidic channel cross. A concentration of 100 mM and a flow velocity of 100 µl/h for each solution was used. Left: Parallel stacking of adjacent measurements, showing the symmetric flow focusing of TDMAO with LPFO in the channel cross. Right: Plot shows the three different structures occurring in the channel cross, i.e. spherical micelles, cylindrical micelles and the evolved disk-like structures (intermediate). The black solid curves show the corresponding fit curves for each structure. 89

Figure 42. SAXS measurements of one line in x-direction for all 9 positions, starting in the middle of the channel cross (cylindrical micelles). A concentration of 100 mM and flow velocities of 100 µl/h each were used. 90

Figure 43. SAXS measurements downstream the NOA-microfluidic chip show the structural evolution of 100 mM TDMAO and 100 mM LPFO solutions with 100 µl/h flow each. The black solid lines show the corresponding fits to the original and intermediate downstream structures. ... 91

Figure 44. COMSOL velocity simulation of a microfluidic chip with 200 µm width, 100 µm height and a perpendicular channel cross. The starting flow rates are 100 µl/h for each inlet. The unit of the color scale bar is [m/s]. Point "E" indicates the first contact of TDMAO and LPFO. The Field was calculated for the mid-plane in vertical direction. 93

Figure 45. (a) Scanned lines (blue and red) in the calculation of mixing times, and (b) the corresponding calculated velocities as function of channel downstream position x. 94

Figure 46. Elapsed time along the streamline, i.e. channel position (left) and interdiffusion across the interface at the corresponding time, assuming 10^{-9} m^2/s as the diffusion coefficient. It shows that interdiffusion across adjacent 10 x 10 micron pixels becomes significant already in the channel cross, but across two pixels only downstream the reaction channel. 96

Figure 47. Concentration profile $c(z,t)$ calculated from Eq. (166) for times from 1 second up to 10^6 seconds corresponding to 12 days. Noticeable concentration changes at distances of ca. 0.5 mm from the interfaces are occurring between 100-1000 seconds, i.e. between ca. 1 minute and 10 minutes, which corresponds to the time scale of the SAXS capillary experiments. 98

Figure 48. SAXS-curves measured at z = -0.5 mm for different times upon interdiffusion. We observe a structural evolution from spherical micelles to disk-like micelles. 99

Figure 49. Cryo-TEM images of a 100 mM TDMAO/LPFO mixture prepared in microfluidic chip and measured 1d after preparation. Cryo-TEM shows single- and multi-wall vesicles with bilayer thickness (thick dark) of 1.9 nm and an interlamellar distance of 20.3 nm. 105

Figure 50. Left: Section of the device design. The red colored channels are from the upper structured chip half and the black lined channels are on the lower chip half. Right: Magnification of the two channel crosses with the different protective and buffer layers, resulting in two separated streams. 109

Figure 51. The left image shows the two separated streams of our chip design. Here the different structure stages can be followed due to the spatial separation. The right image shows the concentric sheath flow, where the different structures are not separately detectable due to the sheathing reagents. 110

Figure 52. Left: SEM image shows the two structured chip halves with the SIFEL layer containing the channel design and the stabilizing PDMS on top. Right: SIFEL-PDMS device with inserted glass capillary. 111

Figure 53. CLSM of the flow of fluorescein and rhodamine b in the SIFEL-hybrid chip. The left image shows the hydrodynamic focusing at the second channel cross. The right picture shows the two separated streams flowing in the glass capillary. 112

Figure 54. CLSM image of the SIFEL hybrid chip with Ca-green, $CaCl_2$ and Cascade blue in buffer solution with flow rates AB 500 µl/h, middle buffer stream 100 µl/h, remaining streams 63 µl/h. 112

Figure 55. (a) Y-scan at position 1 of SIFEL-cap-chip measurements at flow rates A, B 1500 µl/h, middle buffer stream 500 µl/h and remaining streams 6*100 µl/h. The step width for each measured point was 15 µm. (b) y-scan at position 8 at flow rates A, B 1500 µl/h, middle buffer stream 500 µl/h and remaining streams 6*100 µl/h. 113

Figure 56. Comparison of two measurements analyzing the self-assembly process of 20 wt% PI-(b)-PEO in polyimide chip device (blue curve) and SIFEL-hybrid chip (red curve). 114

Figure 57. Scheme of (a) the polyimide microfluidic chip with the three inlets (MC, SC1, SC2), the perpendicular channel cross and the outlet (O), and (b) the SIFEL-capillary hybrid chip with the 3-dimensional design. The four bright gray colored inlets are imprinted into the bottom chip side and the five black inlets into the upper chip side. 121

Figure 58. Scheme of the SIFEL 3D-channel design (left) and confocal laser scanning microscopy image (right) of a cross-section of the glass capillary, showing two rhodamine B streams in the capillary of a SIFEL-capillary chip, still separated by the buffer layer. 122

Figure 59. SAXS measurements of 20 wt% PI_{70}-(b)-PEG_{60}/dioxane in a polyimide microfluidic device along the downstream direction, after mixing with water. The evolution from a broad peak indicating weak segregation into a well-defined Bragg peak at lower q, indicating the formation of an ordered lyotropic micellar phase, is clearly visible. 124

Figure 60. Y-scan through the glass capillary with a step width of 15 µm, with SAXS-curves measured at the corresponding positions. In the experiment a 20 wt% PI_{70}-(b)-PEG_{60}/dioxane solution was investigated at flow rates of 1500 µl/h for water and the polymer solution, 750 µl/h for the middle dioxane buffer stream and 100 µl/h for the sheath streams. The evolution of ordered micellar structures in the center of the capillary can be well observed. 129

Figure 61. SAXS curves of 20 wt% PI_{70}-(b)-PEG_{60}/dioxane measured downstream in x-direction in the SIFEL-capillary microfluidic device with flow rates of (a):1500 µl/h for water and polymer solution (W/PS), 750 µl/h for the middle dioxane buffer stream (M) and 100 µl/h for the remaining buffer streams (R); (b):1500 µl/h (W/PS), 500 µl/h (M) and 100 µl/h (R); (c):1000 µl/h (W/PS), 400 µl/h (M) and 63 µl/h (R); (d):1000 µl/h (W/PS), 200 µl/h (M) stream and 63 µl/h (R). The structural evolution from the weakly segregated polymer/dioxane solution to the ordered, strongly segregated lyotropic liquid crystalline micellar phase can be clearly observed. 130

Figure 62. Temporal evolution of the block copolymer and micellar radii $R*$ and the characteristic distance $d*$ as a function of time after mixing. Micelle formation occurs within the first 10 milliseconds. Within 0.7 seconds the micelles arrange on an ordered lattice, with the maximum order of the resulting lyotropic liquid crystalline phase reached after 2 seconds. 135

Figure 63. SAXS-curves measured along a vertical concentration gradient of a 20 wt% PI_{70}-(b)-PEG_{60}/dioxane and water in a vertical glass capillary. The concentration scan starts at the polymer

rich phase (bottom) and proceeds towards the water rich phase (top). A development of an ordered structure and the subsequent decrease of the micellar core diameter, as indicated by the shift of the formfactor minimum to higher q-values can be observed. 137

Figure 64. Evolution of the polymer radius of gyration Rg (○), the micellar core radius Rc (●) and the unit cell dimension a (■) along the concentration gradient in the vertically aligned capillary from the dioxane-rich into the water-rich phase. 138

Figure 65. Cryo-TEM images of 20 wt% PI_{70}-(b)-PEG_{60}/dioxane/water solution collected after mixing in microfluidic chip. A coexistence of small spherical micelles and larger diameter cylindrical micelles can be observed. 139

Figure 66. Cryo-TEM images of 20 wt% PI-(b)-PEO after reverse phase evaporation. We observe a coexistence of cylindrical micelles and vesicles together with intermediate structures. 140

Figure 67. Scheme of the structural evolution from single block copolymers into spherical micelles, cylindrical micelles and vesicles with the corresponding time scales (milliseconds, hours, days), as observed by selective solvent-induced self-assembly. Whereas the assembly into micelles is very fast and transport-limited, the formation of cylindrical micelles and bilayers requires micellar fusion, which occurs on much longer time scales. 141

Figure 68. SAXS measurement in microfluidic device with a concentration of 20 wt% and flow rates of PEG_{84}-(b)-PLA_{130}/dioxane/H_2O: 1000 µl/h, middle buffer stream: 500 µl/h and remaining buffer streams: 100 µl/h. (a) shows the y-scan at Position 4 and (b) the single selected scattering curves at Position 1, 1.5 and 4. 147

Figure 69. Microfluidic chip experiment with flow rates of 20 wt% PEG_{84}-(b)-PLA_{130}/dioxane /H_2O: 1000 µl/h, middle buffer stream: 400 µl/h, remaining streams: 63 µl/h at x-Position 1 (a), 5 (b) and 6 (c) and the selection of the most pronounced curves of each position in (d). 148

Figure 70. 20 wt% PEG_{84}-(b)-PLA_{130}/dioxane in microfluidic chip with flow rates of polymer solution/H_2O: 1000 [µl/h] each, middle buffer stream: 100 [µl/h], and remaining sheathing streams: 63 [µl/h]. (a) shows a y-scan at position 4 and (b) show selected curves from x-position 1 to 6. . 149

Figure 71. SAXS measurement of the 20 wt% PEG_{217}-(b)-PLA_{532}/dioxane in the SIFEL-capillary hybrid chip with flow velocities of 1000 µl/h for the 20 wt% PEG_{217}-(b)-PLA_{532}/dioxane and water stream each, 200 µl/h for the buffer stream and 63 µl/h for the remaining sheathing streams. 150

Figure 72. Time scan of 20 wt% PEG_{217}-(b)-PLA_{532} /dioxane in 1 mm glass capillary. 152

Figure 73. Concentration scan of (a) 20 wt%, (b) 30 wt% and (c) 40 wt% PEG_{84}-(b)-PLA_{130}/dioxane with water in 1 mm glass capillary of 10 µm wall thickness. 154

Figure 74. Concentration scan of (a) 20 wt%, (b) 30 wt% and (c) 40 wt% PEG_{217}-(b)-PLA_{532}/dioxane with water in 1 mm capillary with 10 µm wall thickness. 157

Figure 75. Structural evolution of 20 wt% PEG_{84}-(b)-PLA_{130} in the MF-chip. The different experiments (A/B: 1000 µl/h, M: 500 µl/h and B: 100 µl/h (red), A/B: 1000 µl/h, M: 400 µl/h and B: 63 µl/h (green), A/B: 1000 µl/h, M: 100 µl/h and B: 63 µl/h (blue) are plotted against the respective distance from the second channel cross to the measurement position. The unit cell dimension a (hollow squares) as well as the core radius Rc (spheres) are depicted. 159

Figure 76. Summary of the fitted values for both PEG-(b)-PLA block copolymers in the capillary concentration scans. The first row shows the unit cell dimension a (hollow square) and the core radius Rc (sphere) of the PEG_{84}-(b)-PLA_{130} whereas red is the 20 wt%, green the 30 wt%, and dark blue the 40 wt% scan. In the second row the PEG_{217}-(b)-PLA_{532} concentration scan with the

different concentrations (20 wt% bright blue, 30 wt% magenta, 40 wt% orange) and also for a and Rc is illustrated..... 160

Figure 77. Outline of the 20 wt% PEG_{217}-(b)-PLA_{532} time dependent SAXS measurements. 161

Figure 78. Cryo-TEM images of PEG_{84}-(b)-PLA_{130} after reverse phase evaporation..... 163

Figure 79. Cryo-TEM of PEG_{217}-(b)-PLA_{532} after reverse phase evaporation. 163

D) List of Tables

Table 1. Calculations for the different shapes, with $R = R1 = R2$. Adapted with permission from Antonietti, M., Förster, S., Vesicles and Liposomes: A Self-Assembly Principle Beyond Lipids. Copyright (2003) Jon Wiley and Sons and Israelachvili, J. N., Mitchell, D. J., Ninham, B. W. Theory of self-assembly of hydrocarbon amphiphiles into micelles and bilayers. J. Chem. Soc., Faraday Trans. 2 1976, 72, 1525 [20,21] 9

Table 2. Resistant test of various polymers and the corresponding solvents. x: dissolution or swelling of the material, o: no change observed, -: not tested 73

Table 3. Fit parameters corresponding to the SAXS curves in Figure 43. The first line belongs to the first curve, the second line belongs to the second curve et cetera. The mesh numbers correspond to the mesh-scan numbers in Figure 40..... 92

Table 4. Structural parameters of the LPFO-, TDMAO and mixed micelles..... 102

Table 5. Fit parameters for SAXS measurements of 20 wt% PI_{70}-(b)-PEG_{60}/dioxane in polyimide microfluidic device. Δx is the channel position with respect to the beginning of the channel cross, Δt the corresponding time after mixing, Rg the radius of gyration, a the unit cell size, Δ the domain size, and $Rc$the micellar core radius..... 127

Table 6. Volumetric flow rates of the water stream QW, the polymer/dioxane stream QPD, the buffer stream QB, the 6 sheath streams QS, the total flow rate $Qtotal$, the calculated widths $wB1$ and $wB2$ of the buffer layer according Eqs. (179) and (181), then mean flow velocity v, the diffusion time tD across the buffer layer, and $x0$-position for the four different flow-focusing experiments #1 - #4 in the 3D-SIFEL capillary hybrid chip..... 133

Table 7. Positions Δx, times after mixing Δt, fitted radius of gyration Rg, unit cell size a, ordered domain size Δ, and micellar core radius Rc as determined by SAXS-experiments of 20 wt% PI_{70}-(b)-PEG_{60}/dioxane in a SIFEL-capillary microfluidic device at different flow rates..... 134

Table 8. Fit values of Figure 68 (b)..... 147

Table 9. Fit values of Figure 69 (d)..... 148

Table 10. Fit values of Figure 70 (b)..... 150

Table 11. Fit parameters of the time scan of 20 wt% PEG_{217}-(b)-PLA_{532} /dioxane in Figure 72 ... 152

Table 12. Fit values for the 20 wt% PEG_{84}-PLA_{130}/dioxane /water SAXS measurements in a 1 mm glass capillary (d=10 µm) shown in Figure 73 (a). 154

Table 13. Fit values for the SAXS measurements of 30 wt% PEG_{84}-PLA_{130}/dioxane /water; in Figure 73 (b)..... 155

Table 14. Fit values for the 40 wt% PEG_{84}-PLA_{130}/dioxane/water SAXS measurements, shown in Figure 73 (c)..... 156

Table 15. Fit values of the 20 wt% PEG_{217}-(b)-PLA_{532}/dioxane with water SAXS measurements in a 1 mm capillary, shown in Figure 74 (a). 157

Table 16. Fit values of the 30 wt% PEG_{217}-(b)-PLA_{532}/dioxane/water SAXS measurements, shown in Figure 74 (b)..... 158

Table 17. Fit values of 40 wt% PEG_{217}-(b)-PLA_{532} /dioxane Figure 74..... 158

Table 18. Δd_A values of microfluidic chip measurements of A: [PEG_{84}-(b)-PLA_{130}/dioxane/H_2O: 1000 µl/h, middle buffer stream: 500 µl/h and remaining buffer streams: 100 µl/h], B: [PEG_{84}-(b)-PLA_{130}/dioxane /H_2O: 1000 µl/h, middle buffer stream: 400 µl/h, remaining streams: 63 µl/h], C: Polymer solution/H_2O: 1000 µl/h each, middle buffer stream: 100 µl/h, and remaining sheathing streams: 63 µl/h]..... 159

E) Publications

Fürst, C., Roth, S.V., Drechsler, M., Förster, S. Self-assembly of block copolymers via micellar intermediate states into vesicles on time scales from milliseconds to days. *Manuscript submitted to Polymer*

Fürst, C., Rosenfeldt, S., Burghammer, M. Di Cola, E., Förster, S. Vesicle formation pathways under very fast and very slow formation conditions. *Manuscript ready for submission*

Fürst, C., Förster, S. Solvent resistant Microfluidic-Hybrid-Chip for three-dimensional hydrodynamic flow focusing. *Manuscript ready for submission*

F) Poster Presentations

May 2014: Fürst, C., Rosenfeldt, S., Burghammer, M., Roth, S.V., Förster, S. Controlled surfactant self-assembly in microfluidics channels investigated with in-situ micro-focus small angle X-ray scattering. *Flow14, Twente*

May 2015: Fürst, C. Seibt, S. With, S. Förster, S. CLSM and SAXS Life-Monitoring of Fast Amphiphile Self-Assembly. *IACIS, Mainz*

April 2016: Fürst, C., Förster, S. In-situ Investigation of Fast Self-Assembly Kinetics of Amphiphiles with Microfluidics and Small Angle X-ray Scattering. *12th Zsigmondy-Colloquium, Regensburg*

Acknowledgment/Danksagung

Natürlich wäre diese Doktorarbeit nicht ohne das Zutun vieler Menschen entstanden. Deshalb möchte ich mich ganz herzlich bei den folgenden Personen bedanken.

Mein Dank gebührt zunächst meinem Doktorvater Prof. Dr. Stephan Förster für die Betreuung während der letzten Jahre. Die stets offene Tür und die ansteckende Begeisterung waren sehr hilfreich und motivierend.

Des Weiteren möchte ich den Sekretärinnen, Elisabeth Düngfelder und Jennifer Hennessy der PC I danken. Ohne ihre Organisation und Hilfe bei jeglichen Bestellungen und Abrechnungen wäre es wohl weitaus anstrengender gewesen. Auch die netten Gespräche haben die Doktorandenzeit sehr versüßt.

Auch den technischen Angestellten, Karlheinz Lauterbach, Christine Thunig und Julia Moßner möchte ich sehr herzlich danken, für ihre Hilfe, ob Abfallentsorgung, Wasserversorgung, Sicherheitsbelehrung oder etwaige Organisation, und ihre stets freundliche Art. Unvergessen bleiben natürlich die vielen Geschichten vom *berühmten Meister* Karlheinz.

Ebenfalls möchte ich mich bei Dr. Sabine Rosenfeldt bedanken für ihre Unterstützung bei Messzeiten in Grenoble, sowie an der Ganesha und den immer wieder netten Gesprächen.

Ein herzliches Dankeschön an Dr. Stephan Hausschild für jegliche Hilfe im IT-Bereich, den vielen Doppelkeksen und 3D-Druck Eulen, sowie seine freundliche Art und unendlich Hilfsbereitschaft.

Einen riesen Dank gebührt auch Dr. Martin Dulle für seine Hilfe rund um SAXS. Seine unerschütterliche gelassene Art auch die 1000ste Streufrage zu beantworten ist bewundernswert. Auch Danke für das Korrekturlesen des SAXS-Teils der Dissertation.

Ich bedanke mich bei Dr. Xuelian Chen für die Unterstützung während der Synchrotron Messzeiten, ihren Humor und ihrer Freundschaft. Die vielen Diskussionen die oft weit über SAXS hinausgingen.

Ebenso danke ich Dr. Katja von Nessen und Dr. Denise Barrelmann-Kahlbohm für ihre Freundschaft. Es ist schön auch bei größerer Entfernung noch Kontakt halten zu können. Danke Katja für das Korrekturlesen.

Ein großes Dankeschön geht an Dr. Sara und Dr. Jan Schröder für die Freundschaft, die gemeinsamen Ausflüge und Feste. Es bedeutet mir sehr viel, dass wir noch so guten Kontakt halten können.

Ich danke Dr. Corinna Stegelmeier für ihre Freundschaft. Mit deiner „Yes, we can.“ Mentalität hast du mich oft motiviert.

Ebenso möchte ich mich bei Susi Seibt und Kirsten Volk für die schöne Zeit bedanken. Ob Sport oder Feiern mit euch zweien macht es Spaß. Danke Susi für das Korrekturlesen.

Ich danke Dr. Sascha Ehlert für die Begleitung in den letzten Jahren. Der gleiche Humor hat so einige lustige Abende und Bürotage beschert.

Ich danke meinen Bürokollegen ob ehemalig Sara, Sascha, Xuelian, oder gegenwärtig, Arne Lerch, Vanessa Leffler und Lina Mayr. Mit euch war die Zeit immer angenehm und lustig. Danke dafür!

Danke Daniela Pirner, für die lustigen Abende und dem Beistand als Leidensgenossin.

Ich bedanke mich unendlich bei der gesamten PC I. Ihr seid klasse! Ob Grillfeste, Geburtstagskuchen, Schoki-& Weinseminare oder natürlich Hilfe bei der Forschung, ich freue mich sehr bei einem so tollen Lehrstuhl gearbeitet zu haben.

Der größte Dank gebührt zu guter Letzt meiner Familie. Danke für eure stetige Unterstützung, auch wenn nicht immer klar war was ich so mache. Margot und Lucki ihr seid die besten Eltern! Ohne eure Hilfe wäre ich niemals so weit gekommen. Danke auch meiner Lieblingsschwester. Raphi, mit dir kann ich über alles reden und wir halten immer zusammen. Und Danke Sebastian mit deiner Art mich zu beruhigen alles zu entkatastrophieren und das Leben zu genießen. Du bist der Beste!

Declaration/(Eidesstattliche) Versicherungen und Erklärung

(§ 5 Nr. 4 PromO)

Hiermit erkläre ich, dass keine Tatsachen vorliegen, die mich nach den gesetzlichen Bestimmungen über die Führung akademischer Grade zur Führung eines Doktorgrades unwürdig erscheinen lassen.

(§ 8 S. 2 Nr. 5 PromO)

Hiermit erkläre ich mich damit einverstanden, dass die elektronische Fassung meiner Dissertation unter Wahrung meiner Urheberrechte und des Datenschutzes einer gesonderten Überprüfung hinsichtlich der eigenständigen Anfertigung der Dissertation unterzogen werden kann.

(§ 8 S. 2 Nr. 7 PromO)

Hiermit erkläre ich eidesstattlich, dass ich die Dissertation selbständig verfasst und keine anderen als die von mir angegebenen Quellen und Hilfsmittel benutzt habe.

(§ 8 S. 2 Nr. 8 PromO)

Ich habe die Dissertation nicht bereits zur Erlangung eines akademischen Grades anderweitig eingereicht und habe auch nicht bereits diese oder eine gleichartige Doktorprüfung endgültig nicht bestanden.

(§ 8 S. 2 Nr. 9 PromO)

Hiermit erkläre ich, dass ich keine Hilfe von gewerblichen Promotionsberatern bzw. -vermittlern in Anspruch genommen habe und auch künftig nicht nehmen werde.

Ort, Datum, Unterschrift